

The University of Maine

DigitalCommons@UMaine

---

Electronic Theses and Dissertations

Fogler Library

---

Spring 5-2020

## Development and Test of High Temperature Surface Acoustic Wave Gas Sensors

Armando E. Ayes Moncada

University of Maine, armando.ayes@maine.edu

Follow this and additional works at: <https://digitalcommons.library.umaine.edu/etd>



Part of the [Acoustics, Dynamics, and Controls Commons](#), [Electrical and Electronics Commons](#), [Electromagnetics and Photonics Commons](#), and the [Nanotechnology Fabrication Commons](#)

---

### Recommended Citation

Ayes Moncada, Armando E., "Development and Test of High Temperature Surface Acoustic Wave Gas Sensors" (2020). *Electronic Theses and Dissertations*. 3150.

<https://digitalcommons.library.umaine.edu/etd/3150>

This Open-Access Thesis is brought to you for free and open access by DigitalCommons@UMaine. It has been accepted for inclusion in Electronic Theses and Dissertations by an authorized administrator of DigitalCommons@UMaine. For more information, please contact [um.library.technical.services@maine.edu](mailto:um.library.technical.services@maine.edu).

**DEVELOPMENT AND TEST OF HIGH TEMPERATURE SURFACE  
ACOUSTIC WAVE GAS SENSORS**

By

Armando Emilio Ayes Moncada

B.S. in Electrical Engineering, University of Maine 2017

A THESIS

Submitted in Partial Fulfillment of the  
Requirements for the Degree of  
Master of Science  
(in Electrical Engineering)

The Graduate School  
The University of Maine  
May 2020

Advisory Committee:

Mauricio Pereira da Cunha, Professor of Electrical and Computer Engineering, Advisor

Robert Lad, Professor of Physics

John Vetelino, Professor of Electrical and Computer Engineering

© Armando Ayes 2020  
All Rights Reserved

# DEVELOPMENT AND TEST OF HIGH TEMPERATURE SURFACE ACOUSTIC WAVE GAS SENSORS

By Armando Emilio Ayes Moncada

Thesis Advisor: Dr. Mauricio Pereira da Cunha

An Abstract of the Thesis Presented  
in Partial Fulfillment of the Requirements for the  
Degree of Master of Science  
(in Electrical Engineering)  
May 2020

The demand for sensors in hostile environments, such as power plant environments, aerospace environments, oil and gas extraction, and high-temperature metallurgy environments, has risen over the past decades in a continuous attempt to increase process control, improve energy and process efficiency in production, reduce operational and maintenance costs, increase safety, and perform condition-based maintenance in equipment and structures operating in high-temperature harsh-environment conditions. The increased reliability, improved performance, and development of new sensors and networks with a multitude of components, especially wireless networks, are the target for operation in harsh environments. Gas sensors, in particular  $H_2$  sensors, operating above  $200^\circ C$  are required in the instrumentation, process control and general safety of a number of industries including coal, natural gas, and nuclear power generation facilities, the aerospace and automotive industries, metallurgical production and defense-related applications.

The surface acoustic wave (SAW) platform is a particularly promising option for high-temperature, harsh-environment gas sensing applications since the platform exhibits advantages, such as battery-free and wireless operation, small size, possibility for scale production using well-developed technologies from the semiconductor industry, and low cost of installation and operation.

In this work, one-port SAW resonators (SAWRs) operating along five different orientations on a commercially available langasite (LGS) wafer employing Pt-Al<sub>2</sub>O<sub>3</sub> electrodes and reflectors were designed, fabricated, and used as high-temperature H<sub>2</sub> sensors. Two of the selected orientations were predicted and confirmed to have temperature-compensated operation above 150°C. A gas sensor test setup was developed, capable of gas cycling between N<sub>2</sub>, O<sub>2</sub> and N<sub>2</sub>/H<sub>2</sub> mixtures under extended high-temperature periods (up to 650°C for over 20 hours). Thin film Pt-Al<sub>2</sub>O<sub>3</sub> was used as the electrode material for the transducers and reflectors capable of high-temperature operation, and also as H<sub>2</sub> sensing film. In addition, yttria-stabilized zirconia (YSZ) thin films with Pt decoration were tested as sensing films aimed to enhance the SAWR sensor response to H<sub>2</sub>. The SAW devices were monitored in excess of 1700 hours in real-time during gas cycling sequences up to 600°C, leading to the following findings: i) the Pt-Al<sub>2</sub>O<sub>3</sub> electrodes performed better for H<sub>2</sub> sensing than the Pt-decorated YSZ sensing film, showing as much as 50% higher frequency variation response in the 200°C to 400°C range; ii) different crystallographic orientations operating on the same LGS wafer experienced different responses to H<sub>2</sub> exposures up to 500°C; iii) the surface oxidation state of the SAWR sensors was shown to have an important impact on subsequent H<sub>2</sub> exposure responses. In addition, a sensor system employing two LGS SAWRs, aligned along two different orientations, has been developed to simultaneously determine H<sub>2</sub> presence and temperature. Finally, wireless interrogation of a SAWR sensor was successful within the gas cycling test fixture, and successful wireless H<sub>2</sub> detection was achieved above 400°C.

## DEDICATION

Para Vilma, que fue mi madre tanto como mi madre, y para Omri, que fue mi hermano tanto como mi hermano. Los llevaré siempre conmigo, y sé que me guardan desde el cielo.

To Vilma, who was my mom just as much as my mom, and to Omri, who was my brother just as much as my brother. I will always have you by my side, and I know you watch over me from heaven.

## ACKNOWLEDGEMENTS

I would like to sincerely thank my advisor, Prof. Mauricio Pereira da Cunha, for all his help for the last few years. His knowledge, guidance and unwavering support were instrumental during my undergraduate and graduate career at the University of Maine.

I would also like to thank Dr. Anin Maskay for all his help with teaching me many skills in the lab, and for his contributions to the IEEE Ultrasonics Symposium conference paper and IET publication submitted in 2017, and his valuable help with the design of the stainless steel box used in this thesis.

I would like to acknowledge my committee members, Prof. Robert Lad and Prof. John Vetelino for their help in my graduate career through valuable coursework and technical knowledge, as well as fruitful technical and personal discussions.

I would also like to acknowledge: FIRST scientists Dr. George Bernhardt, for all his help with device fabrication, and Michael Call, for his help with device fabrication and technical questions regarding any and all topics of automation and instrumentation; Firas Mahyob, for his contributions on developing the YSZ deposition techniques described in this thesis; Prof. Donald Hummels, for his discussions and insights into the signal processing aspects of the wireless measurements discussed in this thesis; John Belding and AMC staff, for their help with fabrication of the test boxes; and Nicholas Aiken, for his contributions to the development of the antennas used in this work.

I would also like to acknowledge to the Department of Energy (Grant numbers DE-FE0026217 and DE-FE0031550) for funding my work; NETL researchers Dr. Paul Ohodnicki and Dr. John Baltrus for their XPS analysis contributions; and the ECE department and FIRST for allowing me to conduct research in their facilities.

Finally, I would like to thank all the friends I have made at the University of Maine for their support, the ECE and FIRST students and staff for their kindness, and my parents for their unending love and motivation throughout the entire journey.

# CONTENTS

DEDICATION .....	iii
ACKNOWLEDGEMENTS .....	iv
LIST OF TABLES .....	x
LIST OF FIGURES .....	xi
LIST OF EQUATIONS .....	xxx
1. INTRODUCTION .....	1
1.1 High-temperature Harsh-environment Sensor Overview and Motivation for High-temperature Gas Sensors .....	2
1.2 Current High-temperature Hydrogen Sensing Technology .....	6
1.2.1 Electrochemical Sensors .....	6
1.2.2 Catalytic Sensors .....	7
1.2.3 Semiconductor Metal Oxide Sensors .....	7
1.2.4 Field-Effect Sensors .....	8
1.2.5 Optical Sensors .....	8
1.3 Acoustic Wave Sensors .....	9
1.3.1 Acoustic Wave Propagation and Piezoelectricity .....	9
1.3.2 Acoustic Wave Devices for Gas Sensing Applications .....	13
1.3.2.1 TSM and LFE Resonators .....	14
1.3.2.2 APM Devices .....	15

1.4	SAW Sensors .....	17
1.4.1	One-port SAWRs .....	20
1.5	High-temperature Operation of SAWR Sensors .....	23
1.5.1	High-temperature Piezoelectric Substrates .....	23
1.5.2	High-temperature Electrodes .....	24
1.5.3	High-temperature Sensing Film .....	26
1.6	Framework for Temperature and Gas Mutli-Sensor System .....	26
1.7	Goals and Scope .....	28
1.8	Organization .....	29
2.	DETERMINATION OF ORIENTATIONS ON THE COMMERCIAL LGS WAFER AND DEVELOPMENT OF THIN FILM MATERIALS FOR HIGH-TEMPERATURE SAW GAS SENSING OPERATION .....	30
2.1	Commercially Available LGS Wafer Analysis for SAW Operation at High Temperature .....	30
2.1.1	Selection of LGS Orientations .....	31
2.1.2	Photolithographic Mask Layout .....	34
2.2	High Temperature Thin Film Materials.....	37
2.2.1	Yttria-Stabilized Zirconia (YSZ) .....	37
2.2.2	Pt-Al <sub>2</sub> O <sub>3</sub> .....	38
2.3	SAWR Sensor Fabrication.....	39

3.	HIGH TEMPERATURE GAS SENSOR TESTING SYSTEM	
	DEVELOPMENT AND IMPLEMENTATION .....	42
3.1	High-temperature Gas Sensor Testing System .....	42
3.1.1	SAW Sensor and thermocouple mounting within stainless steel box for High-temperature gas cycling operation .....	42
3.1.2	Gas Delivery System .....	44
3.1.3	Interrogation Module.....	47
3.2	High-temperature SAW Gas Sensor Setups .....	50
3.2.1	Temperature Uniformity within a Chamber .....	52
3.3	SAWR Sensor High-temperature Characterization Setups.....	54
3.4	Wireless High-temperature SAWR Gas Sensor Testing .....	59
4.	SAWR GAS SENSOR EXPERIMENTAL RESULTS AND DISCUSSION .....	61
4.1	Definition of Tracked Frequency .....	61
4.2	SAWR sensor High-temperature Characterization .....	65
4.2.1	Verification of Temperature Performance of Temperature Compensated Orientations at temperatures above 150°C .....	65
4.2.2	Experimental results for influence of YSZ sensing film on temperature performance of high-temperature SAWR sensors .....	65
4.2.3	Temperature stability performance of Film 1 and Film 2 SAWR Sensors .....	67

4.3	SAWR Sensor Performance under Different Flow Rates and H <sub>2</sub> Concentrations .....	72
4.3.1	SAWR Sensor Response to Different N <sub>2</sub> Flow Rates.....	72
4.3.2	Room temperature Gas Cycling SAWR Sensor Response under 100 sccm and 950 sccm Flow Rates .....	74
4.3.3	SAWR Sensor Response to Different H <sub>2</sub> Concentrations.....	77
4.4	Comparison of YSZ-layered and Bare SAW Gas Sensor Performance .....	78
4.5	Oxygen Treatments for Gas Sensor Operation at Room Temperature.....	82
4.5.1	O <sub>2</sub> Treatments at Room Temperature .....	82
4.5.2	High-temperature conditioning in O <sub>2</sub> and in 4%H <sub>2</sub> .....	87
4.6	Influence of SAWR Sensor Orientation on H <sub>2</sub> Detection.....	92
4.6.1	Extraction of Temperature Sensitivity up to 500°C in N <sub>2</sub> flow.....	92
4.6.2	Influence of Orientation on H <sub>2</sub> Detection up to 500°C.....	94
4.7	Film 1 vs. Film 2 SAW Gas Sensor Performance .....	101
4.8	Multi-sensor System Analysis .....	105
4.9	Wireless Interrogation .....	109
5.	CONCLUSIONS .....	112
5.1	Summary of Work .....	112
5.2	Findings .....	113
5.3	Publications Resulting from this Work.....	114
5.4	Suggested Future Work.....	114
	REFERENCES .....	116

APPENDIX A – DETAILS FOR THE OPERATION OF THE HIGH TEMPERATURE GAS TESTING SYSTEM AND FREQUENCY TRACKING CODE .....	127
APPENDIX B – FREQUENCY RESPONSE OF BARE FABRICATED DEVICES .....	138
APPENDIX C – COMPILED GAS SENSOR TESTING RESULTS .....	145
APPENDIX D – SIGNAL PROCESSING DETAILS OF TIME-GATING ALGORITHMS .....	197
BIOGRAPHY OF THE AUTHOR .....	206

## LIST OF TABLES

Table 1.1	Harsh environment sensor applications .....	4
Table 1.2	High temperature gas sensing needs.....	4
Table 1.3	Reduced notation .....	12
Table 2.1	LGS constants used for SAW calculations [99] .....	31
Table 2.2	Summary of Device Parameters .....	35
Table 3.1	Summary of setups mounted and tested for high-temperature gas cycling. ....	51
Table 3.2	Summary of setups mounted and tested for temperature characterization. ....	55
Table C.1	Summary of results using Setup A4 comparing YSZ-layered vs. Bare Devices at 200°C, 300°C and 400 °C. ....	146
Table C.2	Compiled room temperature results for $\Psi = 26.7^\circ$ devices.....	151
Table C.3	Tabulated results for Setup A3. ....	162
Table C.4	Tabulated results for Setup A6. ....	170
Table C.5	Tabulated results for Setup A7. ....	188
Table C.6	Tabulated results for Setup A6. ....	189

## LIST OF FIGURES

Figure 1.1	Number of sensor deployed globally [39] .....	3
Figure 1.2	Stress components on an elemental volume of an elastic medium acting on the $x_1$ face. ....	10
Figure 1.3	Demonstration of crystallographic rotation through use of Euler Angles $\{\Phi, \Theta, \text{ and } \Psi\}$ .....	13
Figure 1.4	TSM resonator structure. ....	15
Figure 1.5	APM device structure and particle displacement: a) SH-APM device; b) Lamb wave Device. ....	16
Figure 1.6	Rayleigh waves present in SAW devices. ....	17
Figure 1.7	Popular SAW sensor configurations: a) SAW delay line; b) Two-port SAW resonator with short circuit (SC) reflectors; c) One-port SAW resonator with open circuit (OC) reflectors. ....	19
Figure 1.8	Topology of a one-port SAWR with OC reflector gratings. ....	21
Figure 1.9	Example of reflection coefficient for an electrode with a center of reflection not at the geometric center of the electrode. ....	21
Figure 1.10	Power flow angle in SAW devices. ....	22
Figure 1.11	High-temperature electrode problems: a) Agglomeration; b) Hillock Formation; c) Whisker formation [92]. ....	25
Figure 2.1	$K^2$ at 200°C, 300°C, and 400°C for the commercial LGS wafer. Dotted-dashed curve: 200°C; Dotted curve: 300°C; Solid curve: 400°C. ....	33

Figure 2.2	<i>TCD</i> at 200°C, 300°C, and 400°C for the commercial LGS wafer. Dotted-dashed curve: 200°C; Dotted curve: 300°C; Solid curve: 400°C. ....	33
Figure 2.3	AutoCAD layout of photolithographic mask. ....	35
Figure 2.4	Device layout for compensation of NSPUDT effects: a) Synchronous S devices; b) Right Compensated RC devices; c) Left Compensated LC devices. ....	36
Figure 2.5	SEM images of 25 nm YSZ thin films on LGS deposited at different substrate temperatures after high-temperature cycling between 25°C and 750°C: a) 850°C; b) room-temperature. ....	38
Figure 2.6	Schematic of film composition for Pt-Al <sub>2</sub> O <sub>3</sub> thin films: a) Film 1; b) Film 2. ....	39
Figure 2.7	Fabricated wafer section with Bare sensors. ....	40
Figure 2.8	Capacitive coupling for interrogation of YSZ-layered SAWR sensors. ....	41
Figure 3.1	High-temperature gas testing system schematic. ....	43
Figure 3.2	High-temperature stainless steel box: (a) chamber top view; (b) cap top view; (c) chamber side view; (d) cap screwed onto chamber. ....	44
Figure 3.3	SAWRs and TC mounted in stainless steel gas testing chamber. ....	44
Figure 3.4	Gas Delivery System A. ....	46
Figure 3.5	Gas Delivery System B. ....	46
Figure 3.6	Gas Delivery System C. ....	47

Figure 3.7	Physical implementation of the gas delivery system: a) valves and MFC hardware (C1 and C2 denote Chamber 1 and Chamber 2 respectively); b) Control interface connected to PC.....	47
Figure 3.8	RF multiplexer box.....	48
Figure 3.9	Physical implementation of entire high-temperature gas testing system: a) Hardware physical setup in MAL 295; b) Stainless steel box inside Thermolyne 6000 Furnace.....	49
Figure 3.10	Device layout schematic for high-temperature gas testing.....	50
Figure 3.11	TC test in gas chamber.....	53
Figure 3.12	TC test results for gas cycling at 260°C, 360°C, 460°C, and 560°C.....	53
Figure 3.13	SAW sensor temperature characterization setup schematic.....	55
Figure 3.14	Witness TC temperature readings for one round of Profile 1.....	57
Figure 3.15	Witness TC temperature readings for one round of Profile 2.....	58
Figure 3.16	SAW sensor temperature characterization setup.....	58
Figure 3.17	Wireless SAW gas sensor interrogation setup.....	60
Figure 4.1	Frequency response of SAWR oriented along $\Psi = 26.7^\circ$ : a) magnitude of reflection coefficient [dB]; b), real part of admittance [mS]; c) imaginary part of the admittance [mS].....	62
Figure 4.2	Polynomial fitting around minimum $S_{11}$ value to filter out frequency shifting between adjacent points and improve the detection of minima for $S_{11}$ .....	63

Figure 4.3	Frequency response of SAWR oriented along $\Psi = 20.7^\circ$ with RC IDT placement: a) magnitude of reflection coefficient [dB]; b), real part of admittance [mS]; c) imaginary part of the admittance [mS]. . . . .	64
Figure 4.4	Measured and predicted resonant fractional frequency variation normalized to the maximum frequency with respect to measured temperature ( $f_0$ were 191.07 and 190.26 MHz for $\Psi = 14.7^\circ$ and $\Psi = 77.7^\circ$ respectively). Discrete points: measured data and respective uncertainties; solid curves: second order polynomial fits; dashed curves: numerically calculated responses for free surface. Curves A and B: $\Psi = 14.7^\circ$ ; Curves C and D: $\Psi = 77.7^\circ$ [85]. . . . .	66
Figure 4.5	Fractional frequency variation in SAWR sensor oriented along $\Psi = 77.7^\circ$ as a function of temperature ( $f_0$ were 190.4 and 190.2 MHz for 50nmYSZ and Bare devices respectively): Red curve: 50nmYSZ Sensor; Blue curve: Bare Sensor[84]. . . . .	66
Figure 4.6	SEM images for Film 1 (left column) and Film 2 (right column) for the four states discussed in the text. State 1: as fabricated; State 2: 800°C for four hours; State 3: after four rounds using Profile 1; State 4: after for five rounds using Profile 2. . . . .	68
Figure 4.7	Tracked Resonant Frequency vs. Time and Temperature, Profile 1 . . . . .	69
Figure 4.8	Averaged relative frequency variation for Film 1 (blue triangles) and Film 2 (green circles) for setup B3 at the maximum temperature value shown on the right axis ( $f_0$ , Film 1: 188.725MHz, Film 2: 188.093MHz), Profile 1, Section 3.3. . . . .	70

Figure 4.9	Averaged relative frequency variation for Film 1 (blue triangles) and Film 2 (green circles) for setup B4 at the maximum temperature value shown on the right axis ( $f_0$ , Film 1: 186.539MHz; Film 2: 186.093MHz), Profile 2, Section 3.3. ....	71
Figure 4.10	Frequency variation of Setup A5 Device 1 (Film 2 Bare cycled 14.7°) Tracked Frequency response with respect to $f_0 = 190.816$ vs. Different flow rates of N <sub>2</sub> at Room Temperature. ....	73
Figure 4.11	Setup A5 Device 1 Tracked Frequency response vs. Different flow rates of N <sub>2</sub> at 500°C. ....	74
Figure 4.12	Setup A4 Device 4 (Film 2 Bare non-cycled 26.7°) Tracked Frequency at room temperature vs. Gas Exposure with: a) 100 sccm gas flow; b) 950 sccm gas flow. ....	76
Figure 4.13	Setup A5 Device 3 Tracked Frequency at 300°C vs. Gas Exposure for different H <sub>2</sub> concentrations. ....	77
Figure 4.14	Setup A2 Device 3 (Film 2 YSZ non-cycled 14.7°) Tracked Frequency at 300°C vs. Gas Exposure.....	79
Figure 4.15	Setup A2 Device 4 (Film 2 Bare non-cycled 14.7°) Tracked Frequency at 300°C vs. Gas Exposure.....	79
Figure 4.16	Setup A4 Device 2 (Film 2 YSZ non-cycled 14.7°) Tracked Frequency at 297°C vs. Gas Exposure.....	81

Figure 4.17	Setup A4 Measured relative frequency variation due to 4% $H_2$ exposure at the measured temperatures for: Device 1 (Film 2 YSZ non-cycled 14.7°) (pink crosses, dotted-dashed line); Device 2 (Film 2 Bare non-cycled 14.7°) (purple crosses, dotted line); Device 3 (Film 2 YSZ non-cycled 26.7°) (yellow circles, dashed line); Device 4 (Bare 26.7°) (blue circles, solid line). $\Delta f_i$ and $f_{0i}$ are given in Section C.1. ....	81
Figure 4.18	Setup A3 Device 3 (Film 2 Bare non-cycled 26.7°) Tracked Frequency at room temperature vs. Gas Exposure [116]......	83
Figure 4.19	Comparison of Device 3 recoveries due to $N_2$ and $O_2/N_2$ cycling [116]......	85
Figure 4.20	Setup A3 Device 3 (Bare 26.7° Film 2) Tracked Frequency at room temperature vs. Gas Exposure, Second Test [117]......	86
Figure 4.21	Setup A3 Device 3 (Bare 26.7° Film 2) Tracked Frequency at room temperature vs. Gas Exposure, Second Test, direct comparison of normalized frequency variation [117]. ....	87
Figure 4.22	Setup A3 Device 3 (Film 2 Bare non-cycled 26.7°) Tracked Frequency at room temperature vs. Gas Exposure after Conditioning A, B and C (explained in the text) [116]......	88
Figure 4.23	Pt $4f_{7/2}$ binding energies after high-temperature oxidizing treatment. The cross indicates XPS analysis after the high-temperature treatment, the upward triangle indicates XPS analysis after room-temperature $N_2$ exposure, the square indicates XPS analysis after room-temperature $O_2$ exposure, and the diamond indicates XPS analysis after room-temperature $H_2$ exposure [116]......	90

Figure 4.24	Pt $4f_{7/2}$ binding energies after high-temperature reducing conditioning treatment. The cross indicates XPS analysis after the high-temperature treatment, the upward triangle indicates XPS analysis after room-temperature $N_2$ exposure, the square indicates XPS analysis after room-temperature $O_2$ exposure, and the diamond indicates XPS analysis after room-temperature $H_2$ exposure [116].	91
Figure 4.25	a) Measured normalized frequency variation $(f-f_{0\Psi T})/f_{0\Psi T}$ vs. temperature for the LGS orientations used and polynomial fit; b) calculated sensitivity. Device 1 (Film 2 Bare non-cycled $77.7^\circ$ ): squares, dashed red line; Device 2 (Film 2 Bare non-cycled $14.7^\circ$ ): crosses, dotted purple line; Device 3 (Film 2 Bare non-cycled $26.7^\circ$ ): circles, solid blue line. Device 4 (Film 2 Bare non-cycled $32.7^\circ$ ): triangles, dotted-dashed green line; The value of $f_{0\Psi T}$ is 189.927,191.075, 191.934, 191.465MHz for Device 1-Device 4 respectively [118].	93
Figure 4.26	Setup A3 Device 3 (Film 2 Bare non-cycled $26.7^\circ$ Film 2) Tracked Frequency at $186^\circ C$ vs. Gas Exposure.	95
Figure 4.27	Setup A3 Measured relative frequency variation due to $4\%H_2$ exposure at the measured temperatures for: Device 1 (Film 2 Bare non-cycled $77.7^\circ$ ) (orange squares, dashed line); Device 2 (Film 2 Bare non-cycled $14.7^\circ$ ) (purple crosses); Device 3 (Film 2 Bare non-cycled $26.7^\circ$ ) (blue circles); Device 4 (Film 2 Bare non-cycled $32.7^\circ$ ) (green triangles). Data points are connected for convenience and do not imply interpolation. $\Delta f_i$ and $f_{0i}$ are given in Section C.3.1.	96

Figure 4.28	Setup A6 Device 4 (Film 1 Bare non-cycled 26.7°) Tracked Frequency at 220°C vs. Gas Exposure.....	98
Figure 4.29	Setup A6 Measured relative frequency variation due to 4% $H_2$ exposure at the measured temperatures for: Device 1 (Film 1 Bare non-cycled 20.7°) (pink diamonds, dashed-dotted line); Device 2 (Film 1 Bare non-cycled 77.7°) (orange squares, dashed line); Device 3 (Film 1 Bare non-cycled 20.7°) (yellow diamonds, dotted line); Device 4 (Film 1 Bare non-cycled 26.7°) (blue circles, solid line). Data points are connected for convenience and do not imply interpolation. $\Delta f_{Di}$ and $f_{0i}$ are given in Section C.3.2.....	99
Figure 4.30	Setup A7 Device 1 (Film 1 Bare cycled 26.7°) Tracked Frequency at 294°C vs. Gas Exposure.....	100
Figure 4.31	Fractional frequency shift due to 4% $H_2$ exposure for Devices 1-4 at the temperatures measured. Data points are connected for convenience and do not imply interpolation. Device 1 (Film 1 Bare cycled 26.7°) blue circles connected with dotted line; Device 2 (Film 1 Bare cycled 77.7°) orange squares connected dotted line; Device 3 (Film 1 Bare cycled 26.7°) yellow circles connected with dashed line; Device 4 (Film 1 Bare cycled 14.7°) purple squares connected with dashed line. ....	102

Figure 4.32 Fractional frequency shift due to 4% $H_2$  exposure for all Bare devices oriented along  $\Psi = 26.7^\circ$  at the temperatures measured. Data points are connected for convenience and do not imply interpolation. Solid blue line: Film 2 Bare non-cycled  $26.7^\circ$  (Device 4 in Setup A4); dashed blue line: Film 2 Bare non-cycled  $26.7^\circ$  (Device 3 in Setup A3); dotted yellow line: Film 1 Bare non-cycled  $26.7^\circ$  (Device 4 in Setup A6); dashed-dotted green lines: Film 1 Bare cycled (Device 1 and Device 3 from Setup A7). The corresponding  $\Delta f_i$  and  $f_{0i}$  are defined in the corresponding result section for each setup. .... 103

Figure 4.33 Setup A5 Device 1 (Film 2 Bare cycled  $14.7^\circ$ ) Tracked Frequency at  $213^\circ C$  vs. Gas Exposure..... 104

Figure 4.34 Setup A5 (all devices) and Setup A3 (Device 2, Film 2 Bare non-cycled  $14.7^\circ$ ) Measured relative frequency variation due to  $H_2$  exposure at the measured temperatures for: Setup A5 Device 1 (Film 2 Bare cycled  $14.7^\circ$ ) orange crosses, solid line; Setup A5 Device 2 (Film 2 Bare cycled  $14.7^\circ$ ) orange crosses, dotted line; Setup A5 Device 3 (Film 1 Bare cycled  $14.7^\circ$ ) green crosses, dashed-dotted line; Setup A5 Device 4 (Film 1 Bare cycled  $14.7^\circ$ ) green crosses, dashed line; Setup A3 Device 2 (Film 2 Bare non-cycled  $14.7^\circ$ ) purple crosses, dashed line.  $\Delta f_i$  and  $f_{0i}$  are given in Appendix C. .... 105

Figure 4.35	Fractional frequency change with respect to the maximum value of frequency recorded $f_{0maxi}$ for Device 1 (Film 1 Bare cycled 26.7°) and Device 2 (Film 1 Bare cycled 77.7°) (both devices in Chamber 1). Data points are connected via parabolic fitting. Device 1 under N <sub>2</sub> : blue circles, dotted line; Device 1 under H <sub>2</sub> : green circles, dashed-dotted line; Device 2 under N <sub>2</sub> : blue squares, solid line; Device 2 under H <sub>2</sub> : green squares, dotted line. Values of $f_{0maxi}$ are given in Appendix C in Section C.3.3. ....	106
Figure 4.36	Values of $\Delta F_{norm,1} - \Delta F_{norm,2}$ (defined in the text) as a function of temperature. Solid blue curve is under N <sub>2</sub> , dashed green curve is under H <sub>2</sub> . ....	107
Figure 4.37	Zoomed-in section of resulting $\Delta F_{norm,1} - \Delta F_{norm,2}$ values around 270°C. Solid blue curve is under N <sub>2</sub> , dashed green curve is under H <sub>2</sub> . ....	108
Figure 4.38	Zoomed-in portion around 270°C of fractional frequency values for Device 1 (Figure 4.34). Dotted blue curve is under N <sub>2</sub> , dotted-dashed green curve is under H <sub>2</sub> . ....	108
Figure 4.39	Wireless test results analysis at 378°C using 40 MHz bandwidth. ....	109
Figure 4.40	Wireless test results analysis at 478°C using 40 MHz bandwidth. ....	110
Figure 4.41	Wireless test results analysis at 379°C using 10 MHz bandwidth. ....	110
Figure A.1	Dimensions and specifications of fabricated stainless-steel box body by AMC. ....	128
Figure A.2	Dimensions and specifications of fabricated stainless-steel box caps by AMC. ....	128
Figure A.3	User input and output flow diagram for LabVIEW software. ....	129

Figure A.4	Flow diagram for Main LabVIEW script.....	130
Figure B.1	Typical frequency Response $\Psi = 14.7^\circ$ IDT placement S: a) $ S_{11}$ in dB; b) real part of admittance in mS; c) imaginary part of admittance in mS. ....	139
Figure B.2	Typical frequency Response $\Psi = 14.7^\circ$ IDT placement RC: a) $ S_{11}$ in dB; b) real part of admittance in mS; c) imaginary part of admittance in mS. ....	139
Figure B.3	Typical frequency Response $\Psi = 14.7^\circ$ IDT placement LC: a) $ S_{11}$ in dB; b) real part of admittance in mS; c) imaginary part of admittance in mS. ....	140
Figure B.4	Typical frequency Response $\Psi = 20.7^\circ$ IDT placement S: a) $ S_{11}$ in dB; b) real part of admittance in mS; c) imaginary part of admittance in mS. ....	140
Figure B.5	Typical frequency Response $\Psi = 20.7^\circ$ IDT placement RC: a) $ S_{11}$ in dB; b) real part of admittance in mS; c) imaginary part of admittance in mS. ....	141
Figure B.6	Typical frequency Response $\Psi = 20.7^\circ$ IDT placement LC: a) $ S_{11}$ in dB; b) real part of admittance in mS; c) imaginary part of admittance in mS. ....	141
Figure B.7	Typical frequency Response $\Psi = 32.7^\circ$ IDT placement S: a) $ S_{11}$ in dB; b) real part of admittance in mS; c) imaginary part of admittance in mS. ....	142
Figure B.8	Typical frequency Response $\Psi = 32.7^\circ$ IDT placement RC: a) $ S_{11}$ in dB; b) real part of admittance in mS; c) imaginary part of admittance in mS. ....	142

Figure B.9	Typical frequency Response $\Psi = 32.7^\circ$ IDT placement LC: a) $ S_{11} $ in dB; b) real part of admittance in mS; c) imaginary part of admittance in mS. ....	143
Figure B.10	Typical frequency Response $\Psi = 77.7^\circ$ IDT placement S: a) $ S_{11} $ in dB; b) real part of admittance in mS; c) imaginary part of admittance in mS. ....	143
Figure B.11	Typical frequency Response $\Psi = 77.7^\circ$ IDT placement RC: a) $ S_{11} $ in dB; b) real part of admittance in mS; c) imaginary part of admittance in mS. ....	144
Figure B.12	Typical frequency Response $\Psi = 77.7^\circ$ IDT placement LC: a) $ S_{11} $ in dB; b) real part of admittance in mS; c) imaginary part of admittance in mS. ....	144
Figure C.1	Setup A4 test results at nominal furnace temperature $200^\circ\text{C}$ for Device 1. ....	146
Figure C.2	Setup A4 test results at nominal furnace temperature $200^\circ\text{C}$ for Device 2. ....	146
Figure C.3	Setup A4 test results at nominal furnace temperature $200^\circ\text{C}$ for Device 3. ....	147
Figure C.4	Setup A4 test results at nominal furnace temperature $200^\circ\text{C}$ for Device 4. ....	147
Figure C.5	Setup A4 test results at nominal furnace temperature $300^\circ\text{C}$ for Device 1. ....	147
Figure C.6	Setup A4 test results at nominal furnace temperature $300^\circ\text{C}$ for Device 2. ....	148

Figure C.7	Setup A4 test results at nominal furnace temperature 300°C for Device 3. ....	148
Figure C.8	Setup A4 test results at nominal furnace temperature 300°C for Device 4. ....	148
Figure C.9	Setup A4 test results at nominal furnace temperature 400°C for Device 1. ....	149
Figure C.10	Setup A4 test results at nominal furnace temperature 400°C for Device 4. ....	149
Figure C.11	Setup A4 test results at nominal furnace temperature 400°C for Device 3. ....	149
Figure C.12	Setup A4 test results at nominal furnace temperature 400°C for Device 4. ....	150
Figure C.13	Setup A1 Device 3 Test 1 results at room temperature. ....	152
Figure C.14	Setup A1 Device 3 Test 2 results at room temperature. ....	152
Figure C.15	Setup A1 Device 3 Test 3 results at room temperature. ....	152
Figure C.16	Setup A1 Device 3 Test 4 results at room temperature. ....	153
Figure C.17	Setup A1 Device 3 Test 5 results at room temperature. ....	153
Figure C.18	Setup A1 Device 3 Test 6 results at room temperature. ....	153
Figure C.19	Setup A1 Device 3 Test 7 results at room temperature. ....	154
Figure C.20	Setup A1 Device 3 Test 1 results at room temperature. ....	154
Figure C.21	Setup A1 Device 4 Test 1 results at room temperature. ....	154
Figure C.22	Setup A1 Device 4 Test 2 results at room temperature. ....	155

Figure C.23	Setup A1 Device 4 Test 3 results at room temperature. ....	155
Figure C.24	Setup A1 Device 4 Test 4 results at room temperature. ....	155
Figure C.25	Setup A1 Device 4 Test 5 results at room temperature. ....	156
Figure C.26	Setup A1 Device 4 Test 6 results at room temperature. ....	156
Figure C.27	Setup A1 Device 4 Test 7 results at room temperature. ....	156
Figure C.28	Setup A1 Device 4 Test 1 results at room temperature. ....	157
Figure C.29	Setup A3 Device 3 Test 9 results at room temperature. ....	157
Figure C.30	Setup A3 Device 3 Test 10 results at room temperature. ....	157
Figure C.31	Setup A3 Device 3 Test 11 results at room temperature. ....	158
Figure C.32	Setup A4 Device 4 Test 12 results at room temperature. ....	158
Figure C.33	Setup A4 Device 4 Test 13 results at room temperature. ....	158
Figure C.34	Setup A3 Device 3 Test 1 results at room temperature after high-temperature conditioning in oxygen at 650°C. ....	159
Figure C.35	Setup A3 Device 3 Test 2 results at room temperature after high-temperature conditioning in oxygen at 650°C. ....	159
Figure C.36	Setup A Device 4 Test 1 results at room temperature after high-temperature conditioning in oxygen at 650°C. ....	160
Figure C.37	Setup A4 Device 4 Test 2 results at room temperature after high-temperature conditioning in oxygen at 650°C. ....	160
Figure C.38	Setup A3 Device 1 test results at 100°C. ....	163
Figure C.39	Setup A3 Device 1 test results at 200°C. ....	163
Figure C.40	Setup A3 Device 1 test results at 300°C. ....	163

Figure C.41 Setup A3 Device 1 test results at 400°C. ....	164
Figure C.42 Setup A3 Device 1 test results at 500°C. ....	164
Figure C.43 Setup A3 Device 2 test results at 100°C. ....	164
Figure C.44 Setup A3 Device 2 test results at 200°C. ....	165
Figure C.45 Setup A3 Device 2 test results at 300°C. ....	165
Figure C.46 Setup A3 Device 2 test results at 400°C. ....	165
Figure C.47 Setup A3 Device 2 test results at 500°C. ....	166
Figure C.48 Setup A3 Device 3 test results at 100°C. ....	166
Figure C.49 Setup A3 Device 3 test results at 200°C. ....	166
Figure C.50 Setup A3 Device 3 test results at 300°C. ....	167
Figure C.51 Setup A3 Device 3 test results at 400°C. ....	167
Figure C.52 Setup A3 Device 3 test results at 500°C. ....	167
Figure C.53 Setup A3 Device 4 test results at 100°C. ....	168
Figure C.54 Setup A3 Device 4 test results at 200°C. ....	168
Figure C.55 Setup A3 Device 4 test results at 300°C. ....	168
Figure C.56 Setup A3 Device 4 test results at 400°C. ....	169
Figure C.57 Setup A3 Device 4 test results at 500°C. ....	169
Figure C.58 Setup A6 Device 1 test results at 220°C. ....	171
Figure C.59 Setup A6 Device 1 test results at 320°C. ....	171
Figure C.60 Setup A6 Device 1 test results at 420°C. ....	171
Figure C.61 Setup A6 Device 1 test results at 520°C. ....	172

Figure C.62 Setup A6 Device 2 test results at 220°C. ....	172
Figure C.63 Setup A6 Device 2 test results at 320°C. ....	172
Figure C.64 Setup A6 Device 2 test results at 420°C. ....	173
Figure C.65 Setup A6 Device 2 test results at 520°C. ....	173
Figure C.66 Setup A6 Device 3 test results at 220°C. ....	173
Figure C.67 Setup A6 Device 3 test results at 320°C. ....	174
Figure C.68 Setup A6 Device 3 test results at 420°C. ....	174
Figure C.69 Setup A6 Device 3 test results at 520°C. ....	174
Figure C.70 Setup A6 Device 4 test results at 220°C. ....	175
Figure C.71 Setup A6 Device 4 test results at 320°C. ....	175
Figure C.72 Setup A6 Device 4 test results at 420°C. ....	175
Figure C.73 Setup A6 Device 4 test results at 520°C. ....	176
Figure C.74 Setup A7 Device 1 test results at 100°C. ....	177
Figure C.75 Setup A7 Device 1 test results at 150°C. ....	177
Figure C.76 Setup A7 Device 1 test results at 200°C. ....	177
Figure C.77 Setup A7 Device 1 test results at 250°C. ....	178
Figure C.78 Setup A7 Device 1 test results at 300°C. ....	178
Figure C.79 Setup A7 Device 1 test results at 350°C. ....	178
Figure C.80 Setup A7 Device 1 test results at 400°C. ....	179
Figure C.81 Setup A7 Device 1 test results at 450°C. ....	179
Figure C.82 Setup A7 Device 1 test results at 500°C. ....	179

Figure C.83 Setup A7 Device 2 test results at 100°C. ....	180
Figure C.84 Setup A7 Device 2 test results at 150°C. ....	180
Figure C.85 Setup A7 Device 2 test results at 200°C. ....	180
Figure C.86 Setup A7 Device 2 test results at 250°C. ....	181
Figure C.87 Setup A7 Device 2 test results at 300°C. ....	181
Figure C.88 Setup A7 Device 2 test results at 350°C. ....	181
Figure C.89 Setup A7 Device 2 test results at 400°C. ....	182
Figure C.90 Setup A7 Device 2 test results at 450°C. ....	182
Figure C.91 Setup A7 Device 2 test results at 500°C. ....	182
Figure C.92 Setup A7 Device 3 test results at 100°C. ....	183
Figure C.93 Setup A7 Device 3 test results at 150°C. ....	183
Figure C.94 Setup A7 Device 3 test results at 200°C. ....	183
Figure C.95 Setup A7 Device 3 test results at 250°C. ....	184
Figure C.96 Setup A7 Device 3 test results at 300°C. ....	184
Figure C.97 Setup A7 Device 3 test results at 350°C. ....	184
Figure C.98 Setup A7 Device 3 test results at 450°C. ....	185
Figure C.99 Setup A7 Device 4 test results at 100°C. ....	185
Figure C.100 Setup A7 Device 4 test results at 150°C. ....	185
Figure C.101 Setup A7 Device 4 test results at 200°C. ....	186
Figure C.102 Setup A7 Device 4 test results at 250°C. ....	186
Figure C.103 Setup A7 Device 4 test results at 300°C. ....	186

Figure C.104 Setup A7 Device 4 test results at 350°C. ....	187
Figure C.105 Setup A7 Device 4 test results at 400°C. ....	187
Figure C.106 Setup A7 Device 4 test results at 450°C. ....	187
Figure C.107 Setup A7 Device 4 test results at 500°C. ....	188
Figure C.108 Setup A5 Device 1 test results at 220°C. ....	190
Figure C.109 Setup A5 Device 1 test results at 320°C. ....	190
Figure C.110 Setup A5 Device 1 test results at 420°C. ....	190
Figure C.111 Setup A5 Device 1 test results at 520°C. ....	191
Figure C.112 Setup A5 Device 1 test results at 620°C. ....	191
Figure C.113 Setup A5 Device 1 test results at 220°C. ....	191
Figure C.114 Setup A5 Device 1 test results at 320°C. ....	192
Figure C.115 Setup A5 Device 1 test results at 420°C. ....	192
Figure C.116 Setup A5 Device 1 test results at 520°C. ....	192
Figure C.117 Setup A5 Device 1 test results at 220°C. ....	193
Figure C.118 Setup A5 Device 1 test results at 320°C. ....	193
Figure C.119 Setup A5 Device 1 test results at 420°C. ....	193
Figure C.120 Setup A5 Device 1 test results at 520°C. ....	194
Figure C.121 Setup A5 Device 1 test results at 620°C. ....	194
Figure C.122 Setup A5 Device 1 test results at 220°C. ....	194
Figure C.123 Setup A5 Device 1 test results at 320°C. ....	195
Figure C.124 Setup A5 Device 1 test results at 420°C. ....	195

Figure C.125 Setup A5 Device 1 test results at 520°C. ....	195
Figure C.126 Setup A5 Device 1 test results at 620°C. ....	196
Figure D.1 Conjugate frequency spectrum for real-valued time-domain response.....	198
Figure D.2 Array to be passed to Matlab fft functions. ....	198
Figure D.3 Displaced spectrum for complex-valued representation of time-domain response. ....	201
Figure D.4 Phase of the complex-valued time-domain response.....	202
Figure D.5 Time-gated spectra for all algorithms. ....	205

## LIST OF EQUATIONS

Equation 1.1 .....	9
Equation 1.2 .....	10
Equation 1.3 .....	11
Equation 1.4 .....	11
Equation 1.5 .....	11
Equation 1.6 .....	11
Equation 1.7 .....	11
Equation 1.8 .....	12
Equation 1.9 .....	12
Equation 1.10 .....	12
Equation 1.11 .....	14
Equation 1.12 .....	17
Equation 1.13 .....	22
Equation 1.14 .....	26
Equation 1.15 .....	26
Equation 1.16 .....	27
Equation 1.17 .....	27
Equation 1.18 .....	27
Equation 4.1 .....	86
Equation 4.2 .....	105
Equation 4.3 .....	106

# CHAPTER 1

## INTRODUCTION

The demand for wireless sensing in hostile environments where temperatures may rise above 200°C and where a variety of volatile and toxic gases may be present has risen over the past decades as the increased reliability of wireless networks with a multitude of components can improve the energy and process efficiency, reduce operational costs and increase general safety of a variety of industries involved in harsh environment day-to-day operations [1]–[7]. Industries standing to benefit from high-temperature and harsh environment sensors include power generation industries such as fossil-fuel based power and nuclear based energy [8]–[10], the aerospace and automotive industries [11]–[13], the metallurgy industry [14]–[16], and industries focusing on instrumentation for defense applications [1], [17], [18]. In particular, there is a growing interest in reliable gas sensors capable of operating at high temperature and harsh environment operation that will be able to provide constant monitoring of equipment, minimize adverse environmental effects, increase general operational safety, and decrease overall costs at temperatures above 200°C. A number of sensor technologies have shown promise to deliver reliable sensing to harsh environment applications, including resistive-based technologies, piezoelectric acoustic sensors, optical sensors, metal oxide sensors, and SiC-based field-effect devices [13], [19]–[24].

The Surface Acoustic Wave (SAW) platform can function as sensing elements to address a variety of measurands of interest, including temperature [25], [26], pressure [26], [27], strain [28] and gas sensors [29]–[31]. Additionally, with the proper choice of substrate and electrodes, the SAW platform can be extended to high-temperature and harsh-environment operation [1], [4], [5], [32]. SAW devices present attractive characteristics, such as capability of mass production, low cost, small size, and wireless and battery-free operation [33], [34]. These features coupled with the aforementioned capability of operating at high-temperature make this technology particularly attractive as a harsh environment gas sensor platform.

This thesis describes the operation of high-temperature SAW resonators (SAWRs) in the very high frequency (VHF) range as hydrogen gas sensors at temperatures up to 600°C. The scope of the work encompasses the following: the design and fabrication of the harsh environment SAWRs to be used as gas sensing elements; the implementation of a high-temperature test system capable of interrogating multiple SAWR sensors and thermocouples under flow of different gas species; the characterization of the fabricated SAWR platform in the temperature range of 20°C to 850°C operating in air; the characterization of the SAWR sensor platform in N<sub>2</sub>, O<sub>2</sub> and H<sub>2</sub>/N<sub>2</sub> mixtures up to 600°C; developing a multi-sensor system capable of extracting gas and temperature data; and the verification of wireless interrogation of the SAWR platform as a gas sensor.

## **1.1 High-temperature Harsh-environment Sensor Overview and Motivation for High-temperature Gas Sensors**

Sensors are an integral part of modern systems, present in quotidian civilian equipment and activities, industrial processes, and military defense applications. In particular, the advent of interconnected networks of sensors, actuators, and data processing centers collectively referred to as the Internet of Things (IoT) has radically increased the demand for sensors [35]–[38]. As can be observed Figure 1.1, the global number of deployed sensors has shown a steady increase, totalling more than 14 billion as of 2017 [39]. It is estimated that the combined market value of the IoT will grow from \$157 billion in 2017 to more than \$650 billion in 2021, and more than 75 billion sensors deployed by 2025 [39].

This increasing demand for sensor elements and integrated networks is also being observed for harsh-environment applications, in particular for power generation, the automotive, aerospace, and metallurgy industries, and defense applications [1], [3], [6], [28], [40]. Sensor platforms, packaging and interrogation technologies that are adequate for room-temperature sensing are normally incapable of withstanding the common extended excursions to high temperature, temperature shock, and erosive and corrosive conditions

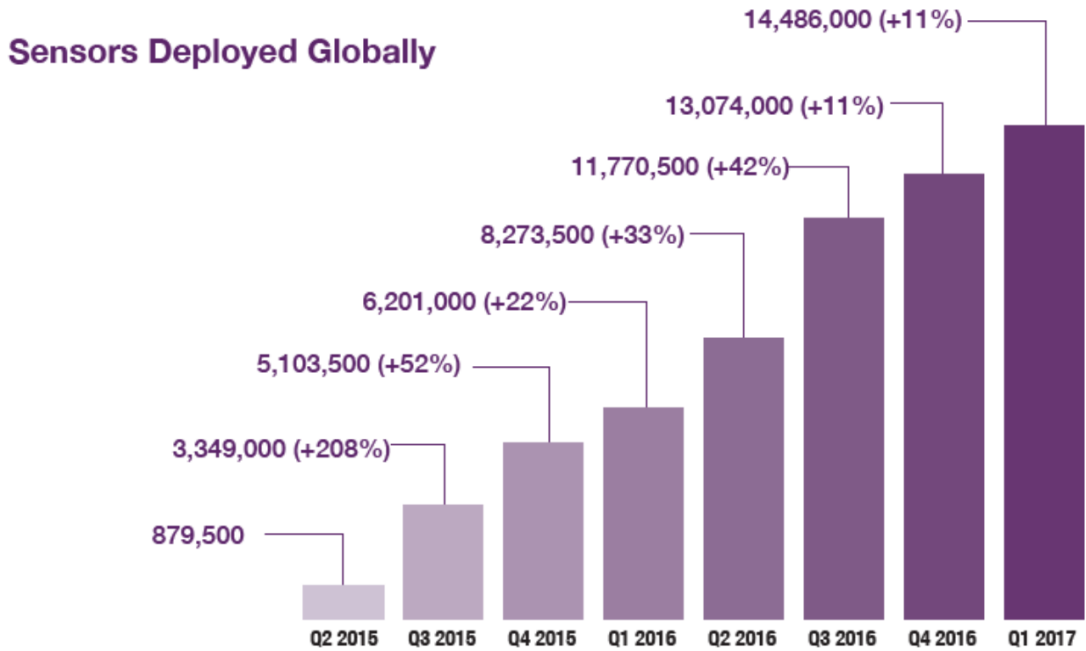


Figure 1.1. Number of sensor deployed globally [39]

seen in many high-temperature, harsh-environment applications [5], [32]. For this reason, application-specific technologies and sensor packages are often employed.

Current high-temperature harsh environment sensor technologies include: resistive-based technologies such as thermocouples and thermistors, piezoelectric acoustic sensors such as bulk acoustic wave (BAW) and SAW devices, optical sensors such as optical fiber sensors, metal oxide sensors such as Taguchi gas sensors, and field-effect devices such as SiC schottky diode and SiC MOSFET sensors. Examples of harsh-environment sensor applications are shown in Table 1.1.

As can be seen from Table 1.1, all of the mentioned sensor platforms have been demonstrated to be functional as harsh environment gas sensors. There is an interest within industry, and by consequence within the scientific community, to develop reliable, precise and cost-efficient gas sensors for high-temperature applications [9], [24]. The power generation, automotive, aerospace, and metallurgy industries as well as defense applications have interest in sensor systems capable of detecting a variety of gases at high-temperature, as shown in Table 1.2. The power generation industry, specifically the coal industry, aims to address the

Table 1.1. Harsh environment sensor applications

Sensor Platform	Applications
Resistive	Temperature [41], Strain [28], Gas [19]
Piezoelectric Acoustic Wave	Temperature [1], Strain [28], Gas [20], [21], Pressure [42]
Optical	Strain, Temperature, Gas, Pressure, Displacement [13], [22]
Metal Oxide	Gas [23]
Field-Effect Devices	Temperature, Pressure [43] Acceleration [44], Gas [24]

increasing demand to generate cleaner energy through an advanced technique for electricity generation known as the integrated gasification combined cycle (IGCC). The first step in the IGCC is the production of synthetic gas (syngas), which entails using steam reforming of hydrocarbons (HC) to produce the syngas, which is a mixture of  $H_2$ ,  $CO$ ,  $H_2O$  and  $CO_2$ . The optimal production of syngas requires in-situ monitoring of gas composition up to  $800^\circ C$  [8]. The automotive and aerospace industries need gas sensors capable of exposures beyond  $800^\circ C$  to detect a variety of gases in exhaust systems, where it is desired to monitor the concentrations of  $O_2$ ,  $H_2$ , HCs,  $CO$ , and  $NO_x$  [45]. For metallurgical applications, it is often desired to monitor environment gas composition in processes in particular  $H_2$ ,  $O_2$ ,  $CO$ ,  $CO_2$  and  $NO_x$  gases [9], [11]. Regarding the aerospace and defense industries, high-temperature gas sensors are required in propulsion systems, where it is critical to monitor the chemical

Table 1.2. High temperature gas sensing needs

Application	Measurands of Interest
Power Generation	$H_2$ , $CO$ , $H_2O$ and $CO_2$
Automotive and Aerospace	$O_2$ , $H_2$ , HCs, $CO$ , and $NO_x$
Metallurgical	$H_2$ , $O_2$ , $CO$ , $CO_2$ and $NO_x$
Defense	$O_2$ , $H_2$ , HCs, $CO$ , and $NO_x$

composition of the environment for the correct high octane propulsion, combustion and efficiency of jet engines and missile systems alike [18].

From the information summarized in Table 1.2, it is clear that the detection of  $H_2$  is useful in a variety of applications. Hydrogen's ubiquitous presence in many industrial processes has steadily increased the demand for reliable sensors. In addition, hydrogen-based energy generation has been recently considered to address clean energy generation profiting from the development of efficient hydrogen production. This application has been an important drive for improved sensor technologies to monitor molecular hydrogen [46]. Due to the hydrogen explosive hazard at concentrations above 4% (lower level explosive limit, LEL) coupled with its odorless and colorless nature there is a special need for sensors capable of detecting hydrogen in gaseous form and thus address the safety concerns [47]–[49].

The demand for high-temperature and harsh-environment hydrogen sensors also comes from the need to address process efficiency [9], [11], [45], [50]. In the automotive and aerospace industry, the increasing need for optimum energy conversion efficiency to limit the generation of hydrocarbon production (important greenhouse emission) requires precise sensors in the exhaust system and even in the engine manifold [45]. These stringent requirements are due to the increasing demand to adopt more intricate combustion mechanisms and systems, where reducing gases including  $H_2$  can be used after a period of oxygen-rich operation to aid in the capture of  $NO_x$  gases which may act as indirect greenhouse gases [11], [50]. The increasingly efficient production and storage of hydrogen also encourages hydrogen use within nuclear power plants, where hydrogen can be present within the nuclear reactor close to temperatures can go beyond  $700^\circ C$  and where non-intrusive, high temperature and harsh environment sensors will be necessary for safety and for process control [51]. Monitoring the presence of hydrogen in industrial processes in the metallurgical industry is important, since the presence of hydrogen is known to affect the tensile strength of materials resulting in embrittlement through a process commonly known as high temperature

hydrogen attack (HTHA). In fact, the tensile strength of the 4140 steel alloy can be reduced up to 67% through this process [11], [16], [52].

The previously listed applications show the importance of having reliable sensors for the detection of gas species, in particular  $H_2$ , in harsh-environments with rapidly changing ambient temperatures. This need for high temperature hydrogen sensing has been addressed by different technologies that will be described in the next section. The SAW platform is a promising alternative for high-temperature operation as hydrogen sensors, considering the proven device stability [1] and the potential for wireless and battery-free operation. Previous work has confirmed that SAW devices employing high-temperature resilient materials are capable of functioning as hydrogen sensors [20]. In this work, SAWRs aligned along multiple orientations of a commercially available langasite (LGS) wafer are explored to detect  $H_2$  and temperature simultaneously. Both Pt-decorated yttria-stabilized zirconia (YSZ) and Pt- $Al_2O_3$  composite films were used as  $H_2$  sensing layers. More details regarding this multi-sensor system will be provided in Section 1.6.

## 1.2 Current High-temperature Hydrogen Sensing Technology

A few sensor technologies have been shown to be appropriate for high-temperature, harsh-environment gas sensing, and in particular for molecular hydrogen. These technologies include electrochemical sensors, catalytic sensors, semiconductor metal oxide sensors, field-effect devices on SiC, optical sensors and acoustic sensors [20], [32], [53]–[56]. This section gives an overview of these technologies. Acoustic sensors are described in more detail in the following section.

### 1.2.1 Electrochemical Sensors

Electrochemical sensors consist of two electrodes placed at the ends of a chemically sensitive solid electrolyte. The reaction of the electrolyte with  $H_2$  gives rise to changes in the potential between two electrodes, which is used as the sensor output [48], [53]. Solid

electrolyte oxide materials  $\text{SrCeO}_3$  and  $\text{CaZrO}_3$  were operated as hydrogen sensors at  $700^\circ\text{C}$  in [57]. Electrochemical sensors have fast response time (typically between 30 to 50 seconds for full scale response) and have a sensing range between 100 to 1000 ppm of hydrogen. For sensor recovery, oxygen must be supplied to these sensors. Typical prices for commercial sensing points can be higher than \$1,000 [53]. Limitations of the electrochemical sensor platform include stability and selectivity, as well as precise control or knowledge of the temperature for response characterization.

### 1.2.2 Catalytic Sensors

Catalytic sensors consist of platinum wires embedded in a ceramic bead. The wires are then connected in a Wheatstone bridge configuration [48]. One of the ceramic beads is passivated to avoid interaction with gases, while the other bead is typically coated with a catalyst to promote the interaction with  $\text{H}_2$ . The reaction with  $\text{H}_2$  will increase the temperature of the coated bead, thereby decreasing the conductivity of the leg of the Wheatstone bridge [48], [53]. Temperature operation ranges can vary from  $450^\circ\text{C}$ - $550^\circ\text{C}$  [48], [53] up to  $1000^\circ\text{C}$  [53]. The hydrogen concentration range for which catalytic sensors are used is between 1 to 5 percent, with response times averaging between 10 to 30 seconds. The cost of the technology can range between typical values of \$500 for sensing points and up to \$1200 for fully operational control units [53]. Limitations of catalytic sensors include precise control or knowledge of the temperature for maximizing gas sensitivity and selectivity.

### 1.2.3 Semiconductor Metal Oxide Sensors

Semiconductor metal oxide sensors consists of a metal oxide sensing element such  $\text{SnO}_2$ ,  $\text{ZnO}$  or  $\text{WO}_3$  placed between two electrodes. Changes in the conductivity of the syste due to  $\text{H}_2$ , which can be catalyzed by means of Pt or Pd, can be used to determine  $\text{H}_2$  concentration [54], [55], [58]. This technology is the most popular and well-developed technology for operation as gas sensors [53]. The maximum sensitivity to gas detection for these devices is actually achieved typically in the temperature range between  $250^\circ\text{C}$  and  $600^\circ\text{C}$ , making

these sensors ideal for operation in this temperature range. Semiconductor metal oxide sensors also present very response times (less than 10 seconds) in the  $H_2$  concentration range between 0-1000 ppm. Typical costs for high-temperature sensing elements ranges between \$300-500 with a functional driving circuit [53]. Limitations of semiconductor metal oxide sensors include consumption of high amounts of power and precise knowledge of the ambient temperature to optimize sensor response to  $H_2$  [53].

#### 1.2.4 Field-Effect Sensors

SiC has shown much promise as a resilient semiconducting material capable of continued operation as a semiconductor at high temperatures courtesy of its wide bandgap (up to 7eV) [44]. Stable oxides are able to be grown on the SiC substrate, including  $SiO_2$  and  $Ga_2O_3$ , which, in conjunction with a high-temperature electrode such as Pt or Au, allows for the operation of field-effect devices such as Metal-Oxide-Semiconductor Field-Effect Transistors (MOSFETs) and schottky diodes at high-temperature. These types of devices have been shown to be capable of Hydrogen detection above 300°C [8], [24], [59]. Hydrogen in the ranges from 50 to 1000 ppm may be detected with field-effect sensors [53]. Much work has been done to advance the technology of SiC sensors due to the promise of mass production of low cost sensors due to the well-established semiconductor industry product development technologies. This demand for increased development and test of SiC sensors can be seen by the body of knowledge dedicated solely to sensors utilizing this material in [60].

#### 1.2.5 Optical Sensors

Optical sensors capable of operation at high-temperature are possible with materials such as sapphire and fused silica as the optical fiber [6], [61]. Optical fiber configurations that function sensor elements include interferometric-based configurations, intensity-based configurations and grating-based configurations [56]. Hydrogen detection may be achieved through noble metal (normally Pd) as the chemically sensitive component, where the dissociation of  $H_2$  through the Pd catalyst mechanism described previously for other types

of sensors causes measurable changes in the real and imaginary parts of the refractive index or detection of changes in surface plasmon resonance [56], [61], [62]. Optical sensors present advantages over other sensor technologies including the possibility of interrogating multiple locations with a single optical box (the optical fiber may run through large areas), operation in the absence of O<sub>2</sub> and largely insensitive to environment noise [53], [62]. However, optical sensors exhibit nonlinear interaction with H<sub>2</sub> across the 0% to 5% concentration range, and the response time of optical sensors is typically higher than one minute [62].

### 1.3 Acoustic Wave Sensors

The acoustic wave platform has been known to be effective as a sensor platform for some time [30], [32], [34], [63]–[66]. The attractiveness of the acoustic wave sensing platform lies in its relative simplicity, low cost of fabrication and operation, and small size [30], [34]. Piezoelectric materials are widely used as the means of exciting acoustic waves in materials due to the fact that mechanical energy is coupled to electrical energy in these types of devices. This section describes the principles of acoustic wave propagation and piezoelectricity, and discusses some types of acoustic wave devices used for sensing applications.

#### 1.3.1 Acoustic Wave Propagation and Piezoelectricity

Acoustic waves in solids exist because the solid behaves as an elastic medium which can be modeled by distributed mass-spring elements [67]. Treating the medium as a continuum, the particle displacement  $\mathbf{u} = u_1\mathbf{x}_1 + u_2\mathbf{x}_2 + u_3\mathbf{x}_3$  is defined as the displacement of any particle from its equilibrium position with component particle displacements in the  $\mathbf{x}$ ,  $\mathbf{y}$ , and  $\mathbf{z}$  (defined as  $x_1, x_2, x_3$ ) given by  $u_1, u_2$  and  $u_3$ , respectively. Contributions from rigid translations and rotations are eliminated by defining the strain as [67]:

$$S_{ij} = \frac{1}{2} \left( \frac{\partial u_i}{\partial x_j} + \frac{\partial u_j}{\partial x_i} \right), \quad (1.1)$$

where  $i, j = 1, 2, 3$  (strain is dimensionless). Figure 1.2 illustrates the definition of internal stresses for an elemental volume, where the stress being applied in the  $x_i$  direction on the

face oriented along the  $x_j$  direction is defined as  $T_{ij}$  ( $T_{ij}$  components are shown in the figure), giving nine components of the stress matrix, the same number of components present in the strain matrix. The stress may be related to the strain in the material by assuming a linear relationship between stress and strain (Hooke's Law). This approximation has been validated for small values of strain (values of  $10^{-5}$  or less support the approximation) [67], which is appropriate for acoustic wave devices. The elastic constitutive equation, then, relating stress and strain can be written using Einstein notation (summation over repeated indices) using the stiffness coefficient tensor  $c$  as [63], [67]:

$$T_{ij} = c_{ijkl}S_{kl}. \tag{1.2}$$

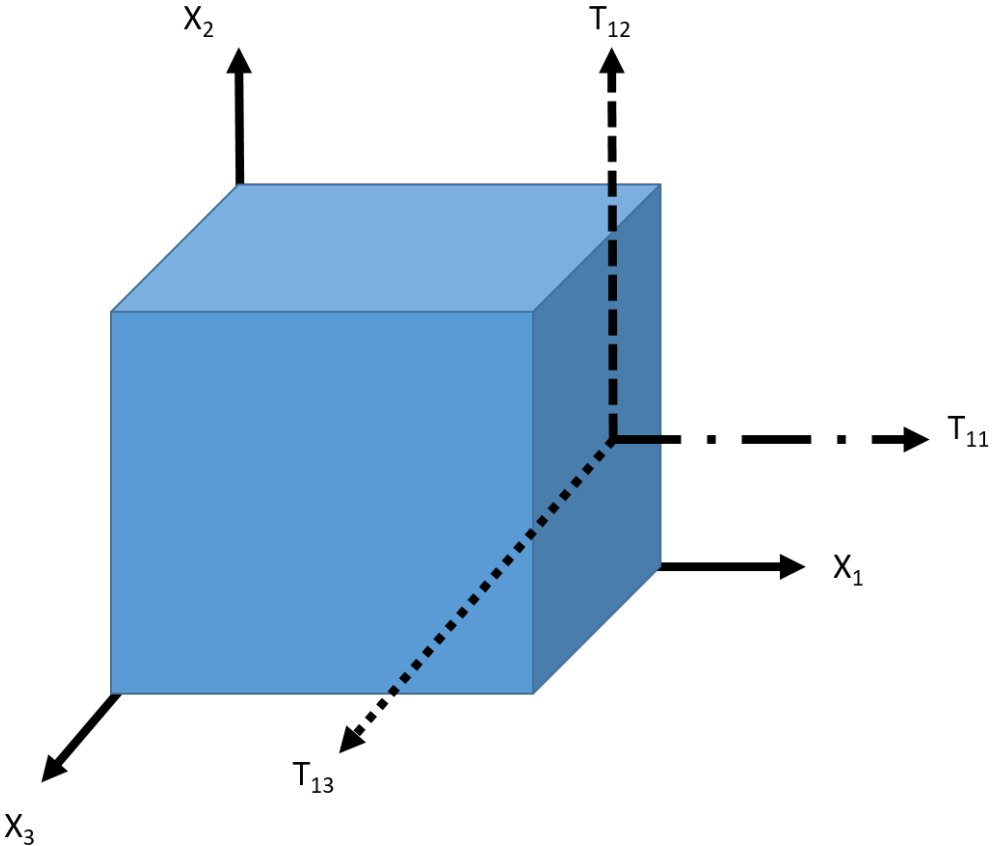


Figure 1.2. Stress components on an elemental volume of an elastic medium acting on the  $x_1$  face.

The previously described displacement vector  $\mathbf{u}$  is a first-rank tensor (requiring one basis vector to identify its components),  $\mathbf{T}$  and  $\mathbf{S}$  are second-rank tensors (requiring two basis vectors to identify each component), and  $\mathbf{c}$  is a fourth-rank tensor (requiring four basis vectors to identify each of its components) [67]. To simplify notation, the quantities may be expressed in terms of the boldface letters, thereby simplifying Equations 1.1 and 1.2 to the following:

$$\mathbf{S} = \nabla_s \mathbf{u}, \quad (1.3)$$

$$\mathbf{T} = \mathbf{c}:\mathbf{S}, \quad (1.4)$$

where the  $\nabla_s$  operator can be defined from Equation 1.1 as  $\nabla_s = 1/2(\nabla\mathbf{u} + \widetilde{\nabla\mathbf{u}})$ , where  $\widetilde{\nabla\mathbf{u}}$  denotes transpose matrix, and the double dot notation is defined as in Equation 1.2 (where summation over repeated indices is assumed) [67]. Application of Newton's Law to the elemental volume gives the general translational equation for motion in a lossless acoustic medium:

$$\nabla \cdot \mathbf{T} = \rho \frac{\partial \mathbf{v}}{\partial t} - \mathbf{F}, \quad (1.5)$$

where  $\mathbf{v} = \partial\mathbf{u}/\partial t$  is the particle velocity and  $\mathbf{F}$  is the body force field. The wave equation for  $\mathbf{v}$  may be constructed by combining Equations 1.3, 1.4, and 1.5 and differentiating with respect to  $t$  to give the following [67]:

$$\nabla \cdot \mathbf{c}:\nabla_s \mathbf{v} = \rho \frac{\partial^2 \mathbf{v}}{\partial t^2} - \frac{\partial \mathbf{F}}{\partial t}, \quad (1.6)$$

Materials exhibiting the piezoelectric effect are used to excite and detect mechanical acoustic waves through the use of electric fields. This is due to the fact that in piezoelectric materials, the presence of an electric fields produces strain in the material and, inversely, the strained material produces an effective electric field. This phenomenon can be accounted for quantitatively by means of the piezoelectric stress tensor  $\mathbf{e}$  (third-rank tensor) and the permittivity tensor  $\epsilon^{\mathbf{S}}$ , modifying the strain/stress relation from 1.2 and coupling to the electric displacement by:

$$\mathbf{T} = -\underline{\mathbf{e}} \cdot \mathbf{E} + \mathbf{c}^E:\mathbf{S}, \quad (1.7)$$

$$\mathbf{D} = \epsilon^{\mathbf{S}} \cdot \mathbf{E} + \mathbf{e}:\mathbf{S} \quad (1.8)$$

Solutions to Equation 1.6 for anisotropic piezoelectric materials subject to the boundary conditions imposed by device design will result in the modes of propagation. Three plane wave solutions will exist, with particle polarization orthogonal to each other.

Assuming that no torque will be present, the stress matrix will be symmetric ( $\mathbf{T}_{ij} = \mathbf{T}_{ji}$ ), which is also the case for the strain matrix from Equation 1.1. This allows for the definition of reduced notation, transforming the number of effective entries of both the stress and strain matrices from 9 to 6, as defined in Table 1.3 [67].

Table 1.3. Reduced notation

Regular indexing $ij$	Reduced Notation $I$
11	1
22	2
33	3
23 and 32	4
13 and 31	5
12 and 21	6

Using this abbreviated notation, Equations 1.7 and 1.8 may be rewritten as [67]:

$$T_J = -e_{Ji}E_j + c_{JI}^E S_I, \quad (1.9)$$

$$D = \epsilon_{ij}^S E_j + e_{iI} S_I \quad (1.10)$$

Without loss of generality, a reference coordinate system is adopted where the propagation direction is selected to be purely in the  $x_1$ -direction. For plane waves in the bulk of materials (unbounded medium), the partial derivatives with respect to  $x_2$  and  $x_3$  are thereby eliminated. This reference coordinate system can be accomplished for any crystallographic orientation by linear transformations given by three Euler angles:  $\{\Phi, \Theta, \text{and } \Psi\}$  [68], [69]. An illustration demonstrating the operation of each of these angles starting from the major crystallographic axis described by coordinate system  $X_1, X_2,$  and  $X_3$  is shown in Figure 1.3, where the cascade of the transformations leads to the final coordinate system

$x_1'''$ ,  $x_2'''$ , and  $x_3'''$ , by means of rotating the axes around the  $x_3$ -axis,  $x_1'$ -axis, and  $x_3''$  by the three Euler angles, respectively. The material constants from Equations 1.9 and 1.10 can be transformed by linear transformations for each angle. Solutions for waves propagating in the x-direction will have uncoupled (pure modes) or coupled (quasi- modes) solutions for particle displacements in each of the three coordinates, where polarization in the  $x_1$ -direction will be longitudinal waves, while particle displacement polarization in the  $x_2$ - and  $x_3$ -directions are shear waves.

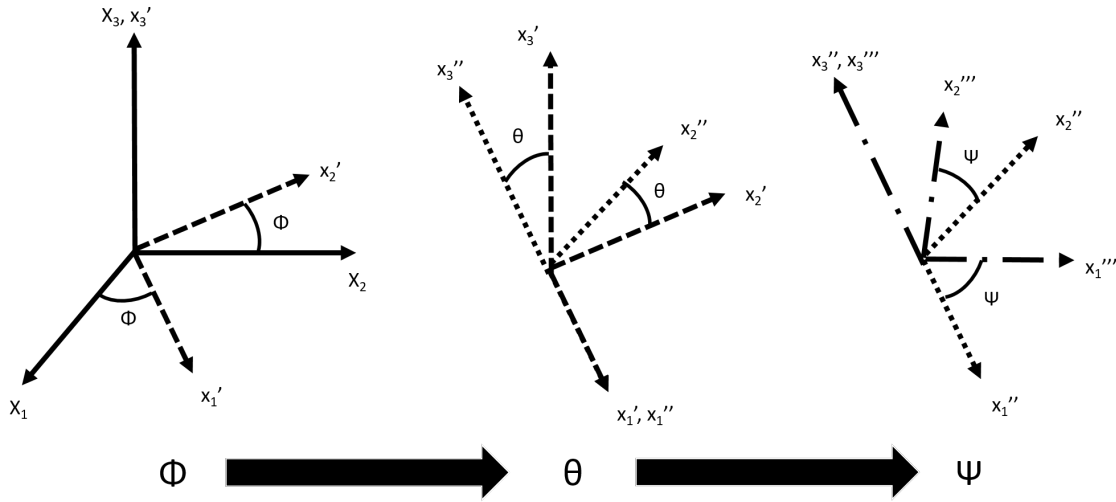


Figure 1.3. Demonstration of crystallographic rotation through use of Euler Angles  $\{\Phi, \Theta,$  and  $\Psi\}$

### 1.3.2 Acoustic Wave Devices for Gas Sensing Applications

Bulk acoustic wave (BAW), SAW and acoustic plate mode (APM) devices have been shown to be capable of operating as gas sensors [30], [63], [64], [70]. BAW devices include thickness-shear-mode (TSM), lateral-field-excited (LFE) resonators and thin film bulk acoustic resonators (FBAR); SAW devices include Rayleigh SAW delay lines and resonators and shear-horizontal SAW (SH-SAW) delay lines and resonators; APM devices include shear-horizontal acoustic plate mode (SH-APM) devices, Lamb-wave acoustic plate mode devices (sometimes referred to as Flexural Plate Wave (FPW) devices), and Love Wave devices [30], [63], [64], [71]. The detection mechanisms can be expressed through perturbation

theory, by noting that small changes in temperature (T), mechanical loading (m), mechanical (c), piezoelectric (e) and dielectric ( $\epsilon$ ) constants and electrical boundary conditions (amongst other factors) will affect the acoustic wave velocity  $v$ , acoustic attenuation  $\alpha$ , or propagation path  $L$ . This is expressed for acoustic wave velocity  $v$  by Equation 1.11 [72]:

$$\frac{\Delta v}{v_0} = \frac{1}{v_0} \left( \frac{\partial v}{\partial T} \Delta T + \frac{\partial v}{\partial m} \Delta m + \frac{\partial v}{\partial c} \Delta c + \frac{\partial v}{\partial e} \Delta e + \frac{\partial v}{\partial \epsilon} \Delta \epsilon + \frac{\partial v}{\partial \sigma} \Delta \sigma + \dots \right) \quad (1.11)$$

A brief description of some of acoustic wave devices used as sensor platforms is presented, while a more detailed description of SAW devices is given in the following section.

### 1.3.2.1 TSM and LFE Resonators

TSM resonators, also known as quartz crystal microbalances (QCMs), consist of thin (thickness  $h_s$ ) AT-cut quartz wafers (for x-propagating waves introduced in Section 1.3.1, the Euler angles for AT-cut quartz are  $\{0^\circ, 35.25^\circ, -90^\circ\}$ ) with electrodes on both sides of the wafer, as shown in Figure 1.4 [63], [73]. Along this orientation, only one of the BAW modes is piezoelectrically active. An alternative excitation scheme is possible where the two electrodes are placed on top of the substrate separated by an electrode gap. This scheme is referred to as Lateral Field Excitation (LFE) and is capable of exciting other modes in AT-cut quartz in addition to the pure shear bulk mode that the TSM resonator excites [74].

The generated shear wave reflects from the opposing side of the crystal and resonance is achieved for frequencies given by  $f_n = (2n\pi)v/(2h_s)$  for  $n = 1, 3, 5 \dots$  [63], [75]. TSM and LFE resonators have been shown to be capable of detecting liquid properties in solutions (aqueous environments) effectively, TSM resonators which only excite pure shear modes and therefore do not leak energy into the liquid [74], [76], and these sensors have also been shown to be capable of functioning as sensors for vapor applications [30], [34], [77], [78]. The principal limitation with regards to high-temperature operation for the TSM and LFE devices, their performance is limited by the  $\alpha - \beta$  transition exhibited by quartz at  $573^\circ\text{C}$ , where the  $\beta$ -quartz structure exhibits no piezoelectric effect [79].

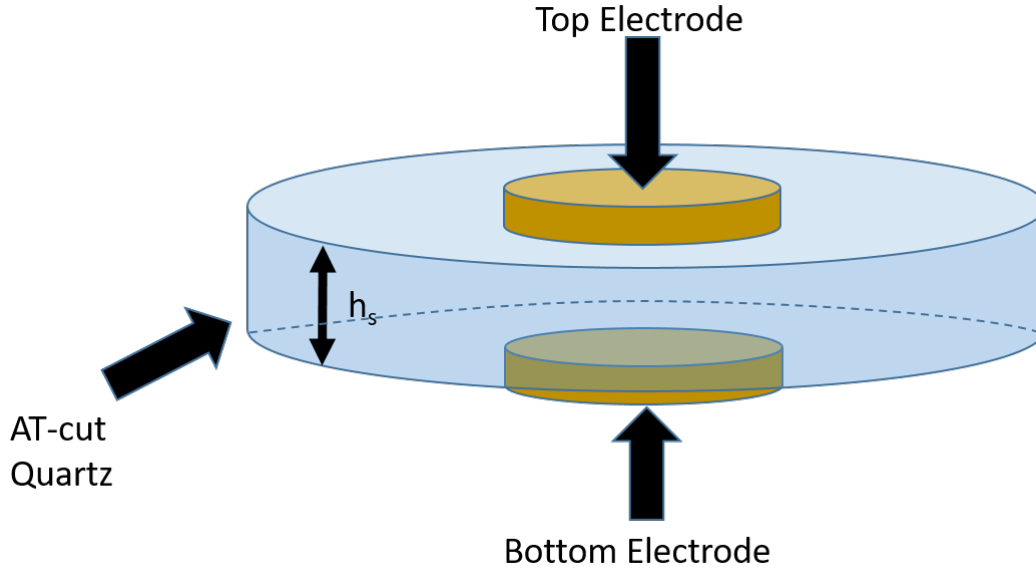


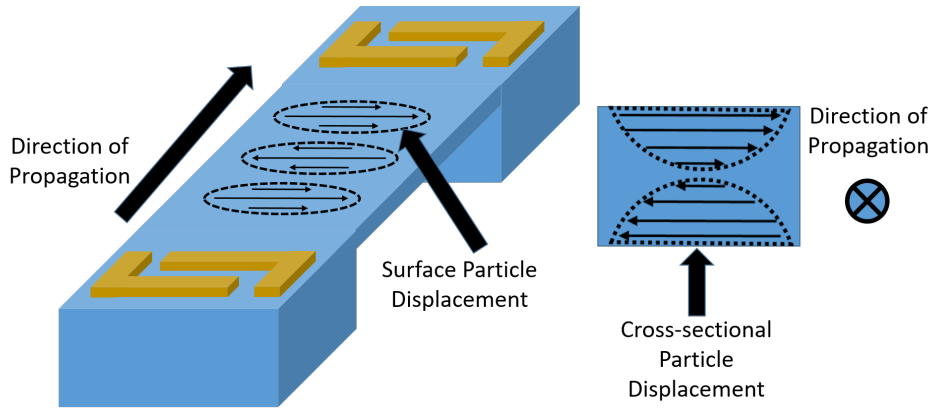
Figure 1.4. TSM resonator structure.

### 1.3.2.2 APM Devices

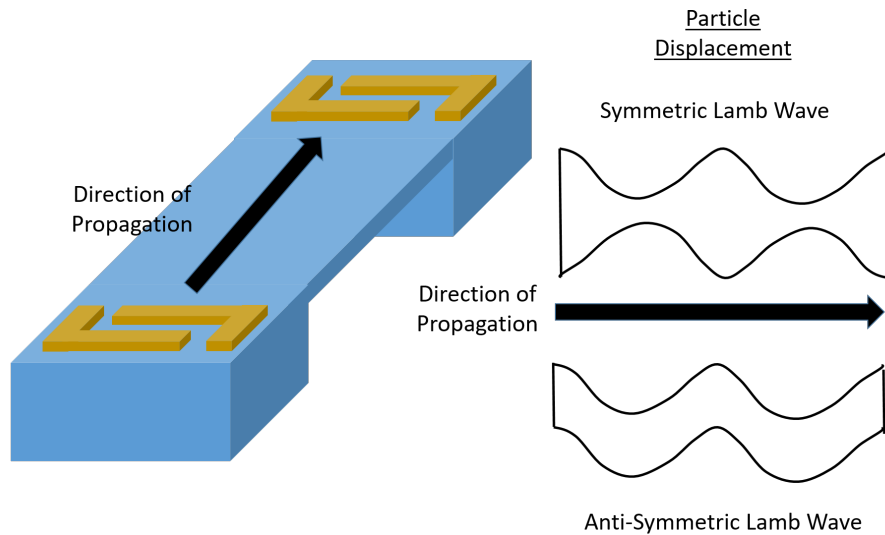
APM devices excite acoustic modes along a thin plate for which boundary conditions on both sides of the plate maintain the wave along the desired direction of propagation [71]. The excitation and detection of APM waves may be achieved through the use of planar interdigitated structures which have the advantage of being one-sided structures and can therefore be deposited using photolithographic processes [30], [34], [64], [71].

SH-APM devices, much like the TSM and LFE devices previously discussed, use thin layers of single-crystal piezoelectric plates (quartz or Lithium Niobate are material options) to propagate their shear waves oriented parallel to the plate surface boundaries [71]. This propagation mode is illustrated in Figure 1.5a. The advantage of SH-APM devices is that the sensitive area is on both sides of the device, and the shear nature of the particle displacement at the surface does not allow for energy leakage into liquids. Due to this SH-APM devices can also be operated in aqueous environments, much as the TSM resonator mode, as well as the capability of gaseous species detection [63], [64].

Lamb wave devices excite waves which have APM particle displacements in the saggital plane (shear-vertical (SV) and longitudinal (P) directions), as shown in Figure 1.5b. [63],



a



b

Figure 1.5. APM device structure and particle displacement: a) SH-APM device; b) Lamb wave Device.

[71]. Due to the particle displacement on both sides of the plate, these devices have been used in differential pressure measurements where differences in partial pressure on both sides of the plate may be detected, which make these types of devices particularly attractive for gas sensing applications [63]. Much work has also been dedicated to developing packaging enabling this type of sensor for liquid phase sensing applications [64].

## 1.4 SAW Sensors

SAW devices are based on waves guided at the surface of the material and can be of the Rayleigh type (particle polarization in the sagittal plane), shear type (particle polarization in the direction normal to the sagittal plane) or of the general type (all three particle polarization components are present) [71], [80]. For x-propagation and a crystal plane normal oriented along the z-axis, assuming that particle displacement on the sagittal plane (y-axis) is zero, the particle displacement can be described by means of Equation 1.12 (assuming the  $e^{j\omega t}$  time variation),

$$\mathbf{u}(x, y, z) = (u_x(z)e^{j\phi_1}\hat{\mathbf{x}} + u_z(z)e^{j\phi_3}\hat{\mathbf{z}})e^{\gamma x}, \quad (1.12)$$

where the  $u_x(z)$  and  $u_z(z)$  represent the particle displacement field amplitudes. These particle polarizations generate elliptical particle displacements which decay with depth rapidly (typically around 90% of the wave energy is within one wavelength of the penetration into the substrate), as shown in Figure 1.6.

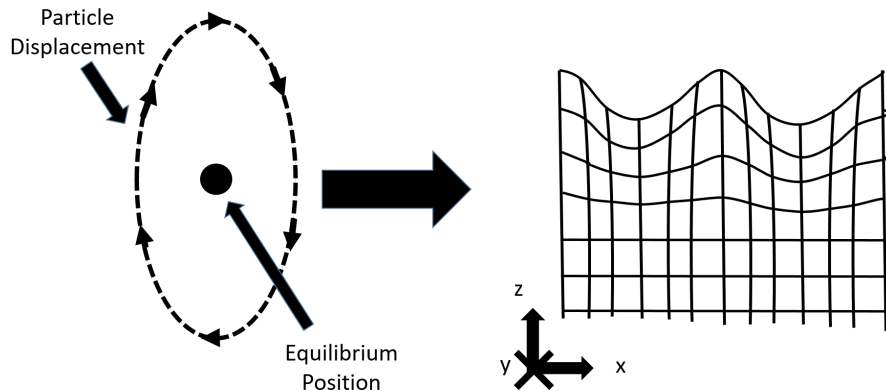
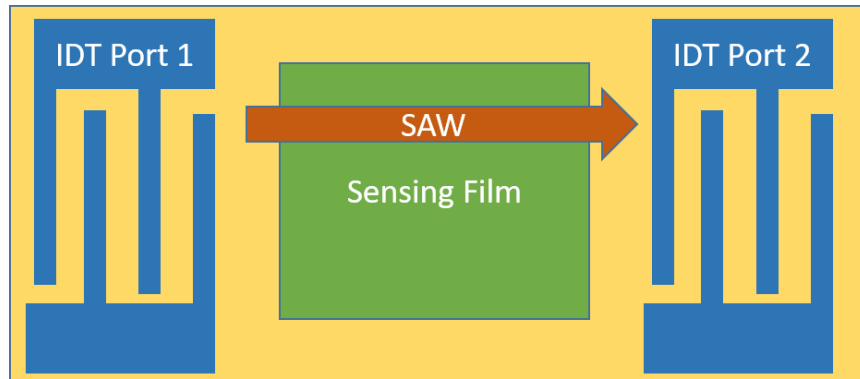


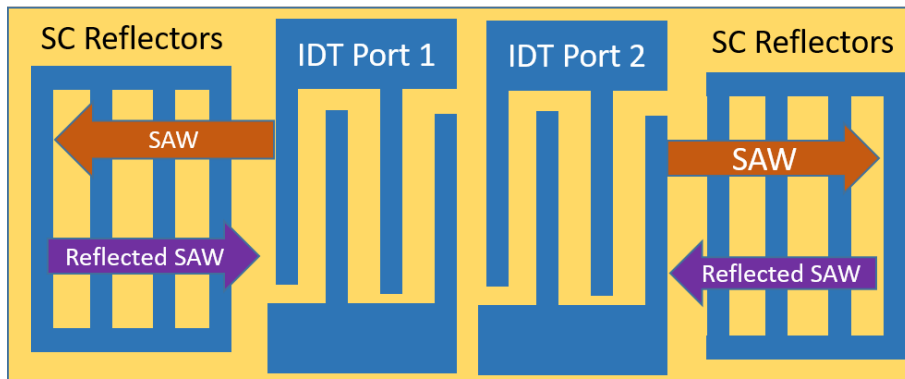
Figure 1.6. Rayleigh waves present in SAW devices.

In the context of SAW sensors, three device configurations are the most popular [28], [30], [34], [63], [66]: the SAW delay line, the two-port SAWR and the one-port SAWR, all of which are schematically shown in Figure 1.7. SAWs can be excited by means of planar electrode structures known as interdigitated transducers (IDTs). For a delay line, the delay or the phase between input and output reflect changes in velocity  $v$  or in propagation length

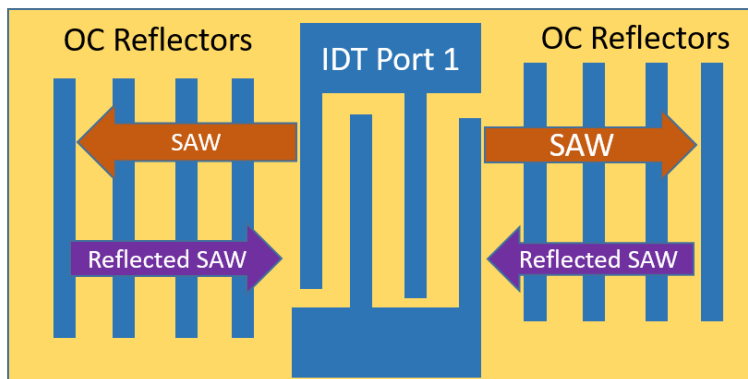
*L.* Changes in the sensing path through the chemical interaction with the environment will perturb the SAW velocity through a variety of mechanisms: mass loading, electroacoustic interactions and changes in material constants of the film or substrate [63], [72]. In the case of the resonators, IDTs are placed within a resonating cavity formed by either short circuit or open circuit electrodes referred to as reflectors [71], [80], [81]. By designing the reflectors and IDTs with periodicity  $\lambda/2$ , resonance will be achieved at the desired frequency considering the SAW velocity along that particular substrate orientation. Sensing films may be placed over the resonating region, the IDT region or over the entire structure for gas sensing purposes, depending on the conductivity of the film (very conductive films will short the IDT structures and reflectors and can therefore not be deposited over the entire structure). Operation characteristics of one-port resonators are further discussed next, since this was the device fabricated and explored in this this work for high-temperature gas sensing experiments.



a



b



c

Figure 1.7. Popular SAW sensor configurations: a) SAW delay line; b) Two-port SAW resonator with short circuit (SC) reflectors; c) One-port SAW resonator with open circuit (OC) reflectors.

### 1.4.1 One-port SAWRs

The structure of a one-port SAW resonator (SAWR) is shown in Figure 1.8 with important features noted. The IDTs should be spaced appropriately to constructively interfere and generate SAW waves close to a frequency determined by the periodicity  $2p$  of the reflector electrodes. The frequency where this periodicity maximizes the reflected wave is given by  $f = v_{SAW}/2p_R$ , where  $v_{SAW}$  is the phase velocity of the SAW and  $p_R$  is the periodicity of the reflectors [80]. The periodicity of the IDT fingers  $p_T$  is usually very similar to  $p_R$ . The reflector gratings are spaced such that the center of reflection of the reflecting structures will meet the Bragg condition for resonance, where the standing wave pattern generated within the resonant cavity will constructively interfere. The equivalent distance for the cavity is labeled as  $L_E$  [80]. The spacing between the reflectors and the IDT structure  $D_{R1}$  and  $D_{R2}$  are adjusted by positioning the IDTs for the strongest energy trapping within the resonating structure. The optimal location will depend on the center of reflection for the individual electrode structures, which is not necessarily the center of the electrode and may be located anywhere within the electrode structure depending on the selected crystal orientation (natural single phase unidirectional transducer (NSPUDT) effect) [81]–[83]. This NSPUDT effect is due to differences in the phase of the reflection coefficient  $\Gamma_1$  (reflection coefficient of a wave incoming from free surface to the electrode-covered region) and  $\Gamma_2$  (reflection coefficient of a wave leaving the electrode-covered region and transitioning to propagation on free surface) as shown in Figure 1.9. This difference in phase results in an effective reflection coefficient  $\Gamma_{Total}$  whose equivalent center of reflection location may be somewhere not corresponding to the geometric center of the electrode. The acoustic aperture  $W$  controls the active overlap of the IDTs and therefore the active area of generation and propagation of the SAW [80], [81].

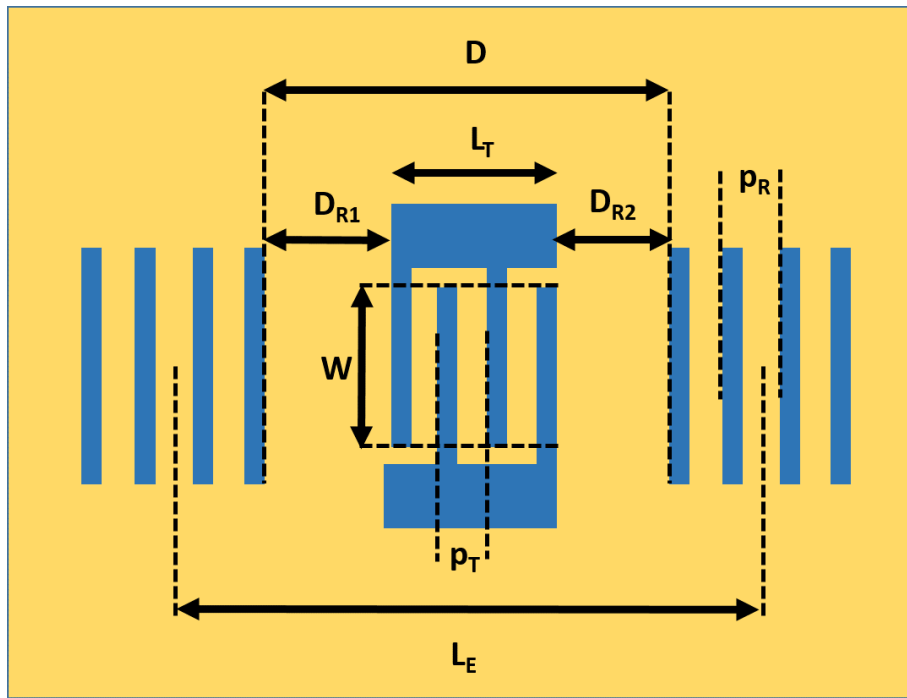


Figure 1.8. Topology of a one-port SAWR with OC reflector gratings.

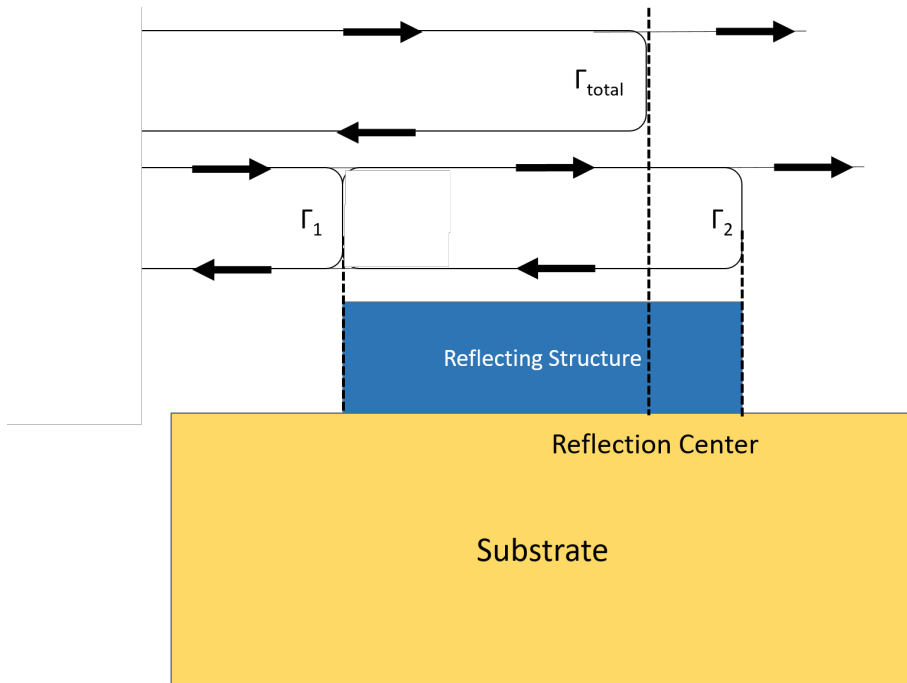


Figure 1.9. Example of reflection coefficient for an electrode with a center of reflection not at the geometric center of the electrode.

Figure 1.10 shows the SAW propagation along an orientation where power flow angle (PFA) is not equal to zero, a phenomenon which can take place for acoustic wave propagation in anisotropic crystals [67]. The SAW propagates along the crystallographic orientation determined by the placement of the exciting IDTs with phase velocity  $v_{SAW}$ . However, the power flow direction (group velocity direction of a wave packet around a certain frequency) is in another direction. IDTs and reflectors must be adjusted to account for this effect for orientations propagating SAWs with  $PFA \neq 0^\circ$  [67], [71], [81].

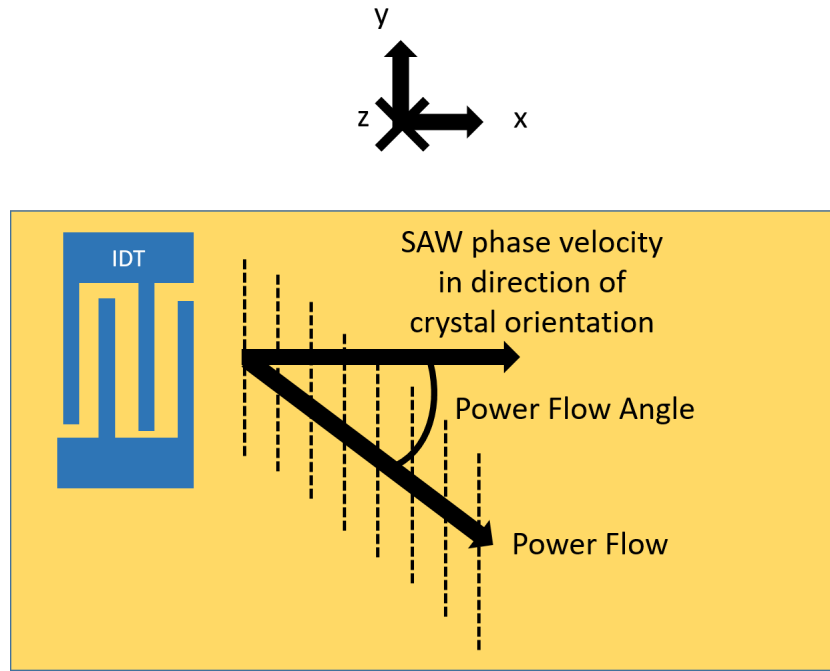


Figure 1.10. Power flow angle in SAW devices.

The temperature dependence of SAWRs is determined by the temperature coefficient of delay (TCD), which is defined as in Equation [81].

$$TCD = \frac{1}{\tau} \frac{\partial \tau}{\partial T} = TCL - TCV, \quad (1.13)$$

where  $TCL = \frac{1}{L} \frac{\partial L}{\partial T}$  and  $TCV = \frac{1}{v} \frac{\partial v}{\partial T}$  are the temperature coefficients of length and velocity, respectively [81]. The TCD is related to the temperature coefficient of frequency by  $TCD = -TCF$ . The TCD is determined by crystallographic orientation and is calculated around a temperature. TCD relates the change in delay (or frequency for TCF) per change in

temperature due to the thermal expansion of the material and the temperature dependence of the rotated acoustic wave material constants at a particular temperature [81]. The one-port SAWR frequency dependence vs. temperature over a temperature range can be modelled by a second degree polynomial [84], [85].

## 1.5 High-temperature Operation of SAWR Sensors

The challenges facing high-temperature operation of SAWRs as gas sensors can be related to three factors: 1) the piezoelectric substrate, 2) the electrodes used as IDTs to excite the SAW and to act as reflector structures, and 3) the choice of sensing film [1]. In addition, mounting and packaging considerations are important, but not as critical as for strain sensing applications [28]. This section discusses the technological advances and challenges associated with the previously mentioned factors.

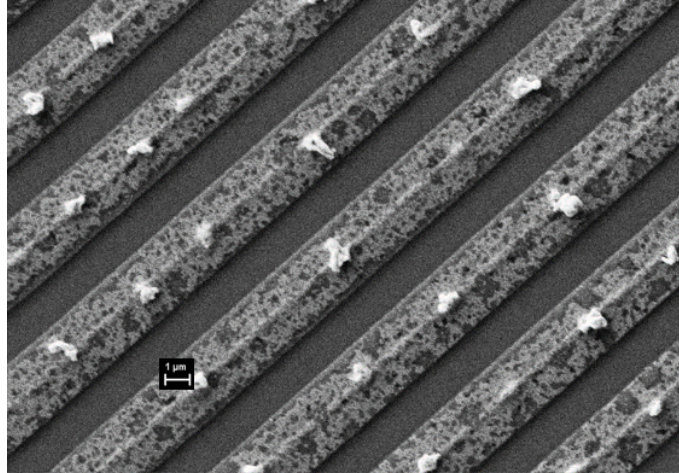
### 1.5.1 High-temperature Piezoelectric Substrates

Piezoelectric materials to be operated at high-temperature should maintain their piezoelectric qualities without undergoing major phase changes, as is the case with Quartz which changes phase around 573°C and becomes non-piezoelectric [79]. Many commonly used piezoelectric materials such as Quartz and LiNbO<sub>3</sub> are limited in the context of high-temperature operation typically to temperatures below 500°C [5]. A number of High-temperature piezoelectric substrates have been identified for operation with SAWR sensors [1], [4], [5], [86], [87]. Some materials for high-temperature applications include AlN and GaN, both of which have applications in the microelectronics industry, as well as the langasite family crystals. These langasite crystals are have a trigonal crystal system and are well-suited for high temperature applications. Common examples of these crystals include LGS, (La<sub>3</sub>Ga<sub>5</sub>SiO<sub>14</sub>),LGT (La<sub>3</sub>Ga<sub>5.5</sub>Ta<sub>0.5</sub>O<sub>14</sub>), and LGN (La<sub>3</sub>Ga<sub>5.5</sub>Nb<sub>0.5</sub>O<sub>14</sub>), as well as some modifications of these crystals using Al [5]. Other types of materials using Ca or Sr instead of La exist such as CNGS (Ca<sub>3</sub>NbGa<sub>3</sub>Si<sub>2</sub>O<sub>14</sub>), CTGS (Ca<sub>3</sub>TaGa<sub>3</sub>Si<sub>2</sub>O<sub>14</sub>), STGS

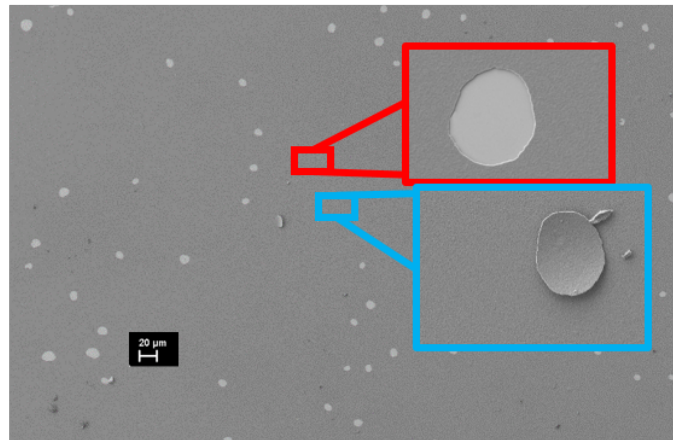
( $\text{Sr}_3\text{TaGa}_3\text{Si}_2\text{O}_{14}$ ) and SNGS ( $\text{Sr}_3\text{NbGa}_3\text{Si}_2\text{O}_{14}$ ) [5]. LGS in particular has been studied extensively with regards to its use as substrate for high-temperature sensors. LGS exhibits no phase transitions up to its melting point of  $1470^\circ\text{C}$  [1], [4], [5], and high quality crystals may be fabricated through Czochralski crystal growth methods [88]. LGS wafers are currently commercially offered by MetaLaser Inc., Roditi International Corporation, MSE Supplies, Shanghai SICCAS High Technology Corporation and Fomos-Materials.

### 1.5.2 High-temperature Electrodes

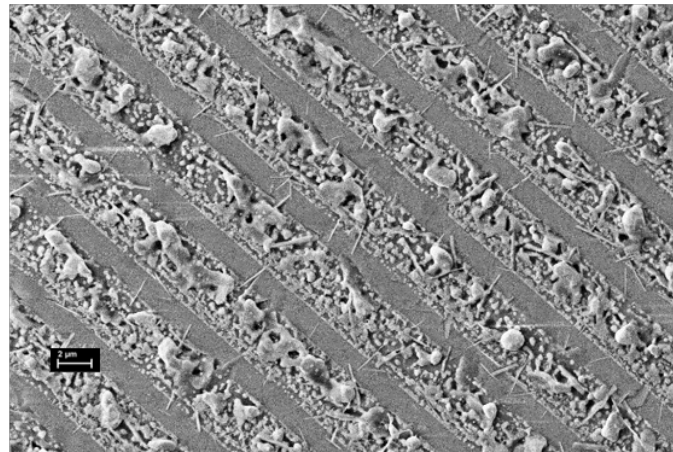
Previous work at the University of Maine has addressed the deposition of thin film metals and metal composites to reliably perform as IDTs and reflectors for SAW devices at high temperature [1], [89]–[91]. The conductivity characteristics of a variety of Pt-alloy films including Pt-Ti, Pt-Co, Pt-Ni, Pt-Cr, Pt-Rh, Pt-Ta, Pt-Al and Pt- $\text{Al}_2\text{O}_3$  films on LGS and other substrates [91]. These results have shown that Pt- $\text{Al}_2\text{O}_3$  alloys retain conductivity when exposed to temperatures up to  $1100^\circ\text{C}$ , which many of the other composite alloys are not capable of achieving [91]. The stability and continued high-temperature operation of the SAWR sensors does not uniquely depend on the materials retaining their conductivity, however. The presence of agglomeration, hillocks, and whiskers, shown in Figure 1.11 [92], have all been identified as factors that may affect the continued stable operation of high-temperature SAW devices [1], [84], [89], [90], [93].



a



b



c

Figure 1.11. High-temperature electrode problems: a) Agglomeration; b) Hillock Formation; c) Whisker formation [92].

### 1.5.3 High-temperature Sensing Film

For a sensitive film overlay, materials capable of withstanding the high-temperature exposure are necessary, as well as materials that are capable of interacting with the desired measurand at high-temperatures. SAW devices on LGS employing Pt electrodes with a  $\text{WO}_3$  sensing film have been developed for detection of  $\text{C}_2\text{H}_4$ , and Pd has been used as both the electrode and active sensing film in a bare-device configuration for the detection of  $\text{H}_2$  above  $200^\circ\text{C}$  [94]. ZnO sensing films have been used on delay line sensors on LGS for detection of  $\text{O}_2$  [21], [95], [96] up to  $650^\circ\text{C}$ .

## 1.6 Framework for Temperature and Gas Mutli-Sensor System

As mentioned in Section 1.4.1, the SAWR sensor frequency vs. temperature dependence can be approximated by means of a second degree polynomial (parabolic fitting) and varies with SAW orientation. For the purposes of the analysis in this work, it will be assumed that the presence of the gas measurand of interest may be modelled by a binary variable, and that the presence of this gas will produce a change in frequency that may be temperature-dependent. The frequency of a SAWR sensor oriented along orientation  $\Psi$  can therefore be approximated as follows:

$$f_\Psi \approx R_\Psi^{N_2}(T) + S_\Psi(T) \times G, \quad (1.14)$$

where  $R_\Psi^{N_2}(T)$  is the temperature dependence of the frequency assuming a  $\text{N}_2$  baseline, and  $S_\Psi(T) \times G$  is a frequency shift due to the introduction of the gas measurand of interest (in the context of this thesis the measurand will be a mixture of 4% $\text{H}_2$  in balance  $\text{N}_2$ ) into the system with respect to the  $\text{N}_2$  baseline.  $R_\Psi^{N_2}(T)$  is assumed to be only a function of temperature  $T$ , and  $S_\Psi(T) \times G$  is assumed to be both a function of temperature  $T$  and of the binary variable  $G$  denoting presence of  $\text{H}_2$  ( $G = 1$ ) or the absence of  $\text{H}_2$  ( $G = 0$ ).  $R_\Psi^{N_2}(T)$  may be assumed to be parabolic fitting of experimental data and can be represented by:

$$R_\Psi^{N_2}(T) = A_\Psi(T - T_{0\Psi})^2 + B_\Psi, \quad (1.15)$$

where  $A_\Psi$  is an orientation-dependent parameter modulating the openness of the parabola used for the fit,  $T_{0\Psi}$  is the temperature of temperature-compensated operation, and  $B_\Psi$  is a correction term to match the resulting parabola to the experimental data.

Considering  $G = 0$ , the frequency difference between two sensors oriented along  $\Psi_1$  and  $\Psi_2$  will be given by:

$$\Delta f = f_{\Psi_1} - f_{\Psi_2} = (A_{\Psi_1} - A_{\Psi_2})T^2 - (2A_{\Psi_1}T_{0\Psi_1} + 2A_{\Psi_2}T_{0\Psi_2})T + C, \quad (1.16)$$

where  $C = A_{\Psi_1}T_{0\Psi_1}^2 - A_{\Psi_2}T_{0\Psi_2}^2 + (B_{\Psi_1} - B_{\Psi_2})$ . Equation 1.16 reveals that this frequency difference can be used to calculate temperature linearly assuming that  $(A_{\Psi_1} - A_{\Psi_2})$  is close to zero. For  $G = 1$ , the same result holds, but with the addition of the temperature dependent  $S_\Psi$  terms:

$$\Delta f = f_{\Psi_1} - f_{\Psi_2} = (A_{\Psi_1} - A_{\Psi_2})T^2 - (2A_{\Psi_1}T_{0\Psi_1} + 2A_{\Psi_2}T_{0\Psi_2})T + C + (S_{\Psi_1}(T) - S_{\Psi_2}(T)). \quad (1.17)$$

Equations 1.16 and 1.17 show that it is possible to make two calibration curves with temperature, one for  $G = 1$  and one for  $G = 0$ . Then, an estimate of the temperature obtained from the frequency reading of either sensor can be used to determine whether  $G = 1$  or  $G = 0$  is more likely.

It was the scope of this work to test the feasibility of the framework provided for the binary exposure to gas species and a temperature dependent frequency modifier due to gas exposure ( $S_\Psi$ ). However, for a gas frequency modifier that is both a function of temperature and gas concentration, the framework may be altered by including the continuous variable  $g$  denoting the concentration of the gas measurand of interest:

$$\Delta f = f_{\Psi_1} - f_{\Psi_2} = (A_{\Psi_1} - A_{\Psi_2})T^2 - (2A_{\Psi_1}T_{0\Psi_1} + 2A_{\Psi_2}T_{0\Psi_2})T + C + (S_{\Psi_1}(T, g) - S_{\Psi_2}(T, g)). \quad (1.18)$$

In Equation 1.18, the frequency modifiers are  $S_{\Psi_1}$  and  $S_{\Psi_2}$  are now both a function of temperature and gas concentration. The feasibility of a sensor system with this kind of operation would involve the characterization of the frequency modifiers as both a function

of temperature and gas concentration, creating a three-dimensional surface for  $S_{\Psi_i}$  as both a function of temperature  $T$  and gas concentration  $g$ .

## 1.7 Goals and Scope

As has been noted in Section 1.1, high-temperature gas sensors are required in a number of applications and can be expected to operate in harsh-environments with rapidly fluctuating temperatures and gas compositions. The reliability of sensor systems employed for these applications will depend on the sensor system ability of differentiating between temperature and gas-related effects. The goal of this thesis was to investigate the use of high-temperature LGS SAWR sensors to simultaneously detect gas and temperature at operating temperatures up to 600°C as detailed in Section 1.6. As case-study, this work used high purity N<sub>2</sub>, 4.7 grade O<sub>2</sub>, and a 4%H<sub>2</sub>/96%N<sub>2</sub> gas mixture.

The scope of this thesis focused on addressing the following objectives in order to probe the feasibility of the two-sensor system mathematically formulated in Section 1.6:

- developing SAWR sensors operating along different crystallographic orientations on the commercially available LGS wafer to vary temperature dependence;
- implementing a high-temperature gas testing system capable of extended periods of gas cycling at temperatures up to 650°C;
- testing the use of yttria-stabilized zirconia (YSZ) and Pt-Al<sub>2</sub>O<sub>3</sub> thin films as sensitive elements to vary the gas responsiveness of sensor elements with respect to devices not employing the YSZ film under laboratory condition exposures to 4%H<sub>2</sub> mixtures in N<sub>2</sub> balance; and
- integrate the obtained results to analyze the feasibility of a two-SAWR sensor system.

It was not within the scope of this work to investigate the selectivity of the developed sensors to other reducing gases, such as CH<sub>4</sub> or hydrocarbon gases.

## 1.8 Organization

To address the objectives and report on the findings listed in Section 1.7, this thesis is organized into the following chapters after this introduction:

- The second chapter details the design and fabrication and temperature characterization of SAWRs to be used as the sensors. The selection of five SAW crystallographic orientations on the commercial LGS wafer, two of which were predicted to have temperature-compensated operation ( $TCD = 0$ ) above  $150^{\circ}\text{C}$ , is presented. The development of high-temperature materials for sensing films and electrode operation, including yttria-stabilized zirconia (YSZ) and Pt- $\text{Al}_2\text{O}_3$  is described. The fabrication of one-port SAWR sensors at the University of Maine cleanroom facilities is discussed.
- The third chapter presents the development and implementation of a high-temperature gas testing system capable of characterizing the fabricated SAWR sensor gas response up to  $650^{\circ}\text{C}$ . In this chapter, the sensor setups used to acquire experimental results are also detailed.
- The fourth chapter presents the experimental findings for SAWR sensor operation as gas sensors. Temperature characterization of the selected LGS orientations is detailed. Stability of two Pt- $\text{Al}_2\text{O}_3$  thin film compositions with respect to temperature cycling up to  $850^{\circ}\text{C}$  for over 300 hours is also presented. Gas cycling results for five LGS orientations up to  $600^{\circ}\text{C}$  obtained using the high-temperature gas testing system are also detailed. The feasibility of using a two-sensor system to predict temperature and gas data is presented. Wireless measurements of a SAWR sensor under gas cycling environment up to  $478^{\circ}\text{C}$  are given.
- The fifth and final chapter gives a summary of the work and suggested future work.

## CHAPTER 2

# DETERMINATION OF ORIENTATIONS ON THE COMMERCIAL LGS WAFER AND DEVELOPMENT OF THIN FILM MATERIALS FOR HIGH-TEMPERATURE SAW GAS SENSING OPERATION

This chapter details the investigation of SAW orientations for high-temperature gas sensing applications, as well as the development of sensing films and electrodes for high-temperature SAWRs to perform as hydrogen gas sensors. A search for sufficiently strong electromechanically coupled and possibly temperature-compensated orientations was carried out on a commercially available LGS described by Euler angles  $\{0^\circ, 138.5^\circ, 26.7^\circ\}$ . As a result from this search, five orientations were selected and a photolithographic mask was generated for the fabrication of LGS one-port resonators. The development of thin-films for high-temperature sensing and transduction for the SAWR sensors based on Yttria-Stabilized Zirconia (YSZ) and Pt-Al<sub>2</sub>O<sub>3</sub> is also discussed in this chapter.

### 2.1 Commercially Available LGS Wafer Analysis for SAW Operation at High Temperature

This section details the calculation of SAW properties on the commercially available LGS plane characterized by Euler Angles  $\{0^\circ, 138.5^\circ, 26.7^\circ\}$ . The calculations aimed at extracting relevant SAW properties for device design including the electromechanical coupling coefficient ( $K^2$ ), the power flow angle (PFA), the temperature coefficient of delay (TCD), and the SAW velocity. The calculations were carried out using matrix method calculations as discussed in [87], [97]. The extraction of the  $K^2$  and TCD parameters allowed for the selection of five orientations of interest for the purpose of device operation as high-temperature gas sensors. The layout of a photolithographic mask for one-port resonator fabrication is also presented.

### 2.1.1 Selection of LGS Orientations

Calculations were carried out on the commercially available LGS wafer plane, given by Euler angles by  $\{0^\circ, 138^\circ, 26.7^\circ\}$ . Calculations using constants from Nicolay and Aubert were performed [98]–[100] in conjunction with Matlab scripts from Dr. Mauricio Pereira da Cunha developed as indicated in [87], [97]. The materials constants at  $20^\circ\text{C}$  (stiffness coefficients  $c$ , piezoelectric constants  $e$ , and permittivity constants  $\epsilon_r$ , density  $\rho$  and temperature coefficients of expansion  $\alpha$ ) and the corresponding first and second order temperature coefficients of stiffness [99] are shown in Table 2.1. The first and second order temperature coefficients allow for the interpolation of experimental data to a second order fitting for all the material constants, thereby allowing extrapolation of the room temperature constants to  $800^\circ\text{C}$  with a high degree of accuracy [99].

Table 2.1. LGS constants used for SAW calculations [99]

Constant	Value at $20^\circ\text{C}$	First Order Coefficient (ppm/ $^\circ\text{C}$ )	Second Order Coefficient (ppb/ $^\circ\text{C}^2$ )
$c_{11}$	$18.89 \times 10^{10} \text{ N/m}^2$	-65	-39
$c_{13}$	$10.15 \times 10^{10} \text{ N/m}^2$	-84	-86
$c_{14}$	$1.442 \times 10^{10} \text{ N/m}^2$	-304	88
$c_{33}$	$26.83 \times 10^{10} \text{ N/m}^2$	-105	-55
$c_{44}$	$5.33 \times 10^{10} \text{ N/m}^2$	-63	-80
$c_{66}$	$4.237 \times 10^{10} \text{ N/m}^2$	-29	-23
$e_{11}$	$-0.4371 \text{ C/m}^2$	469.8	-428.5
$e_{14}$	$0.1039 \text{ C/m}^2$	-713.8	1594
$\epsilon_{r11}$	19.05	134.5	118
$\epsilon_{r33}$	51.81	-787.0	658.6
$\rho$	$5764 \text{ kg/m}^3$	—	—
$\alpha_{11}$	—	5.2	6.7
$\alpha_{33}$	—	3.72	1.1

The initial parameters of interest were  $K^2$  and  $TCD$ , and so these parameters were calculated for the selected LGS plane as a function of the last Euler angle  $\Psi$ . The results for  $K^2$  and  $TCD$  at  $200^\circ\text{C}$ ,  $300^\circ\text{C}$ , and  $400^\circ\text{C}$  are shown in Figures 2.1 and 2.2, respectively. The

minimum acceptable  $K^2$  for SAWR fabrication was taken to be 0.1%. In addition, the search targeted the identification of temperature-compensated orientations at temperatures above 100°C. Figure 2.1 shows that  $K^2$  is not very sensitive to temperature variations in the selected temperature range. The orientations selected for fabrication are highlighted in Figures 2.1 and 2.2 by the vertical dashed lines. The selected orientations along  $\Psi = 14.7^\circ$  and  $77.7^\circ$  have 0.15% and with temperature compensation around 200°C and 300°C, respectively. Orientations with  $\Psi = 26.7^\circ, 20.7^\circ$  and  $32.7^\circ$  were also chosen since around these orientations the highest  $K^2$  is observed and previous University of Maine fabrications along  $\Psi = 26.7^\circ$  and  $32.7^\circ$  have shown good results for high-temperature SAWRs [1], [20], [28], [84]. All of the orientations were selected to be integer number of degrees away from the one-port resonator oriented along  $\Psi = 26.7^\circ$  which defines the commercially available wafer.

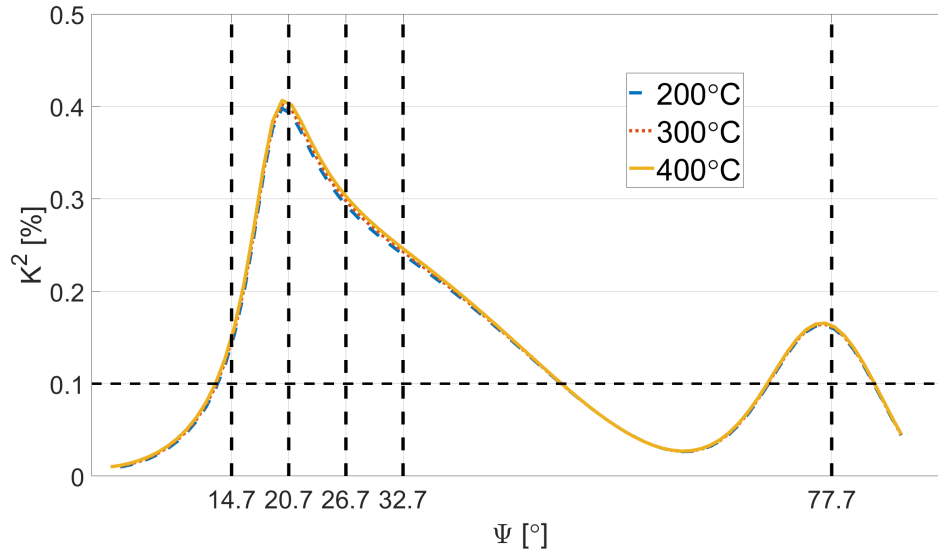


Figure 2.1.  $K^2$  at 200°C, 300°C, and 400°C for the commercial LGS wafer. Dotted-dashed curve: 200°C; Dotted curve: 300°C; Solid curve: 400°C.

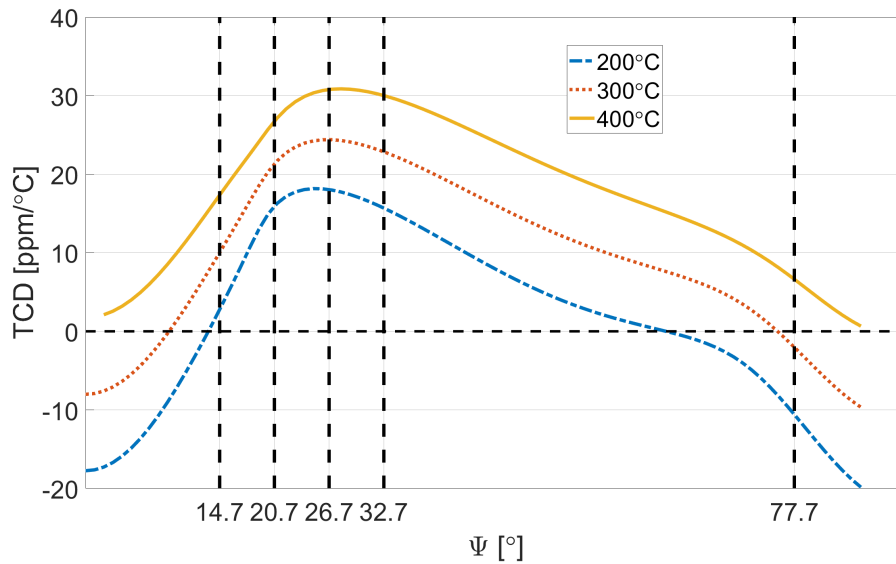


Figure 2.2.  $TCD$  at 200°C, 300°C, and 400°C for the commercial LGS wafer. Dotted-dashed curve: 200°C; Dotted curve: 300°C; Solid curve: 400°C.

### 2.1.2 Photolithographic Mask Layout

A photolithographic mask was generated for the fabrication of one-port SAWRs with open circuit reflectors oriented along the crystallographic orientations previously mentioned. Open-circuit reflectors were chosen because it has been shown that the short-circuit grating on LGS with Pt-based structures leaks energy onto the connecting busbar, while the open-circuit grating is able to concentrate the energy within the grating [101]. Figure 2.3 shows the layout of the mask generated using AutoDesk’s AutoCAD software. The phase velocity  $v_p$  and the power flow angle  $PFA$  were calculated for each orientation at room temperature and the IDT electrode thickness determined using a 1:1 mark to space ratio (duty cycle of 50%) for an operational frequency  $f_0$  around 195MHz. The periodicity of electrodes in the IDT regions  $p$  was equal to  $\lambda/2$ , where  $\lambda$  is given by  $\lambda = v_p/f_0$ . LGS exhibits the NSPUDT effect discussed in section 1.4.1 [81]–[83]. The precise determination of the spacings between the IDTs and the reflector electrodes can be determined through calculations of the reflection coefficients  $\Gamma_1$  and  $\Gamma_2$  in Figure 1.9 to obtain the center of reflection. However, precise calculation of these parameters requires a finite element analysis of the reflecting structure that takes mass loading into account (especially if the reflecting structures are based of a heavy electrodes such as Pt). Since proper FEM/BEM calculation tools and electrode characterization data were not available at the time of design, three different positionings of the IDT with respect to the resonant cavity of three SAWRs were laid out for the orientations  $\Psi = 14.7^\circ, 20.7^\circ, 32.7^\circ$  and  $77.7^\circ$ . The three IDT positionings were denoted S, RC and LC, and are illustrated in Figure 2.4. For devices S (synchronous), the geometric center of the first reflector on either side of the IDTs was placed a distance  $\lambda/4$  away from the last IDT electrode. For RC devices (right-compensated), the IDT structure was moved a distance of  $\lambda/8$  to the right such that the space between the last IDT electrode on the right side and the first reflector was a distance of  $\lambda/8$ . For LC devices (left-compensated), the same applies, but the IDT structure was moved to the left. This three IDT positioning schemes were not done for devices oriented along  $\Psi = 26.7^\circ$  because the device template

had previously accounted for the NSPUDT effect and was determined that synchronous positioning was optimal for this orientation. The design details for the each orientation on the mask can be found in Table 2.2.

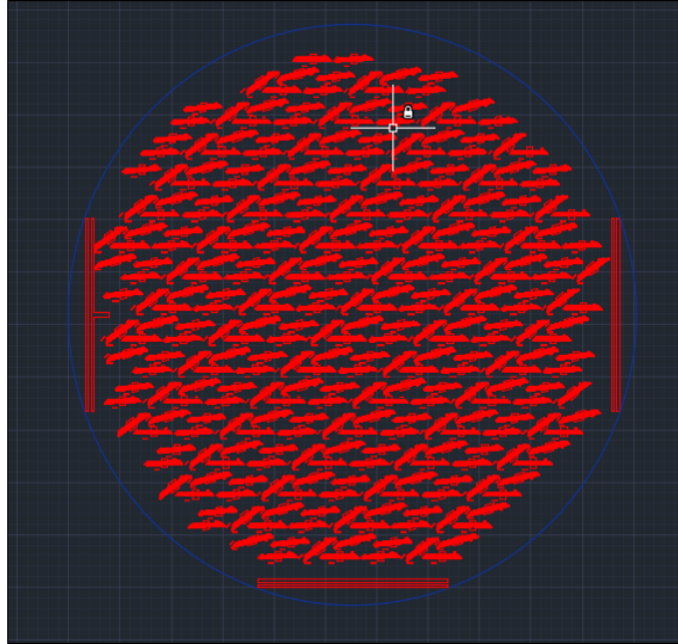
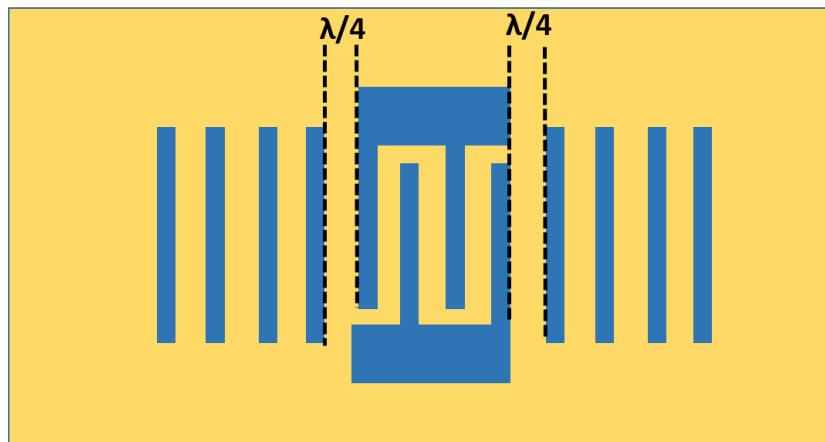


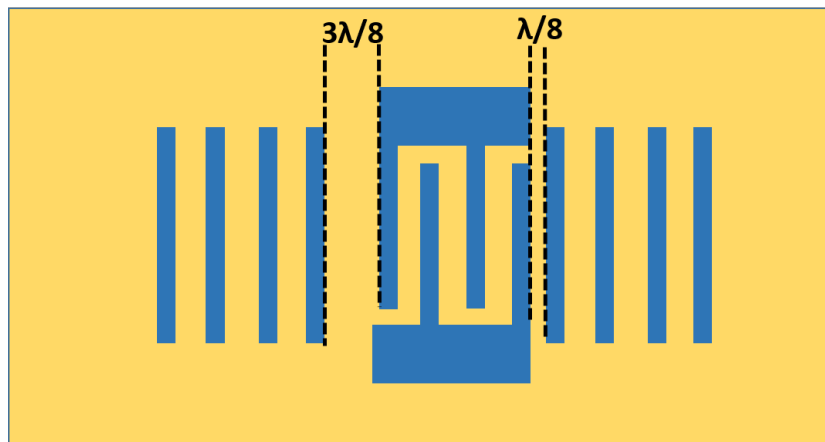
Figure 2.3. AutoCAD layout of photolithographic mask.

Table 2.2. Summary of Device Parameters

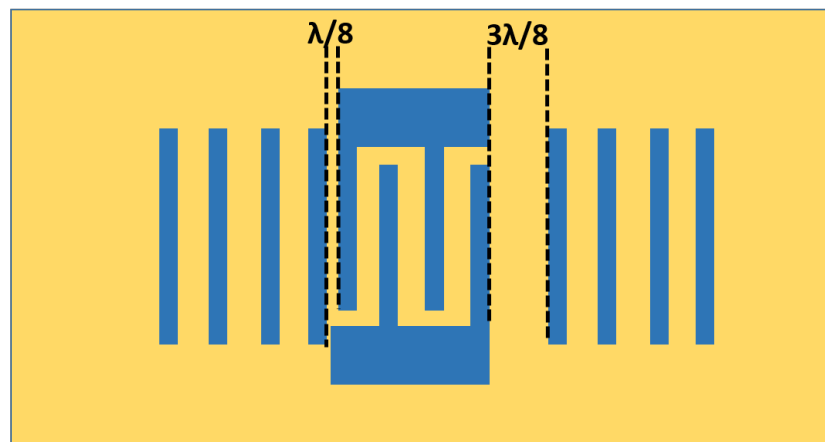
$\Psi$ ( $^{\circ}$ )	Predicted Compensated Temperature ( $^{\circ}\text{C}$ )	$K^2$ (%)	$\lambda$ ( $\mu\text{m}$ )	PFA ( $^{\circ}$ )	W ( $\lambda$ )	IDT Pairs	Reflectors on each side
14.7	200	0.15	13.4	26	61	120	411
20.7	NA	0.37	13.9	12	51	80	411
26.7	20	0.27	14	0	51	80	411
32.7	NA	0.23	14	-3	51	80	411
77.7	300	0.15	13.1	-16	61	120	411



a



b



c

Figure 2.4. Device layout for compensation of NSPUDT effects: a) Synchronous S devices; b) Right Compensated RC devices; c) Left Compensated LC devices.

## 2.2 High Temperature Thin Film Materials

Two thin film materials were explored in this work with the purpose of developing SAWR high-temperature hydrogen gas sensors. Yttria-Stabilized Zirconia (YSZ) was explored as the sensing layer to be decorated with Pt particles functioning as catalysts for the interaction with  $H_2$ , and Platinum Alumina ( $Pt-Al_2O_3$ ) was explored as a double-purpose sensing layer and electrode material for the IDTs and reflectors. Design and Fabrication details for each of these materials is presented in this section. The deposition of these high-temperature materials was done using the RF magnetron sputtering and electron-beam (e-beam) evaporation deposition chamber described in [102].

### 2.2.1 Yttria-Stabilized Zirconia (YSZ)

YSZ is a metal-oxide material consisting of  $ZrO_2$  base stabilized using a quantity of yttria ( $Y_2O_3$ ) [103]. The use of yttria has been shown to stabilize the cubic phase of the epitaxially grown thin films of  $ZrO_2$  [103]. YSZ has been identified as a material capable of acting as a sensing layer for gas sensing applications in the domain of optical sensing at high-temperatures [104]. YSZ has previously been shown to operate reliably at  $500^\circ C$  and detectable changes in surface properties such as conductivity and plasmon resonance have been documented and indicate that electrochemical gas sensing of  $O_2$  and  $H_2$  is possible at high-temperature using YSZ thin films [104], [105]. Particles of Au and Ag have been embedded in the YSZ to act as catalysts in both reducing and oxidizing environments to promote the selectivity and surface response of the YSZ film in the context of optical sensors [106]–[108]. In this work, YSZ thin films with Pt decoration to act as catalyst for  $H_2$  dissociation into the YSZ material were developed and outfitted for use in conjunction with the one-port SAWRs previously described.

YSZ films were deposited using RF magnetron sputtering. An 8%  $Y_2O_3$ -92% $ZrO_2$  YSZ alloy target was used as the deposition source in a pressure of 3 mTorr of 5% $O_2$ /95%Ar gas mixture. The deposition of YSZ directly on top of LGS substrate for substrate temperatures

of room-temperature (25°C) and 600°C was conducted. SEM images of the YSZ thin films 25 nm thick deposited at substrate temperatures of 600°C and 25°C are shown in Figure 2.5a and 2.5b, respectively, after the samples were cycled in a furnace between 750°C and 25°C with one-hour soaking periods in air. It was found in this work that the YSZ thin film deposited at high-temperature (Figure 2.5a) showed no signs of stress-induced hillocks, while the thin-film deposited at room-temperature (Figure 2.5) showed small formations of approximately 50 nm in diameter and hillocks approximately 500 nm in diameter. The hillock formation is undesirable for the propagation of SAWs as it can lead to increased diffraction and scattering, as well as lead to inconsistent and drifting sensor responses. For this reason, YSZ thin films for SAWs were grown at a substrate temperature above 600°C. The Pt particles to serve as catalyst for H<sub>2</sub> adsorption and dissociation into the YSZ thin film were created through the e-beam evaporation of a Pt flux for an equivalent film thickness between 0.5-3 nm.

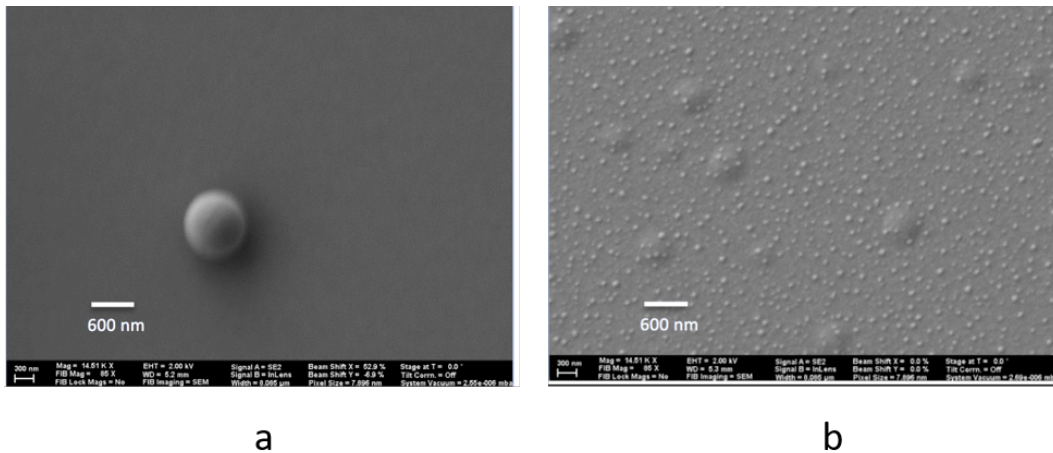


Figure 2.5. SEM images of 25 nm YSZ thin films on LGS deposited at different substrate temperatures after high-temperature cycling between 25°C and 750°C: a) 850°C; b) room-temperature.

### 2.2.2 Pt-Al<sub>2</sub>O<sub>3</sub>

To excite the SAW on LGS, the composite of Pt-Al<sub>2</sub>O<sub>3</sub> was selected as material for the IDTs and reflector electrodes due to its resilience to high-temperature exposures and

acceptable conductivity after extended high-temperature excursions [1], [89], [109]. This material can also function as the sensing film SAWR gas sensor, thereby fulfilling the purpose of both transducer and sensing film.

Two Pt-Al<sub>2</sub>O<sub>3</sub> film structures were investigated in this work and are depicted in Figure 2.6. Film 1 from Figure 2.6a was fabricated through deposition of a 10 nm layer of Zr in oxidizing pressure (becoming ZrO<sub>2</sub> in the process) functioning as an adhesion layer, followed by the deposition of 170 nm 82%Pt-18%Al<sub>2</sub>O<sub>3</sub> atomic percent composite film. Film 2 from Figure 2.6b was fabricated by depositing the same ZrO<sub>2</sub> adhesion layer, followed by a 10 nm pure Pt layer, a 10 nm graded transition from pure Pt to the 82%Pt-18%Al<sub>2</sub>O<sub>3</sub> composition, after which 150 nm of the composite was deposited. The purpose of Film 2 (graded film) was to alleviate stress hillocks that had previously been observed in high-temperature Pt-Al<sub>2</sub>O<sub>3</sub> films (see Section 1.5.2) through the graded layers, which should function as buffer or matching layers due to the different thermo-coefficients of expansion between LGS and the Pt-Al<sub>2</sub>O<sub>3</sub> electrode layer. The depositions for the electrodes were done by e-beam evaporation of Zr, Pt and Al targets in oxygen partial pressure of 10<sup>-5</sup> Torr.

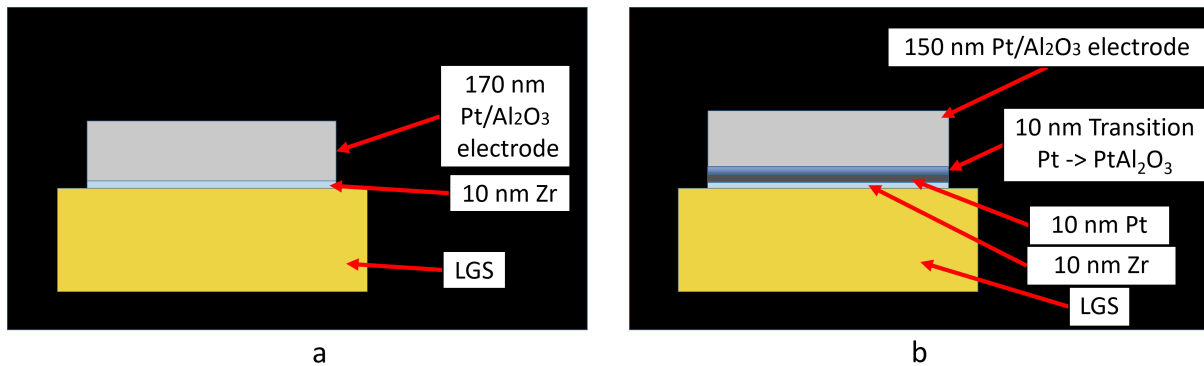


Figure 2.6. Schematic of film composition for Pt-Al<sub>2</sub>O<sub>3</sub> thin films: a) Film 1; b) Film 2.

### 2.3 SAWR Sensor Fabrication

One-port SAWRs were fabricated with Pt-Al<sub>2</sub>O<sub>3</sub> electrodes and reflectors of both Film 1 and Film 2 (following the nomenclature from Section 2.2.2). LGS wafers obtained from

Fomos-Materials (4" in diameter) were diced into sections of approximately  $30\text{mm} \times 30\text{mm}$ , Photolithography was conducted on the diced sections of the wafers to transfer SAWR IDT and reflector pattern. Deposition of Pt-Al<sub>2</sub>O<sub>3</sub> as described previously was conducted. In order to deposit films evenly for all of the selected orientations, the wafer holder was rotated 360° every 22 seconds for the entire duration of the e-beam evaporation deposition, which normally lasted about an hour for an entire deposition. Lift-off was then used to reveal the desired patterns on the wafer. SAWR sensors which use the Pt-Al<sub>2</sub>O<sub>3</sub> itself as the gas sensing layer will be referred to from now on in this thesis as Bare sensors. The wafer was cleaned using a procedure of acetone, iso-propanol, methanol and DI water rinsing followed by drying with a N<sub>2</sub> stream, and then placed in an alumina crucible and annealed in air at 800°C for four hours before being probed on wafer. Figure 2.7 shows a photograph of a typical fabricated wafer with an indent SEM image of the resulting IDT electrodes employing Film 1 after the cleaning procedure but before the annealing process. It can be seen from Figure 2.7 that the fabricated electrodes are thinner than the nominal value away from the electrode center due to photoresist shadowing during the rotation of the wafer holder. Overall, only about 40% of the electrode width has the nominal thickness described previously due to the rotation during deposition.

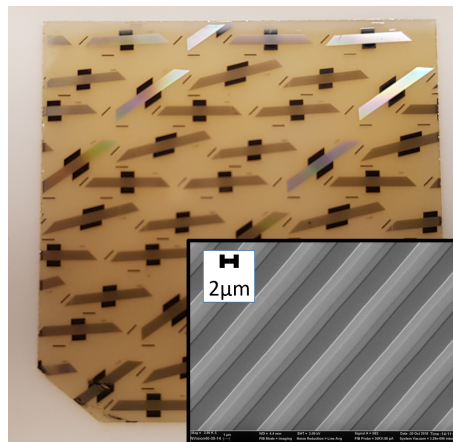


Figure 2.7. Fabricated wafer section with Bare sensors.

For the fabrication of devices employing a Pt-decorated YSZ sensing thin film, a 15 nm layer of YSZ was deposited on top of the entire wafer section. Deposition of the YSZ film over the entire wafer was necessary since at 600°C substrate temperature the photoresist patterning would be destroyed. The YSZ overlay over the entire wafer with SAWRs on it was then decorated with 1 nm of Pt as catalyst as previously described in Section 2.2.1. These devices will be referred to from here on as YSZ-layered sensors. After the deposition, the devices were cleaned and annealed as described in the previous paragraph. At the bondpad locations, photolithography was used to deposit an adhesion layer of 50 nm of Zr followed by 50 nm of pure Pt over the Pt-decorated YSZ thin film directly above the device bond pads, and Pt paste was subsequently applied using an emulsion screen. This allowed for the interrogation of the SAWR sensors through capacitive coupling [110], as shown in Figure 2.8, since the YSZ performs electrically as an insulating layer. Additionally, some devices were fabricated with a 50 nm layer of YSZ deposited at room-temperature prior to the findings of the high-temperature substrate deposition strategy. Photoresist was applied over the bond-pads and removed after the deposition to reveal only the bondpads while the 50 nm layer of Pt-decorated YSZ remained over the remainder of the SAWR sensor. These devices will be referred to from here on as 50nmYSZ sensors.

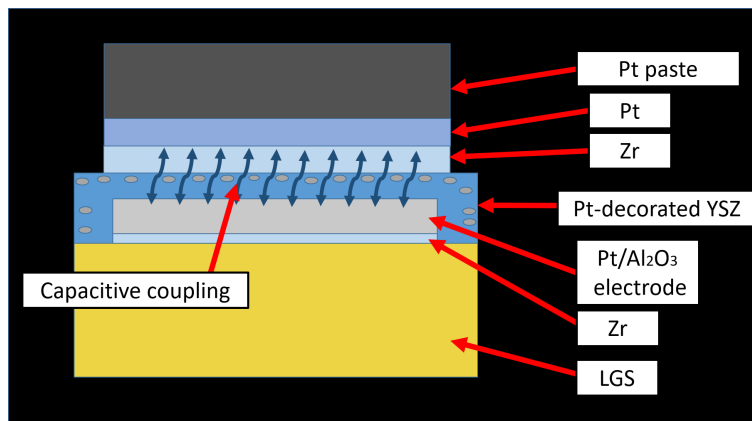


Figure 2.8. Capacitive coupling for interrogation of YSZ-layered SAWR sensors.

## CHAPTER 3

### HIGH TEMPERATURE GAS SENSOR TESTING SYSTEM DEVELOPMENT AND IMPLEMENTATION

This chapter addresses the design and implementation of a gas testing system for monitoring the resonant frequency of SAWR gas sensors in real-time during gas cycling at temperatures up to 600°C. In addition, the SAWR setups used for both gas testing using the high-temperature gas testing system are detailed. A temperature characterization system allowing the continued temperature cycling up to 850°C of devices while being monitored in real-time is also presented. The test setup for a wireless measurements of a SAWR inside the gas testing system is described.

#### **3.1 High-temperature Gas Sensor Testing System**

In order to test SAWR sensor response to high-temperature exposures to H<sub>2</sub>, a gas testing system capable of excursions to temperatures above 200°C was developed. The schematic for the system is shown in Figure 3.1. The system developed was capable of interrogating a total of four SAW gas sensors in two chambers of a stainless steel box, with a thermocouple in each chamber. A PC controlled the interrogation module (data acquisition from the SAWR gas sensors and thermocouples) and the gas delivery system. This section will describe the details of the stainless steel box and the mounting of SAWRs within it, as well as the gas delivery and interrogation modules of the system.

##### **3.1.1 SAW Sensor and thermocouple mounting within stainless steel box for High-temperature gas cycling operation**

A stainless steel box with two chambers for the allocation of two SAW sensors and one thermocouple per chamber was designed under this project, and fabricated at the University of Maine's Advanced Manufacturing Center (AMC). The purpose of this box was to house the SAW gas sensors a small volume and stable gas testing chambers, also capable of

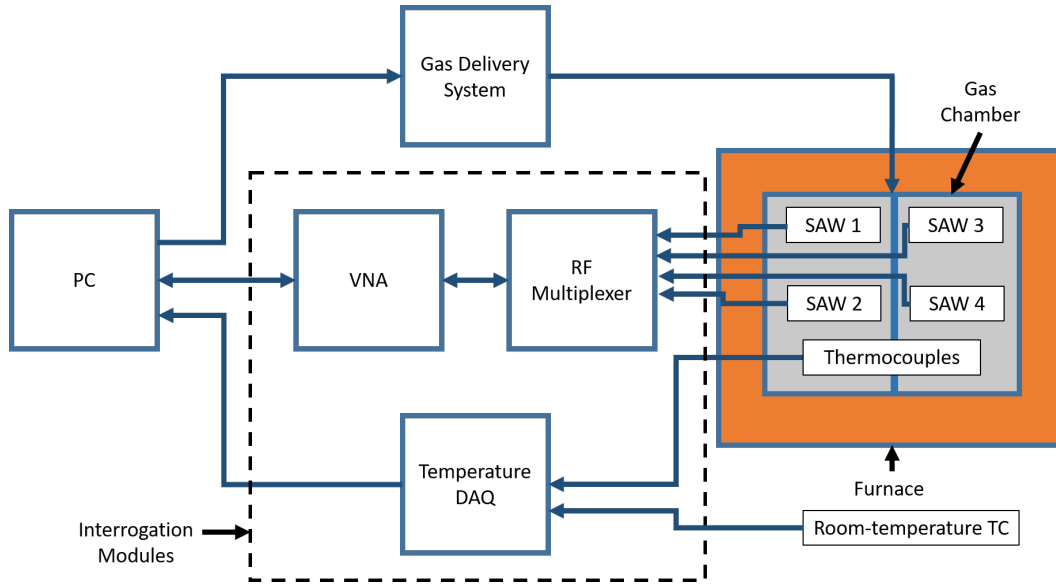


Figure 3.1. High-temperature gas testing system schematic.

withstanding temperatures up to 700°C. A total of three identical boxes were fabricated, and Figure 3.2 shows a photograph of one of them. Each box had a total side length of 3", and each chamber had dimensions of 2.25" × 0.95" × 0.5". A total of ten 1/8" NPT threaded holes, five per chamber, allowed for the interrogation of two SAW gas sensors through high-temperature Inconel Coaxial cables and one thermocouple (TC) per chamber, as well as two apertures for gas flow (inlet and outlet) as shown in Figure 3.2c.

Figure 3.3 shows the the introduction in each chamber of two high-temperature Inconel coaxial cables acquired from Thermocoax, one KMQIN-125E-24 Omega K-type Inconel thermocouple (TC). The SAWRs were held inside the chamber by 4mil Pt wire, and 1 mil Pt wire was used to provide electrical connections between the high-temperature coaxial cables and the SAWRs. The Pt wires were all welded using a Unitek resistance welder. The TCs on each chamber were mounted on top of a piece of LGS to mimic the temperature seen by the SAWRs.

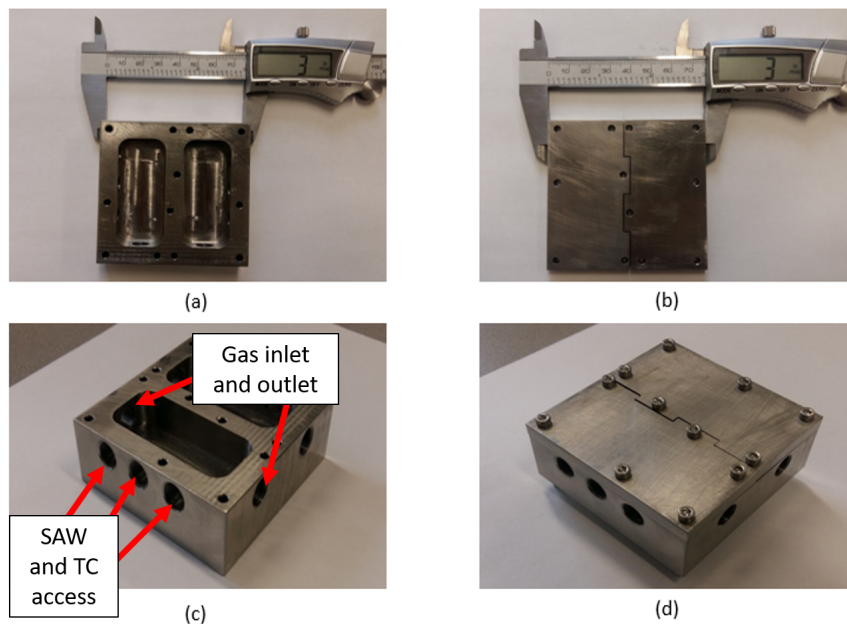


Figure 3.2. High-temperature stainless steel box: (a) chamber top view; (b) cap top view; (c) chamber side view; (d) cap screwed onto chamber.

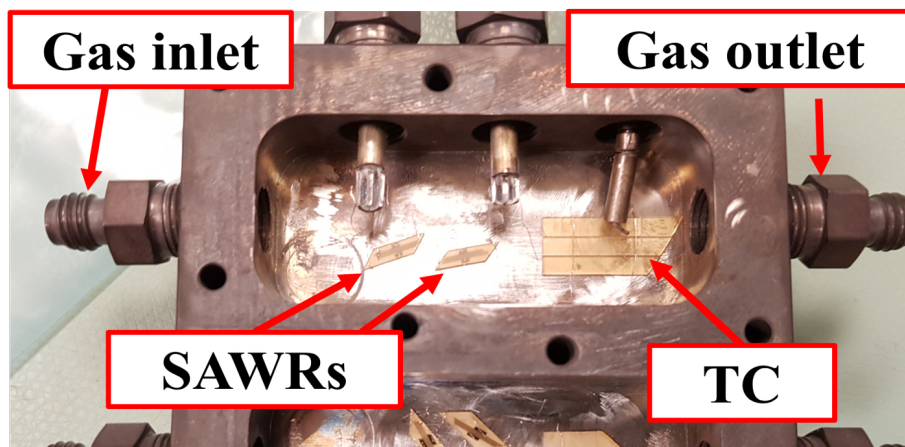


Figure 3.3. SAWRs and TC mounted in stainless steel gas testing chamber.

### 3.1.2 Gas Delivery System

The gas delivery system was designed to deliver constant flow of  $N_2$ ,  $O_2$  and a mixture of  $H_2$  in  $N_2$  balance, and the interrogation module was designed to monitor the shift in the SAWR sensor resonant frequency shifts due to the introduction of  $H_2$  into the system. The system was also designed to deliver  $O_2$  to study the effects of oxidation prior to and after reductions in the  $H_2$  environment. The gases delivered were 99.999% purity  $N_2$  (referred

to from now on as  $N_2$ ) provided through the lab  $N_2$  outlets from the Microwave Acoustics Laboratory (MAL) located in the Engineering Science and Research Building (ESRB) room 295, 4.7 grade (99.997% purity)  $O_2$  provided by the University of Maine Central Supply in K-type (5ft tall) cylinders (referred to from now on as  $O_2$ ), and specialty  $N_2/H_2$  mixtures obtained from the University of Maine Central Supply with ratios of 96%/4% (referred to from now on as 4% $H_2$ ) or 98%/2% (referred to from now on as 2% $H_2$ ). Gases were delivered to the test box chambers at a flow rate of either 100sccm or 950sccm. For this purpose, three major iterations of the gas delivery system were implemented.

The schematic for gas delivery system A is shown in Figure 3.4. This gas delivery system was capable of delivering  $N_2$  and  $O_2$  to both Chamber 1 and Chamber 2, and was able to deliver the 4% $H_2$  mixture to Chamber 2 but isolated the delivery of 4% $H_2$  from being delivered to Chamber 1. It used two three-way valves and one isolation valve to select which gas would be delivered to mass-flow controller 1 (MFC1) and mass-flow controller 2 (MFC2). Therefore, this setup had a control group of sensors (in Chamber 1), which were never exposed to 4% $H_2$ , and a group of sensors that were exposed to the reducing environment in 4% $H_2$  (in Chamber 2). In this regard, this setup is similar to the one used in [20].

The schematic for Gas Delivery System B is shown in Figure 3.5. This gas delivery system was capable of delivering three gases,  $N_2$ ,  $O_2$ , and 4% $H_2$ , independently at any moment to either Chamber 1 and Chamber 2. This was done through the addition of a three-way valve in the place of the isolation valve from Gas Delivery System A. System B retained the capability of exposing only one chamber to 4% $H_2$ , but allowed for the flexibility of choosing the chamber which would be exposed to 4% $H_2$  in software and also allowed for the exposure of both chambers to 4% $H_2$  simultaneously.

The schematic for Gas Delivery System C is shown in Figure 3.6. This gas delivery system was capable of delivering all four gases,  $N_2$ ,  $O_2$ , 4% $H_2$  and 2% $H_2$  independently at any moment to either Chamber 1 and Chamber 2, while retaining all the advantages of

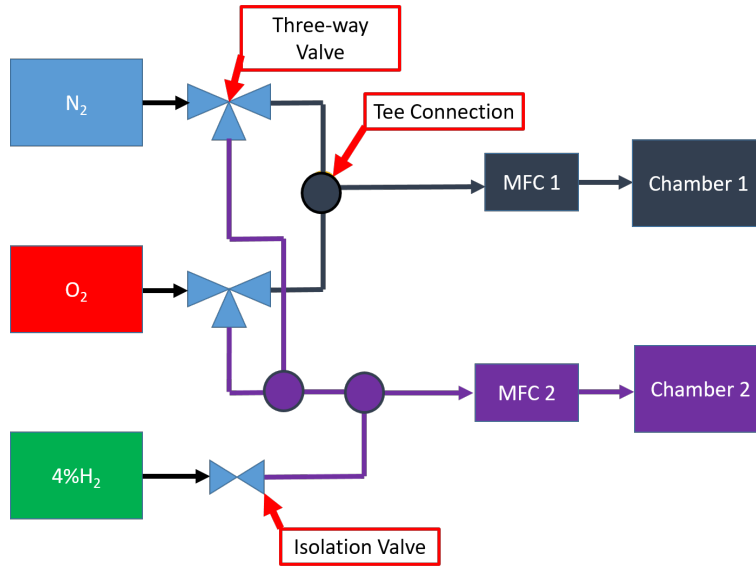


Figure 3.4. Gas Delivery System A.

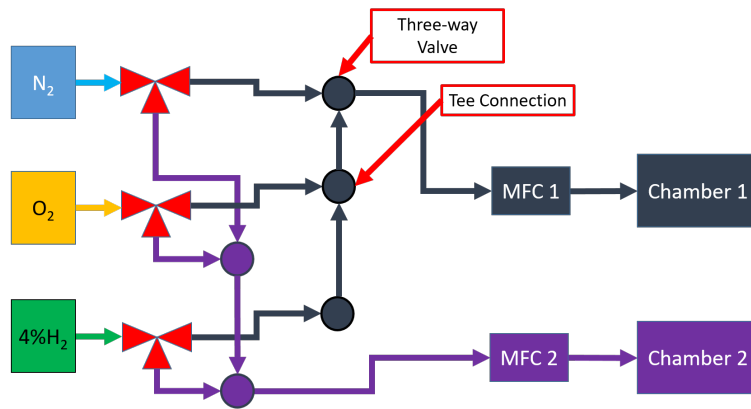


Figure 3.5. Gas Delivery System B.

System B. This was done through the addition of one more three-way valve and two tee connections.

The physical implementation of the valve and MFC setup along with the control interface block are shown in Figure 3.7 for Gas Delivery System C. Advanced Pressure Technology (AP Tech) three-way valves and two Tylan 2900 series MFCs were used, while a control box outfitted with a Measurement Computing USB-2408 data acquisition module and an 8-relay module employing SRD-05VDC-SL-C relays for the control of the valves was implemented.

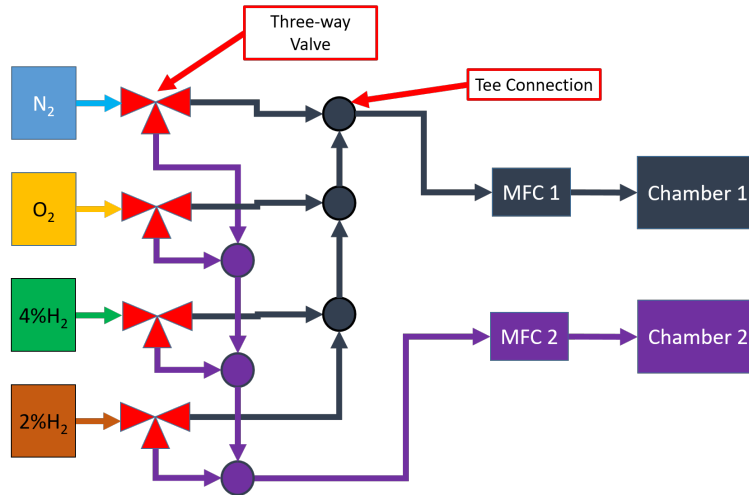


Figure 3.6. Gas Delivery System C.

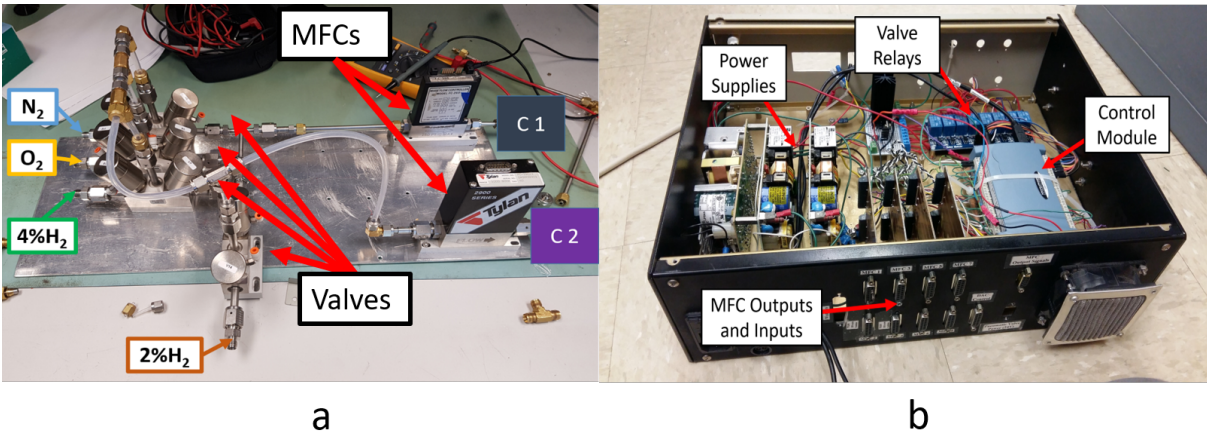


Figure 3.7. Physical implementation of the gas delivery system: a) valves and MFC hardware (C1 and C2 denote Chamber 1 and Chamber 2 respectively); b) Control interface connected to PC.

### 3.1.3 Interrogation Module

The SAWR Sensor and TC interrogation module allowed for the series interrogation of up to four SAW sensors and three TCs. An RF multiplexer box (shown in Figure 3.8), containing Mini-Circuits 4-way RF switch ZSWA-4-30DR operated by NI USB 6501 module was used with a single Agilent Technologies E5071C Vector Network Analyzer (VNA) to interrogate the SAWR sensors. The K-type TCs were interrogated by means of three NI USB TC-01 modules. The physical implementation of the entire system is shown in Figure 3.9, with the

stainless-steel box mounted inside a Thermolyne Furnace 6000. The VNA settings such as IF bandwidth, number of points and frequency sweep span, as well as how often the sensors were interrogated before and after gas transitions and during periods of steady gas flow, varied according to the test and will therefore be specified when addressing the measurements for a particular test in Chapter 4. The SAWR sensors were always interrogated in series. The TC associated with the SAWR in question would be interrogated immediately before and after recording the frequency response, thereby associating a particular temperature with each frequency sweep by taking the average of these two temperatures (under steady state conditions, the difference between the anterior and posterior temperature readings was less than  $0.25^{\circ}\text{C}$  even at temperatures up to  $500^{\circ}\text{C}$ ). The SAWR sensors were interrogated as fast as possible for 5-10 minute periods before and after gas transitions. For example, if the a frequency sweep for a single SAWR sensor took 15 seconds to complete, the interrogation of four SAWR sensors would take one minute. During periods of steady gas flow, the SAWR sensors were usually interrogated once every five minutes. Details on the software developed in LabVIEW for the control of the gas delivery system and interrogation modules is given in Appendix A.

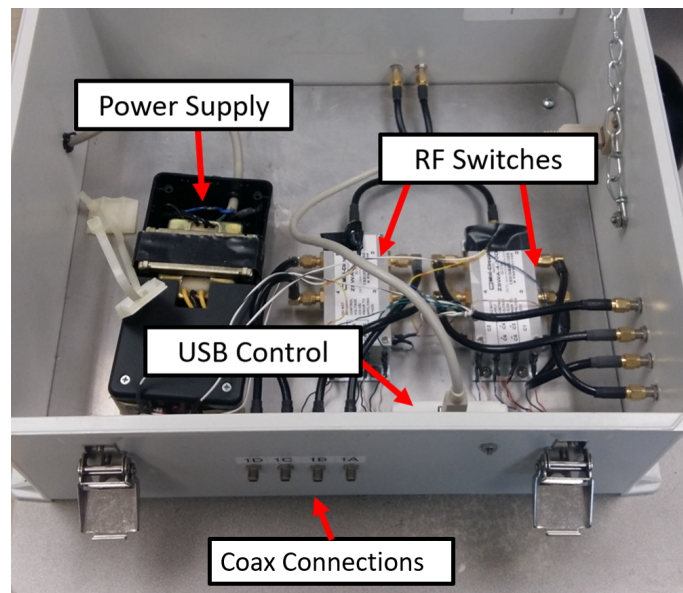
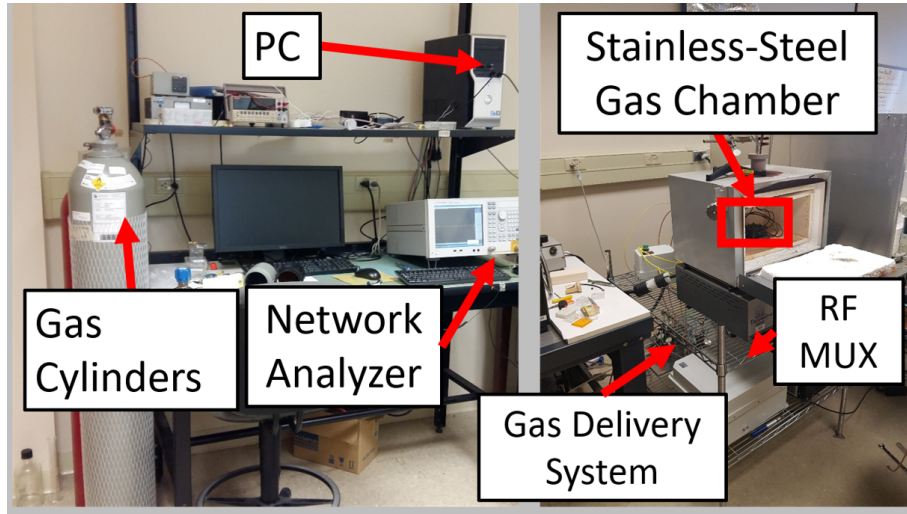
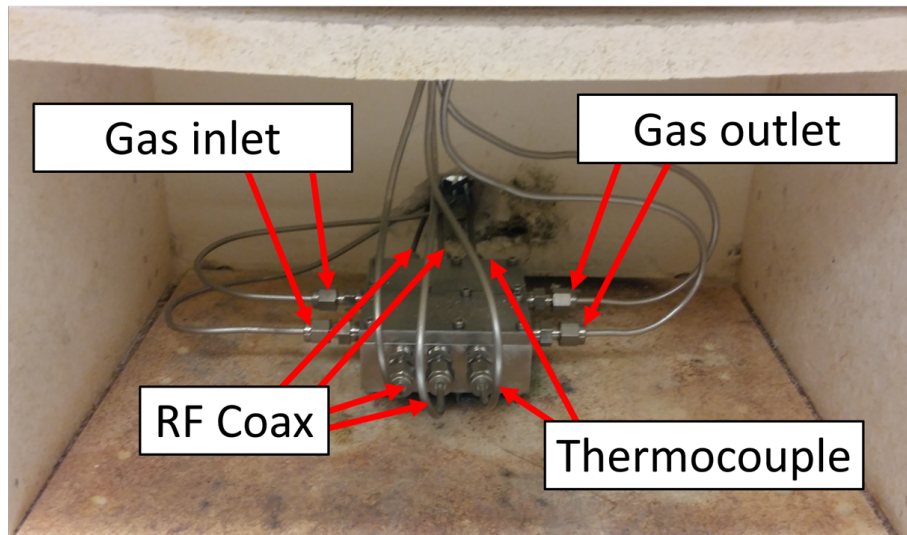


Figure 3.8. RF multiplexer box.



a



b

Figure 3.9. Physical implementation of entire high-temperature gas testing system: a) Hardware physical setup in MAL 295; b) Stainless steel box inside Thermolyne 6000 Furnace.

### 3.2 High-temperature SAW Gas Sensor Setups

The general device layout schematic for the tests that are discussed in Chapter 4 is shown in Figure 3.10. A total of 8 different setups using the device layout schematic from Figure 3.10 were mounted and tested. All devices mounted had previously been annealed at 800°C for four hours after fabrication [28], [84], [93]. The device layouts are detailed in Table 3.1 with the corresponding gas delivery system used for that particular setup, where the device description follows the following formula: the type of film employed (Film 1 or Film 2); the use of 15 nm YSZ sensing film (YSZ) or no YSZ sensing film (Bare); whether the device had previously been temperature-cycled in an alumina crucible using four rounds of Profile 1 in Figure 3.14 from Section 3.3 (cycled) or if they were not cycled using Profile 1 (non-cycled); and the SAWR orientation (for example, 26.7°). Table 3.1 will be referenced in Chapter 4 when addressing the gas cycling results. The exposure profile (the order, duration and number of times each gas was delivered) varied with the tests performed using each setup. This information will be given when describing the results, and the gas exposure profile will always be given in the same plot when addressing the results.

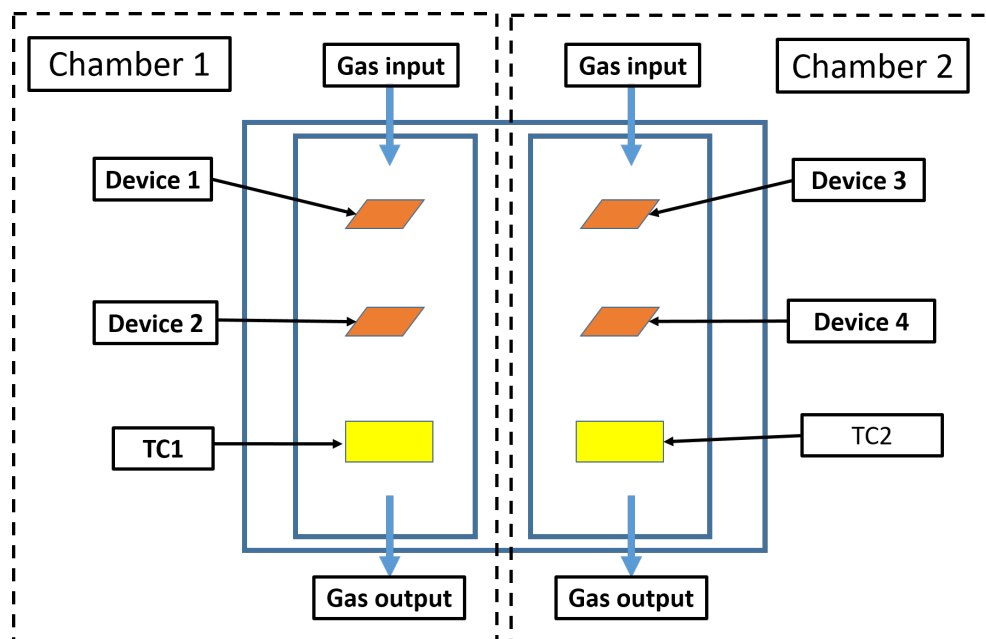


Figure 3.10. Device layout schematic for high-temperature gas testing.

Table 3.1. Summary of setups mounted and tested for high-temperature gas cycling.

Setup	Device 1	Device 2	Device 3	Device 4	Delivery System
A1	Film 1 Bare non-cycled 26.7°	A			
A2	Film 1 YSZ non-cycled 14.7°	Film 1 Bare non-cycled 14.7°	Film 1 YSZ non-cycled 14.7°	Film 1 Bare non-cycled 14.7°	A
A3	Film 2 Bare non-cycled 77.7°	Film 2 Bare non-cycled 14.7°	Film 2 Bare non-cycled 26.7°	Film 2 Bare non-cycled 32.7°	B
A4	Film 2 YSZ non-cycled 14.7°	Film 2 Bare non-cycled 14.7°	Film 2 YSZ non-cycled 26.7°	Film 2 Bare non-cycled 26.7°	B
A5	Film 2 Bare cycled 14.7°	Film 2 Bare cycled 14.7°	Film 1 Bare cycled 14.7°	Film 1 Bare cycled 14.7°	C
A6	Film 1 Bare non-cycled 20.7°	Film 1 Bare non-cycled 77.7°	Film 1 Bare non-cycled 20.7°	Film 1 Bare non-cycled 26.7°	C
A7	Film 1 Bare cycled 26.7°	Film 1 Bare cycled 77.7°	Film 1 Bare cycled 26.7°	Film 1 Bare cycled 77.7°	C

Test Setup A1 and A2 used Gas Delivery System A, and therefore had a control group of sensors in Chamber 1 that were not exposed to reducing environments at all. Setup A1 was used to verify the functionality of the test setup system. Setup A2 was used to compare the SAWR gas sensor performance of bare devices and YSZ-layered devices (YSZ in Table 3.1). Setups A3 and A4 used Gas Delivery System B and were able to expose all four devices to 4% $H_2$  simultaneously. Setup A3 was used to compare the response of four different LGS orientations to 4% $H_2$  exposures. Setup A4 was used to confirm the results obtained using Setup A2 comparing the performance of YSZ-layered devices vs. Bare devices, and also to assess Bare and YSZ-layered devices oriented both at  $\Psi = 14.7^\circ$  and  $\Psi = 26.7^\circ$ . Setups A5-A7 used Gas Delivery System C. Setup A5 was used to compare SAWR gas sensor performance of devices employing Film 1 electrodes vs. Film 2 electrodes to 4% $H_2$  and

2% $H_2$  exposures. Setup A7 was used to gain information about the performance of SAWR gas sensors oriented along  $\Psi = 20.7^\circ$  and also to further confirm results observed for devices oriented along  $\Psi = 77.7^\circ$  and  $\Psi = 26.7^\circ$ . Finally, Setup A7 was used to characterize SAW gas sensors oriented along  $\Psi = 77.7^\circ$  and  $\Psi = 26.7^\circ$  up to  $500^\circ C$  and to assess the possibility of using these two orientations as the components of the multi-sensor system described in Section 1.6.

### 3.2.1 Temperature Uniformity within a Chamber

It should be noted from Figure 3.3 and 3.10 that there is a difference in location between the location of the TC inside the chamber and the location of the SAWR gas sensor closest to the gas inlet. A test was conducted with two TCs, one at the location of the SAWRs closest to the gas inlet (TC1) and one located where the TC would normally be located during a test (TC2), as shown in Figure 3.11. Gas cycling was then conducted to examine the differences in detected temperature. The test was conducted at  $260^\circ C$ ,  $360^\circ C$ ,  $460^\circ C$  and  $560^\circ C$  using flow rates of 950sccm for the gases cycled which was the highest flow rate used during SAWR gas sensor tests and therefore the one that could affect the temperature variation within the chamber the most. The results are shown in Figure 3.12. There is a temperature dependent gradient between the location of TC1 and TC2, with the temperature of TC1 (location of the sensors during SAW sensor testing) being higher than the recorded temperature of TC2 (location of the TC during SAW sensor testing). This gradient was on average  $1.6^\circ C$ ,  $1.8^\circ C$ ,  $1.9^\circ C$  and  $3.2^\circ C$  at the temperatures tested and mentioned above, respectively.

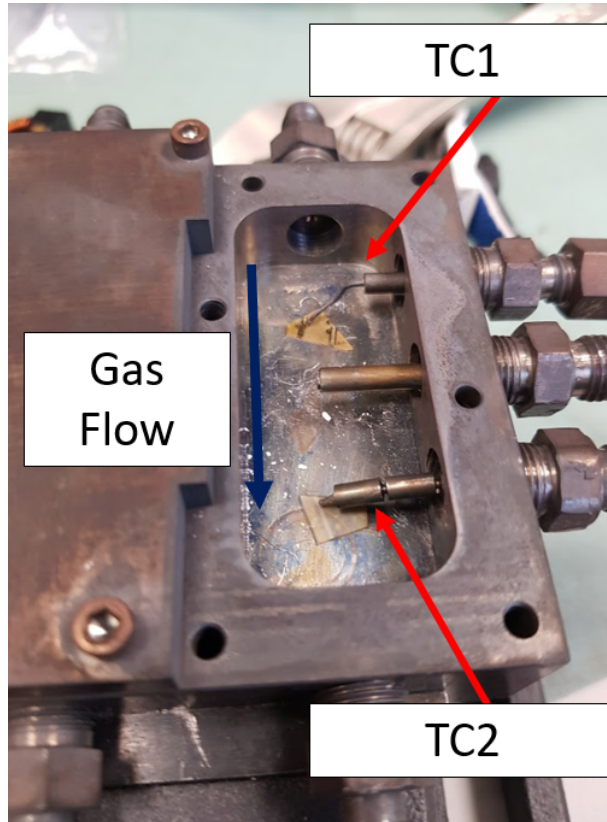


Figure 3.11. TC test in gas chamber.

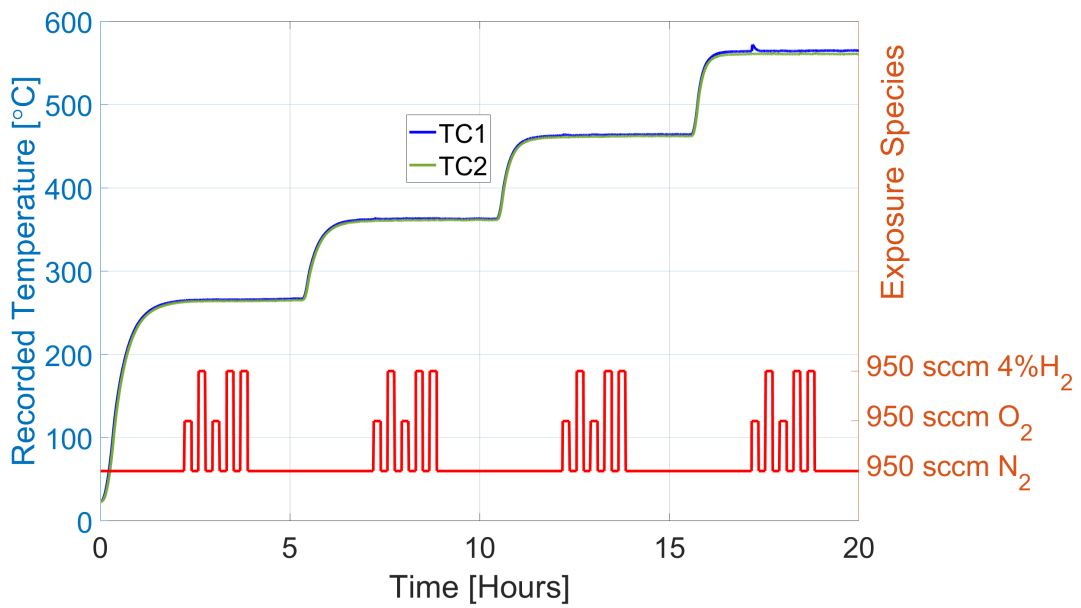


Figure 3.12. TC test results for gas cycling at 260°C, 360°C, 460°C, and 560°C.

For temperatures of 260°C and 360°C, gas transitions did not cause fluctuations in the temperature recorded by either TC greater than 0.8°C. For 460°C, transitions from N<sub>2</sub> to O<sub>2</sub> produced temperature fluctuations of less than 1.2°C in TC1 and less than 0.8°C in TC2, and transitions from N<sub>2</sub> to 4%O<sub>2</sub> produced less than 0.5°C fluctuations in both TC1 and TC2. At 560°C, the first transition from N<sub>2</sub> to O<sub>2</sub> produced a temperature fluctuation of 6°C in TC1 and approximately 1°C fluctuation for TC2, as can be seen in Figure 3.12. Further transitions from N<sub>2</sub> to O<sub>2</sub> produced fluctuation less than 2°C in TC1 and less than 1°C in TC2. Finally, temperature fluctuations due to transitions from N<sub>2</sub> to 4%O<sub>2</sub> were less than 1°C for both TCs at 560°C. These results showed that temperature variations recorded by TC1 (closest to gas input) are larger than temperature variations recorded by TC2 (closest to gas outlet), but the difference in temperature variations detected at all temperatures tested between N<sub>2</sub> flow and 4%O<sub>2</sub> flow are less than 1°C.

### 3.3 SAWR Sensor High-temperature Characterization Setups

In addition to the high-temperature gas testing system, high-temperature characterization of SAWR sensors was conducted in a separate environment so that it could be performed in parallel with high-temperature gas testing of SAWR gas sensors. This setup was located in ESRB Room 284. The schematic for this testing environment is shown in Figure 3.13. In this case, a two-port Agilent 8753D VNA was used to interrogate two SAWR sensors during temperature cycling tests up to 850°C in a Thermolyne 4800 box furnace. A single KMQIN-125E-24 Omega K-type Inconel TC in conjunction with an NI 9213 TC module was used to measure the approximate temperature of the devices in the same way as in the high-temperature gas testing setup described previously (one prior and one after the frequency sweep, which were averaged to associate a temperature with that particular frequency sweep). Frequency sweeps with 1601 points, bandwidth of 10 MHz centered at 190 MHz and IF bandwidth of 3kHz were used for all the tests cited in Chapter 4.

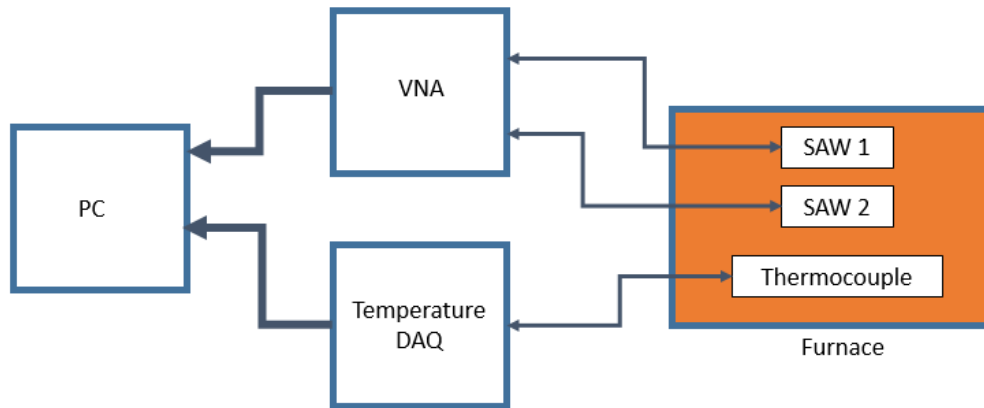


Figure 3.13. SAW sensor temperature characterization setup schematic.

All tests used two SAWR sensors mechanically secured to an Inconel plate using 4 mil Pt wire and electrically connected to high-temperature coaxial cables using 1 mil Pt wire. The witness TC was placed in close proximity to the SAWR sensors in air. Four setups were tested with the temperature characterization setup. All of the mounted sensors had previously been annealed at 800°C for four hours in an alumina crucible, and this was the only temperature treatment the devices experienced before being mounted for testing. The test setup configurations are given in are given in Table 3.2.

Table 3.2. Summary of setups mounted and tested for temperature characterization.

Setup	Device 1	Device 2	Devices in Crucible
B1	Film 1 Bare 14.7°	Film 1 Bare 77.7°	No
B2	Film 1 Bare 77.7°	Film 1 50YSZ 77.7°	No
B3	Film 1 Bare 26.7°	Film 2 Bare 26.7°	Yes
B4	Film 1 Bare 77.7°	Film 1 Bare 77.7°	Yes

Setup B1 was implemented to compare the experimentally measured temperature dependence of orientations  $\Psi = 14.7^\circ$  and  $\Psi = 77.7^\circ$  to the predicted temperature dependence and verify the temperature of compensation ( $TCD = 0$ ). The devices were tested from  $125^\circ\text{C}$  to  $400^\circ\text{C}$  in  $25^\circ\text{C}$  increments. Once the temperature was stable, 151 sweeps were taken at each temperature step. Setup B2 was tested in order to compare the temperature dependence of Bare and 50nmYSZ-layered SAW sensors (50YSZ in Table 3.2) oriented along  $\Psi = 77.7^\circ$ . The devices were tested from  $175^\circ\text{C}$  to  $375^\circ\text{C}$  in  $25^\circ\text{C}$  increments.

Both Setup B3 and B4 had additional devices placed in an alumina crucible to partake in the temperature cycling, as shown in Figure 3.16. SEM images were taken from devices employing either Film 1 or Film 2 as fabricated (State 1) and after annealing at  $800^\circ\text{C}$  for four hours in an alumina crucible. Setup B3 was tested to compare the temperature performance of all devices employing Film 1 electrodes and reflectors vs. Film 2 IDTs and reflectors up to  $715^\circ\text{C}$ . This was done by exposing the devices to four rounds of temperature cycling from nominal furnace temperatures were of  $300^\circ\text{C}$  and  $750^\circ\text{C}$ . The witness TC recordings for one round of this temperature profile, labeled Profile 1, are shown in Figure 3.14. The TC recorded on average  $280^\circ\text{C}$  for the nominal  $300^\circ\text{C}$  soaking periods and  $714^\circ\text{C}$  for the nominal  $750^\circ\text{C}$  soaking periods. Profile 1 consisted of four 1-hour cycles between  $280^\circ\text{C}$  to  $715^\circ\text{C}$ , followed by a 10-hour soaking period at  $715^\circ\text{C}$  and punctuated by another four 1-hour cycles between  $280^\circ\text{C}$  to  $715^\circ\text{C}$ . SEM images were taken after this test (State 3). The average and standard deviation of the SAW sensors after 45 minutes at the upper holding temperatures ( $714^\circ\text{C}$ , for a total of 30 measurements for each average) were extracted.

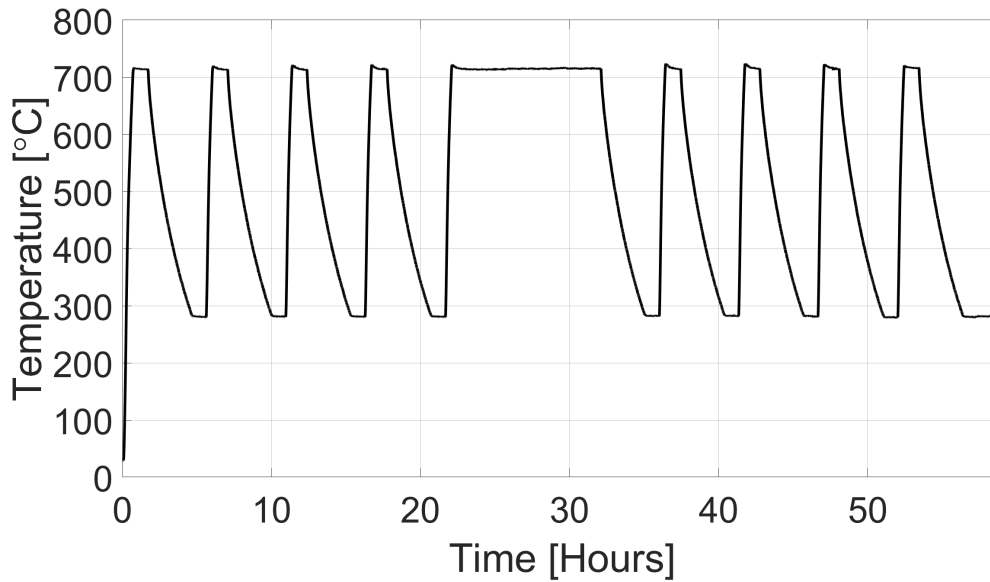


Figure 3.14. Witness TC temperature readings for one round of Profile 1.

Setup B4 was tested to compare the temperature performance of all devices employing Film 1 electrodes and reflectors vs. Film 2 IDTs and reflectors up to 850°C using five rounds of temperature cycling from nominal furnace temperatures 350°C to 890°C. The witness TC recordings for one round of this temperature profile, labeled Profile 2, are shown in Figure 3.15. The TC recorded on average 328°C for the nominal 350°C soaking periods and 843°C for the nominal 890°C soaking periods. Profile 2 consisted of four 1-hour cycles between 328°C to 843°C, followed by a 10-hour soaking period at 843°C and punctuated by another four 1-hour cycles between 280°C to 715°C. SEM images were taken after this test (State 4). The average and standard deviation of the SAW sensors after 45 minutes at the upper holding temperatures (843°C, for a total of 30 measurements for each average) were extracted. Figure 3.16 shows the physical layout of tests B3 and B4. Tests B1 and B2 were similar, except no devices were in an alumina crucible.

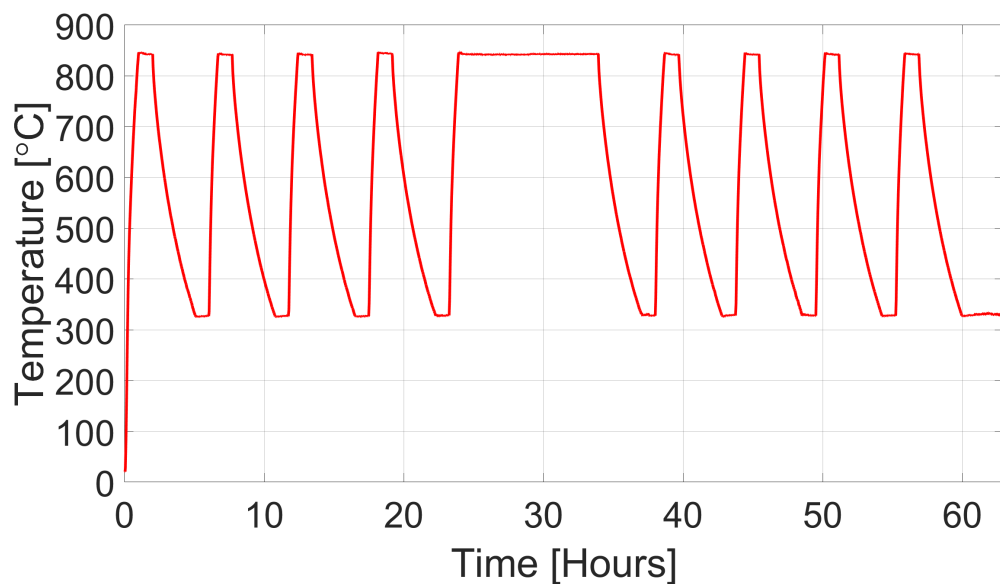


Figure 3.15. Witness TC temperature readings for one round of Profile 2.

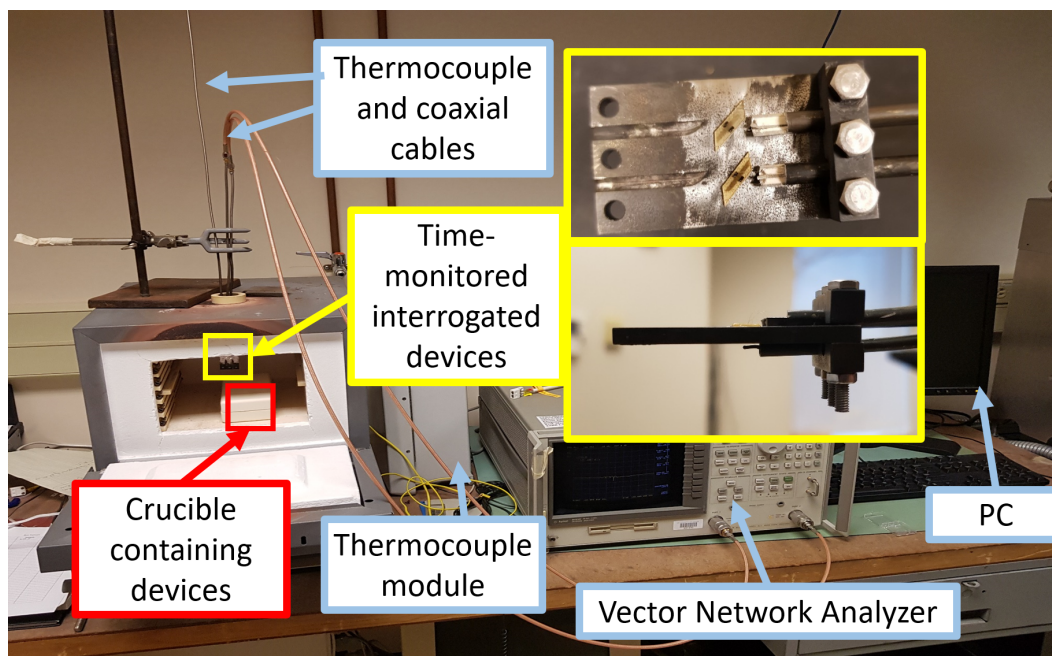


Figure 3.16. SAW sensor temperature characterization setup.

### 3.4 Wireless High-temperature SAWR Gas Sensor Testing

High-temperature gas cycling tests were conducted on a SAW sensor through wireless interrogation. The method of inductive coupling using antennas with 4 and 3 loops developed in [111] were used to wirelessly interrogate a Film 1 Bare cycled (using Profile 1) device oriented along  $\Psi = 26.7^\circ$ . The SAWR was attached to the 3-loop antenna using Aremco 571 high-temperature epoxy and connected electrically to the gold traces of the antenna using 1 mil wire. This antenna will be referred to from now on as the Sensor Antenna. Alumina plates were further adhered at the corners of the sensor antenna using the same epoxy, and the 4-loop was placed on top of the alumina plates and adhered with the same epoxy. This top antenna will be referred to as the Interrogating Antenna. The distance between the traces of the Sensor and Interrogating antennas was equal to 3 mm. The whole setup was then placed inside one of the high-temperature stainless steel boxes and electrically connected to an Inconel coaxial cable. This setup was then tested at 400°C and 500°C nominal furnace temperatures using a frequency span of 40 MHz centered at 190 MHz; and at 400°C using a frequency span of 10 MHz centered at 191 MHz. In all cases, the number of points was 10,001 and the IF bandwidth was 1 kHz. The setup is shown in Figure 3.17.

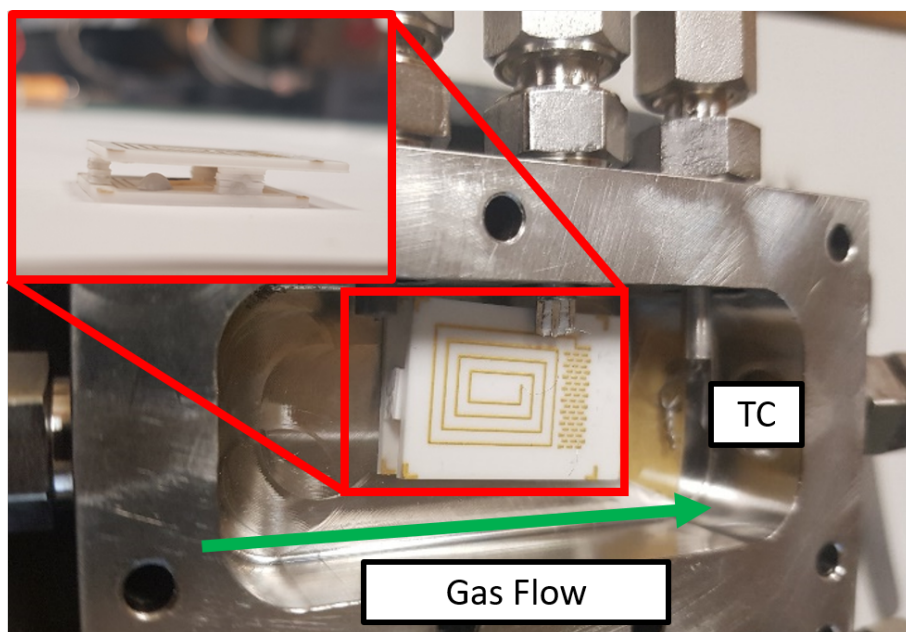


Figure 3.17. Wireless SAW gas sensor interrogation setup.

## CHAPTER 4

### SAWR GAS SENSOR EXPERIMENTAL RESULTS AND DISCUSSION

This chapter presents and discusses the results obtained from the developed high-temperature SAWR gas sensors. The high-temperature characterization of SAWRs using the setups described in Section 3.3 are shown in Section 4.2. Gas sensor test results are discussed in Sections 4.3-4.9 using the setups described in Section 3.2. The performance of YSZ-layered sensors vs. Bare sensors is compared in Section 4.4. The findings involving the impact of oxygen treatments for the SAW gas sensor operation at room temperature are given in Section 4.5. H<sub>2</sub> sensing results for different SAWR sensor orientations up to 500°C are given in Section 4.6. Comparison of H<sub>2</sub> sensing using Film 1 and Film 2 (defined in Section 2.2.2) as electrodes are shown in Section 4.6. The feasibility of utilizing SAWR sensors oriented along  $\Psi = 26.7^\circ$  and  $\Psi = 77.7^\circ$  as components of a two-sensor system to simultaneously detect H<sub>2</sub> presence and read ambient temperature is presented in Section 4.8. Finally, wireless SAWR gas sensor measurements are given in Section 4.9.

#### 4.1 Definition of Tracked Frequency

The fabricated SAWRs were probed at room temperature using a Cascade MicroTech wafer probing station. The results for each of the orientations previously mentioned,  $\Psi = 14.7^\circ, 20.7^\circ, 26.7^\circ, 32.7^\circ$  and  $77.7^\circ$  are given in Appendix B according to the mask design definitions given in Section 2.1.2 (S, RC, and LC). It was found that the S IDT positioning scheme gave a clearer frequency response with less spurious modes for SAWRs oriented along the high-temperature orientations ( $\Psi = 14.7^\circ, 77.7^\circ$ ) when compared to the performance of RC and LC devices. For this reason, the section of the mask that had higher concentration of S devices was normally selected to fabricate devices. To present the method of tracking resonant frequencies used to monitor the SAWR resonant frequency, an example is given below based on a typical frequency response of a SAWR sensor oriented along  $\Psi = 26.7^\circ$ .

Figure 4.1 shows a typical frequency response of a SAWR oriented along  $\Psi = 26.7^\circ$ . Figure 4.1a is a plot of the magnitude of the reflection coefficient  $|S_{11}|$  in dB, and Figure 4.1b and 4.1c are plots of the real and imaginary part of the admittance in mS, respectively. One can track the minimum value of the  $|S_{11}|$  or the maximum value of the real part of the admittance. It was found that there was no difference in tracking either of these variables when monitoring changes due to temperature or gas exposure to gas exposure. The results presented tracked the minimum value of  $|S_{11}|$ .

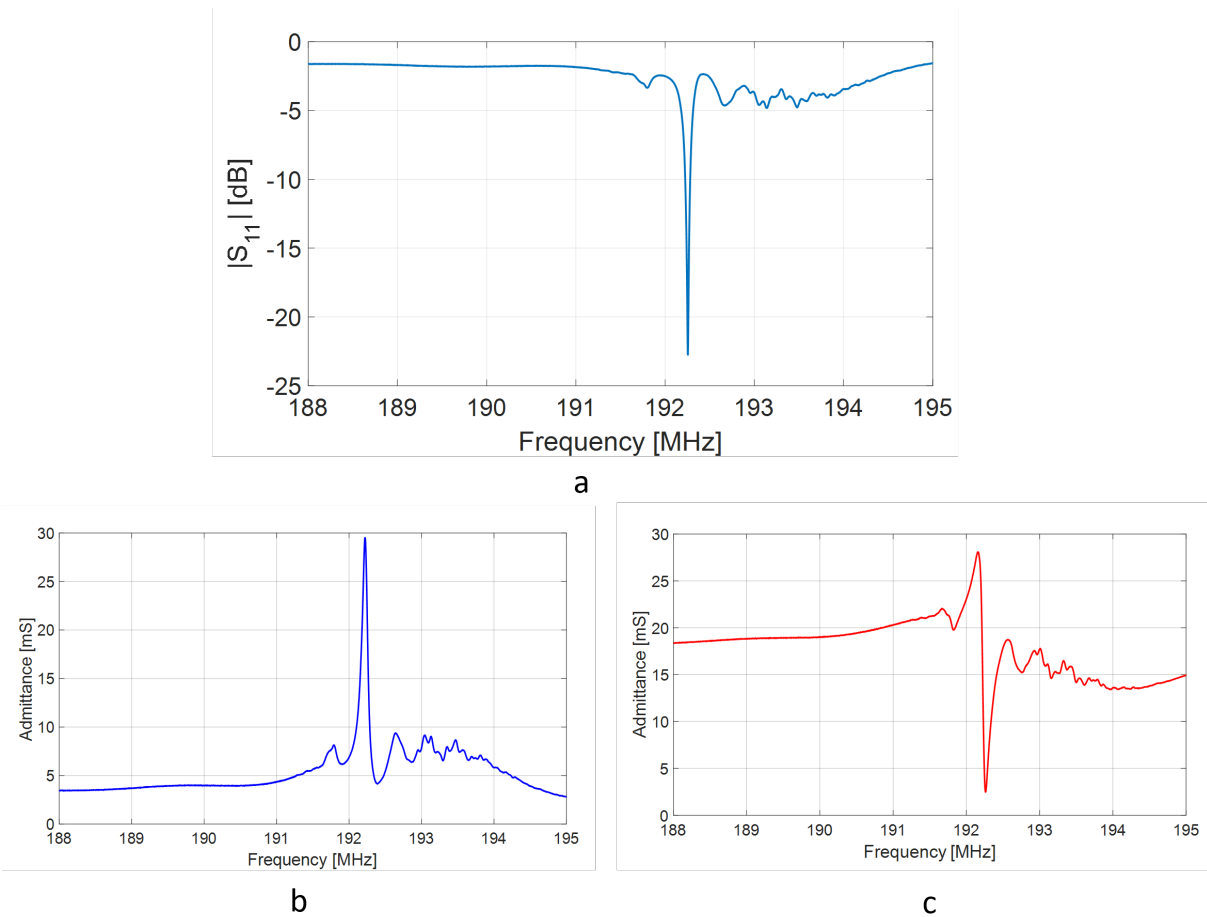


Figure 4.1. Frequency response of SAWR oriented along  $\Psi = 26.7^\circ$ : a) magnitude of reflection coefficient [dB]; b), real part of admittance [mS]; c) imaginary part of the admittance [mS].

Figure 4.2 shows a zoomed-in window to the resonant frequency of the device. At this magnification, it is possible to see the data points at which the VNA measured the  $S_{11}$ .

The E7071C has an  $S_{11}$  measurement accuracy of  $\pm 0.007$  dB at the desired frequency range, and so frequency shifting may occur between two adjacent points if the magnitudes are close enough at that minimum [112]. For this reason, parabolic fitting was used with a 10-30kHz bandwidth (depending on the frequency step used for the tests, since this dictates the number of points available for the polynomial fitting near the resonant frequency) for all measurements in order to eliminate this frequency switching as shown in Figure 4.2.

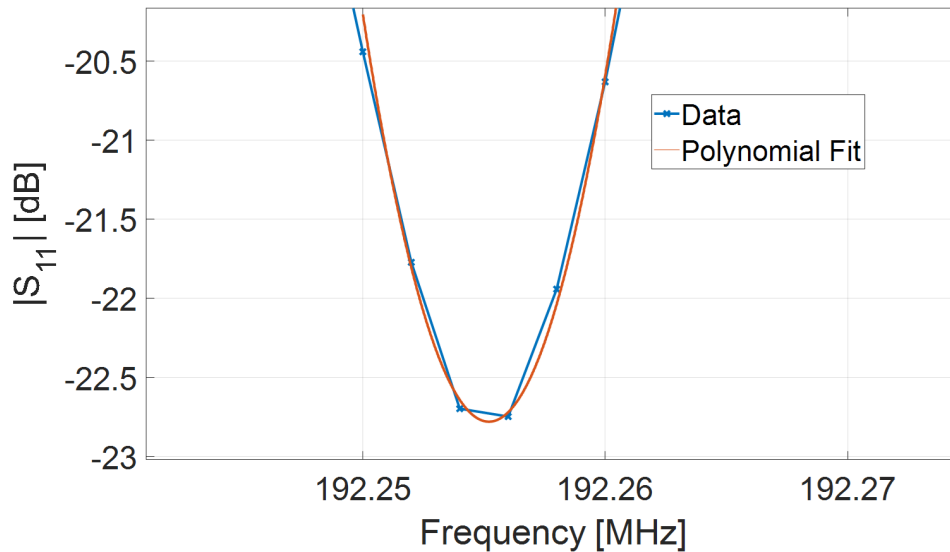


Figure 4.2. Polynomial fitting around minimum  $S_{11}$  value to filter out frequency shifting between adjacent points and improve the detection of minima for  $S_{11}$ .

Figure 4.3 shows a typical frequency response of a SAWR oriented along  $\Psi = 20.7^\circ$  with RC IDT placement. To track the resonant frequency of devices with multiple resonances such as the one shown in Figure 4.3, one of the frequency peaks was designated at the beginning of the test as the frequency peak to be tracked, and that frequency peak was tracked throughout the remainder of the test. This solution worked best for tests with a temperature range spanning less than  $200^\circ\text{C}$ , and often failed during tests that had wider temperature ranges (from room temperature to  $750^\circ\text{C}$  for example) as it is often the case that some resonant frequencies become more pronounced at different temperatures and this

prevented the selection of a particular peak at the beginning of a test for consistent tracking under the technique implemented.

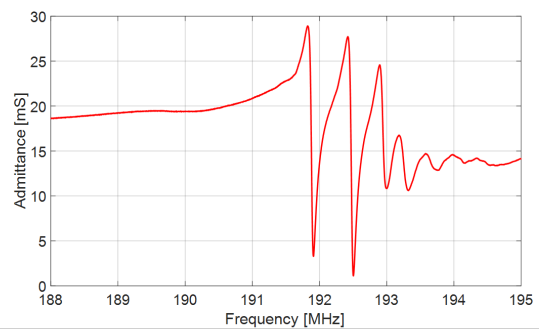
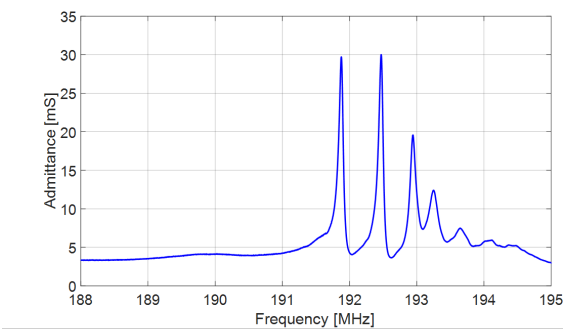
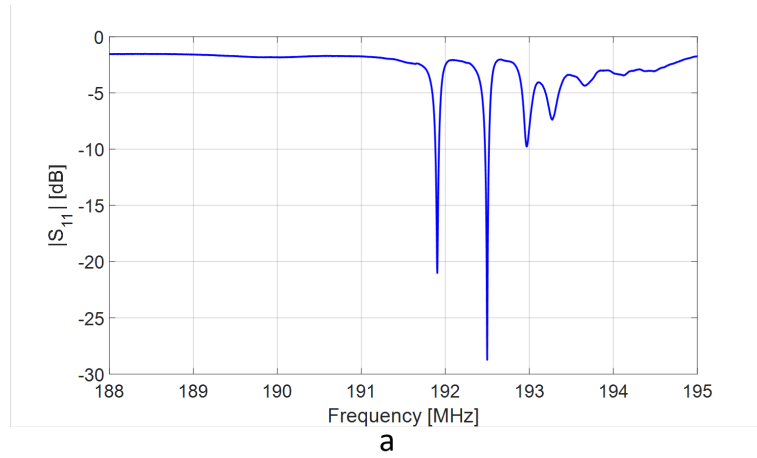


Figure 4.3. Frequency response of SAWR oriented along  $\Psi = 20.7^\circ$  with RC IDT placement: a) magnitude of reflection coefficient [dB]; b), real part of admittance [mS]; c) imaginary part of the admittance [mS].

For gas cycling tests, unless otherwise specified, the frequency shifts measured from figures are assumed to be measured from the instant before the gas transition in question to the moment before the next gas transition.

## 4.2 SAWR sensor High-temperature Characterization

This section will present the results obtained using the test setups described in Section 3.3 under Table 3.2.

### 4.2.1 Verification of Temperature Performance of Temperature Compensated Orientations at temperatures above 150°C

As described in Section 2.1.1, SAWR sensors oriented along  $\Psi = 14.7^\circ$  and  $\Psi = 77.7^\circ$  were predicted to have compensated temperature behaviour around 180°C and 310°C respectively. The results obtained using Setup B1 are shown in Figure 4.4. The measured temperature of compensation for SAWR sensors oriented along  $\Psi = 14.7^\circ$  and  $\Psi = 77.7^\circ$  was found to be approximately 150°C and 290°C, respectively [85]. Discrepancies between predicted and measured results are expected due to uncertainties in the thermal coefficients used in the calculations, as well as the influence of the Pt-Al<sub>2</sub>O<sub>3</sub> electrodes, which were not taken into account during calculations. The results proved that these two orientations are of interest for operation around their respective temperatures of compensation, and also to provide different temperature dependence of sensors being employed as components of multi-sensor systems, such as the one proposed in Section 1.6.

### 4.2.2 Experimental results for influence of YSZ sensing film on temperature performance of high-temperature SAWR sensors

Test setup B2 was tested to compare the temperature performance of Bare and 50nmYSZ SAWR sensors oriented along  $\Psi = 77.7^\circ$ . The results are shown in Figure 4.5. There was approximately a 5°C shift upwards in temperature of compensation for the 50nmYSZ sensor when compared to the Bare sensor, which is within expected experimental margins of error considering the performance of similar sensors. This indicates that the YSZ film does not significantly affect the temperature sensitivity of the SAWR sensors when compared to their Bare counterparts [84].

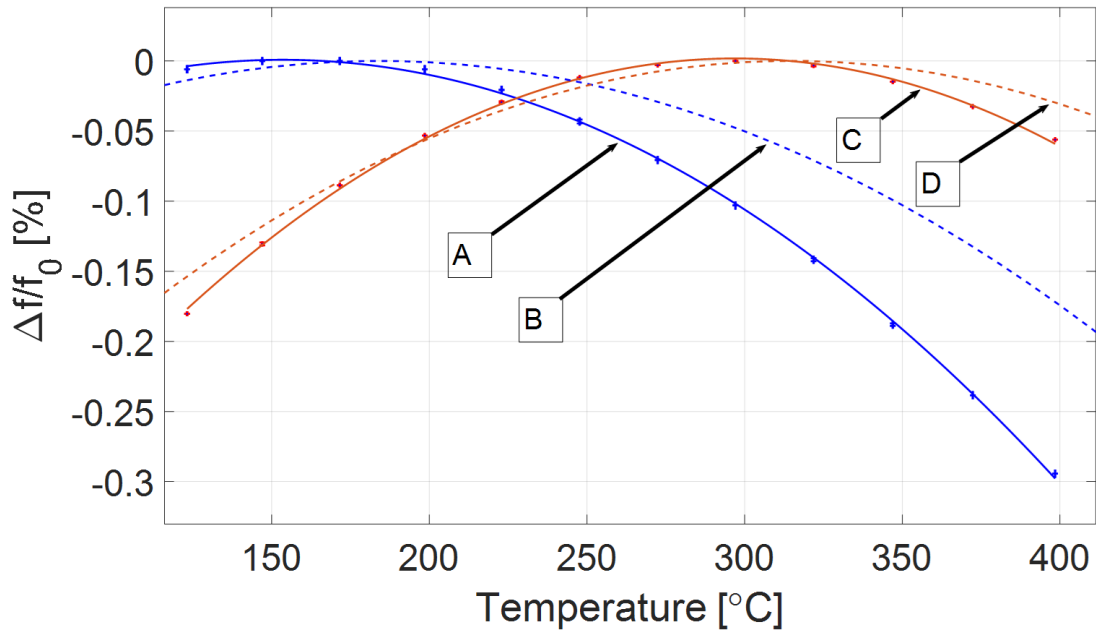


Figure 4.4. Measured and predicted resonant fractional frequency variation normalized to the maximum frequency with respect to measured temperature ( $f_0$  were 191.07 and 190.26 MHz for  $\Psi = 14.7^\circ$  and  $\Psi = 77.7^\circ$  respectively). Discrete points: measured data and respective uncertainties; solid curves: second order polynomial fits; dashed curves: numerically calculated responses for free surface. Curves A and B:  $\Psi = 14.7^\circ$ ; Curves C and D:  $\Psi = 77.7^\circ$  [85].

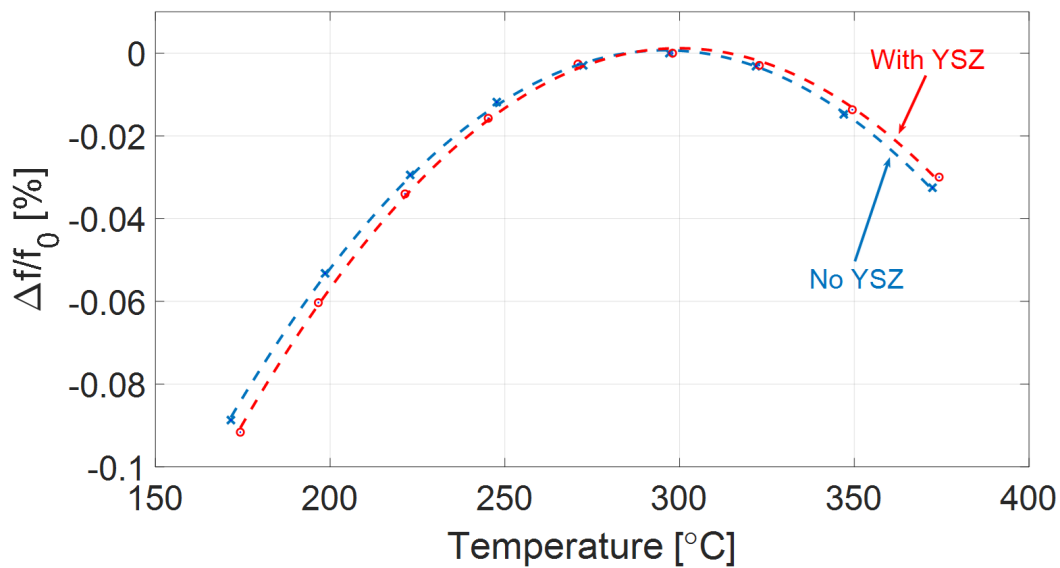


Figure 4.5. Fractional frequency variation in SAWR sensor oriented along  $\Psi = 77.7^\circ$  as a function of temperature ( $f_0$  were 190.4 and 190.2 MHz for 50nmYSZ and Bare devices respectively): Red curve: 50nmYSZ Sensor; Blue curve: Bare Sensor[84].

### 4.2.3 Temperature stability performance of Film 1 and Film 2 SAWR Sensors

Both Setup B3 and B4 were used to study the stability performance of Bare SAWR sensors employing either Film 1 or Film 2 electrodes and reflectors as described in Section 2.2.2. SEM images taken of the IDTs of each Film 1 and Film 2 for the four different states described in Section 3.3 are shown in Figure 4.6 [93]. Both films are indistinguishable at State 1, with smooth surfaces and no signs of deterioration. After annealing at 800°C for four hours, Film 1 (State 2 left) already showed the formation of stress hillocks and material agglomeration, ranging in diameter from 400 nm to 1000 nm and a density of approximately 1 hillock/ $3\mu\text{m}^2$  (0.35 hillocks/ $\mu\text{m}^2$ ). Film 2 (State 2 right) showed no sign of hillock formation nor any material agglomeration due to the annealing process. For State 3 (after heating in Profile 1, Section 3.3, Figure 3.14), Film 1 continued to show hillocks ranging from 400 nm to 1000 nm, whereas Film 2 still showed no sign of hillock formation or material agglomeration. Upon exposure to multiple cycling between 328°C and 843°C (State 4, Figure 3.15), the thinner parts of the electrodes as discussed in Chapter 2.3, showed signs of agglomeration for both Films 1 and 2. Interestingly, though, the center part of the graded Film 2 electrodes, i.e., the part that has the nominal film thickness of 180 nm seemed to be unaffected by the Profile 2 five rounds of cycling up to 843 °C. Film 1, on the other hand, not only suffered severe agglomeration at the thinner part of the electrodes, but also showed evidence of absence of material at the center part of the electrode, where the nominal thickness is 180 nm.



An example of the continuous-time frequency peak tracking of a Bare Film 1 sensor oriented along  $\Psi = 26.7^\circ$  during one of the rounds conducted for Profile 1 (described in Section 3.3) is shown in Figure 4.7. As mentioned, in Section 3.3, the average and standard deviation of the SAWR sensors after 45 minutes at the upper holding temperatures (715°C and 850°C, for a total of 30 measurements for each average) were extracted.

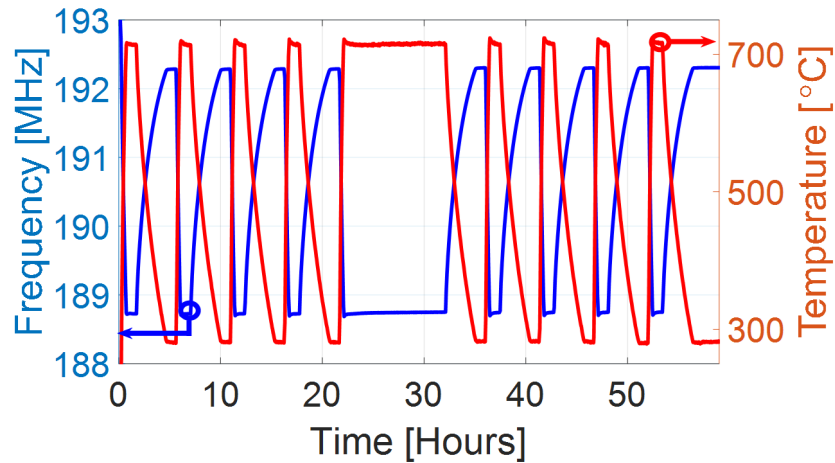


Figure 4.7. Tracked Resonant Frequency vs. Time and Temperature, Profile 1

Figure 4.8 plots the average frequency variation of the last 30 measurements of each cycling period at the highest temperature, which is shown on the right axis of the plot, for both Film 1 (blue triangles) and Film 2 (green circles) SAWRs, where the reference frequency,  $f_0$ , is 188.725MHz for Film 1 and 188.093MHz for Film 2. The standard deviation in the frequency measurements was smaller than 0.002% (comparable or smaller than the size of the shapes used in Figure 4.8). The resonant frequency variations of the soaking periods are consistently higher than subsequent excursions to the same temperature in the cycles following, revealing that, although the TC mounted on the rear side of the Inconel plate shows a stable temperature (Figure 3.16), the 1-hour shorter periods are not enough for the SAWR sensors to reach a stable temperature even though it is enough time for the TC to register a stable temperature during the same time frame. These differences are less than about 12kHz, which for a temperature sensitivity around 10kHz/°C for this orientation

at 700°C corresponds to a maximum temperature difference of 1.2°C [113]. This value of temperature variation is comparable to fluctuations in temperature due to the furnace controller and thermocouple. Therefore, after the middle of the third round the Pt-Al<sub>2</sub>O<sub>3</sub> electrode for both Films 1 and 2 had reached a stable operating frequency. This similarity in stabilization time existed despite the difference in film quality observed after SEM analysis (State 3). This suggests that the mitigation of stress hillocks accomplished at this sensor state was not the main culprit for the initial device drift during the first rounds of Profile 1 heating [93].

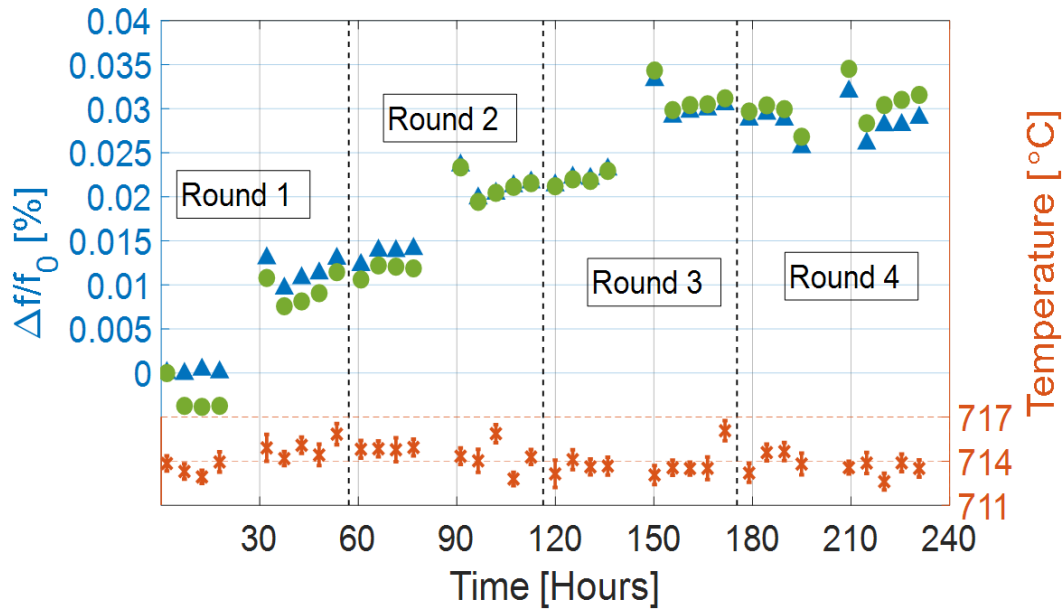


Figure 4.8. Averaged relative frequency variation for Film 1 (blue triangles) and Film 2 (green circles) for setup B3 at the maximum temperature value shown on the right axis ( $f_0$ , Film 1: 188.725MHz, Film 2: 188.093MHz), Profile 1, Section 3.3.

Figure 4.9 shows the SAWR sensor continuous-time measurements conducted for five rounds of Profile 2. The average frequency variation of the last 30 measurements of each cycling period at the highest temperature is shown on the right axis of the plot for both Film 1 (blue triangles) and Film 2 (green circles) SAWRs, where  $f_0$  is 186.539MHz for Film 1 and 186.093MHz for Film 2. In this case, both Film 1 and Film 2 exhibited frequency variations that did not suggest stable operating frequency even after 5 rounds of Profile 2.

The Film 1 SAWR drifted approximately 44 kHz after the fourth soaking period (Feature A in Figure 4.9), while Film 2 SAWR drifted approximately 113 kHz (Feature B in Figure 4.9). Subsequently Film 1 SAWR drifted approximately 39.4 kHz after the fifth soaking period (Feature C in Figure 4.9), while Film 2 SAWR drifted approximately 85.8 kHz (Feature D in Figure 4.9). These frequency variations can be correlated to the significant electrode deterioration observed in Figure 4.6 for both Films 1 and 2. Suggested future work should investigate the performance of sensors that do not require rotation during deposition. Under such fabrication conditions, and based on the SEM images of Figure 4.6, in particular the center part of the electrode of nominal thickness, Film 2 could potentially lead to stable operating frequencies for SAW resonators employing Pt-Al<sub>2</sub>O<sub>3</sub> thin films at temperatures above 850°C [93].

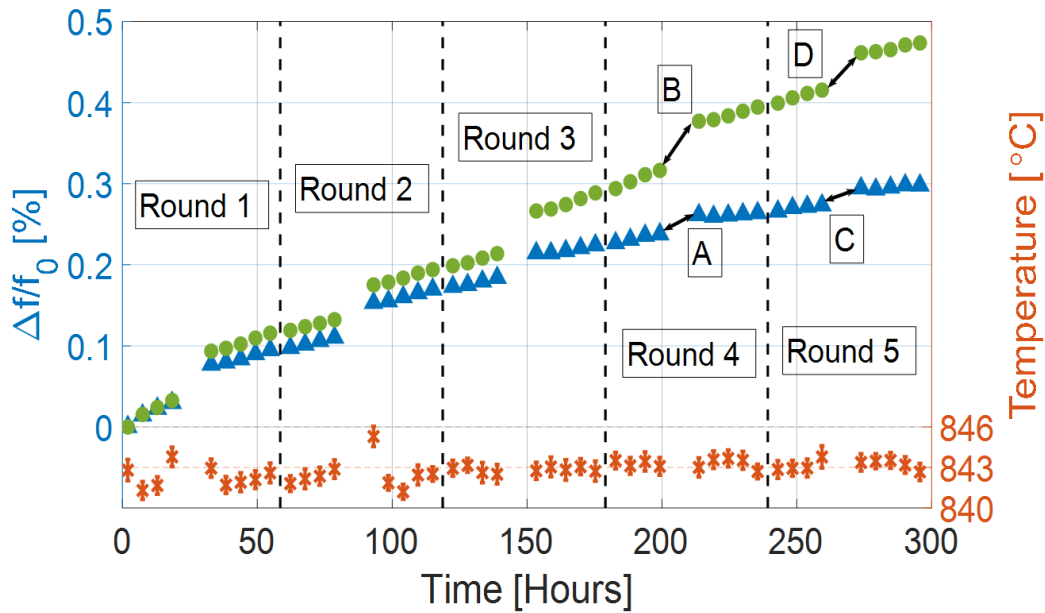


Figure 4.9. Averaged relative frequency variation for Film 1 (blue triangles) and Film 2 (green circles) for setup B4 at the maximum temperature value shown on the right axis ( $f_0$ , Film 1: 186.539MHz; Film 2: 186.093MHz), Profile 2, Section 3.3.

### 4.3 SAWR Sensor Performance under Different Flow Rates and H<sub>2</sub> Concentrations

This section describes results involving the characterization of the SAWR gas sensor system using different gas delivery flow rates and concentrations of H<sub>2</sub>. Specifically, N<sub>2</sub> flow rate was varied from 100 sccm to 950 sccm at both room temperature and 500°C. Gas cycling between N<sub>2</sub>, O<sub>2</sub> and 4%H<sub>2</sub> at room temperature was conducted, first with 100 sccm flow rate and then with 950 sccm flow rates to compare the SAWR sensor response to gas transitions using both delivery flow rates. Gas testing was also conducted at 300°C to compare the impact of H<sub>2</sub> (4% vs. 2%) concentration on gas sensor response. **All results presented in this and in following sections for gas cycling results show the tracked frequency plotted on the left axis with a blue dotted-dashed line, the temperature of the test plotted on the top-right axis with a red dotted line, and the exposure profile plotted on bottom-right axis with a solid green line.**

#### 4.3.1 SAWR Sensor Response to Different N<sub>2</sub> Flow Rates

In order to test the impact of varying gas delivery flow rates on tracked frequency, SAWR sensors in Setup A5 (Section 3.2) were tested at room temperature and at 500°C under 100 sccm of N<sub>2</sub> flow, which was then increased to 150 sccm, 200 sccm, 400 sccm, 800 sccm, and 950 sccm of N<sub>2</sub> every 20 minutes. The devices were interrogated 5 times before and after each gas transition with 2001 points and a 2 MHz span centered at 191 MHz at room-temperature and with 5001 points and a 5 MHz span centered at 192.5 MHz at 500°C, for a frequency step of 1 kHz in both cases. The result for Device 1 (Film 2 Bare cycled 14.7°) of Setup A5 at room temperature is shown in Figure 4.10. The result shows that the tracked frequency varies approximately 400 Hz during the entire test at room temperature, which is less than the frequency step for these tests. This result suggested that there was no significant effect of flow rate at room-temperature.

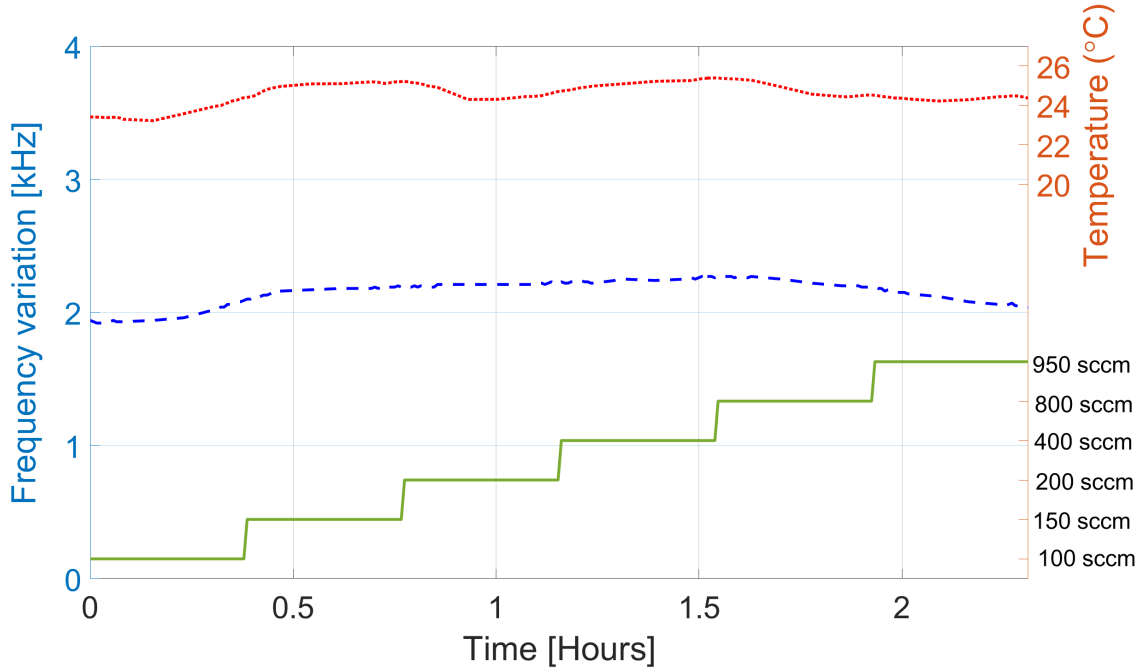


Figure 4.10. Frequency variation of Setup A5 Device 1 (Film 2 Bare cycled  $14.7^\circ$ ) Tracked Frequency response with respect to  $f_0 = 190.816$  vs. Different flow rates of  $N_2$  at Room Temperature.

The test for Device 1 of Setup A5 at  $500^\circ\text{C}$  is shown in Figure 4.11. Tracked frequency varied approximately 7 kHz from 100 sccm to the final introduction of 950 sccm. This result shows that the flow rate may produced a frequency variation of about 7 kHz at  $500^\circ\text{C}$  as the flow rate was varied from 100 sccm to 950 sccm. At  $500^\circ\text{C}$ , a 6 kHz frequency variation is equivalent to a temperature variation of approximately  $1^\circ\text{C}$  for the orientation tested ( $14.7^\circ$ ). Temperature variations close to  $1^\circ\text{C}$  are plausible at locations in the chamber close to the gas inlet. This small temperature variation is not detected at the location near the gas outlet by the TC as can be seen in Figure 4.11. In any case, during the tests that are presented throughout the remainder of this Chapter, the flow rate should not vary more than  $\pm 10$  sccm during gas transitions, as the specifications of the mass flow controllers are metered to have an accuracy of 1.0% at full scale (1000 sccm for both MFCs used) [114] and the command input to the MFCs was varied according to the conversion parameters specified in [115].

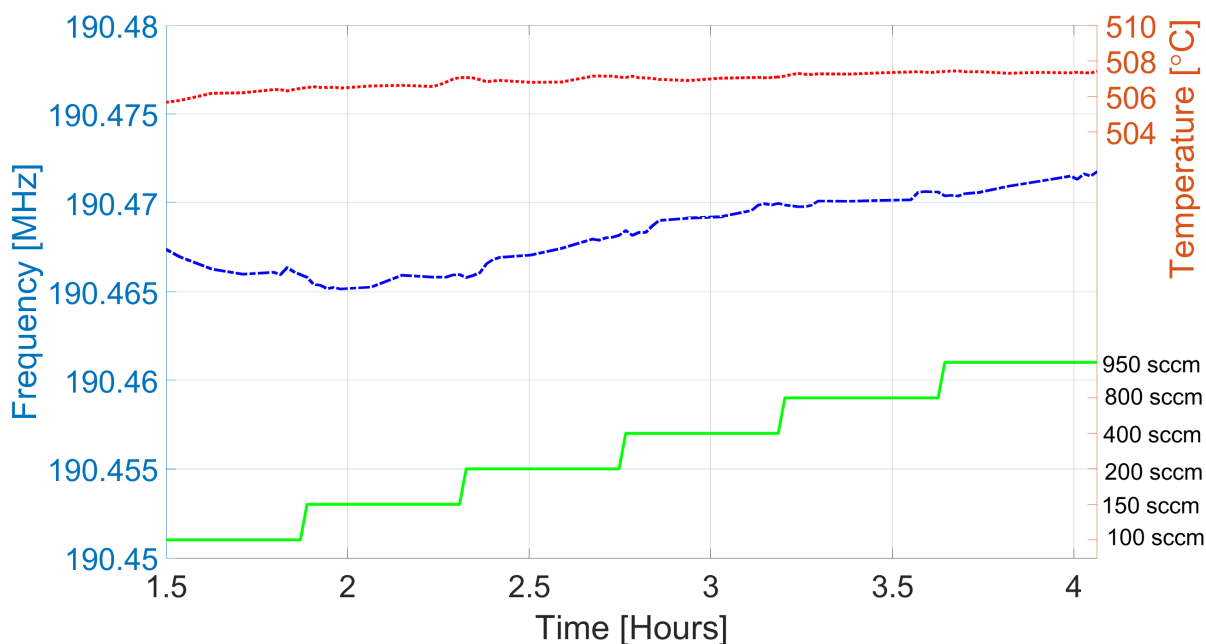
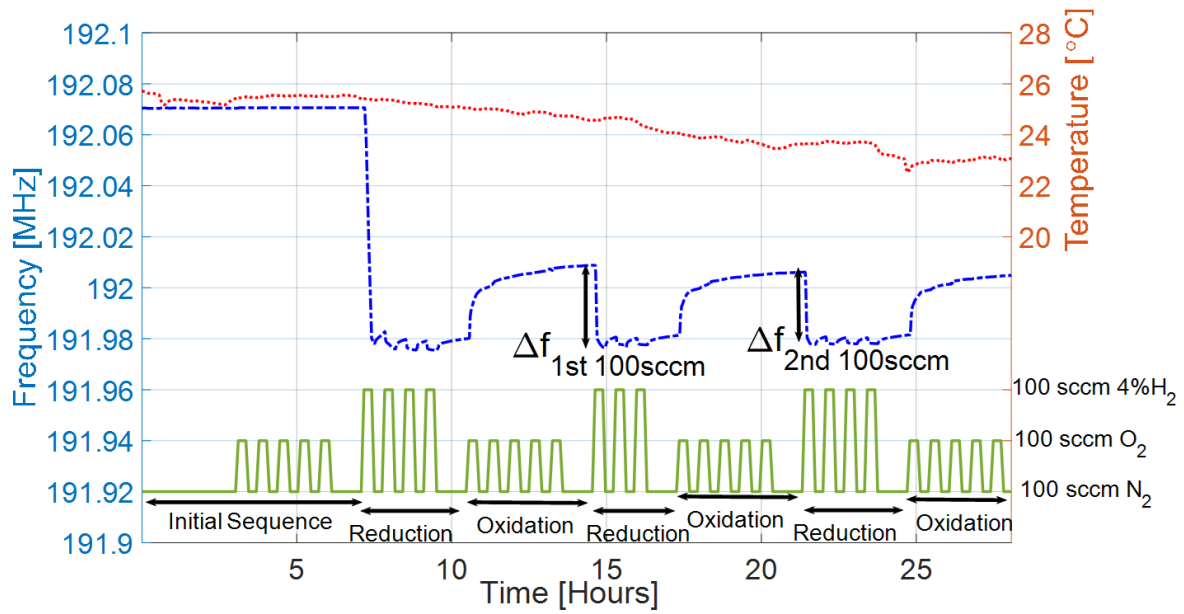


Figure 4.11. Setup A5 Device 1 Tracked Frequency response vs. Different flow rates of  $N_2$  at  $500^\circ C$ .

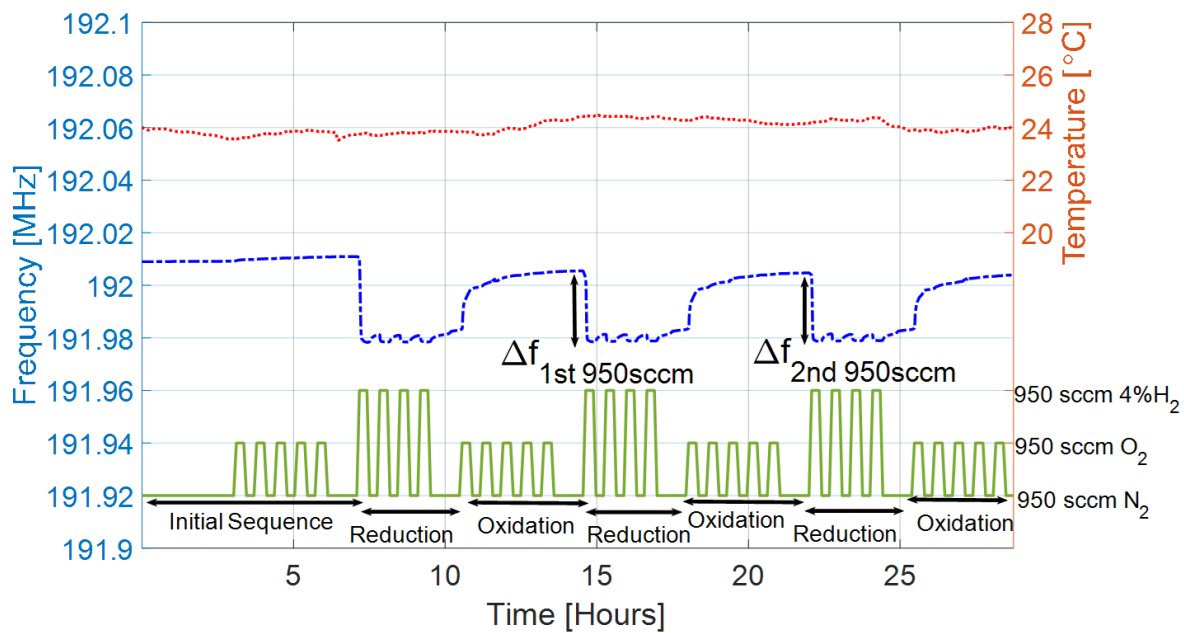
#### 4.3.2 Room temperature Gas Cycling SAWR Sensor Response under 100 sccm and 950 sccm Flow Rates

To test the impact of gas cycling SAWR sensor response under different flow rates, Setup A4 was tested at room-temperature immediately after mounting using 2001 points, 10 MHz span (frequency step of 5 kHz) and 3kHz IF bandwidth . Figure 4.12 shows the obtained results for Device 4 (Film 2 Bare non-cycled  $26.7^\circ$ ) in Setup A4 for a test under 100 sccm flow and followed up immediately by a test under 950 sccm flow. The gas exposure profile was identical for both 100 sccm and 950 sccm and consisted of either 20 min or 60 min cycles between  $N_2$ ,  $O_2$  and  $4\%H_2$  under 100 sccm for the first test (Figure 4.12a) and 950 sccm for the second test (Figure 4.12b). The frequency shifts labeled in Figure 4.12 refer to the measurements performed immediately before the introduction of  $4\%H_2$  into the chamber until the measurement immediately before the end of the  $H_2$  exposure (for a total of 20 min exposure measurement). The frequency shifts in 100 sccm flow labeled as  $\Delta f_{1st100sccm}$  and  $\Delta f_{2nd100sccm}$  correspond to the first response  $4\%H_2$  after each respective oxidation sequence,

and have a magnitude of 32.3 kHz and 29.3 kHz, respectively. The frequency shifts in 950 sccm flow labeled as  $\Delta f_{1st950sccm}$  and  $\Delta f_{2nd950sccm}$  have magnitudes of 27.0 kHz and 26.1 kHz, respectively. The very first response to 4% $H_2$  occurring at around 7 hours for both tests deals with initial surface oxidation states, and its increased magnitude compared to  $\Delta f_{1st100sccm}$  and  $\Delta f_{2nd100sccm}$  will be explained in Section 4.5. Considering the frequency variations observed after the 4% $H_2$  exposures, the results obtained suggest that the frequency shift due to 4% $H_2$  exposure is not significantly affected due to flow rate delivery for 100 sccm and 950 sccm flow rates.



a



b

Figure 4.12. Setup A4 Device 4 (Film 2 Bare non-cycled 26.7°) Tracked Frequency at room temperature vs. Gas Exposure with: a) 100 sccm gas flow; b) 950 sccm gas flow.

### 4.3.3 SAWR Sensor Response to Different H<sub>2</sub> Concentrations

To test the impact of H<sub>2</sub> concentration on SAWR sensor response, Setup A5 was tested using 5001 points, 10 MHz span (2 kHz frequency step) and 2 kHz IF bandwidth at 300°C. Figure 4.13 shows the results obtained for Device 3 (Film 1 Bare cycled 14.7°) in Setup A5, where 2-hour N<sub>2</sub> purging periods were used between 1-hour reducing periods in either 4%H<sub>2</sub> or 2%H<sub>2</sub>. The first reduction is not labeled, as it will be discussed in Section 4.5. The features labeled in Figure 4.13 correspond to the frequency shifts measured from the measurement immediately preceding the introduction of H<sub>2</sub> to the end of the 1-hour reducing period in H<sub>2</sub>. For 4%H<sub>2</sub>, the features were 8.0kHz and 10.6kHz in magnitude ( $\Delta f_{1st4\%}$  and  $\Delta f_{2nd4\%}$ ) and for 2%H<sub>2</sub>, the features were 8.9 kHz and 8.6 kHz in magnitude ( $\Delta f_{1st2\%}$  and  $\Delta f_{2nd2\%}$ ). These results indicated that the saturation level for H<sub>2</sub> interaction with the SAWR sensors has already been reached at 2%, and additional concentration up to 4% does not significantly increase H<sub>2</sub> interaction with the SAWR sensors, which is consistent with [20], [21] which indicate that higher gas concentrations after exposure for sufficient time do not have a significant impact on sensor response.

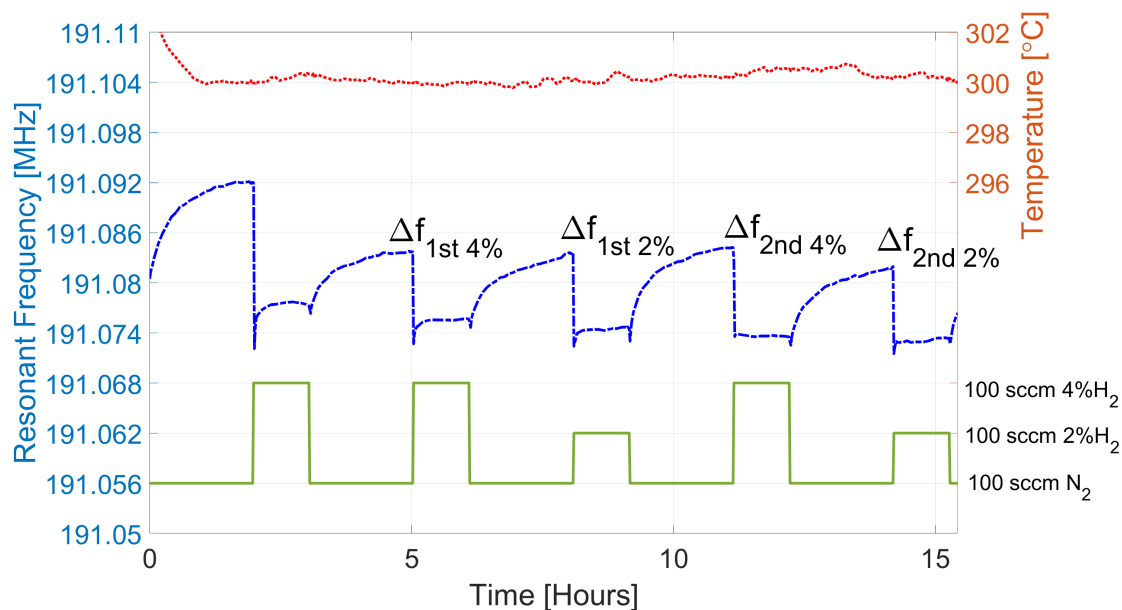


Figure 4.13. Setup A5 Device 3 Tracked Frequency at 300°C vs. Gas Exposure for different H<sub>2</sub> concentrations.

#### 4.4 Comparison of YSZ-layered and Bare SAW Gas Sensor Performance

This section presents the comparison between SAWR sensor performance at high-temperature for the detection of 4% $H_2$  using Bare and YSZ-layered devices. Setup A2 compared Bare and YSZ-layered devices at 300°C and Setup A4 compared YSZ-layered vs. Bare SAWR sensor SAWR sensors at 200°C, 300°C and 400°C.

YSZ-layered (15 nm YSZ thickness with 1 nm Pt decoration as described in Section 2.3) and Bare SAWR sensors employing Film 2 for electrodes and reflectors were tested around 280°C using Setup A2 was using 10,001 points, 5 MHz span (500 Hz frequency steps) with a center frequency of 192.5 MHz and IF bandwidth of 1 kHz. The devices were cycled with 20-min periods in either  $O_2$  or 4% $H_2$  with 1-hour purging periods in  $N_2$ . The results are shown in Figure 4.14 and for Figure 4.15 for Device 3 (Film 2 YSZ non-cycled 14.7°) and Device 4 (Film 2 Bare non-cycled 14.7°), respectively. The frequency tracking of Device 4 experienced larger ripples, most likely to a defective connection with the 1 mil Pt wire. Three features are marked on each figure, the shifts in frequency due to exposure to 4% $H_2$  after the oxidation periods marked in the figures. The magnitude for the frequency shifts for Device 3 were 19.7kHz, 18.7kHz, and 18.8kHz for  $\Delta f_{1stYSZA3}$ ,  $\Delta f_{2ndYSZA3}$  and  $\Delta f_{3rdYSZA3}$  respectively. The magnitude for Device 4 were 29.3kHz, 25.3kHz and 25.2kHz for  $\Delta f_{1stBareA3}$ ,  $\Delta f_{2ndBareA3}$  and  $\Delta f_{3rdBareA3}$  respectively. This result suggests that the Pt-decorated YSZ layer actually impeded  $H_2$  from reaching the sensing film at the surface of the SAWR sensors, and thus the Pt-decorated YSZ does not increase the Pt- $Al_2O_3$  based SAWR sensor response to  $H_2$ .

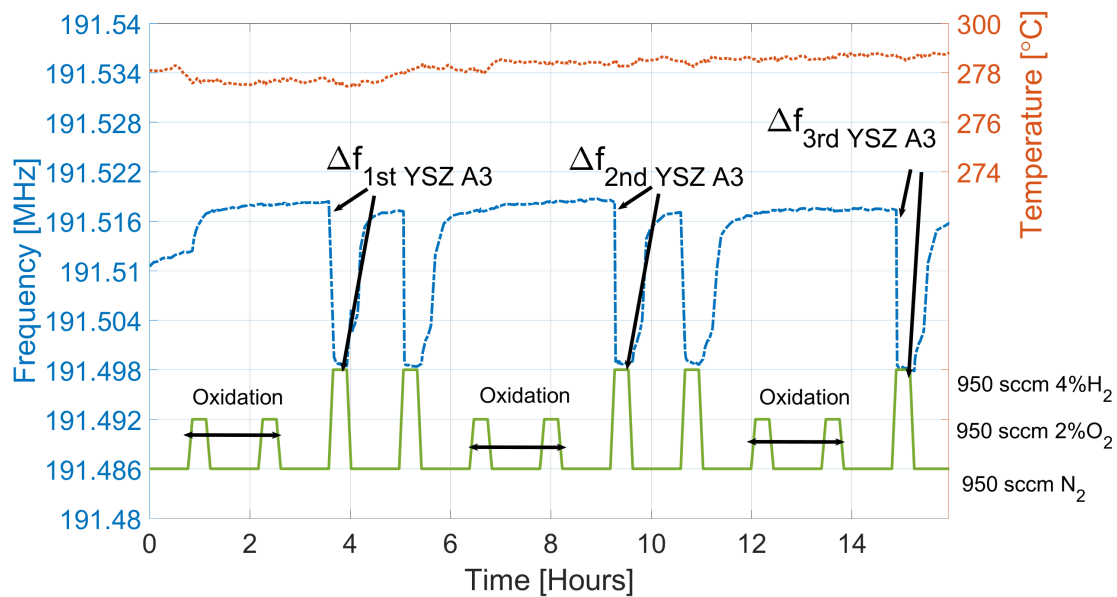


Figure 4.14. Setup A2 Device 3 (Film 2 YSZ non-cycled 14.7°) Tracked Frequency at 300°C vs. Gas Exposure.

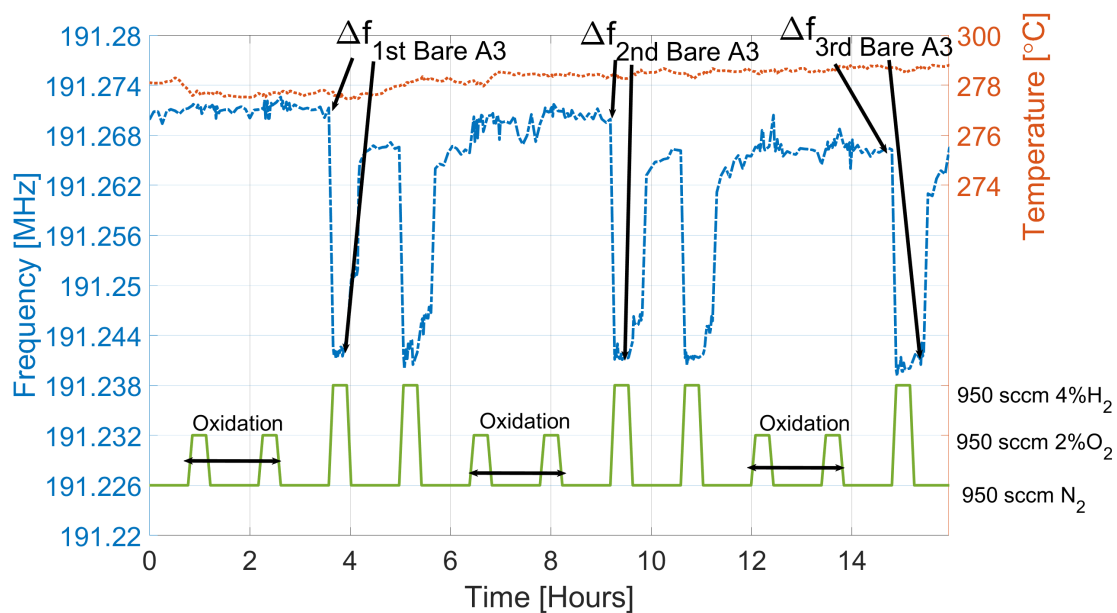


Figure 4.15. Setup A2 Device 4 (Film 2 Bare non-cycled 14.7°) Tracked Frequency at 300°C vs. Gas Exposure.

These results were confirmed using Setup A4, which was tested at 200°C, 300°C and 400°C using 2001 points, 10 MHz span (5 kHz frequency step) centered at 190 MHz and an IF bandwidth of 5 kHz. As an example, the results for Device 2 (Film 2 Bare non-cycled 14.7°) is shown in Figure 4.16. The gas exposure profile consisted of 3-hour oxidation periods and 90-min reduction periods separated by 1-hour N<sub>2</sub> purging periods, all in 100 sccm gas flow. Three frequency shifts ( $\Delta f_A$ ,  $\Delta f_B$  and  $\Delta f_C$  in Figure 4.16) were recorded for each device at each test temperature. The first frequency shift  $\Delta f_A$  is in most cases higher in magnitude than the second  $\Delta f_B$  and third  $\Delta f_C$  frequency shifts, as will be clarified in Section 4.5. The average of  $\Delta f_B$  and  $\Delta f_C$  was taken at each temperature for each device ( $\Delta f_i$ ) and was normalized to  $f_{0i}$ , defined as the last frequency recorded at the end of the reducing period corresponding to  $\Delta f_B$  at a particular temperature for a particular device (in the example Figure 4.16, the  $f_{0i}$  was 190.886 MHz). The resulting normalized  $\Delta f_i/f_{0i}$  are plotted in Figure 4.17 versus temperature, where the average temperature recorded within the corresponding chamber was used to associate the normalized  $\Delta f_i/f_{0i}$  to a temperature value. A compilation of all results is given in Section C.1. The measurements are connected within the figure for convenience and do not to imply extrapolation. Device 1 (Film 2 YSZ non-cycled 14.7°) and Device 2 (Film 2 Bare non-cycled 14.7°) showed frequency shifts within measurement accuracy (5 kHz) from their counterparts in Setup A2 (the results from Figures 4.14 and 4.15), which confirm the fact that the YSZ layer actually impeded the interaction between H<sub>2</sub> and the SAWR sensors. The same was true at the test temperatures of 200°C and 400°C for these devices. Additional evidence for this claim came from the comparison of Device 3 (Film 2 YSZ non-cycled 26.7°) and Device 4 (Film 2 Bare non-cycled 26.7°), where Device 4 (Bare 26.7°) across all test temperatures exhibited over 50% higher frequency shifts than Device 3 (YSZ 26.7°).

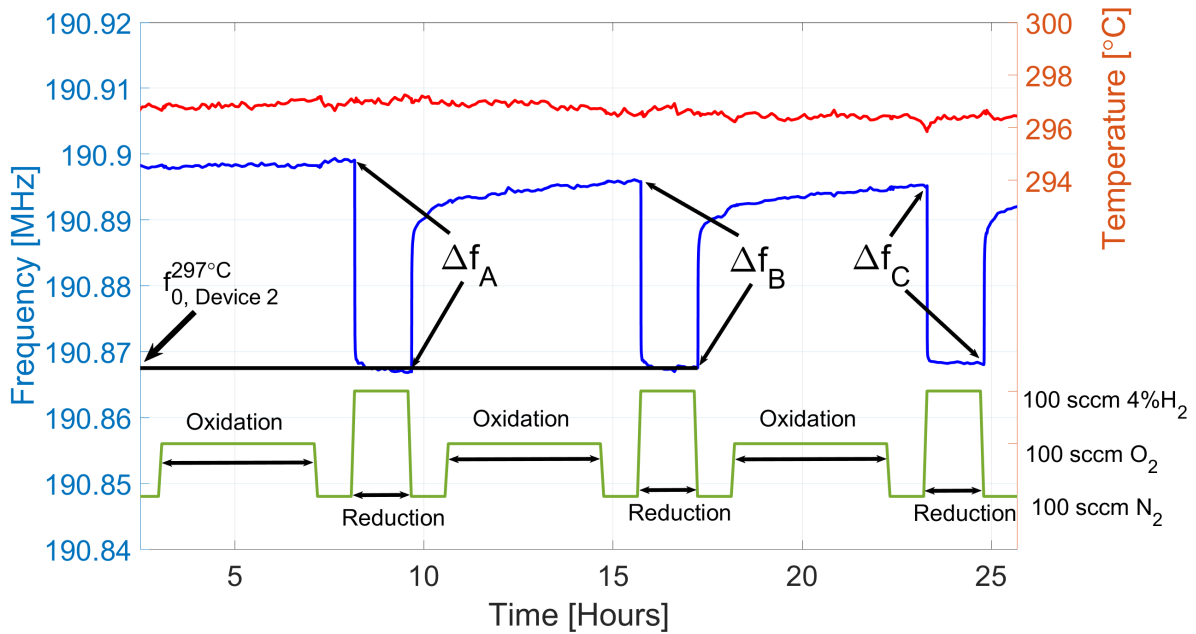


Figure 4.16. Setup A4 Device 2 (Film 2 YSZ non-cycled 14.7°) Tracked Frequency at 297°C vs. Gas Exposure.

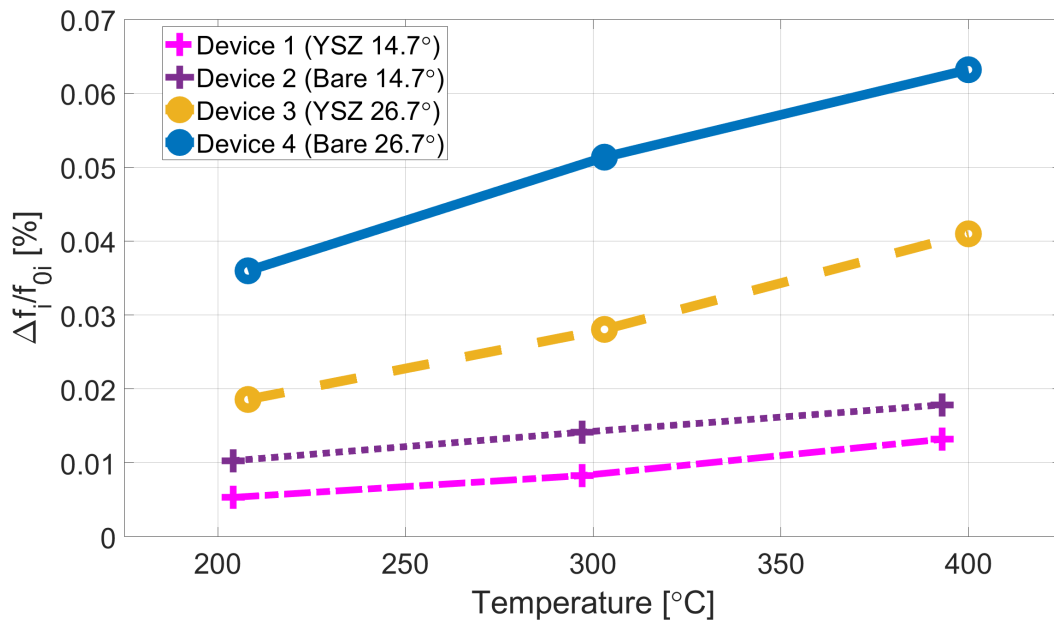


Figure 4.17. Setup A4 Measured relative frequency variation due to 4% $H_2$  exposure at the measured temperatures for: Device 1 (Film 2 YSZ non-cycled 14.7°) (pink crosses, dotted-dashed line); Device 2 (Film 2 Bare non-cycled 14.7°) (purple crosses, dotted line); Device 3 (Film 2 YSZ non-cycled 26.7°) (yellow circles, dashed line); Device 4 (Bare 26.7°) (blue circles, solid line).  $\Delta f_i$  and  $f_{0i}$  are given in Section C.1.

## 4.5 Oxygen Treatments for Gas Sensor Operation at Room Temperature

As has been observed in some of the previous results, the first frequency shift caused due to the introduction of  $H_2$  was observed to be consistently higher than subsequent frequency shifts due to  $H_2$  interaction with the sensors throughout the remainder of the test. This led to the hypothesis that the oxidation state of the sensors may play an important role in the subsequent  $H_2$  detection. For this reason, room-temperature gas cycling room-temperature gas cycling tests were conducted on Setup A3 using  $O_2$  treatments at room temperature. Additionally, Setup A3 was subject to high-temperature conditioning treatments at in  $O_2$   $500^\circ C$  and  $650^\circ C$  and in  $4\%H_2$  at  $500^\circ C$ , brought back to room-temperature where gas cycling tests were performed. Researchers Dr. Paul R. Ohodnicki and Dr. John Baltrus from the National Energy Technology Laboratory (NETL) in Pittsburgh, PA contributed valuable X-ray Photoelectron Spectroscopy (XPS) analysis that clarified the results obtained using SAWR sensors.

### 4.5.1 $O_2$ Treatments at Room Temperature

Setup A3 was exposed to a gas-cycling test at room temperature immediately after mounting using 10 MHz span with a center frequency of 190 MHz, an IF bandwidth of 5 kHz, and 2001 points (5 kHz frequency step). The gases were delivered with a flow rate of 950 sccm, and the profile consisted of either 25 or 60 min cycles between  $N_2$ ,  $O_2$  and  $4\%H_2$ . Figure 4.18 shows the results for Device 3 (Film 2 Bare non-cycled  $26.7^\circ$ ). The sequence of these exposures was designed to include several repeated exposures to either  $4\%H_2$  (reduction periods labeled R1, R2 and R3) or  $O_2$  (oxidation periods labeled O1, O2 and O3), with 60-min purging periods in  $N_2$  between reduction and oxidation (P1, P2 and P3). The events of frequency variations due to gas cycling are labeled, and correspond to the 90.7 kHz frequency shift due to the first exposure to  $4\%H_2$  exposure ('A'), sensor recovery frequency shifts due to  $4\%H_2/N_2$  cycling with shorter 25 min periods in  $N_2$  without any prior oxidizing treatments averaging 5.7 kHz for the instances recorded in this test ('B'),

sensor recovery due to 1-hour  $N_2$  purging periods averaging 6.2 kHz ('C'), sensor recovery of 28.3 kHz, 26.8 kHz and 24.5 kHz after oxidizing cycles O1, O2 and O3 respectively ('D1', 'D2' and 'D3',) and frequency shifts of 34.3 kHz and 33.3 kHz due to 4% $H_2$  exposure after the oxidizing treatments ('E1', 'E2'). Features B and C were consistent (less than 1 kHz standard deviation) throughout the test and are therefore labeled as the same feature. The complete results for several measurements taken from Setup A1 (Device 3, Film 1 Bare non-cycled 26.7° and Device 4, Film 1 Bare non-cycled 26.7°) and Setup A4 (Device 4, Film 2 Bare non-cycled 26.7°) for results obtained using 950 sccm gas flow are given in Appendix C in Section C.2.1. Figure 4.18 revealed that sensor resonant frequency shift due to 4% $H_2$  after oxidation periods (Features 'E') are less than half when compared to Features 'A', which might be attributed to the initial reduction of the sensor surface through exposure to 4% $H_2$ . As such, the surface state prior to Feature 'A' is not recovered by subsequent oxidation cycling at room temperature in a reasonable time frame [116].

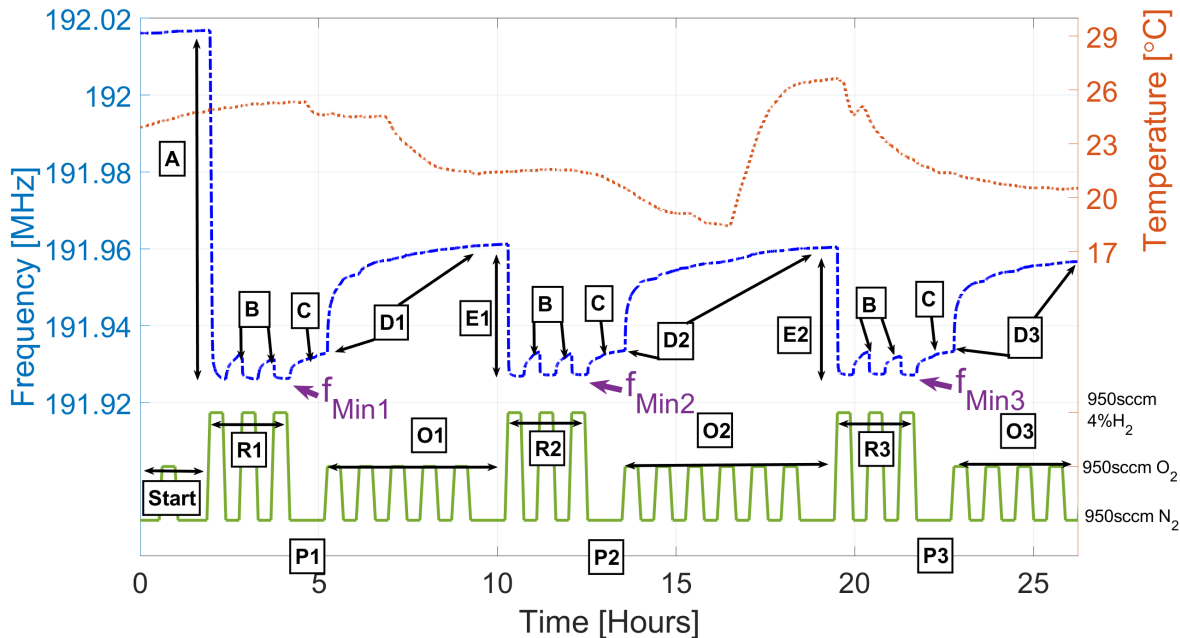


Figure 4.18. Setup A3 Device 3 (Film 2 Bare non-cycled 26.7°) Tracked Frequency at room temperature vs. Gas Exposure [116]

The frequency recovery of the SAWR sensor during purging periods  $P_i$  were compared with the frequency recovery during oxidation periods  $O_i$  (Figure 4.18) in order to analyze the relevance of using the oxygen cycling with respect to the use of  $N_2$  alone. Figure 4.19 shows the frequency variation during the periods  $P_i$  and  $O_i$ , subtracted from the minimum frequency before  $P_i$ ,  $f_{min1}$ . Exponential fitting was extrapolated during the first three minutes of the oxidizing period in Figure 4.19 to give the purging period  $P_i$  and the oxidizing period  $O_i$  the same starting point in time. Other than this exponential fitting during the three initial minutes of the  $O_i$  periods, all other points indicated in Figure 4.19 are measured data. As can be observed from Figure 4.19, the recovery due to oxygen cycling decreases slightly after multiple reduction/oxidation cycle periods  $O_i$ . At the end of the one-hour period shown in Figure 4.19, the frequency recovery for Feature D2 compared to D1 decreases by 2 kHz, and for D3 compared to D2, 1 kHz. The response plotted Figure 4.19 is a typical response obtained out of 18 of these cycling period experiments repeated with four different similar SAWR devices. After 22 minutes, the frequency recovery with oxygen cycling for all the  $D_i$  is at least 5 times greater than the recovery due to  $N_2$  purging alone. In the worst case shown at the 22min mark, D3 recovered 22.7 kHz compared to the 4.5 kHz recovery with  $N_2$ . After 57 minutes, the D3 recovery amounts to 25.3 kHz, and the frequency recovery of purging periods amounts to 6.1kHz, representing still a four-fold increase in sensor frequency recovery after approximately one hour. It is also interesting to observe that most of the frequency recovery using the oxygen cycling takes place during a few minutes, and that between the 22 min mark and the 57 min mark only an extra 10% increase in frequency recovery is obtained for a 65% increase in recovery time [116].

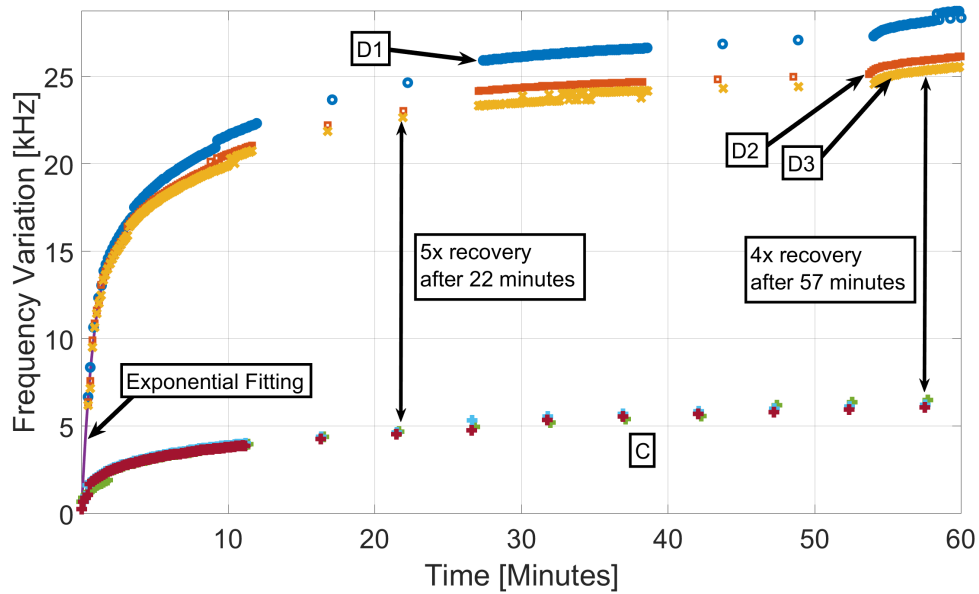


Figure 4.19. Comparison of Device 3 recoveries due to  $N_2$  and  $O_2/N_2$  cycling [116].

After 3 hours idling (no measurements taken) in 100 sccm flow of  $N_2$ , the same Setup A3 was tested to at room temperature using frequency sweeps of 6MHz centered at 191MHz with 10001 points and an IF bandwidth of 1kHz. The results are shown in Figure 4.20. The gas delivery profile was identical to the profile from the previous test shown in Figure 4.18. The features in Figure 4.20 marked as E3 and E4 correspond to the frequency shifts after the introduction of 4% $H_2$  after  $O_2$  treatments, and corresponded to features E1 and E2 marked in Figure 4.18. The magnitudes of E3 and E4 were 27.9 kHz and 28.4 kHz in magnitude respectively. These results showed that after 4 of these reductions, the magnitude of frequency shift does not seem to decrease further after the oxidation treatments [117].

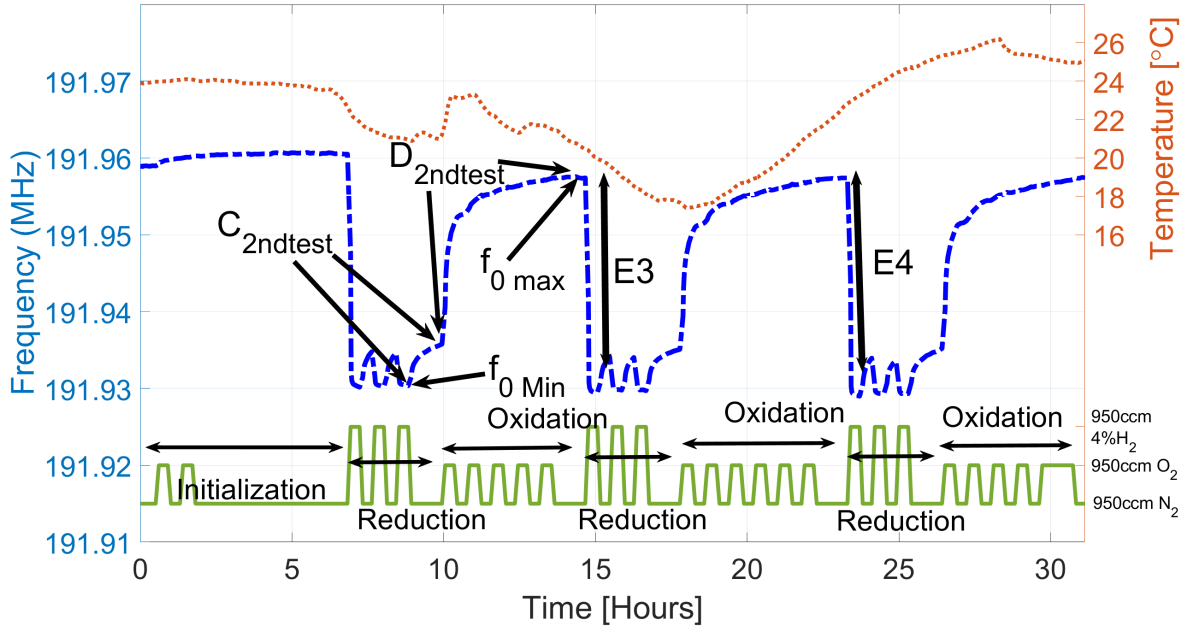


Figure 4.20. Setup A3 Device 3 (Bare 26.7° Film 2) Tracked Frequency at room temperature vs. Gas Exposure, Second Test [117].

The tracked frequency of the device in this test was normalized according to the values of  $f_{0min}$  and  $f_{0max}$  marked in Figure 4.20 through Equation 4.1.

$$f_n = 100 \frac{f - f_{0min}}{f_{0max} - f_{0min}} \quad (4.1)$$

Figure 4.21 plots the normalized measured frequency  $f_n$  for Features  $C_{2ndtest}$  and  $D_{2ndtest}$  and exponential fitting used to give the same starting point. After the first  $O_2$  around the 20-min mark, the sensor recovered to 78% of  $f_{0max}$ , as opposed to 15% for  $N_2$  alone, for a five-times larger frequency recovery for the referred 20-minute period. After 68 min in the  $O_2/2$  cycling, the sensor recovered 90% of  $f_{0max}$ , while in  $N_2$  that number drops to 21% [117].

It should be noted that the impact of gas treatments prior to 4% $H_2$  have a reduced effect at temperatures above 200°C, as can be seen from the oxidation periods Figure 4.16, Figure 4.33 and Figure 4.28. As mentioned, the improvement at room-temperature is five-fold, while at temperatures above 200°C there is an improvement of less than 20%.

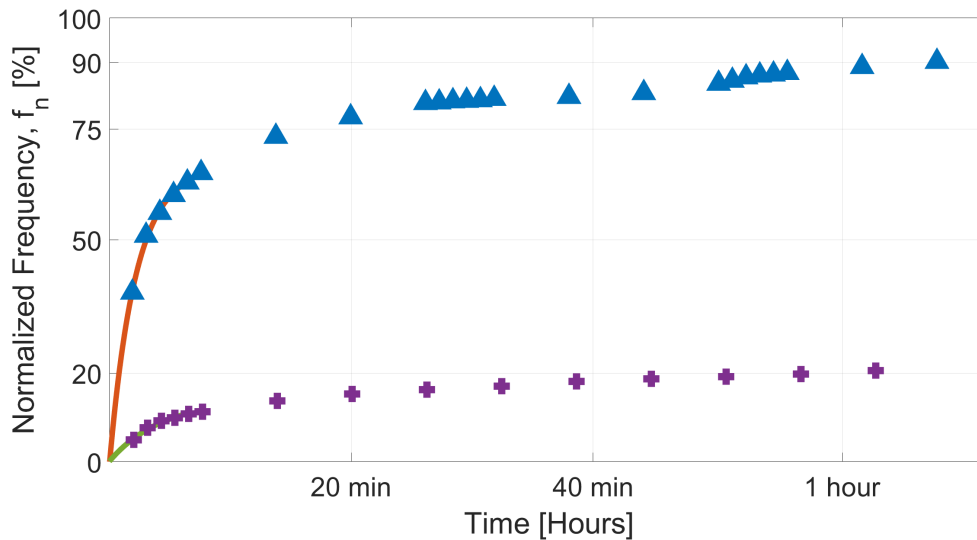


Figure 4.21. Setup A3 Device 3 (Bare 26.7° Film 2) Tracked Frequency at room temperature vs. Gas Exposure, Second Test, direct comparison of normalized frequency variation [117].

#### 4.5.2 High-temperature conditioning in O<sub>2</sub> and in 4%H<sub>2</sub>

Test Setup A3 was heated to 500°C in 100 sccm N<sub>2</sub> flow, switched to 4%H<sub>2</sub> 100 sccm flow for 3 hours at 500°C, and allowed to cool down to room temperature in 4%H<sub>2</sub> (Conditioning A). A room temperature gas cycling tests was conducted following this similar to the ones described previously in Section 4.5.1, with the exception of gases delivered using 100 sccm instead of 950 sccm. VNA settings were 10,001 points, 10 MHz span centered at 190 MHz and IF bandwidth of 1 kHz. Setup A3 was then heated to 500°C in N<sub>2</sub>, switched to O<sub>2</sub> 100 sccm flow for 3 hours at 500°C, and allowed to cool down to room temperature in O<sub>2</sub> (Conditioning B) and tested similarly at room temperature. The setup was then heated to 650°C in N<sub>2</sub>, switched to O<sub>2</sub> 100 sccm flow for 3 hours at 650°C, and allowed to cool down to room temperature in O<sub>2</sub> (Conditioning C) and tested similarly at room temperature. The results at room temperature after each conditioning for Device 3 are shown in Figure 4.22. The results showed that the SAWR sensor did not respond the gas cycling at room temperature after Conditioning A. The curve labeled Conditioning B in Figure 4.22 showed that the

device begins to respond to gas cycling at room temperature, with an initial response to H<sub>2</sub> of 41.2 kHz and subsequent variations in the range of 3 to 5 kHz when exposed to H<sub>2</sub> even after oxidizing periods. Finally, the curve labeled Conditioning C showed that exposure to 650°C further increases the device frequency variation to O<sub>2</sub> and H<sub>2</sub> cycling when compared to the response after exposure to the oxidation environment at 500°C. The feature marked in Figure 4.22 as  $\Delta f_1$  was of 73.2 kHz, markedly higher than the features  $\Delta f_1$  and  $\Delta f_2$  of 18.8kHz and 14.2 kHz respectively [116]. This oxidation conditioning at 650°C was repeated once for Setup A3 and done twice for Setup A4, and the results for Device 3 (Fim 2 Bare non-cycled 26.7°) in Setup A3 and Device 4 (Film 2 Bare non-cycled 26.7°) in Setup A4 are given in Appendix C in Section C.2.2.

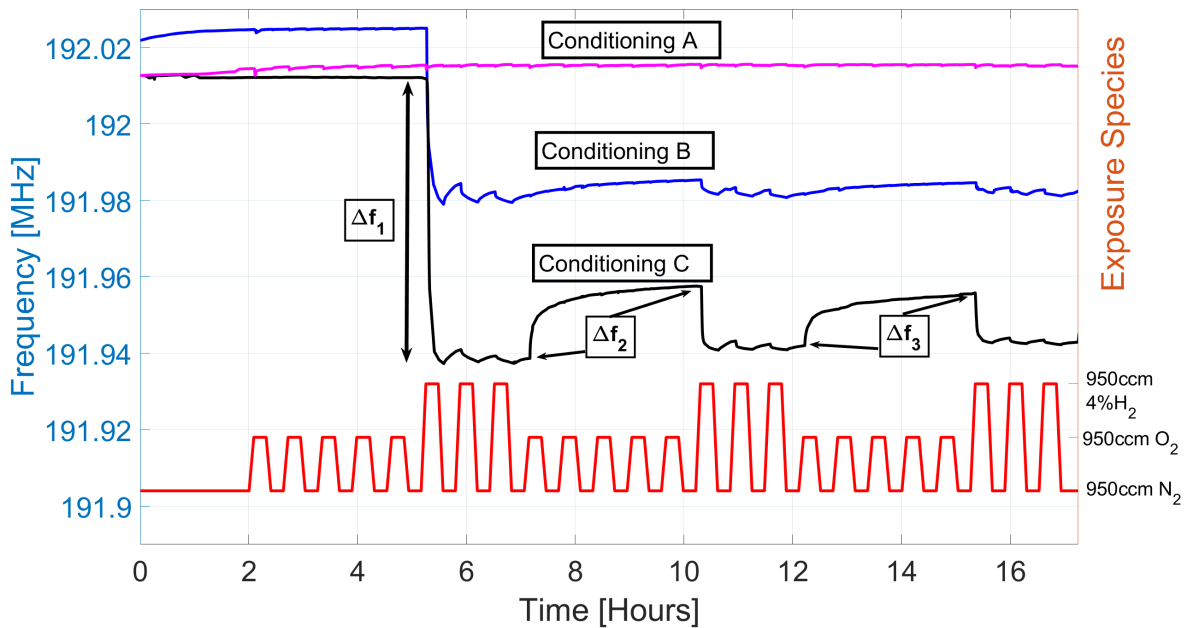


Figure 4.22. Setup A3 Device 3 (Film 2 Bare non-cycled 26.7°) Tracked Frequency at room temperature vs. Gas Exposure after Conditioning A, B and C (explained in the text) [116].

These results were additionally confirmed by XPS analysis performed by researchers Dr. John Baltrus and Dr. Paul Ohodnicki from the (NETL) at Pittsburgh, PA. Bare SAWR sensors employing Film 1 were sent to NETL. The XPS measurements were carried out with a PHI 5600ci instrument using monochromatic Al  $K\alpha$  X-rays. The pass energy of the analyzer was 23.5 eV and the scan step size was 0.1 eV. Binding energies were referenced to the Al 2s peak, which was assigned a binding energy of 119.5 eV. Charge neutralization was employed to minimize the effects of sample charging with the parameters for neutralization remaining constant over all samples. The stability of neutralization was confirmed by measuring the Na 1s peak (adventitious Na particles on the sample), which maintained a constant value of  $1072.56 \pm 0.04$  eV. Peak positions were measured by fitting the spectra using CasaXPS software. The samples were exposed to 20 minutes of either O<sub>2</sub>, N<sub>2</sub> or 10% H<sub>2</sub>/Ar gases at atmospheric pressure using a 30 sccm flow rate in a reaction chamber attached to the XPS instrument, which permitted XPS analysis after gas treatment without exposure to air. For conditioning at 600°C, the temperature was raised at a rate of 10°C/min up to the target temperature, then held for the designated time, before cooling back to room temperature, typically over a period of 1 hour. This procedure was aimed to mimic the conditioning and gas cycling performed on the SAWR sensors at UMaine. The results for conditioning in O<sub>2</sub> are shown in Figure 4.23. Figure 4.23 shows XPS Pt 4f<sub>7/2</sub> binding energies measured after exposure to different gas species immediately after the sample was conditioned at 600°C in oxidizing environment. The coordinate axis in Figure 4.23 shows the time during which the sample was exposed to the treatment in question (high-temperature conditioning or room temperature gas exposure). For the measurements, the sample was taken at the end of each gas exposure into vacuum for XPS analysis at room temperature. The highest Pt 4f<sub>7/2</sub> binding energies are measured after O<sub>2</sub> exposure while the lowest binding energies are measured after 10% H<sub>2</sub> exposure. The N<sub>2</sub> exposures generally result in intermediate Pt 4f<sub>7/2</sub> binding energies. The lowest Pt 4f<sub>7/2</sub> binding energy (70.9 eV) corresponds to Pt metal [116].

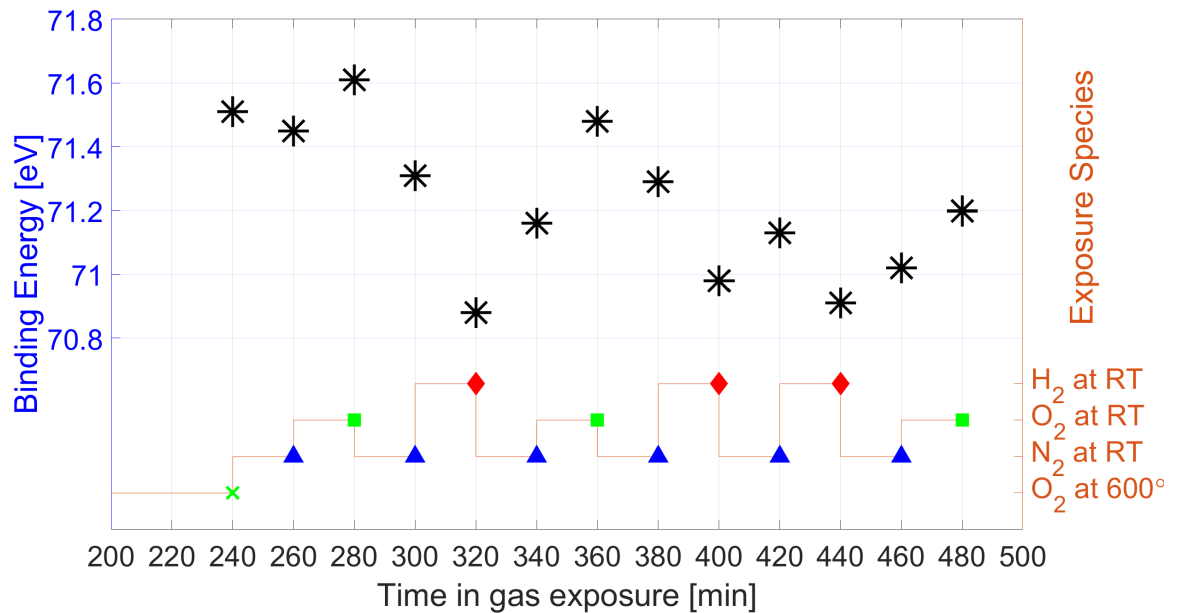


Figure 4.23. Pt  $4f_{7/2}$  binding energies after high-temperature oxidizing treatment. The cross indicates XPS analysis after the high-temperature treatment, the upward triangle indicates XPS analysis after room-temperature  $N_2$  exposure, the square indicates XPS analysis after room-temperature  $O_2$  exposure, and the diamond indicates XPS analysis after room-temperature  $H_2$  exposure [116].

The largest difference in Pt  $4f_{7/2}$  binding energies between an  $O_2$  and 10%  $H_2$  treatment in the series was measured upon the first 10%  $H_2$  exposure, where the XPS analysis showed that there was about a 0.7 eV difference in binding energies between the oxidized state (measured in the figure at the 280 minute-mark) and the reduced state (measured at the 320 minute-mark). This initial shift in binding energy corresponds to the initial shift in resonant frequency in Figure 4.22  $\Delta f_1$ . The subsequent periods in  $N_2$  and  $O_2$  caused an approximate 0.6 eV shift in binding energy (measured at the 360 minute-mark with respect to the 320 mark), showing that the previous oxidation state at 280 minute-mark was not fully achieved, consistent with the results for the SAWR sensors. The next reduction treatment (400 minute-mark) reported a shift in binding energy of about 0.5 eV, corresponding to the second frequency shift in Figure 4.22  $\Delta f_2$ . The measurements taken at the 440 minute-mark for the SAW experiments and exhibited a variation in binding energy of about 0.2 eV

with respect to the 420 minute-mark. The final oxidation period (measured at the 480 minute-mark) reported a 0.3 eV binding energy shift with respect to the last reduced state (440 minute-mark), corresponding to the lower achieved recovery after the second oxidation period in Figure 4.22 [116].

Additionally, conditioning in reducing environment was also conducted at 600°C and gas cycling was also performed. The results are shown in Figure 4.24. In this case, The initial oxidation state of the surface does not allow for subsequent shifts in binding energy using room-temperature O<sub>2</sub> treatments higher than 0.3 eV, consistent with the inoperable state of the SAWR sensor after this type of high-temperature conditioning [116].

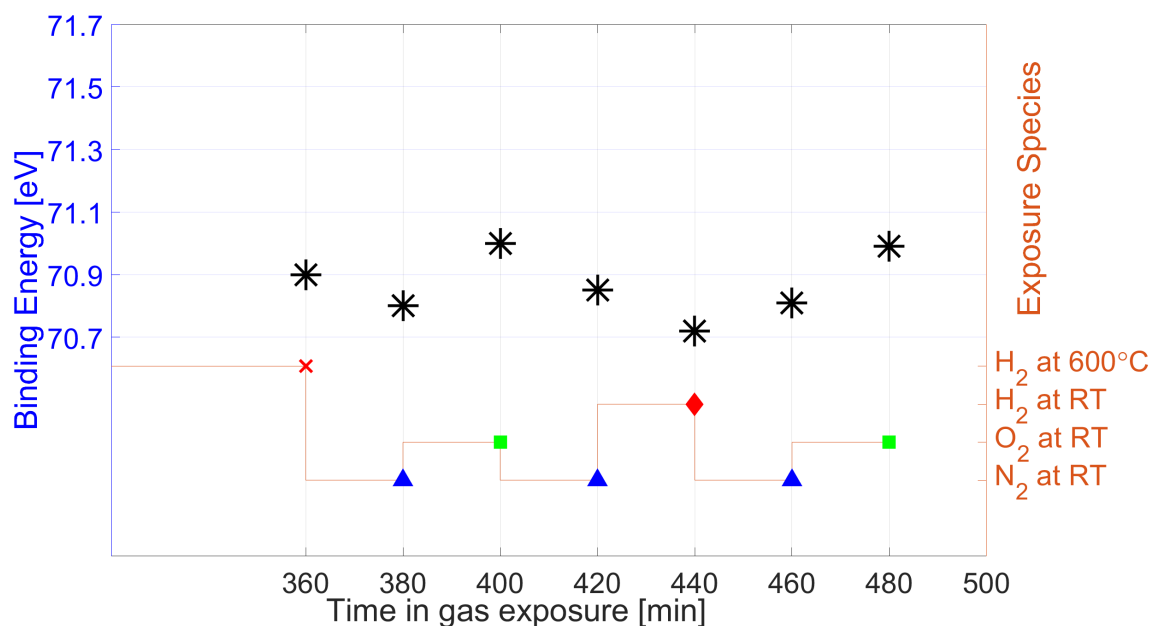


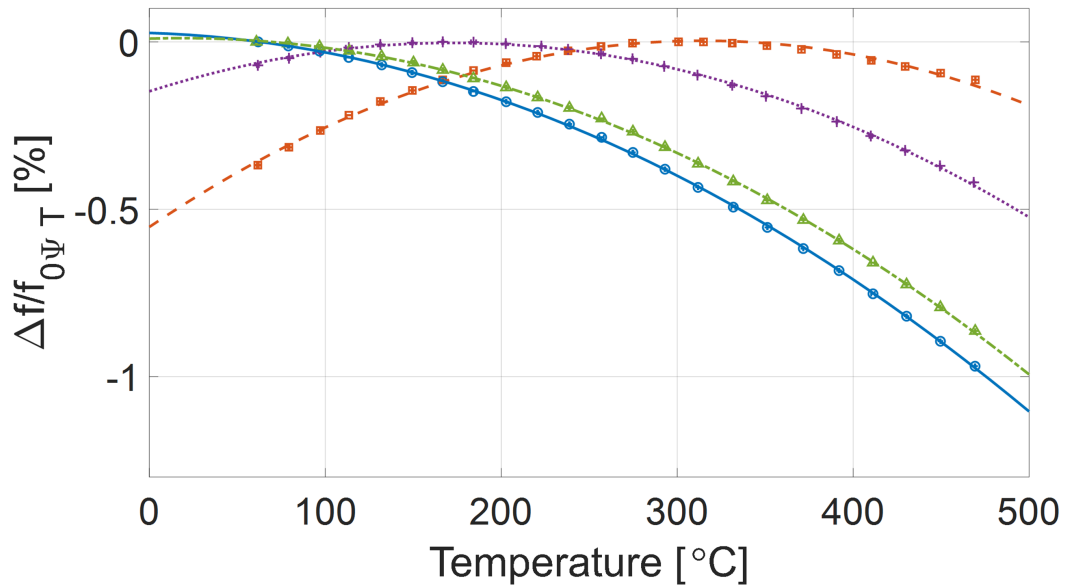
Figure 4.24. Pt 4f<sub>7/2</sub> binding energies after high-temperature reducing conditioning treatment. The cross indicates XPS analysis after the high-temperature treatment, the upward triangle indicates XPS analysis after room-temperature N<sub>2</sub> exposure, the square indicates XPS analysis after room-temperature O<sub>2</sub> exposure, and the diamond indicates XPS analysis after room-temperature H<sub>2</sub> exposure [116].

## 4.6 Influence of SAWR Sensor Orientation on H<sub>2</sub> Detection

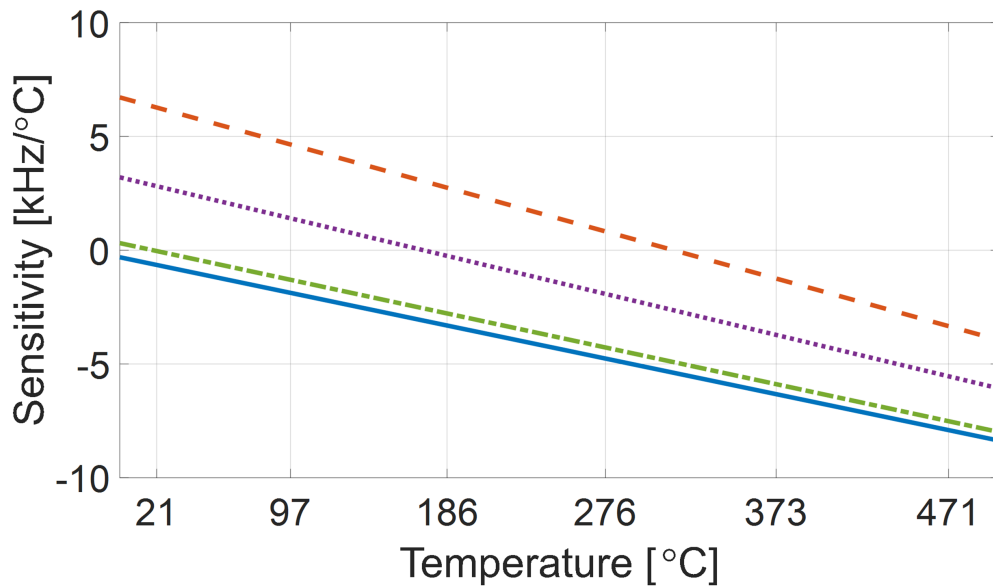
The SAWR sensor orientation was found to influence the magnitude of the frequency shifts observed due to introduction of H<sub>2</sub>. To test the influence of SAWR sensor orientation on H<sub>2</sub> detection, Setups A3, A6 and A7 were tested up to 500°C.

### 4.6.1 Extraction of Temperature Sensitivity up to 500°C in N<sub>2</sub> flow

The frequency dependency with temperature for the SAWRs mounted in Setup A3 (Device 1: Film 2 Bare non-cycled 77.7°; Device 2: Film 2 Bare non-cycled 14.7°; Device 3: Film 2 Bare non-cycled 26.7°; Device 4: Film 2 Bare non-cycled 32.7°) was obtained. This work was done to assess the influence of possible temperature variations or fluctuations in the gas readings. The SAWRs temperature dependence was extracted in a constant N<sub>2</sub> flow by subjecting the setup to increments of 20°C from 60°C to 480°C and held at temperature for 2 hours, while the sensors were interrogated every 5 minutes. The average resonant frequency at each temperature was taken after one hour had transpired giving 12 measurements per temperature step. A second degree polynomial approximation (parabolic) was used to extrapolate the results to the range between 0 and 500°C. Figure 4.25a plots the average data measured for the orientations used, normalized to the maximum measured value of frequency for that orientation  $f_{0\Psi T}$ . Figure 4.25b shows the respective temperature sensitivity curves calculated from the experimental results shown in Figure 4.25a [118].



a



b

Figure 4.25. a) Measured normalized frequency variation  $(f - f_{0\Psi T})/f_{0\Psi T}$  vs. temperature for the LGS orientations used and polynomial fit; b) calculated sensitivity. Device 1 (Film 2 Bare non-cycled  $77.7^\circ$ ): squares, dashed red line; Device 2 (Film 2 Bare non-cycled  $14.7^\circ$ ): crosses, dotted purple line; Device 3 (Film 2 Bare non-cycled  $26.7^\circ$ ): circles, solid blue line. Device 4 (Film 2 Bare non-cycled  $32.7^\circ$ ): triangles, dotted-dashed green line; The value of  $f_{0\Psi T}$  is 189.927, 191.075, 191.934, 191.465 MHz for Device 1-Device 4 respectively [118].

#### 4.6.2 Influence of Orientation on H<sub>2</sub> Detection up to 500°C

The devices in Setup A3 were tested at the following discrete furnace setup temperature: room temperature (no heating, furnace off), 100°C, 200°C, 300°C, 400°C, and 500°C. These values correspond to the following actual temperature in the chambers averaged from measurements by the TCs in both chambers throughout the entire test after reaching a stable temperature: 21°C, 91°C, 186°C, 276°C, 373°C and 471°C, respectively. The VNA settings were set to a frequency sweep of 10 MHz centered at 190 MHz with 2001 points and an IF bandwidth of 5kHz.

Figure 4.26 shows the results for Device 3 (Film 2 Bare non-cycled 26.7°). The test started with an initialization sequence consisting of N<sub>2</sub> flow while the setup reaches a stable temperature, and an initial oxidation period of three 20-min O<sub>2</sub> and N<sub>2</sub> cycles, followed by an hour period in N<sub>2</sub> as a purging period. Reduction periods consisted of four 20-min H<sub>2</sub> and four 20-min N<sub>2</sub> cycles followed by a 1-hour purging period in N<sub>2</sub>. Oxidation periods consisted of four 20-min O<sub>2</sub> and four 20-min N<sub>2</sub> cycles followed by an hour purging period in N<sub>2</sub>. The frequency shift labeled as  $\Delta f_1$  in Figure 4.26 is due to the first 20-min exposure to H<sub>2</sub> after the first oxidation period. Similarly,  $\Delta f_2$  was recorded after the second oxidation period. The resonant frequency at the end of the first 20-min exposure to H<sub>2</sub> after the first oxidation period (Feature  $\Delta f_1$ ) was adopted as the reference frequency for that test at that particular temperature and particular device [118]. The results for all devices and test temperatures are given in Appendix C in Section C.3.1.

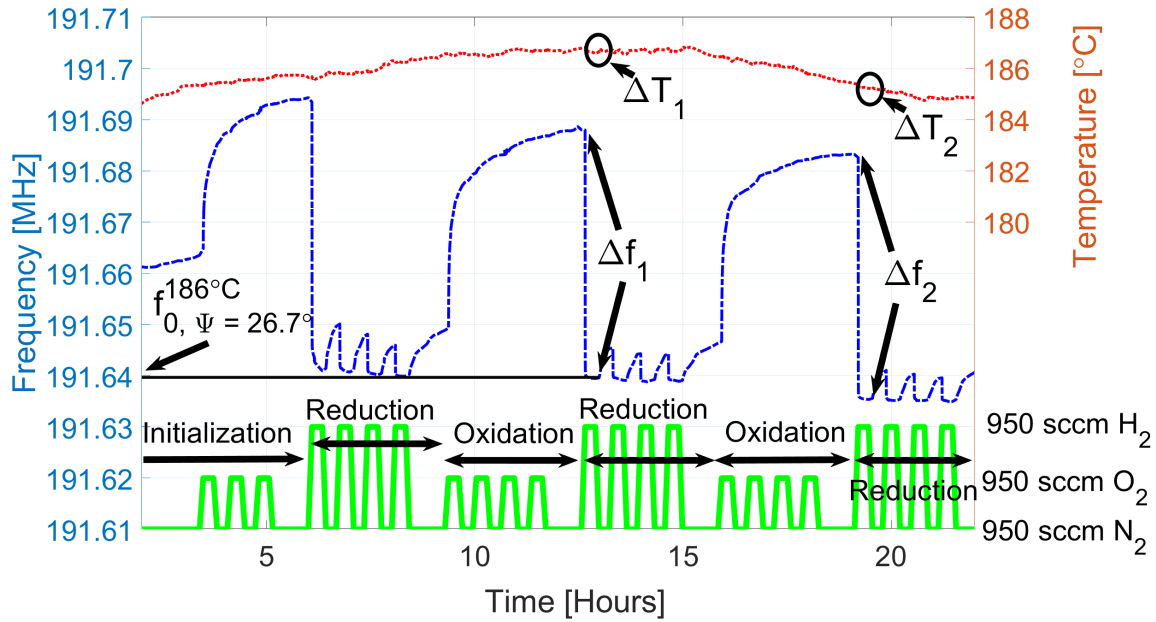


Figure 4.26. Setup A3 Device 3 (Film 2 Bare non-cycled 26.7° Film 2) Tracked Frequency at 186°C vs. Gas Exposure.

Figure 4.27 plots the average of  $\Delta f_1$  and  $\Delta f_2$  ( $\Delta f_i$ ) normalized by the respective resonant frequency  $f_{0i}$  as a function of temperature for the devices in Setup A3. The data points are connected for convenience and do not imply interpolation. There is a marked difference in frequency variation due to the insertion of  $H_2$  for the different orientations tested. From weaker to stronger frequency response to  $H_2$  the orientations can be ordered as:  $\Psi = 77.7^\circ$ ,  $\Psi = 14.7^\circ$ ,  $\Psi = 32.7^\circ$  and  $\Psi = 26.7^\circ$ . This order remained true from room temperature to the maximum temperature measured of 471°C. The data points at 471°C for Device 3 and Device 4 appear to have decreased considerably, while the data points for Device 1 and 2 remained the same from their values at 373°C, This may have been due to inconsistencies in the gas delivery system at this particular temperature for Chamber 2 (housing both Device 3 and Device 4).  $\Delta T_1$  and  $\Delta T_1$  shown in Figure 4.26, which represents the temperature variation due to the switching from the  $N_2$  gas to the 4% $H_2$  mixture, could compromise the frequency variation results due to exposure to  $H_2$  in Figure 4.27. The measured temperature variation by the TCs between the time the frequencies were measured to obtain the potential

change in fractional frequency that was dependent on this measured temperature variation. For the averaged measured temperatures 21°C, 91°C, 186°C, 276°C, 373°C and 471°C the respective maximum  $\Delta T_i$  were: -0.5°C, -0.3°C, -0.2°C, -0.4°C, -0.6°C, and -0.7°C. Using the sensitivity curve given in Figure 4.25, the maximum temperature induced frequency variation is also given in Appendix C. These frequency variations are smaller than the shapes used to plot Figure 4.27, and thus found to not significantly affect the conclusions established from Figure 4.27 in terms of the influence of the different orientations on the detection of H<sub>2</sub>.

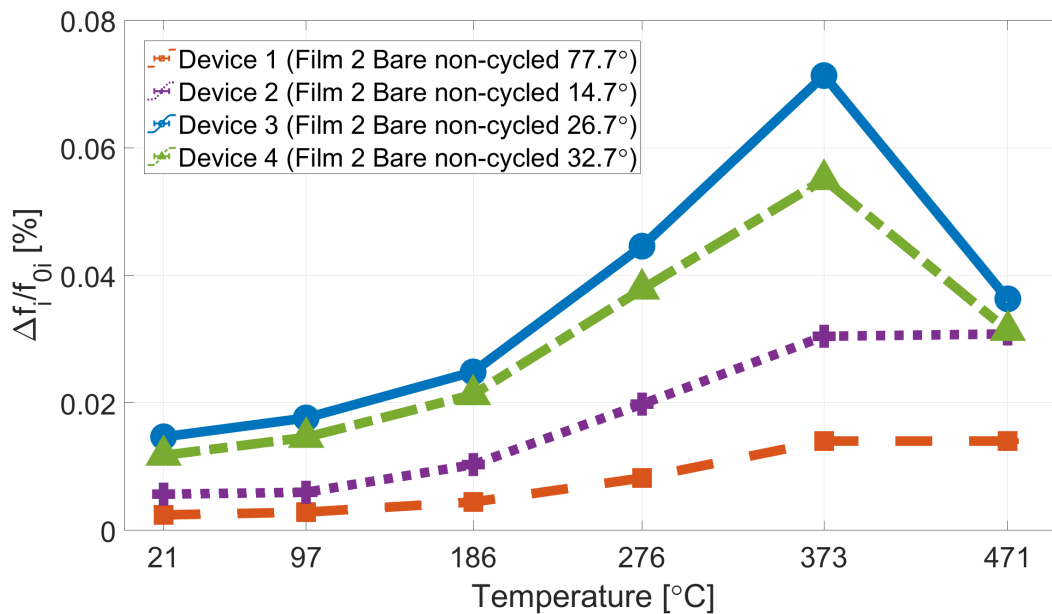


Figure 4.27. Setup A3 Measured relative frequency variation due to 4% H<sub>2</sub> exposure at the measured temperatures for: Device 1 (Film 2 Bare non-cycled 77.7°) (orange squares, dashed line); Device 2 (Film 2 Bare non-cycled 14.7°) (purple crosses); Device 3 (Film 2 Bare non-cycled 26.7°) (blue circles); Device 4 (Film 2 Bare non-cycled 32.7°) (green triangles). Data points are connected for convenience and do not imply interpolation.  $\Delta f_i$  and  $f_{0i}$  are given in Section C.3.1.

Based on the results of Figure 4.27, the magnitude of the frequency shifts due to introduction of H<sub>2</sub> seemed to be associated with  $K^2$  for each orientation (see Section 2.1), with the exceptions of orientations  $\Psi = 77.7^\circ$  and  $\Psi = 14.7^\circ$ , which have almost the same  $K^2$ . Setup A6 was tested to verify whether or not coupling coefficient plays an important role in the magnitude of frequency shifts due to the introduction of H<sub>2</sub>. Two devices oriented along  $\Psi = 20.7^\circ$  (Device 1, Film 1 Bare non-cycled 20.7° and Device 3, Film 1 Bare non-cycled 20.7°) were tested alongside a device oriented along  $\Psi = 26.7^\circ$  (Device 4, Film 1 Bare non-cycled 26.7°) and  $\Psi = 77.7^\circ$  (Device 2, Film 1 Bare non-cycled 77.7°), since, from Figure 2.1, the orientation  $\Psi = 20.7^\circ$  has a  $K^2$  value of 0.4%, compared to the  $K^2$  values of  $\Psi = 26.7^\circ$  and  $\Psi = 77.7^\circ$  of 0.3% and 0.15%, respectively. Setup A6 was tested using VNA settings of a frequency sweep of 10 MHz centered at 190 MHz with 5001 points (2 kHz frequency step) and an IF bandwidth of 2kHz, at the nominal furnace temperatures of 220°C, 320°C, 420°C and 525°C. The results for Device 4 (Film 1 Bare non-cycled 26.7°) at nominal furnace temperature of 220°C are shown in Figure 4.28. Four features were recorded for each test and each device. Feature A in Figure 4.28 corresponds to the first frequency shift due to H<sub>2</sub> introduction. Feature B corresponds to the frequency shift due to H<sub>2</sub> after a 1-hour purging period in N<sub>2</sub>. Feature C corresponds to the frequency shift due to H<sub>2</sub> after a 3-hour purging period in N<sub>2</sub>. Feature D corresponds to the frequency shift due to H<sub>2</sub> after a 1-hour oxidation period separated from reductions by a 1-hour N<sub>2</sub> period. The reference frequency for each device and temperature was chosen to be the last measurement at the end of the reducing period corresponding to Feature D. This was done because this is the only 4%H<sub>2</sub> exposure which immediately followed an oxidation period, as was the case with the results recorded for Figure 4.26. The results for each feature of all the tests conducted for Setup A6 are given in Appendix C in Section C.3.2. The temperature variation within any particular chamber for any particular test was less than  $\pm 2^\circ\text{C}$  from the average recorded up to 500°C, which is within the measurement accuracy of the TCs [119].

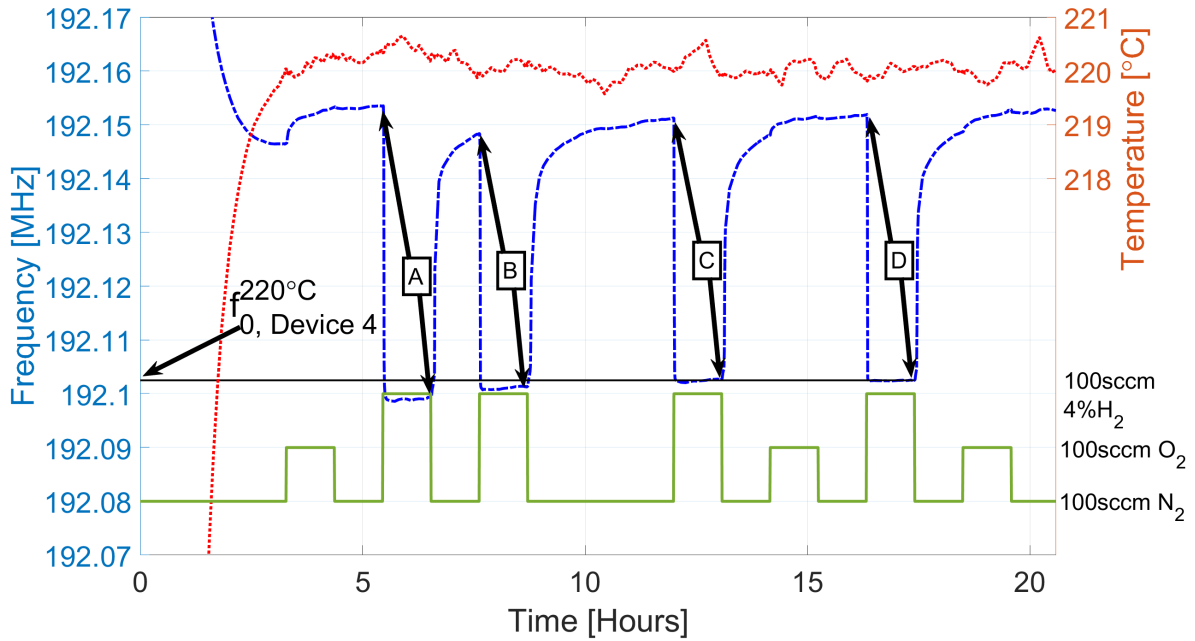


Figure 4.28. Setup A6 Device 4 (Film 1 Bare non-cycled  $26.7^\circ$ ) Tracked Frequency at  $220^\circ\text{C}$  vs. Gas Exposure.

The frequency shifts associated with Feature D for each device ( $\Delta f_{Di}$ ) were normalized to the reference frequency  $f_{0i}$  defined as the last frequency measurement associated with Feature D, and the resulting values are plotted with respect to temperature in Figure 4.29. The data points are connected for convenience and do not imply interpolation. The relative frequency variations measured for the device oriented along  $\Psi = 26.7^\circ$  and for the devices oriented along  $\Psi = 20.7^\circ$  were comparable at all temperatures (within 0.01%), which suggested that coupling coefficient may not be the only parameter responsible for the differences in observed frequency shifts due to the introduction of  $\text{H}_2$ . Other possible parameters determining the magnitude of frequency shifts due to the introduction of  $\text{H}_2$  to be considered in future studies are: strip reflection coefficient, diffraction, and bulk irradiation.

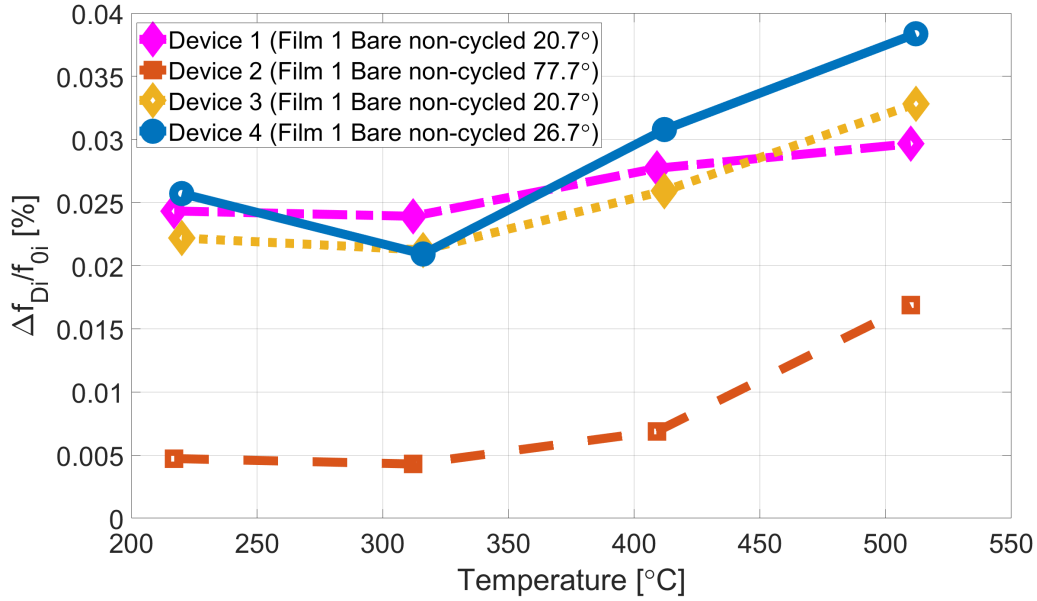


Figure 4.29. Setup A6 Measured relative frequency variation due to 4% $H_2$  exposure at the measured temperatures for: Device 1 (Film 1 Bare non-cycled 20.7°) (pink diamonds, dashed-dotted line); Device 2 (Film 1 Bare non-cycled 77.7°) (orange squares, dashed line); Device 3 (Film 1 Bare non-cycled 20.7°) (yellow diamonds, dotted line); Device 4 (Film 1 Bare non-cycled 26.7°) (blue circles, solid line). Data points are connected for convenience and do not imply interpolation.  $\Delta f_{D_i}$  and  $f_{0_i}$  are given in Section C.3.2.

Setup A7 tested Bare devices oriented along  $\Psi = 26.7^\circ$  (Device 1: Film 1 Bare cycled 26.7°, and Device 3: Film 1 Bare cycled 26.7°) and  $\Psi = 77.7^\circ$  (Device 2: Film 1 Bare cycled 77.7°, and Device 4: Film 1 Bare cycled 77.7°) employing Film 1 as electrodes and reflectors that had been previously been cycled using Profile 1 in an alumina crucible. These orientations had not been previously tested in the same chamber and it was desired to characterize them in the same environment, since they presented the largest difference in response due to the introduction of 4% $H_2$ . Setup A7 was tested using VNA settings of a frequency sweep of 10 MHz centered at 190 MHz with 5001 points (2 kHz frequency step) and an IF bandwidth of 2kHz, at the nominal furnace temperatures from 100°C to 500°C in 50 °C increments. The results for Device 1 (Film 1 Bare cycled 26.7°) at nominal furnace temperature of 300°C are shown in Figure 4.30. All gases were delivered using 100 sccm flow rate. The exposure profile consisted of 3 hours in  $N_2$  to allow for cooling, an oxidation

period consisting of 2 hours in O<sub>2</sub> and 2 hours in N<sub>2</sub>, the two reductions of one hour in 4%H<sub>2</sub> separated by a N<sub>2</sub> purging period 3 hours long. The temperature measured by the witness TC in the corresponding chamber was averaged for a four hour period starting 1.5 hours before the 1st reduction and ending 1.5 hours after the end of the 1st reduction and considering the one hour reduction in H<sub>2</sub> exposure. The largest standard deviation measured for this time range across all temperatures was less than 0.3°C, which was recorded at the nominal furnace temperature of 150°C in chamber 1. Two frequency values were obtained for each device at each test and labeled as  $f_{NiT_j}$  and  $f_{HiT_j}$  corresponding to the average of the 10 measurements obtained immediately prior to the beginning of the 1st reduction and immediately prior to the end of the 1st reduction. The standard deviation of these measurements was less than 1 kHz in all cases. The compiled results for all sensors and values for acquired data are given in Appendix C in Section C.3.3.

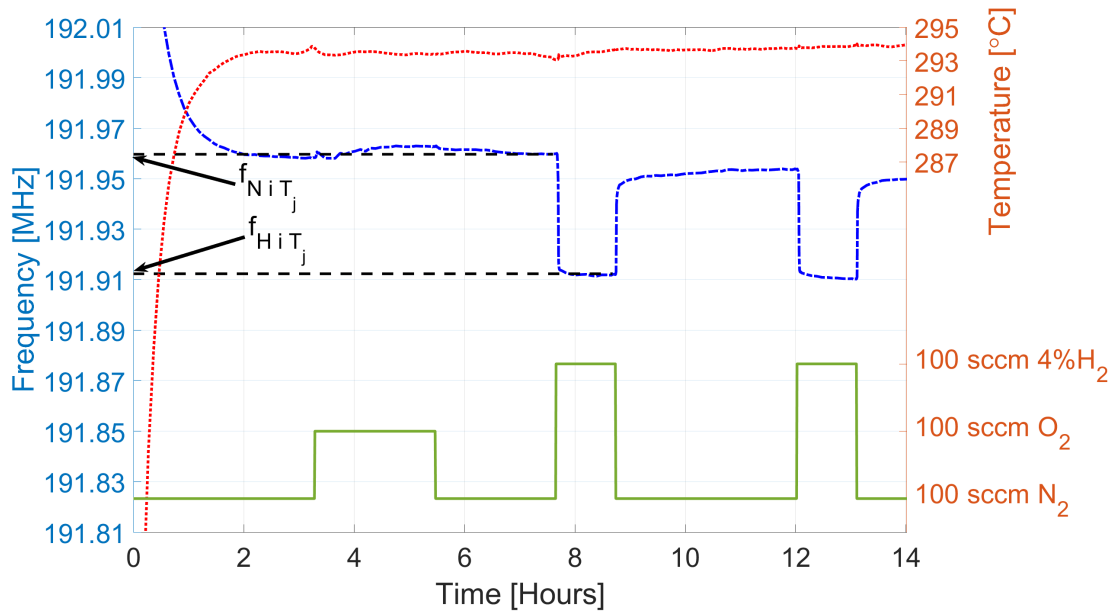


Figure 4.30. Setup A7 Device 1 (Film 1 Bare cycled 26.7°) Tracked Frequency at 294°C vs. Gas Exposure.

The average and standard deviation values temperature for the chamber, the recorded average value  $f_{NiT_j}$  and  $f_{HiT_j}$  and the magnitude of the frequency shift from  $f_{NiT_j}$  to  $f_{HiT_j}$  defined as  $\Delta f_i$  are given in Appendix C in Section C.3.3. At the nominal furnace

temperatures of 400 and 500°C, a data acquisition error did not allow for the interrogation of Device 3 at those temperatures. The values of  $\Delta f_i$  were normalized with respect to the corresponding value of  $f_{HiT_j}$  and the results for each device are shown in Figure 4.31. The standard deviation both in frequency and in temperature are smaller than the shapes used to plot the results. The data points are connected for convenience but do not imply interpolation between the data points. A dotted line was used to connect the data points of devices in Chamber 1 (Device 1 with blue circles and Device 2 with orange squares), and dashed line was used to connect the data points of devices in Chamber 2 (Device 3 with yellow circles and Device 4 with purple squares). The results confirmed a difference in the magnitude of the frequency shift due to 4% $H_2$  of at least 0.015% between devices oriented along  $\Psi = 26.7^\circ$  and  $\Psi = 77.7^\circ$ . Also notable from the results is that there is decrease in relative frequency shifts in the temperature range from 200°C to 350°C when compared to the shifts recorded from 100°C to 200°C, after which an increase in relative frequency shifts is observed for all devices above 400°C.

#### 4.7 Film 1 vs. Film 2 SAW Gas Sensor Performance

Figure 4.32 shows the fractional frequency change due to the introduction of 4% $H_2$  for all Bare devices oriented along  $\Psi = 26.7^\circ$ . Figure 4.32 shows that the SAWR sensor response for devices employing Film 2 that had not been previously cycled were 0.04% larger in the temperature range from 250°C to 400°C than Devices employing Film 1, both previously cycled and non-cycled.

Setup A5 was used to compare the SAWR sensor performance of Bare devices oriented along  $\Psi = 14.7^\circ$  previously cycled employing Film 1 (Device 3 and 4) and Film 2 (Device 1 and 2) at 200°C, 300°C, 400°C, 500°C and 600°C, resulting in the highest temperature for which successful  $H_2$  detection was observed during this work. The VNA settings were set to 5001 points, 5 MHz span centered at 192.5 MHz with IF bandwidth of 1 kHz. Before each test, the entire setup was heated to 650°C in 100 sccm  $N_2$  flow, switched to 100 sccm

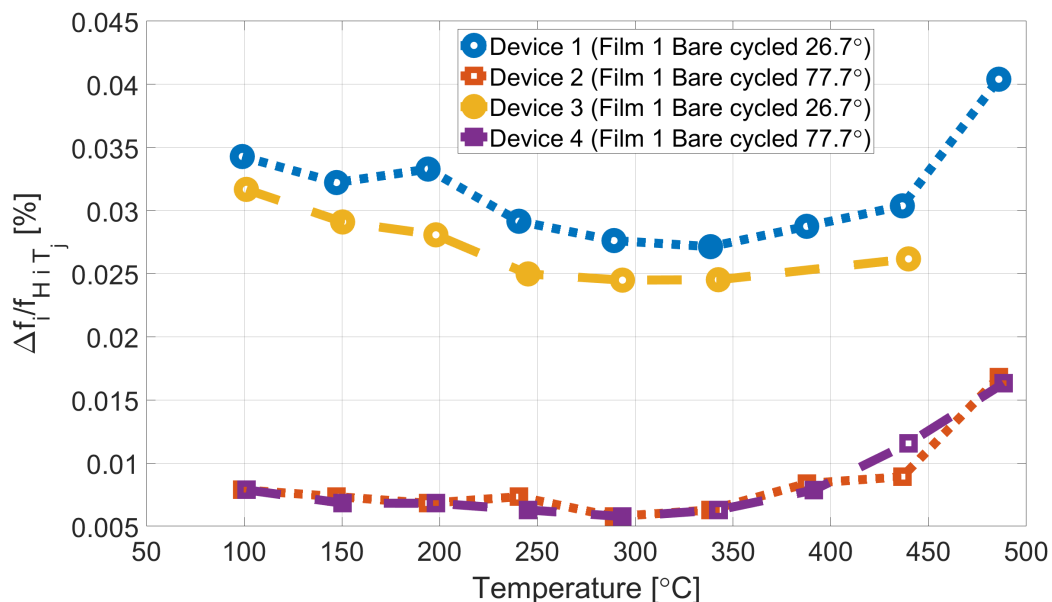


Figure 4.31. Fractional frequency shift due to 4% $H_2$  exposure for Devices 1-4 at the temperatures measured. Data points are connected for convenience and do not imply interpolation. Device 1 (Film 1 Bare cycled 26.7°) blue circles connected with dotted line; Device 2 (Film 1 Bare cycled 77.7°) orange squares connected dotted line; Device 3 (Film 1 Bare cycled 26.7°) yellow circles connected with dashed line; Device 4 (Film 1 Bare cycled 14.7°) purple squares connected with dashed line.

of  $O_2$  flow for three hours and allowed to cool to the test temperature in 100 sccm  $O_2$  flow, at which point gas cycling at the temperature was conducted. Example result at 213°C for Device 1 (Film 2 Bare cycled 14.7° are shown in Figure 4.33. For these tests, gases were delivered with 100 sccm flow and the gas delivery profile consisted of 1-hour reduction periods in  $H_2$  followed by 1-hour, 2-hour and 3-hour purging periods in  $N_2$ , and oxidation periods with 1-hour and 2-hour 100 sccm of  $O_2$  flow with 1-hour  $N_2$  purging periods separating the oxidation from the reductions. Six frequency shifts were noted. Feature A in Figure 4.33 corresponds to the first frequency shift due to  $H_2$  introduction. Feature B corresponds to the frequency shift due to  $H_2$  after a 1-hour purging period in  $N_2$ . Feature C corresponds to the frequency shift due to  $H_2$  after a 2-hour purging period in  $N_2$ . Feature D corresponds to the frequency shift due to  $H_2$  after a 2-hour purging period in  $N_2$ . Feature E corresponds to the frequency shift due to  $H_2$  after a 1-hour oxidation period separated from reductions by

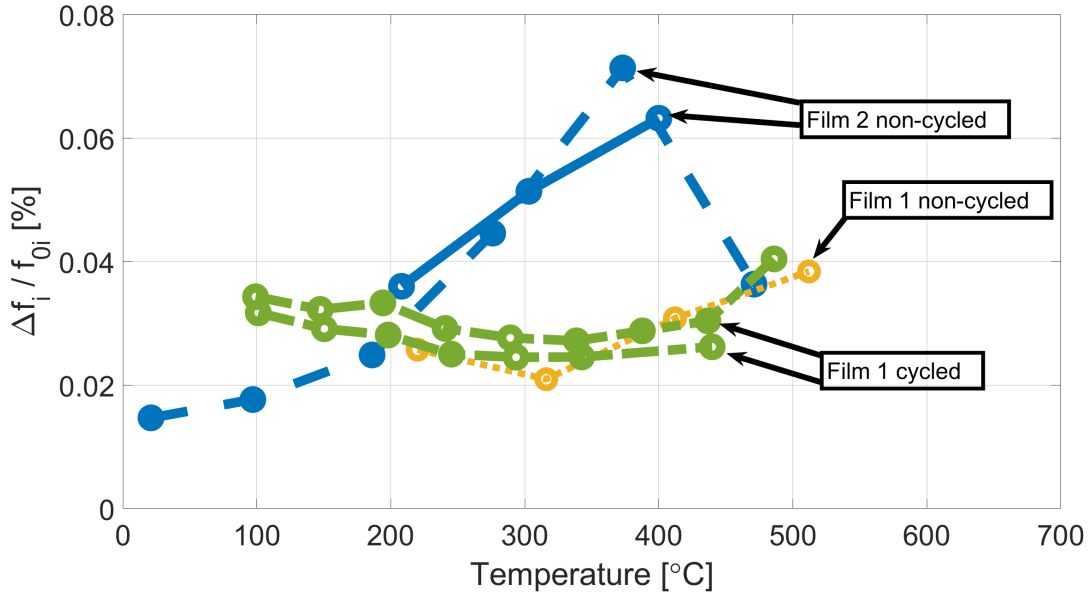


Figure 4.32. Fractional frequency shift due to 4% $H_2$  exposure for all Bare devices oriented along  $\Psi = 26.7^\circ$  at the temperatures measured. Data points are connected for convenience and do not imply interpolation. Solid blue line: Film 2 Bare non-cycled  $26.7^\circ$  (Device 4 in Setup A4); dashed blue line: Film 2 Bare non-cycled  $26.7^\circ$  (Device 3 in Setup A3); dotted yellow line: Film 1 Bare non-cycled  $26.7^\circ$  (Device 4 in Setup A6); dashed-dotted green lines: Film 1 Bare cycled (Device 1 and Device 3 from Setup A7). The corresponding  $\Delta f_i$  and  $f_{0i}$  are defined in the corresponding result section for each setup.

a 1-hour  $N_2$  period. Feature F corresponds to the frequency shift due to  $H_2$  after a 2-hour oxidation period separated from reductions by a 1-hour  $N_2$  period.

The results for all sensors at all temperature for these tests are tabulated in Appendix C in Table C.6. The temperature variation within any particular chamber for any particular test was less than  $\pm 2^\circ C$  from the average recorded up to  $500^\circ C$ , which is within the measurement accuracy of the TCs [119]. The frequency shifts related to Feature A were consistently 15%-35% higher than subsequent frequency shifts, which is related to the high-temperature conditioning performed before the test. This was due to the high-temperature oxygen conditioning at  $650^\circ C$  before the tests. This phenomenon was studied at room temperature and was explored in Section 4.5. A reference frequency  $f_{0i}$  for each device at each test temperature was defined as the last measured frequency at the end of Feature F. The average

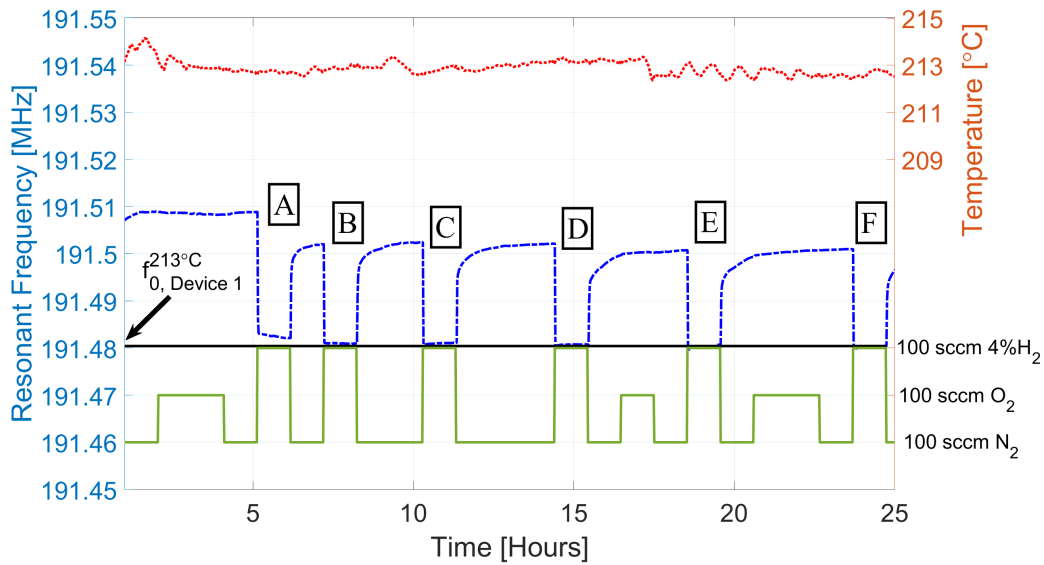


Figure 4.33. Setup A5 Device 1 (Film 2 Bare cycled 14.7°) Tracked Frequency at 213°C vs. Gas Exposure.

of the frequency shifts associated with Features E and F were taken ( $\Delta f_i$ ) and normalized to  $f_{0i}$ . This was done because these features were oxidized prior to the H<sub>2</sub> exposure. These results are plotted in Figure 4.34, where the data points have been connected convenience and do not imply interpolation. Additionally, the results for Device 2 from Setup A3 (Film 2 Bare non-cycled 14.7°) are also plotted in Figure 4.34. At 500°C, the response for Device 2 from Setup A5 (Bare Film 2 cycled 14.7°) was compromised, most likely due to the beginning of a malfunction in electrical connection, and at 600°C the response for Device 2 was untraceable, likely due to failure in the 1 mil Pt connection. These results revealed that the recorded fractional frequency shifts recorded near 300°C and 400°C for the Film 2 Bare cycled devices were not significantly higher than Film 1 Bare cycled devices, whereas the fractional frequency shifts due to H<sub>2</sub> for Film 2 Bare non-cycled devices around those temperatures were higher than the other measured devices, suggesting that the observation made from Figure 4.32 of higher sensor response to 4%H<sub>2</sub> exposures in the temperature range from 250°C to 400°C for Film 2 Bare devices only holds for non-cycled devices. At 600°C, the frequency shifts for Device 1 were higher than the recorded shifts for Device 3 and Device

4, and it was noted that the results at 600°C decreased with respect to the results acquired at 500°C.

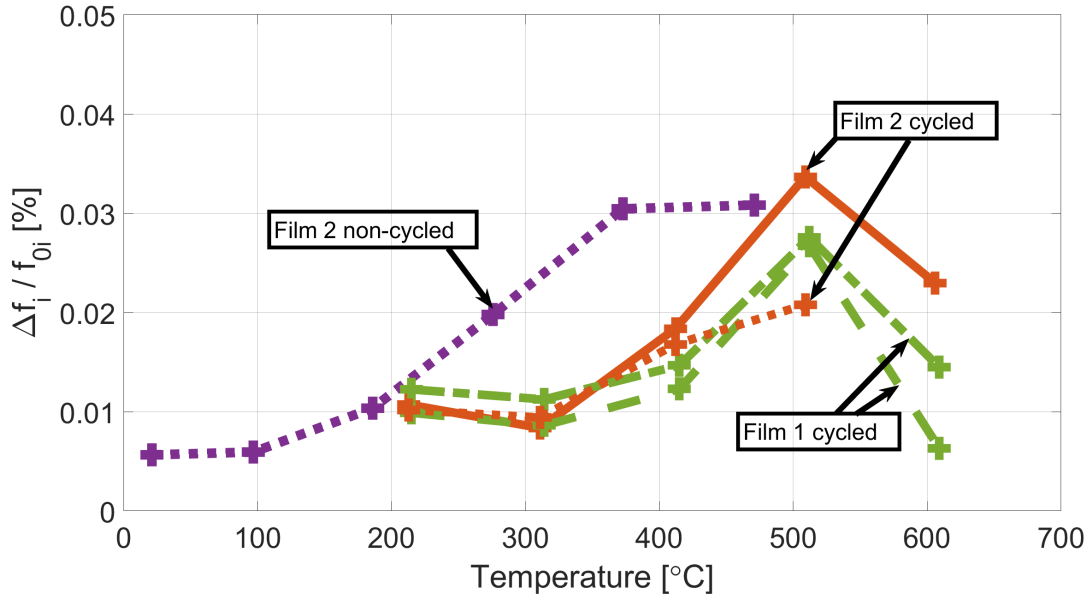


Figure 4.34. Setup A5 (all devices) and Setup A3 (Device 2, Film 2 Bare non-cycled 14.7°) Measured relative frequency variation due to H<sub>2</sub> exposure at the measured temperatures for: Setup A5 Device 1 (Film 2 Bare cycled 14.7°) orange crosses, solid line; Setup A5 Device 2 (Film 2 Bare cycled 14.7°) orange crosses, dotted line; Setup A5 Device 3 (Film 1 Bare cycled 14.7°) green crosses, dashed-dotted line; Setup A5 Device 4 (Film 1 Bare cycled 14.7°) green crosses, dashed line; Setup A3 Device 2 (Film 2 Bare non-cycled 14.7°) purple crosses, dashed line.  $\Delta f_i$  and  $f_{0i}$  are given in Appendix C.

#### 4.8 Multi-sensor System Analysis

The results obtained from Setup A7 (end of Section 4.6) were used to verify the feasibility of a two-sensor system as outlined in Section 1.6. For convenience, Equation 1.14 is repeated here:

$$f_{\Psi} \approx R_{\Psi}^{N_2}(T) + S_{\Psi}(T) \times G, \quad (4.2)$$

where  $R_{\Psi}^{N_2}(T)$  is the temperature dependence of the frequency assuming a N<sub>2</sub> baseline, and  $S_{\Psi}(T) \times G$  is a frequency shift due to the introduction of 4% H<sub>2</sub> with respect to the N<sub>2</sub>

baseline, where  $G = 1$  represents the presence of  $H_2$ . The  $R_{\Psi}^{N_2}(T)$  and the  $S_{\Psi}(T)$  term have been experimentally determined for the two sensors oriented along  $\Psi = 26.7^\circ$  and  $\Psi = 77.7^\circ$ .

The fractional frequency changes relative to the highest measured frequency value of  $f_{NiT_j}$ , defined as  $f_{0maxi}$ , were taken for Device 1 and Device 2 ( $f_{0max1} = 192.600MHz$  at  $99^\circ C$  for Device 1 and  $f_{0max2} = 190.834MHz$  at  $289^\circ C$  for Device 2, as shown in Table C.5). The normalized fractional frequency variation under both nitrogen and hydrogen is defined as:

$$\Delta F_{nomr,i} = \frac{\Delta f_{totali}}{f_{0maxi}} = 100 \times \frac{f_{NiT_j \text{ or } HiT_j} - f_{0maxi}}{f_{0maxi}} [\%]. \quad (4.3)$$

The results are shown in Figure 4.35, where parabolic fitting has been used to interpolate the values both under  $N_2$  and under  $H_2$  for Device 1 and Device 2. The parabolic fitting had R2 values of 0.9998 for Device 1 under  $N_2$ , 0.9999 for Device 1 under  $H_2$ , 0.9889 for Device 2 under  $N_2$  and 0.9913 for Device 2 under  $H_2$ . In this temperature range, the  $S_{\Psi}(T)$  for both sensors were sufficiently constant across the temperature range to allow for polynomial approximation of both the  $G = 0$  and  $G = 1$  case.

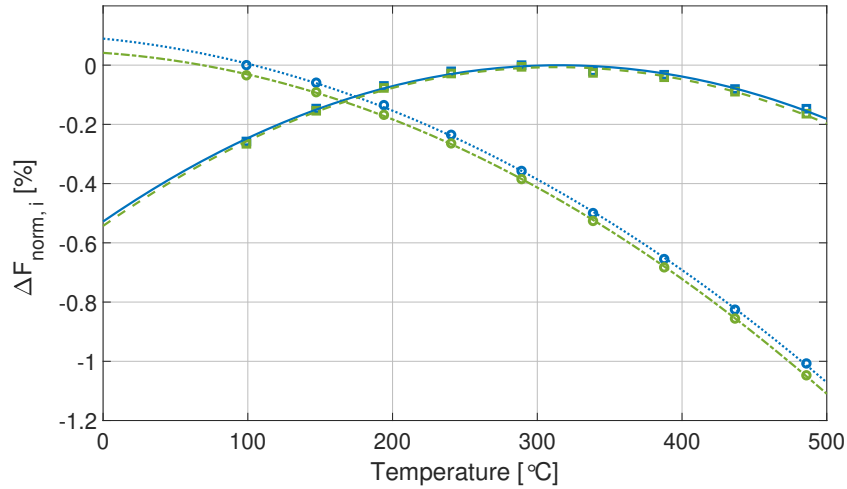


Figure 4.35. Fractional frequency change with respect to the maximum value of frequency recorded  $f_{0maxi}$  for Device 1 (Film 1 Bare cycled  $26.7^\circ$ ) and Device 2 (Film 1 Bare cycled  $77.7^\circ$ ) (both devices in Chamber 1). Data points are connected via parabolic fitting.

Device 1 under  $N_2$ : blue circles, dotted line; Device 1 under  $H_2$ : green circles, dashed-dotted line; Device 2 under  $N_2$ : blue squares, solid line; Device 2 under  $H_2$ : green squares, dotted line. Values of  $f_{0maxi}$  are given in Appendix C in Section C.3.3.

The difference  $\Delta F_{norm,1} - \Delta F_{norm,2}$  between Device 1 and Device 2 under both N<sub>2</sub> and H<sub>2</sub> is shown in Figure 4.36. As can be seen from Figure 4.36, the difference between the frequency readouts of the devices is approximately linear in this temperature range.

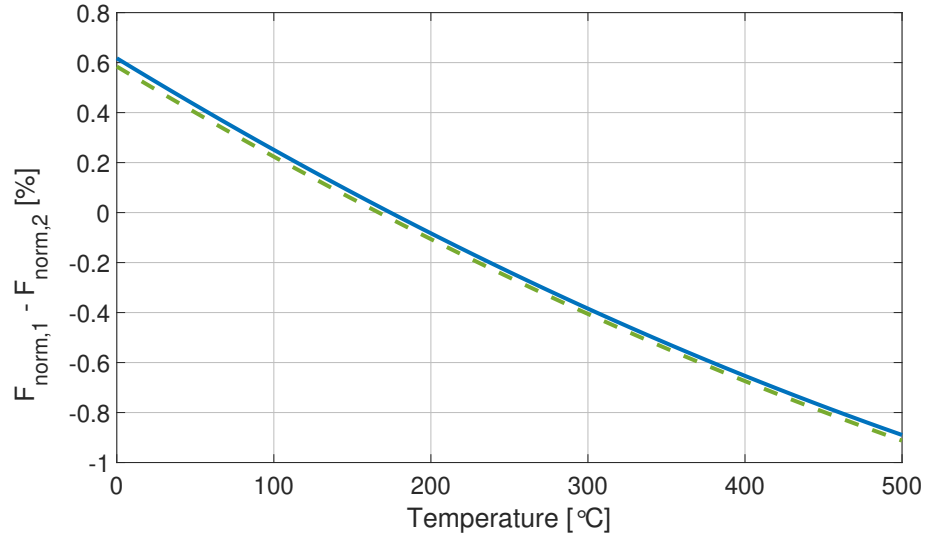


Figure 4.36. Values of  $\Delta F_{norm,1} - \Delta F_{norm,2}$  (defined in the text) as a function of temperature. Solid blue curve is under N<sub>2</sub>, dashed green curve is under H<sub>2</sub>.

A zoomed-in portion into the region around 270°C from Figure 4.36 is shown below in Figure 4.37. For a difference  $\Delta F_{norm,1} - \Delta F_{norm,2}$  of between the two devices of 0.3%, there are two possible temperatures for which this readout could be interpreted: 263°C and 271°C, whose difference is shown in the figure as  $\Delta T$ , depending on whether there is H<sub>2</sub> presence or not, respectively. The difference between these two temperatures is shown in the figure as  $\Delta T$ . A zoomed-in plot around 270°C from Figure 4.35 is shown in Figure 4.38, relating the two possible temperature identified in Figure 4.37 with four possible values for  $\Delta F_{norm,1}$ , identified in Figure 4.38 as 1 to 4. For a  $\Delta F_{norm,1}$  sensor reading of 0.293%, corresponding to Point 1, the temperature is determined to be 263°C in N<sub>2</sub> environment. For a  $\Delta F_{norm,1}$  reading of 0.311%, corresponding to Point 2, the temperature is determined to be 271°C in N<sub>2</sub> environment. For a  $\Delta F_{norm,1}$  reading of 0.321%, corresponding to Point 3, the temperature is determined to be 263°C in H<sub>2</sub> environment. For a  $\Delta F_{norm,1}$  reading of 0.338%, corresponding to Point 4, the temperature is determined to be 271°C in H<sub>2</sub>

environment. The difference between Points 2 and 3, which are the closest possible  $\Delta F_{norm,1}$  readings out of the four possible values of  $\Delta F_{norm,1}$  is equal to 0.01%. This difference corresponds to approximately 19kHz for a normalization value of  $f_{0max1} = 192.600\text{MHz}$ , which is detectable using the current methods of interrogation.

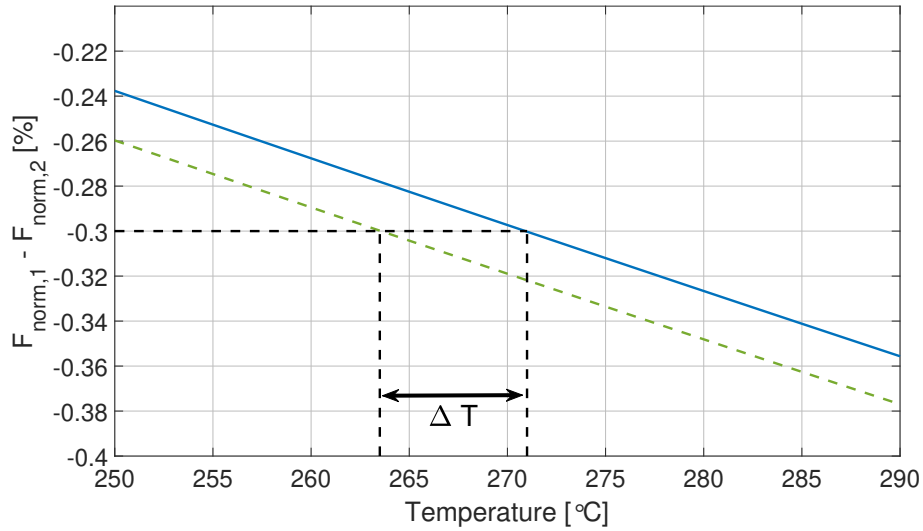


Figure 4.37. Zoomed-in section of resulting  $\Delta F_{norm,1} - \Delta F_{norm,2}$  values around 270°C. Solid blue curve is under  $N_2$ , dashed green curve is under  $H_2$ .

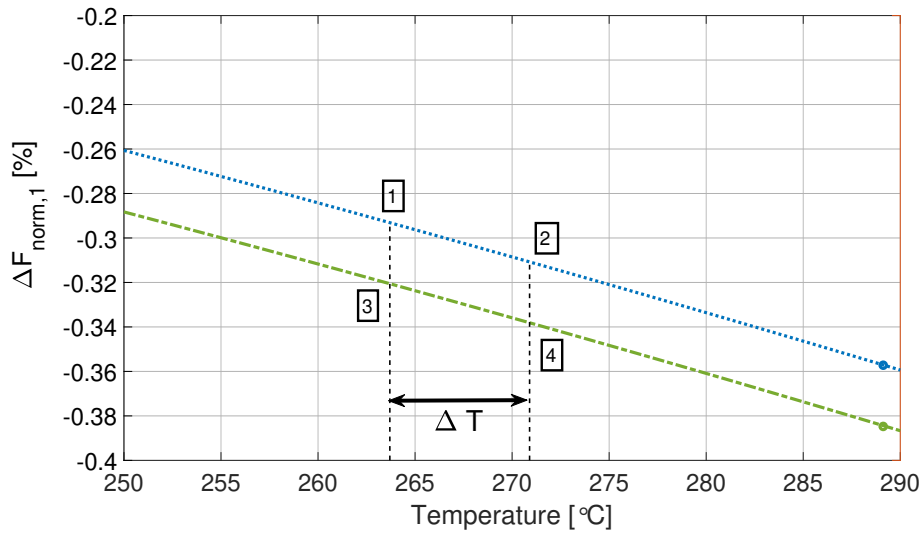


Figure 4.38. Zoomed-in portion around 270°C of fractional frequency values for Device 1 (Figure 4.34). Dotted blue curve is under  $N_2$ , dotted-dashed green curve is under  $H_2$ .

## 4.9 Wireless Interrogation

The test setup described in Section 3.4 was tested at 400°C and 500°C using VNA settings of 10,001 points, 40 MHz span centered at 190 MHz and IF bandwidth of 1 kHz; and 400°C with VNA settings of 10,001 points, 10 MHz span centered at 191 MHz and IF bandwidth of 1 kHz. The gas exposure used consisted of 5 hours in N<sub>2</sub>; followed by a two-hour period in O<sub>2</sub> followed by a two-hour period in N<sub>2</sub> to allow for device oxidation at the test temperature; and two 1-hour periods in 4%H<sub>2</sub> separated by a three-hour purging period in N<sub>2</sub>. Time-gating was performed from 0.6 μs to 5 μs on the acquired frequency spectra. A moving-average filter was applied to the presented data. The results for the 40 MHz bandwidth measurements are shown in Figures 4.39 and 4.40 for 400°C and 500°C nominal furnace temperature, respectively; and the results for the 10 MHz bandwidth at 400°C nominal furnace temperature are shown in Figure 4.41.

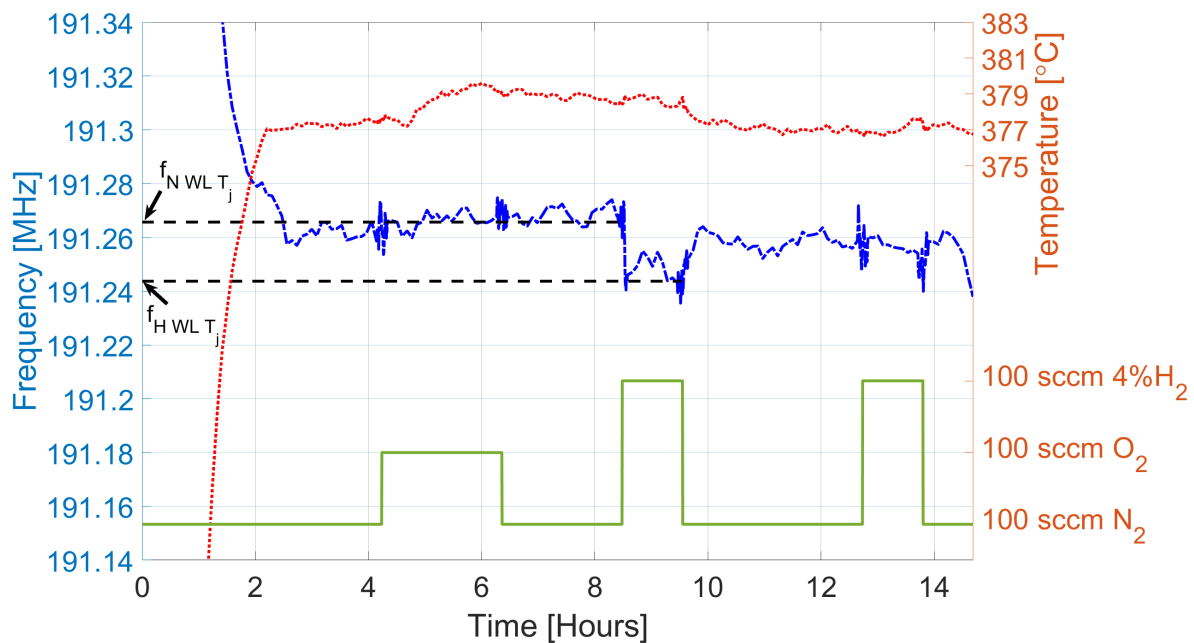


Figure 4.39. Wireless test results analysis at 378°C using 40 MHz bandwidth.

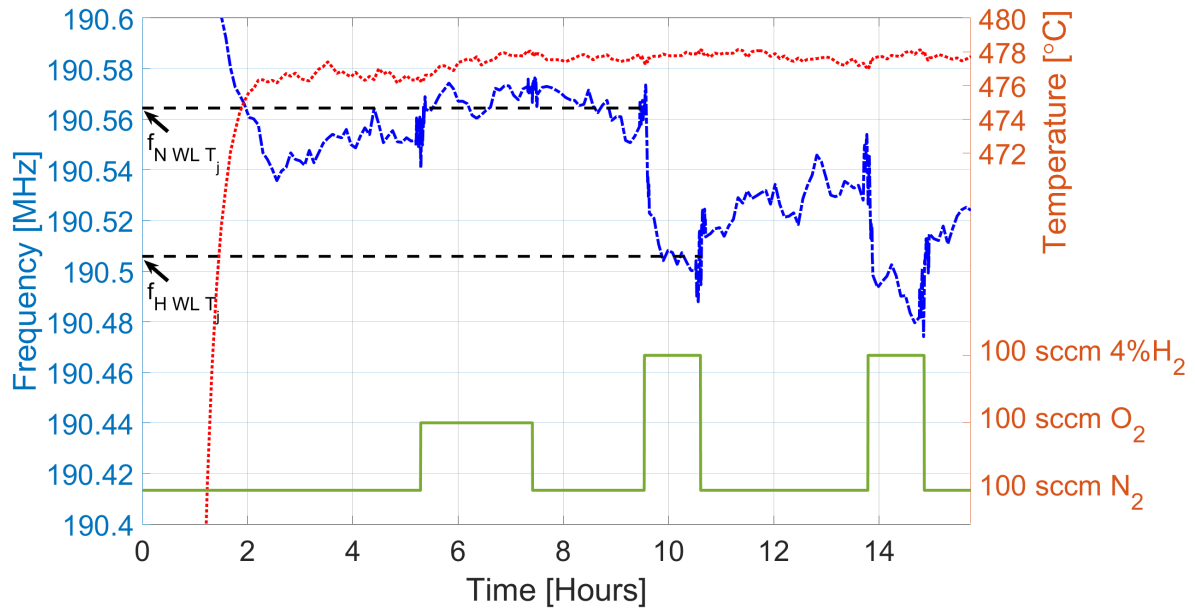


Figure 4.40. Wireless test results analysis at 478°C using 40 MHz bandwidth.

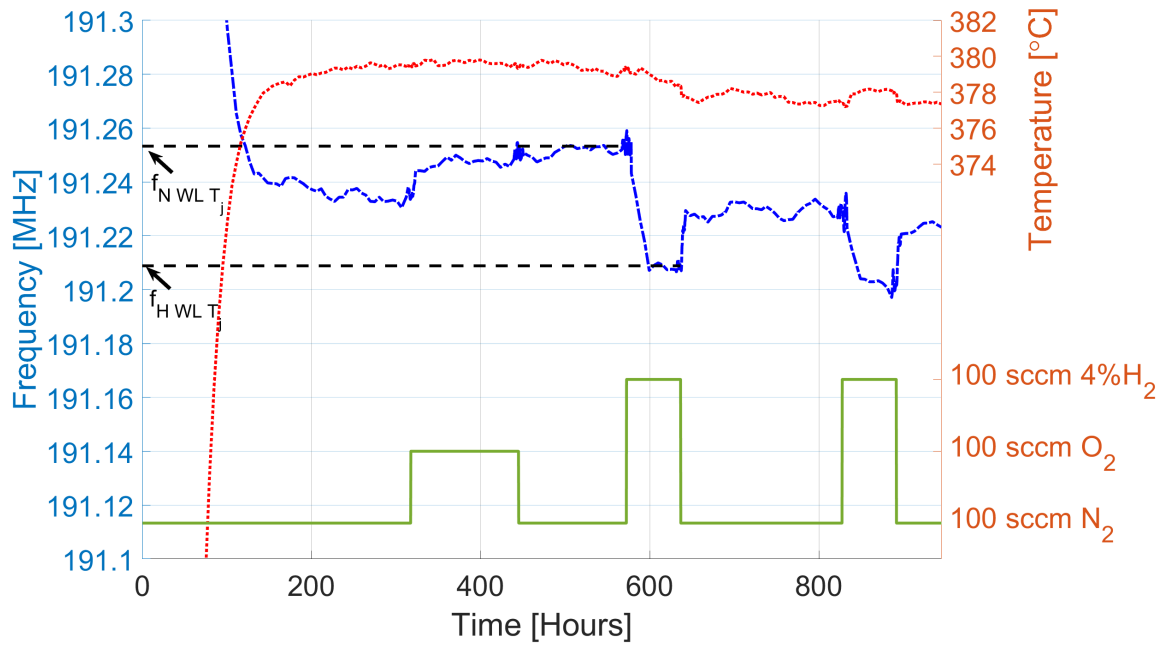


Figure 4.41. Wireless test results analysis at 379°C using 10 MHz bandwidth.

The average temperature and standard deviation in temperature during a 4-hour period starting 1.5 hour prior to the first reduction and ending 1.5 hours after the end of the first reduction was taken for each test. The ten frequency measurements prior to the start of the first reduction were taken at each temperature and the average was defined as  $f_{NWL T_j}$ . A value was similarly defined for the 10 measurements prior to the end of the first reduction and defined as  $f_{HWL T_j}$ . Wireless measurements of the  $H_2$  induced frequency shifts were possible at both 378°C and 477°C, which corresponded to less than 10 kHz differences from the values obtained using wired measurements of Setup 1 (for the 10 MHz bandwidth measurements at 378°C). It is noticeable from the figures that the standard deviation for the frequency measurements is as much as five times larger for the 40 MHz bandwidth measurements with respect to the 10 MHz, indicating that smaller bandwidths are desired in particular for these wireless measurements. For the 40 MHz bandwidth case, the standard deviation in frequency falls between 5 and 8 kHz, which is noticeably larger than for the 10 MHz bandwidth (between 1 and 2 kHz). This increase in uncertainty is mostly due to the 4 kHz frequency steps in the case of 40 MHz compared to the 1 kHz steps in the case of 10 MHz bandwidth. In the wireless operation, there is also added frequency uncertainty due to the time-gating signal processing.

## CHAPTER 5

### CONCLUSIONS

#### 5.1 Summary of Work

Chapter 2 presented the selection of orientations on the commercial LGS wafer, the development of thin film materials for high-temperature SAW gas sensors including yttria-stabilized zirconia thin films to be employed as sensing layers and Pt-Al<sub>2</sub>O<sub>3</sub> composite electrodes for high-temperature SAWR operation. And the fabrication of one-port SAWR sensors.

Chapter 3 detailed the development and implementation of a high-temperature gas sensor testing system. Three stainless steel boxes with two chambers each, capable of housing and interrogating two SAWR sensors and one TC in each chamber, were designed and fabricated. The developed gas delivery system and SAWR sensor interrogation modules were also detailed. A summary of the test setups used to acquire the experimental results was also presented.

Chapter 4 presented the experimental results obtained from SAWR sensor temperature and gas response characterization. Temperature characterization of developed SAWR sensors was conducted up to 500°C. Temperature cycling of two different Pt-Al<sub>2</sub>O<sub>3</sub> film compositions (graded and non-graded) was undertaken up to 715°C for more than 200 hours and up to 850°C for more than 300 hours. Gas cycling up to 600°C confirmed the ability of SAWR sensors operating along five different orientations of the commercially available LGS wafer ( $\Psi = 14.7^\circ$ ,  $\Psi = 20.7^\circ$ ,  $\Psi = 32.7^\circ$ ,  $\Psi = 20.7^\circ$ , and  $\Psi = 32.7^\circ$ ) to operate as gas sensors. Pt-decorated YSZ-layered devices were compared to Bare devices up to 400°C with regards to SAWR sensor response to 4% H<sub>2</sub>. The impact of oxygen gas treatments at room temperature and up to 650°C on SAWR gas sensor operation was studied. Film 1 (graded film) and Film 2 (non-graded film) Pt-Al<sub>2</sub>O<sub>3</sub> devices were compared in the 200°C-600°C sensor range. A two-sensor system employing devices oriented along  $\Psi = 26.7^\circ$  and  $\Psi = 77.7^\circ$  was

characterized in the temperature range from 100°C to 500°C. Finally, successful wireless interrogation of a SAWR sensor above 450°C was achieved.

## 5.2 Findings

The work in this thesis resulted in the following findings:

- Two orientations (described by the last Euler angle  $\Psi$ ) were predicted and confirmed to have compensated-temperature operation above 150°C:  $\Psi = 14.7^\circ$  and  $\Psi = 77.7^\circ$ .
- High-temperature cycling of graded and non-graded Pt-Al<sub>2</sub>O<sub>3</sub> films revealed stable operation for cycling up to 715°C for more than 200 hours. Hillock and agglomeration removal was possible from the center of the IDTs for SAWR sensors exposed to temperature cycling up to 850°C for over 300 hours using a graded thin film deposition technique.
- Pt-Al<sub>2</sub>O<sub>3</sub> films were found to have 50% higher SAWR sensor response to 4%H<sub>2</sub> exposures than Pt-decorated YSZ-layered SAWR sensors.
- It was found that O<sub>2</sub> treatments at room temperature resulted in a five times larger frequency variation recovery in the first 20 minutes when compared to the same time-lapse in N<sub>2</sub> environment for room temperature SAWR sensor operation. These results were corroborated by XPS analysis performed by researchers from NETL at Pittsburgh, PA.
- It was found that the SAWR sensor orientation has an influence on H<sub>2</sub> detection in the temperature range from room temperature to 600°C.
- Successful characterization of a two-sensor system utilizing  $\Psi = 26.7^\circ$  and  $\Psi = 77.7^\circ$  devices was successful in the 100°C-500°C temperature range.
- Successful wireless operation revealed that it is possible to use the SAWR sensors as wireless, high-temperature H<sub>2</sub> sensors.

### 5.3 Publications Resulting from this Work

This work resulted in the following publications:

- A. Ayes, P. R. Ohodnicki, R. J. Lad, and M. Pereira Da Cunha, "Enhanced Hydrogen Gas Detection Using SAW Sensor Through Oxygen Pre-Treatment," 2019 IEEE Int. Ultrasonics Symposium, pp. 189–192, 2019.
- A. Ayes and M. Pereira Da Cunha, "Influence of Langasite Crystal Orientation on Hydrogen Gas Detection up to 400°C," 2019 IEEE Int. Ultrasonics Symposium, pp. 735–738, 2019.
- A. Ayes, G. Bernhardt, and M. Pereira da Cunha, "Removal of Stress Hillocks from Platinum-Alumina Electrodes Used in High-temperature SAW Devices," 2019 IEEE Int. Ultrasonics Symposium, pp. 727–730, 2019.
- A. Ayes, A. Maskay, and M. Pereira Da Cunha, "Predicted and measured temperature compensated surface acoustic wave devices for high-temperature applications," IET Electronic Letters, vol. 53, no. 11, pp. 699–700, 2017.
- A. Maskay, A. Ayes, R. Lad, M. Pereira da Cunha; "Stability of Pt/Al<sub>2</sub>O<sub>3</sub> langasite SAW sensors with Al<sub>2</sub>O<sub>3</sub> capping layer and yttria-stabilized zirconia sensing layer", 2017 IEEE Int. Ultrasonics Symposium, 2017.

### 5.4 Suggested Future Work

Suggestions for future work based on the findings of these work:

- Improve SAWR design of selected high-temperature orientations  $\Psi = 14.7^\circ$  and  $\Psi = 77.7^\circ$  to eliminate spurious modes. Additionally, the design of SAW delay lines along these orientations is recommended for more in depth analysis of the mechanisms of different sensing films and the interaction with other types of gases.

- Analysis of the impact of different concentrations of H<sub>2</sub> and other gases on SAW response. This may be potentially accomplished by developing faster interrogation methods, for example, parallel device interrogation as opposed to series interrogation, in order to extract time-constant information of the H<sub>2</sub> interaction with the SAWR sensors.
- Refinement of thin film deposition techniques to increase immediate film stability. The elimination of stress hillocks and agglomeration from the center of the IDT electrodes using the graded Pt interface is promising, and more work should be dedicated to advancing deposition techniques that avoid the problems that were observed at the edge of the electrodes.
- Continued improvements to be made to the developed high-temperature gas testing system. For example, controlling the furnace setpoints and soaking periods with the same PC that controls the data acquisition and gas delivery modules would allow for the automation of week-long and even month-long testing.

## REFERENCES

- [1] M. Pereira da Cunha. “Wireless sensing in hostile environments”. In: *IEEE Intl. Ultrasonics Symposium, IUS* (2013), pp. 1337–1346. ISSN: 19485719.
- [2] P. Davulis. “Characterization of the Elastic , Piezoelectric , and Dielectric Properties of Langatate At High Temperatures Up To 900 C”. Ph. D. University of Maine, 2013.
- [3] M. Werner and W. Fahrner. “Review on materials, microsensors, systems, and devices for high-temperature and harsh-environment applications”. In: *IEEE Transactions on Industrial Electronics* 48.2 (2001), pp. 249–257. ISSN: 02780046.
- [4] X. Jiang, K. Kim, S. Zhang, et al. “High-temperature piezoelectric sensing”. In: *Sensors (Switzerland)* 14.1 (2013), pp. 144–169. ISSN: 14248220.
- [5] S. Zhang and F. Yu. “Piezoelectric materials for high temperature sensors”. In: *Journal of the American Ceramic Society* 94.10 (2011), pp. 3153–3170. ISSN: 00027820.
- [6] A. Ghazanfari, W. Li, M. Leu, et al. “Advanced ceramic components with embedded sapphire optical fiber sensors for high temperature applications”. In: *Materials and Design* 112 (2016), pp. 197–206. ISSN: 18734197.
- [7] J. Fergus. “Materials for high temperature electrochemical NO<sub>x</sub> gas sensors”. In: *Sensors and Actuators, B: Chemical* 121.2 (2007), pp. 652–663. ISSN: 09254005.
- [8] R. Loloee, B. Chorpening, S. Beer, et al. “Hydrogen monitoring for power plant applications using SiC sensors”. In: *Sensors and Actuators, B: Chemical* 129.1 (2008), pp. 200–210. ISSN: 09254005.
- [9] S. Akbar, P. Dutta, and C. Lee. “High-Temperature Ceramic Gas Sensors : A Review”. In: *International Journal of Applied Ceramic Technology* 311.x (2006), pp. 302–311.
- [10] Y. Liu, J. Parisi, X. Sun, et al. “Solid-state gas sensors for high temperature applications-a review”. In: *Journal of Materials Chemistry A* 2.26 (2014), pp. 9919–9943. ISSN: 20507496.
- [11] A. Trinchi, S. Kandasamy, and W. Wlodarski. “High temperature field effect hydrogen and hydrocarbon gas sensors based on SiC MOS devices”. In: *Sensors and Actuators B : Chemical* 133 (2008), pp. 705–716.
- [12] R. Turner, P. Fuierer, R. Newnham, et al. “Materials for high temperature acoustic and vibration sensors: A review”. In: *Applied Acoustics* 41.4 (1994), pp. 299–324. ISSN: 0003682X.

- [13] V. Latini, V. Striano, G. Coppola, et al. “Fiber optic sensors system for high temperature monitoring of aerospace structures”. In: *Photonic Materials, Devices, and Applications II*. Ed. by Ali Serpengüzel, Gonçal Badenes, and Giancarlo C Righini. Vol. 6593. International Society for Optics and Photonics. SPIE, 2007, pp. 223–231.
- [14] R. Fachberger and A. Erlacher. “Monitoring of the temperature inside a lining of a metallurgical vessel using a SAW temperature sensor”. In: *Procedia Chemistry* 1.1 (2009), pp. 1239–1242. ISSN: 18766196.
- [15] J. Chen, J. Zhang, M. Wang, et al. “High-temperature hydrogen sensor based on platinum nanoparticle-decorated SiC nanowire device”. In: *Sensors and Actuators, B: Chemical* 201 (2014), pp. 402–406. ISSN: 09254005.
- [16] R. Lewis. “Sax’s dangerous properties of industrial materials”. In: *Choice Reviews Online* 30.05 (1993), pp. 30–2435–30–2435. ISSN: 0009-4978.
- [17] M. Apostol, T. Vuoristo, and V. Kuokkala. “High temperature high strain rate testing with a compressive SHPB”. In: *Journal de Physique Archives* 110 (2003), pp. 459–464. ISSN: 11554339.
- [18] G. Hunter, J. Wrbanek, R. Okojie, et al. “Development and application of high temperature sensors and electronics for propulsion applications”. In: *Sensors for Propulsion Measurement Applications*. Ed. by Valentin Korman. Vol. 6222. Intl. Society for Optics and Photonics. SPIE, 2006, pp. 76–87.
- [19] C. Tragut and K. Härdtl. “Kinetic behaviour of resistive oxygen sensors”. In: *Sensors and Actuators: B. Chemical* 4.3-4 (1991), pp. 425–429. ISSN: 09254005.
- [20] J. Thiele and M. Pereira Da Cunha. “High temperature LGS SAW gas sensor”. In: *Sensors and Actuators, B: Chemical* 113.2 (Feb. 2006), pp. 816–822. ISSN: 09254005.
- [21] P. Zheng, D. Greve, Irving J. Oppenheim, et al. “Langasite surface acoustic wave sensors: Fabrication and testing”. In: *IEEE Transactions on Ultrasonics, Ferroelectrics, and Frequency Control* 59.2 (Feb. 2012), pp. 295–303. ISSN: 08853010.
- [22] B. Lee. “Review of the present status of optical fiber sensors”. In: *Optical Fiber Technology* 9.2 (2003), pp. 57–79. ISSN: 10685200.
- [23] H. Meixner and U. Lampe. “Metal oxide sensors”. In: *Sensors and Actuators, B: Chemical* 33.1-3 (1996), pp. 198–202. ISSN: 09254005.

- [24] A. Spetz, P. Tobias, A. Baranzahi, et al. “Current status of silicon carbide based high-temperature gas sensors”. In: *IEEE Transactions on Electron Devices* 46.3 (1999), pp. 561–566. ISSN: 00189383.
- [25] J. Neumeister, R. Thum, and E. Lüder. “A SAW Delay-line oscillator as a high resolution temperature sensor”. In: *Sensors and Actuators: A. Physical* 22.1-3 (1990), pp. 670–672. ISSN: 09244247.
- [26] Y. Vlassov, A. Zlov, N. Pashem, et al. “1993 E E E International Frequency Control Symposium”. In: (1993), pp. 1–5.
- [27] H. Scherr, G. Scholl, F. Seifert, et al. “Quartz pressure sensor based on SAW reflective delay line”. In: *Proceedings of the IEEE Ultrasonics Symposium* 1.2 (1996), pp. 347–350. ISSN: 10510117.
- [28] A. Maskay. “Microwave Acoustic SAW Resonators for Stable High-temperature Harsh-Environment Static and Dynamic Strain Sensing Applications”. Ph. D. Thesis. University of Maine, 2018, p. 174.
- [29] L. Rana, R. Gupta, M. Tomar, et al. “ZnO/ST-Quartz SAW resonator: An efficient NO<sub>2</sub> gas sensor”. In: *Sensors and Actuators, B: Chemical* 252.2 (2017), pp. 840–845. ISSN: 09254005.
- [30] J. Devkota, P. Ohodnicki, and D. Greve. “SAW sensors for chemical vapors and gases”. In: *Sensors (Switzerland)* 17.4 (2017), pp. 13–15. ISSN: 14248220.
- [31] L. Yang, C. Yin, Z. Zhang, et al. “The investigation of hydrogen gas sensing properties of SAW gas sensor based on palladium surface modified SnO<sub>2</sub> thin film”. In: *Materials Science in Semiconductor Processing* 60. July 2016 (2017), pp. 16–28. ISSN: 13698001.
- [32] D. Greve, T. Chin, P. Zheng, et al. “Surface acoustic wave devices for harsh environment wireless sensing”. In: *Sensors (Switzerland)* 13.6 (2013), pp. 6910–6935. ISSN: 14248220.
- [33] J.. Tressler, S. Alkoy, and R. Newnham. “Piezoelectric sensors and sensor materials”. In: *Journal of Electroceramics* 2.4 (1998), pp. 257–272. ISSN: 13853449.
- [34] B. Drafts. “Acoustic Wave Sensors”. In: *IEEE Transactions on Microwave Theory and Techniques* 49.4 (2001), pp. 795–802.
- [35] P. Fraga-Lamas, T. Fernández-Caramés, M. Suárez-Albela, et al. “A review on internet of things for defense and public safety”. In: *Sensors (Switzerland)* 16.10 (2016), pp. 1–44. ISSN: 14248220.

- [36] L. Xu, E. Xu, and L. Li. “Industry 4.0: State of the art and future trends”. In: *International Journal of Production Research* 56.8 (2018), pp. 2941–2962. ISSN: 1366588X.
- [37] S. Madakam, R. Ramaswamy, and S. Tripathi. “Internet of Things (IoT): A Literature Review”. In: *Journal of Computer and Communications* 03.05 (2015), pp. 164–173. ISSN: 2327-5219.
- [38] N. Khalil, M. Abid, D. Benhaddou, et al. “Wireless sensors networks for Internet of Things”. In: *IEEE ISSNIP 2014 - 2014 IEEE 9th International Conference on Intelligent Sensors, Sensor Networks and Information Processing, Conference Proceedings* April (2014), pp. 1–6. arXiv: 1606.08407.
- [39] P. Woodgate, I. Coppa, and N. Hart. *Global Outlook 2018 : Spatial Information Industry*. August. CRC SI, 2018. ISBN: 9780646930343.
- [40] J. Shieh, J. Huber, N. Fleck, et al. “The selection of sensors”. In: *Progress in Materials Science* 46.3-4 (2001), pp. 461–504. ISSN: 00796425.
- [41] C. Wang, S. Akbar, and M. Madou. “Ceramic based resistive sensors”. In: *Journal of Electroceramics* 2.4 (1998), pp. 273–282. ISSN: 13853449.
- [42] T. Hoang, P. Rey, M. Vaudaine, et al. “Temperature-compensated structure for SAW pressure sensor in very high temperature”. In: *Proceedings of the IEEE International Frequency Control Symposium and Exposition* (2007), pp. 40–44.
- [43] D. Senesky, K. Cheng, A. Pisano, et al. “Harsh Environment Silicon Carbide Sensors for Health and Performance Monitoring of Aerospace Systems: A Review”. In: *IEEE Sensors Journal* 9.11 (2009), pp. 1472–1478. ISSN: 15581748.
- [44] J. Casady and R. Johnson. “Status of silicon carbide (SiC) as a wide-bandgap semiconductor for high-temperature applications: A review”. In: *High-Temperature Electronics* 39.96 (1998), pp. 511–524.
- [45] G. Müller, G. Krötz, and J. Schalk. “New Sensors for Automotive and Aerospace Applications”. In: *Physica Status Solidi (a)* 185.1 (2001), pp. 1–14. ISSN: 00318965.
- [46] Y. Najjar. “Hydrogen safety: The road toward green technology”. In: *International Journal of Hydrogen Energy* 38.25 (2013), pp. 10716–10728. ISSN: 03603199.
- [47] T. Hübner, L. Boon-Brett, G. Black, et al. “Hydrogen sensors - A review”. In: *Sensors and Actuators, B: Chemical* 157.2 (Oct. 2011), pp. 329–352. ISSN: 09254005.

- [48] L. Boon-Brett, J. Bousek, G. Black, et al. “Identifying performance gaps in hydrogen safety sensor technology for automotive and stationary applications”. In: *International Journal of Hydrogen Energy* 35.1 (2010), pp. 373–384. ISSN: 03603199.
- [49] W. Buttner, M. Post, R. Burgess, et al. “An overview of hydrogen safety sensors and requirements”. In: *International Journal of Hydrogen Energy* 36.3 (2011), pp. 2462–2470. ISSN: 03603199.
- [50] N. Docquier and S. Candel. “Combustion control and sensors: A review”. In: *Progress in Energy and Combustion Science* 28.2 (2002), pp. 107–150. ISSN: 03601285.
- [51] C. Forsberg. “Hydrogen, nuclear energy, and the advanced high-temperature reactor”. In: *International Journal of Hydrogen Energy* 28.10 (2003), pp. 1073–1081. ISSN: 03603199.
- [52] ISO. *Technical Report Iso / Tr*. Tech. rep. 2004.
- [53] V. Aroutiounian. “Hydrogen detectors”. In: *International Scientific Journal for Alternative Energy and Ecology* 3.23 (2005), pp. 21–31.
- [54] J. Moon, H. Hedman, M. Kemell, et al. “Hydrogen sensor of Pd-decorated tubular TiO<sub>2</sub> layer prepared by anodization with patterned electrodes on SiO<sub>2</sub>/Si substrate”. In: *Sensors and Actuators, B: Chemical* 222 (2016), pp. 190–197. ISSN: 09254005.
- [55] N. Barsan and U. Weimar. “Fundamentals of Metal Oxide Gas Sensors”. In: *MCS 2012 – The 14th International Meeting on Chemical Sensors* (2012), pp. 618–621.
- [56] S. Silva, L. Coelho, O. Frazão, et al. “A review of palladium-based fiber-optic sensors for molecular hydrogen detection”. In: *IEEE Sensors Journal* 12.1 (2012), pp. 93–102. ISSN: 1530437X.
- [57] K. Katahira, H. Matsumoto, H. Iwahara, et al. “Solid electrolyte hydrogen sensor with an electrochemically-supplied hydrogen standard”. In: *Sensors and Actuators, B: Chemical* 73.2-3 (2001), pp. 130–134. ISSN: 09254005.
- [58] D. Ponnusamy, A. Prasad, and M. Sridharan. “CdO-TiO<sub>2</sub> nanocomposite thin films for resistive hydrogen sensing”. In: *Microchimica Acta* 183.1 (2016), pp. 311–317. ISSN: 14365073.
- [59] M. Soo, K. Cheong, and A. Noor. “Advances of SiC-based MOS capacitor hydrogen sensors for harsh environment applications”. In: *Sensors and Actuators, B: Chemical* 151.1 (2010), pp. 39–55. ISSN: 09254005.

- [60] NASA. *NASA Glenn Research Center Silicon Carbide Electronics and Sensors*.
- [61] P. Ohodnicki, J. Baltrus, and T. Brown. “Pd/SiO<sub>2</sub> and AuPd/SiO<sub>2</sub> nanocomposite based optical fiber sensors for H<sub>2</sub> sensing applications”. In: *Sensors and Actuators, B: Chemical* 214 (2015), pp. 159–168. ISSN: 09254005.
- [62] Y. Zhang, H. Peng, X. Qian, et al. “Recent advancements in optical fiber hydrogen sensors”. In: *Sensors and Actuators, B: Chemical* 244 (2017), pp. 393–416. ISSN: 09254005.
- [63] D.. Ballantine, S.. Martin, A. Ricco, et al. *Acoustic Wave Sensors: Theory, Design, and Physico-Chemical Applications*. January 1997. San Diego: Academic Press Inc., 2016.
- [64] M. Vellekoop. “Acoustic wave sensors and their technology”. In: *Ultrasonics* 36.1-5 (1998), pp. 7–14. ISSN: 0041624X.
- [65] J. Hornsteiner, E. Born, G. Fischerauer, et al. “Surface acoustic wave sensors for high-temperature applications”. In: *Proceedings of the Annual IEEE International Frequency Control Symposium* (1998), pp. 615–620. ISSN: 01616404.
- [66] J. Cheeke and Z. Wang. “Acoustic wave gas sensors”. In: *Sensors and Actuators, B: Chemical* 59.2 (1999), pp. 146–153. ISSN: 09254005.
- [67] B.A. Auld. *Acoustic Fields and Waves in Solids Volume I; Second Edition*. Robert E. Krieger Publishing Company, 1990.
- [68] J.B. Marion. *Classical Dynamics of Particles and Systems, Second Edition*. Saunders College Publishing, 1970.
- [69] A. Fahmy and E. Adler. “Transformation of Tensor Constants of Anisotropic Materials Due To Rotations of the Co-Ordinate Axes.” In: *Proceedings of the Institution of Electrical Engineers* 122.5 (1975), pp. 591–592. ISSN: 00203270.
- [70] J. Vetelino and A. Reghu. *Introduction to Sensors*. CRC Press, 2011.
- [71] B.A. Auld. *Acoustic Fields and Waves in Solids Volume II; Second Edition*. Robert E. Krieger Publishing Company, 1990.
- [72] A. Ricco, S. Martin, and T. Zipperian. “Surface Acoustic Wave Gas Sensors Based on Conductivity Changes”. In: *Sensors and Actuators* 8 (1985), pp. 319–333.

- [73] J. Vig. *Introduction to Quartz Frequency Standards*. Tech. rep. U.S. Army Electronics Technology and Devices Laboratory, 1992, pp. 1–55.
- [74] Y. Hu, W. Pinkham, L. French, et al. “Pesticide detection using a lateral field excited acoustic wave sensor”. In: *Sensors and Actuators, B: Chemical* 108.1-2 SPEC. ISS. (2005), pp. 910–916. ISSN: 09254005.
- [75] J. Rosenbaum. *Bulk Acoustic Wave Theory and Devices*. Artech House, 1988.
- [76] R. Schmitt, J. Allen, J. Vetelino, et al. “Bulk acoustic wave modes in quartz for sensing measurand-induced mechanical and electrical property changes”. In: *Sensors and Actuators, B: Chemical* 76.1-3 (2001), pp. 95–102. ISSN: 09254005.
- [77] R. Williams, A. Upadhyayula, and V. Bhethanabotla. “High frequency thickness shear mode devices for organic vapor sensing”. In: *Sensors and Actuators, B: Chemical* 122.2 (2007), pp. 635–643. ISSN: 09254005.
- [78] Y. Chen and C. Liu. “Sensitivity analysis of lateral field excited acoustic wave gas sensors with finite element method”. In: *Japanese Journal of Applied Physics* 50.7 PART 2 (2011). ISSN: 00214922.
- [79] M. Lider and H. Yurtseven. “ $\alpha$ - $\beta$  Transition in Quartz: Temperature and Pressure Dependence of the Thermodynamic Quantities for  $\beta$ -Quartz and  $\beta$ -Cristobalite as Piezoelectric Materials”. In: *Autoimmunity Highlights* 5.4 (2014), pp. 1–9. ISSN: 20383274.
- [80] K. Hashimoto. *Surface Acoustic Wave Devices in Telecommunications*. Springer, 2000.
- [81] D. Morgan. *Surface Acoustic Wave Filters with Applications to Electronic Comms. and Signal Processing*. Academic Press, 2007.
- [82] D. Morgan, S. Zhgoon, and A. Shvetsov. “One-port SAW resonators using natural SPUDT substrates”. In: *IEEE Transactions on Ultrasonics, Ferroelectrics, and Frequency Control* 54.10 (2007), pp. 1936–1942. ISSN: 08853010.
- [83] M. Pereira Da Cunha and S. Fagundes. “Metal strip reflectivity and NSPUDT orientations in langanite, langasite, and gallium phosphate”. In: *IEEE Transactions on Ultrasonics, Ferroelectrics, and Frequency Control* 49.6 (2002), pp. 815–819. ISSN: 08853010.
- [84] A. Maskay, A. Ayes, R. Lad, et al. “Stability of Pt/Al<sub>2</sub>O<sub>3</sub>-based electrode langasite SAW sensors with Al<sub>2</sub>O<sub>3</sub> capping layer and yttria-stabilized zirconia sensing layer”. In: *IEEE International Ultrasonics Symposium, IUS* (2017), pp. 2–5. ISSN: 19485727.

- [85] A. Ayes, A. Maskay, and M. Pereira Da Cunha. “Predicted and measured temperature compensated surface acoustic wave devices for high-temperature applications”. In: *Electronics Letters* 53.11 (2017), pp. 699–700. ISSN: 14248220.
- [86] S. Fagundes and M. Pereira da Cunha. “NSPUDT orientations in new materials”. In: Institute of Electrical and Electronics Engineers (IEEE), Jan. 2003, pp. 525–528.
- [87] M. Pereira da Cunha and S. Fagundes. “Investigation on recent quartz-like materials for SAW applications”. In: *IEEE Transactions on Ultrasonics, Ferroelectrics and Frequency Control* 46.6 (Aug. 2002), pp. 1583–1590. ISSN: 0885-3010.
- [88] J. Bohm, R. Heimann, M. Hengst, et al. “Czochralski growth and characterization of piezoelectric single crystals with langasite structure: LGS, LGN, and LGT. Part I”. In: *Journal of Crystal Growth* 204.1 (1999), pp. 128–136. ISSN: 00220248.
- [89] M. Pereira da Cunha, R. Lad, T. Moonlight, et al. “High temperature stability of langasite surface acoustic wave devices”. In: *Proceedings - IEEE Ultrasonics Symposium*. 2008, pp. 205–208.
- [90] D. Frankel, G. Bernhardt, B. Sturtevant, et al. “Stable electrodes and ultrathin passivation coatings for high temperature sensors in harsh environments”. In: *Procs. of IEEE Sensors* (2008), pp. 82–85.
- [91] D. Frankel, S. Moulzolf, M. Pereira da Cunha, et al. “Influence of composition and multilayer architecture on electrical conductivity of high temperature Pt-alloy films”. In: *Surface and Coatings Technology* 284 (2015), pp. 215–221. ISSN: 02578972.
- [92] G. Bernhardt and M. Call. *Internal Images*. Tech. rep. University of Maine.
- [93] A. Ayes, G. Bernhardt, and M. Pereira da Cunha. “Removal of Stress Hillocks from Platinum-Alumina Electrodes Used in High-temperature SAW Devices”. In: *2019 IEEE International Ultrasonics Symposium (IUS)* (2019), pp. 727–730.
- [94] J. Thiele and M. Pereira da Cunha. “High temperature LGS SAW devices with Pt/WO/sub 3/ and Pd sensing films”. In: Institute of Electrical and Electronics Engineers (IEEE), July 2004, pp. 1750–1753.
- [95] P. Zheng, D. Greve, I. Oppenheim, et al. “Langasite SAW temperature and oxygen multi-sensor”. In: *Proceedings of the IEEE International Frequency Control Symposium and Exposition*. 2011. ISBN: 9781612841106.

- [96] P. Zheng, D. Greve, and I. Oppenheim. “Langasite surface acoustic wave gas sensors: Modeling and verification”. In: *IEEE Transactions on Ultrasonics, Ferroelectrics, and Frequency Control* 60.3 (2013), pp. 579–586. ISSN: 08853010.
- [97] E. Adler. “Matrix Methods Applied to Acoustic Waves in Multilayers”. In: *IEEE Transactions on Ultrasonics, Ferroelectrics, and Frequency Control* 37.6 (1990), pp. 485–490. ISSN: 08853010.
- [98] P. Nicolay, O. Elmazria, F. Sarry, et al. “New measurement method to characterize piezoelectric SAW substrates at very high temperature”. In: *Proceedings - IEEE Ultrasonics Symposium*. 2008, pp. 1877–1880.
- [99] P. Nicolay and T. Aubert. “A numerical method to derive accurate temperature coefficients of material constants from high-temperature SAW measurements: App. to langasite”. In: *IEEE Transactions on Ultrasonics, Ferroelectrics, and Frequency Control* 60.10 (2013), pp. 2137–2141. ISSN: 08853010.
- [100] P. Nicolay and T. Aubert. “A promising method to derive the temperature coefficients of material constants of SAW and BAW materials. first application to LGS”. In: *IEEE Transactions on Ultrasonics, Ferroelectrics, and Frequency Control* 61.8 (2014), pp. 1335–1343. ISSN: 08853010.
- [101] B. Meulendyk and M. Pereira Da Cunha. “Transverse waveguide mode suppression for Pt-electrode SAW resonators on quartz and LGS”. In: *IEEE Transactions on Ultrasonics, Ferroelectrics, and Frequency Control* 58.12 (2011), pp. 2727–2736. ISSN: 08853010.
- [102] S. Moulzolf, D. Frankel, and R. Lad. “In situ four-point conductivity and Hall effect apparatus for vacuum and controlled atmosphere measurements of thin film materials”. In: *Review of Scientific Instruments* 73.6 (2002), p. 2325. ISSN: 00346748.
- [103] H. Fukumoto, T. Imura, and Y. Osaka. “Heteroepitaxial growth of yttria-stabilized zirconia (ysz) on silicon”. In: *Japanese Journal of Applied Physics* 27.8 A (1988), pp. L1404–L1405. ISSN: 13474065.
- [104] J. Baltrus, P. Ohodnicki, N. Joy, et al. “Examination of charge transfer in Au/YSZ for high-temperature optical gas sensing”. In: *Applied Surface Science* 313 (2014), pp. 19–25. ISSN: 01694332.
- [105] P. Rogers, G. Sirinakis, and M. Carpenter. “Direct observations of electrochemical reactions within Au-YSZ thin films via absorption shifts in the Au nanoparticle surface plasmon resonance”. In: *Journal of Physical Chemistry C* 112.17 (2008), pp. 6749–6757. ISSN: 19327447.

- [106] N. Joy, C. Settens, R. Matyi, et al. “Plasmonic based kinetic analysis of hydrogen reactions within Au-YSZ nanocomposites”. In: *Journal of Physical Chemistry C* 115.14 (2011), pp. 6283–6289. ISSN: 19327447.
- [107] G. Sirinakis, R. Siddique, I. Manning, et al. “Development and characterization of Au-YSZ surface plasmon resonance based sensing materials: High temperature detection of CO”. In: *Journal of Physical Chemistry B* 110.27 (2006), pp. 13508–13511. ISSN: 15206106.
- [108] Z. Zhao, V. Rossi, J. Baltrus, et al. “Ag Nanoparticles Supported on Ytria-Stabilized Zirconia: A Synergistic System within Redox Environments”. In: *Journal of Physical Chemistry C* 120.9 (2016), pp. 5020–5032. ISSN: 19327455.
- [109] R. Behanan, S. Moulzolf, M. Call, et al. “Thin films and techniques for SAW sensor operation above 1000°C”. In: *IEEE International Ultrasonics Symposium, IUS* (2013), pp. 1013–1016. ISSN: 19485719.
- [110] S. Moulzolf, R. Behanan, T. Pollard, et al. “Capacitively coupled IDT for high temperature SAW devices”. In: *IEEE International Ultrasonics Symposium, IUS* (2013), pp. 255–258. ISSN: 19485719.
- [111] N. Aiken. “VHF Near Field Antenna Design for Wireless Sensing Applications in Harsh Environments”. Honors Thesis. University of Maine, 2019.
- [112] *Keysight Technologies E5071C ENA Network Analyzer E5092A Configurable Multiport Test Set Datasheet*. Tech. rep. Keysight Technologies, 2017.
- [113] M. Pereira da Cunha, A. Maskay, R. J. Lad, et al. “Pt-Ni / Pt-Zr electrodes for stable SAW resonator operation during repeated temperature cycling up to 1000°C”. In: *2015 IEEE International Ultrasonics Symposium, IUS 2015* (2015), pp. 1–4.
- [114] Tylan Industries. *TN2900 Mass Flow Controller Manual*. Tech. rep. Celerity, Inc., 2007.
- [115] Tylan Industries. *Celerity Tylan Mass Flow Controller User Manual*. Tech. rep. Celerity, Inc., 2008.
- [116] A. Ayes, P. Ohodnicki, J. Baltrus, et al. “Improved Hydrogen Detection through Oxygen Surface Conditioning Verified by SAW Resonators and XPS”. 2020.
- [117] A. Ayes, P. Ohodnicki, R. Lad, et al. “Enhanced Hydrogen Gas Detection Using SAW Sensor Through Oxygen Pre-Treatment”. In: *IEEE Ultrasonics Symposium 2019* (2019), pp. 189–192.

- [118] Armando Ayes and M. Pereira Da Cunha. “Influence of Langasite Crystal Orientation on Hydrogen Gas Detection up to 400 °C”. In: *IEEE Ultrasonics Symposium 2019* (2019), pp. 735–738.
- [119] National Instruments. *USB-TC01 Specifications*. Tech. rep. National Instruments, 2017, pp. 1–10.
- [120] J. Proakis and D. Manolakis. *Digital Signal Processing: Principles, Algorithms, and Applications. Fourth Edition*. Pearson Prentice Hall, 2007.
- [121] T. Pollard. *Chirp-z transform algorithm*. Internal Documentation.

## APPENDIX A

### DETAILS FOR THE OPERATION OF THE HIGH TEMPERATURE GAS TESTING SYSTEM AND FREQUENCY TRACKING CODE

This Appendix presents details for the high-temperature gas testing system described in Chapter 3. The design details for the high-temperature stainless steel box are given. A description of the LabVIEW Software developed for controlling the gas delivery system and SAWR sensor and TC interrogation module is also presented. Frequency tracking code including parabolic approximation and peak selection is also given.

#### A.1 Stainless Steel Box details

The stainless steel box used for high-temperature testing was designed on AutoCad with the assistance of Dr. Anin Maskay. A total of three boxes were fabricated at the Advanced Manufacturing Center (AMC) at the University of Maine. The exact dimensions for the box (Figure A.1) and the caps (Figure A.2) are given below.

Male NPT-threaded connectors from Swagelok were used in order to give access to the Thermocoax high-temperature Inconel coaxial cables, Omega Inconel-sheath TCs and to the 1/8" diameter stainless-steel tubing for gas input and output. The exact part numbers were: i) for access with the coaxial cables: SS-4M0-1-2BT (Stainless Steel Swagelok Tube Fitting, Bored-through Male Connector, 4mm Tube OD x 1/8 in. Male NPT); ii) for access with the TCs: SS-200-1-2BT (Stainless Steel Swagelok Tube Fitting, Bored-through Male Connector, 1/8 in. Tube OD x 1/8 in. Male NPT); iii) SS-200-1-2 (Stainless Steel Swagelok Tube Fitting, Male Connector, 1/8 in. Tube OD x 1/8 in. Male NPT). The caps were secured onto the stainless steel box body using 316 stainless steel 40 mm M3 screws with corresponding 316 stainless steel nuts.

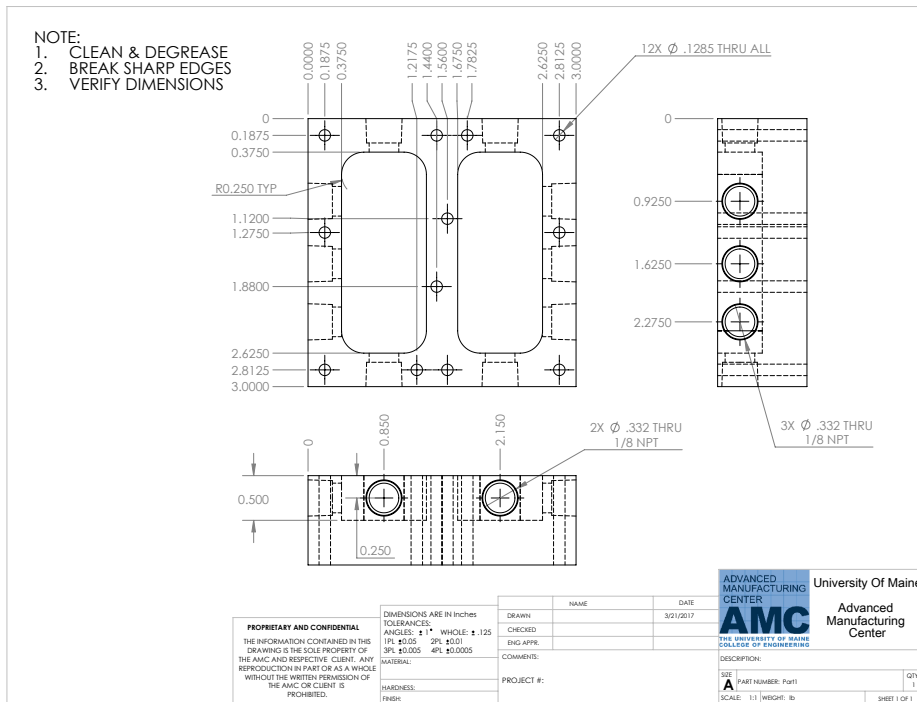


Figure A.1. Dimensions and specifications of fabricated stainless-steel box body by AMC.

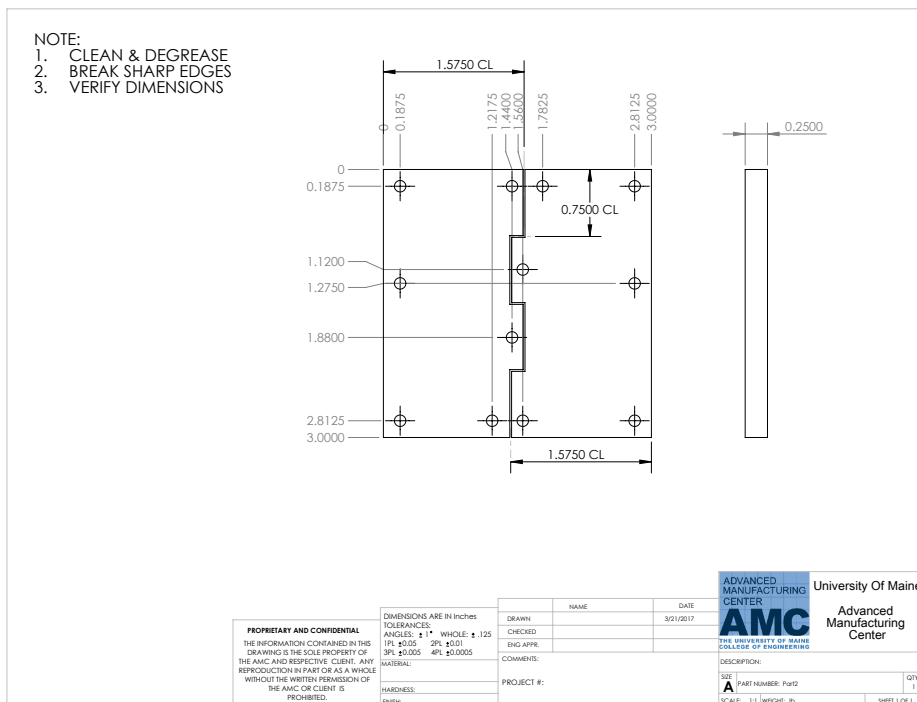


Figure A.2. Dimensions and specifications of fabricated stainless-steel box caps by AMC.

## A.2 Software Details

The block diagram for the functionality of the main LabVIEW script developed can be found in Figure A.3. The last iteration of the Main LabVIEW script may be found in the MAL10 network file center under:

```
\\MAL10\Grads\AAyes\Labview\LabVIEW_LatestFolder\OPERATION_AS_OF  
20200121\Measurements_RT_Table_20191114_LF.vi
```

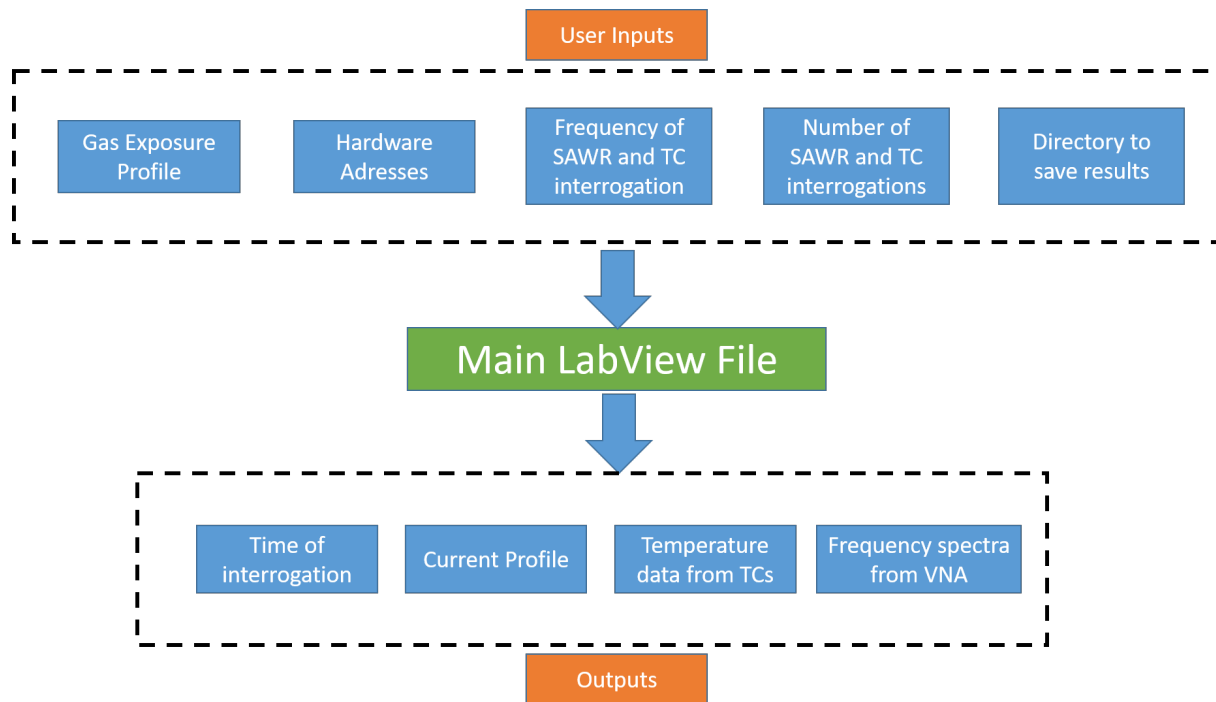


Figure A.3. User input and output flow diagram for LabVIEW software.

The user inputs are given into the LabVIEW Front Panel, and the Main function runs until the completion of the specified gas exposure profile. The relevant user inputs include gas exposure profile, hardware addresses to communicate with the VNA and USB control modules controlling the RF multiplexer and gas delivery system, The frequency of interrogations, the number of interrogations and the directory to save the results. These data is communicated to the main function via input fields and a table in the LabVIEW Front Panel. The flow diagram for the Main LabVIEW function is shown in Figure A.4.

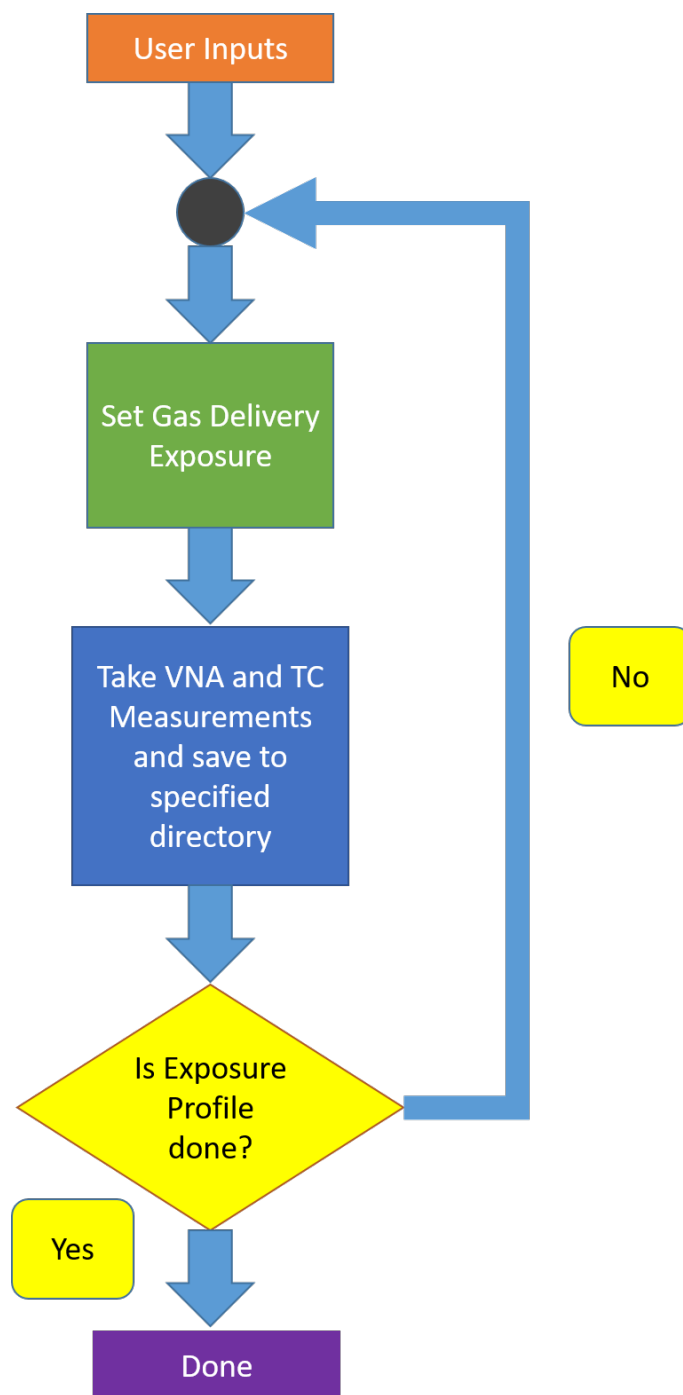


Figure A.4. Flow diagram for Main LabVIEW script.

The two blocks in the Main function flow diagram functioning to set the gas delivery exposure and to take the measurements are modularized functions. The block diagram of this iteration contains the information necessary for specifying the gas exposure species in the input table for the Main LabVIEW function. The latest iteration of the gas delivery function is in the MAL10 network file center under:

```
\\MAL10\Grads\AAyes\Labview\LabVIEW_LatestFolder\OPERATION_AS_OF  
20200121\Gas_control_Design_10_Ayes_20190804.vi
```

The latest iteration of the interrogation module for taking measurements is in the MAL10 network file center under:

```
\\MAL10\Grads\AAyes\Labview\LabVIEW_LatestFolder\OPERATION_AS_OF  
20200121\VNA_Measure_20180921_RT.vi
```

Additionally, there is a TC interrogation module which is called within the interrogation module. The latest iteration of this TC interrogation module is in the MAL10 network file center under:

```
\\MAL10\Grads\AAyes\Labview\LabVIEW_LatestFolder\OPERATION_AS_OF  
20200121\TC_measure_Ayes_Final_numeric_chamber.vi
```

### **A.3 Frequency Tracking Code**

Matlab frequency tracking code that includes polynomial fitting around resonant frequency and the selection of a peak to track during a test for data collected by the LabVIEW software can be found below and also in MAL10 under:

```
\\MAL10\Grads\AAyes\MATLAB\Peak_Analysis_withPeakApprox_20191018
```

```
%clear all;  
% close all;
```

```

% clear all;
%if using Z:\AAyes\Measurements\Gas Measurements\Data
%then specify currentfolder = 1;
%if using \\MAL10\Grads\AAyes\Measurements\Gas Measurements\Data
%then specify currentfolder = 2;
currentfolder = 2;

if currentfolder == 1
    s = what;
    homedir = s.path;
    test = homedir(1,45:length(homedir));
else if currentfolder == 2
    s = what;
    homedir = s.path;
    test = homedir(1,56:length(homedir));
else
    error('Choose a correct value for currentfolder')
end
end

%The code will plot the results for a test using the gas setup
%developed starting TEST30. In order to run it, Select the folder
%of the desired test to be analyzed. This folder must contain four
%folders: Device0, Device1, Device2 and Device3. Upon execution of
%the code, the results with respect to gas profile and temperature
%will be plotted and the resulting plots will be saved in the
%folder.

```

```
% User inputs: these inputs are for the titles of the plots, they
%specify what type of device is being worked with in each
%scenario.
%They must be the same length
```

```
Devicetypes(1,:) = '26S Film 1';
Devicetypes(2,:) = '77RC Film 1';
Devicetypes(3,:) = '26S Film 1';
Devicetypes(4,:) = '77RC Film 1';
```

```
% code for accessing each device folder
for j = 0:3
    newdir = num2str(j);
    newdir = strcat('Device',newdir);
    newdir = strcat(homedir,'\ ',newdir);
    cd(newdir);
    cd;
    Device = j;
    if Device == 0 || Device == 1
        chamber = 1;
    else
        chamber = 2;
    end
end
```

```

chambernum = num2str(chamber);
Devicenum = num2str(Device);
% title generation for pictures
titulo = strcat('Device ',Devicenum, ', ', ',Devicetypes(j+1,:), ...
', Chamber', chambernum);

i = 0;
filename = num2str(i);
filename_data = strcat('SData',filename);

% Determine how many peaks at the beginning of the test for
%each device and which one to follow

prompt = 'What is the desired prominence of peaks? ';
prominence = input(prompt);
SData = importdata(filename_data);
frequency = SData(:,1);
mag = SData(:,2);
maginv = -mag;
figure(1); clf;
findpeaks(maginv, frequency, 'MinPeakProminence',prominence, ...
'Annotate', 'extents')
prompt = 'Which peak should one track (1 is leftmost)? ';
peaktotrack = input(prompt);

while exist(filename, 'file') == 2 % continue the loop as long

```

```

                                                    %as there are files

data = importdata(filename);
SData = importdata(filename_data);
time_device(i + 1,1) = data(1,1);
roomtemp(i + 1,1) = data(1,5);
temp1 = data(1,3);
temp2 = data(1,4);
temp(i+1,1) = (temp1 + temp2)/2;
frequency = SData(:,1);
frequency = frequency/1e6;
mag = SData(:,2);

% get the inverse of mag for peak analysis
maginv = -mag;
[pks, locs] = findpeaks(maginv, 'MinPeakProminence', ...
prominence);
Ind = locs(peaktotrack,1);
min_freq(i + 1,1) = frequency(Ind);
profile(i + 1,1) = data(1,2);

% polynomial approximation
dist = 2;
fnew = frequency(Ind - dist:Ind + dist);
magnew = mag(Ind - dist: Ind + dist);
p1 = polyfit(fnew, magnew, 2);
fpoly = linspace(frequency(Ind - dist), ...
frequency(Ind + dist), 1001);

```

```

magpoly = polyval(p1, fpoly);
[Min_magpoly, Ind_poly] = min(magpoly);
min_freqpoly(i + 1, 1) = fpoly(Ind_poly);

i = i + 1;
filename = num2str(i);
filename_data = strcat('SData', filename);
end

cd(homedir);
cd;
figure(1); clf; yyaxis left; plot(time_device/3600, ...
min_freqpoly, 'b')
figure(1); yyaxis right; plot(time_device/3600, profile, 'r')

title1 = strcat(titulo, ...
' Gas Profile, Peak Tracking and Peak Approx, in hours');

yyaxis left; ylabel('Frequency (MHz)'); xlabel('Time (hours)');
yyaxis right; ylabel('Profile State');
set(gca, 'FontSize', 18);

grid on;

savefig(title1);

```

```

figure(2); clf; yyaxis left; plot(time_device/3600,...
min_freqpoly, 'b')
figure(2); yyaxis right; plot(time_device/3600, temp, 'r')

title2 = strcat(titulo ,...
' Temperature, Peak Tracking and Peak Approx, in hours ');

yyaxis left; ylabel('Frequency (MHz)'); xlabel('Time (min)');
yyaxis right; ylabel('Temperature (\circ C)');
set(gca, 'FontSize', 18);

grid on;

savefig(title2);

end

```

## APPENDIX B

### FREQUENCY RESPONSE OF BARE FABRICATED DEVICES

The typical frequency response of devices oriented along  $\Psi = 14.7^\circ, 20.7^\circ, 32.7^\circ$  and  $77.7^\circ$  for IDT placements S, RC, and LC (described in Section 2.1.2). Results are given for: magnitude of reflection coefficient ( $S_{11}$ ) in the corresponding figure inset a) (in dB); real part of the admittance in the corresponding inset b) (in mS); and imaginary part of the admittance in the corresponding inset c) (in mS).

#### B.1 Typical Frequency Response of Fabricated SAWRs

Devices oriented along  $\Psi = 14.7^\circ$  for IDT placement S, RC and LC are given in Figures B.1-B.2. Devices oriented along  $\Psi = 20.7^\circ$  for IDT placement S, RC and LC are given in Figures B.4-B.6. Devices oriented along  $\Psi = 32.7^\circ$  for IDT placement S, RC and LC are given in Figures B.7-B.9. Devices oriented along  $\Psi = 77.7^\circ$  for IDT placement S, RC and LC are given in Figures B.10-B.12.

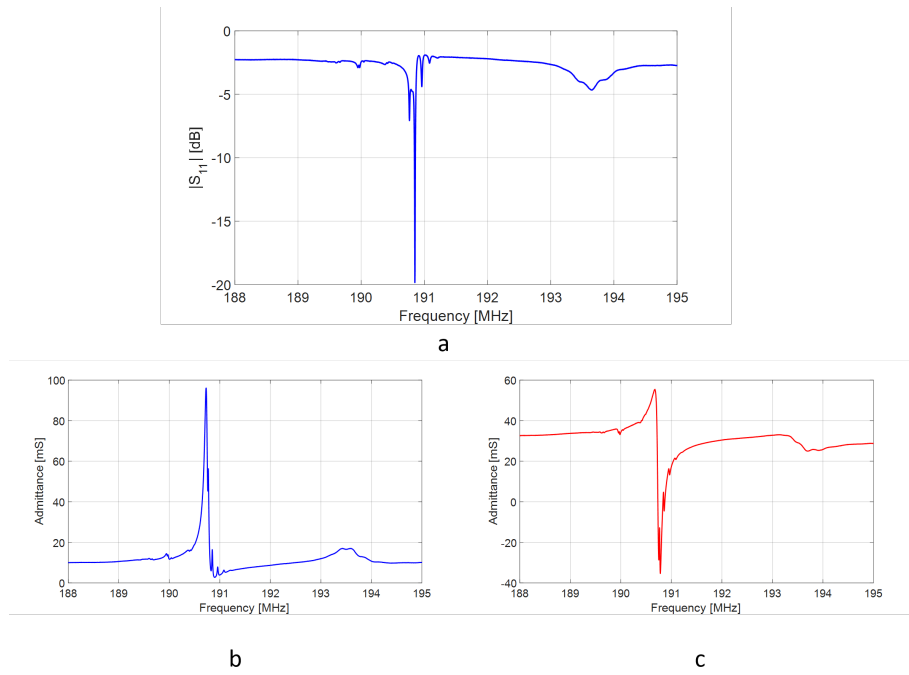


Figure B.1. Typical frequency Response  $\Psi = 14.7^\circ$  IDT placement S: a)  $|S_{11}|$  in dB; b) real part of admittance in mS; c) imaginary part of admittance in mS.

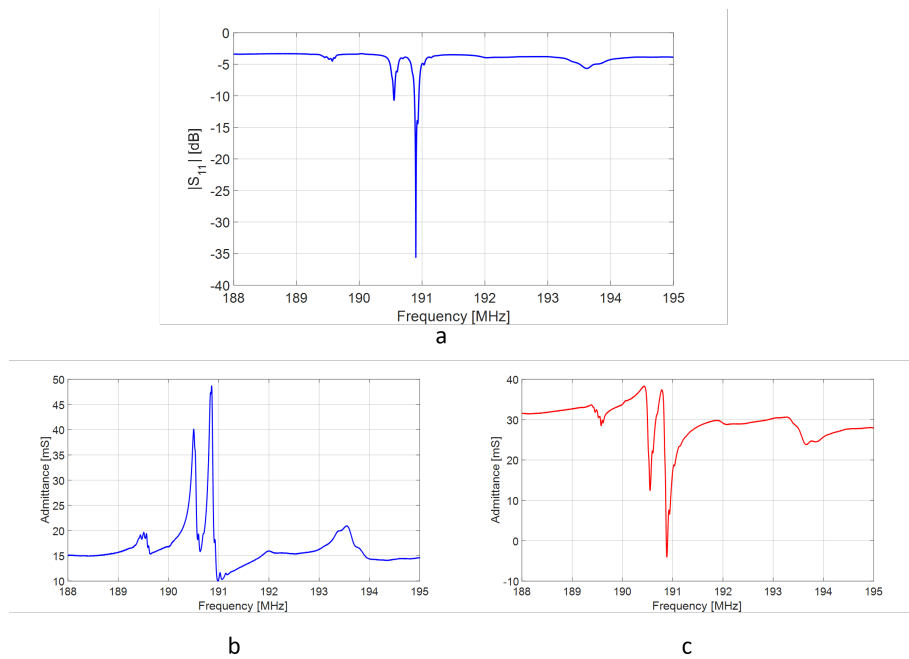


Figure B.2. Typical frequency Response  $\Psi = 14.7^\circ$  IDT placement RC: a)  $|S_{11}|$  in dB; b) real part of admittance in mS; c) imaginary part of admittance in mS.

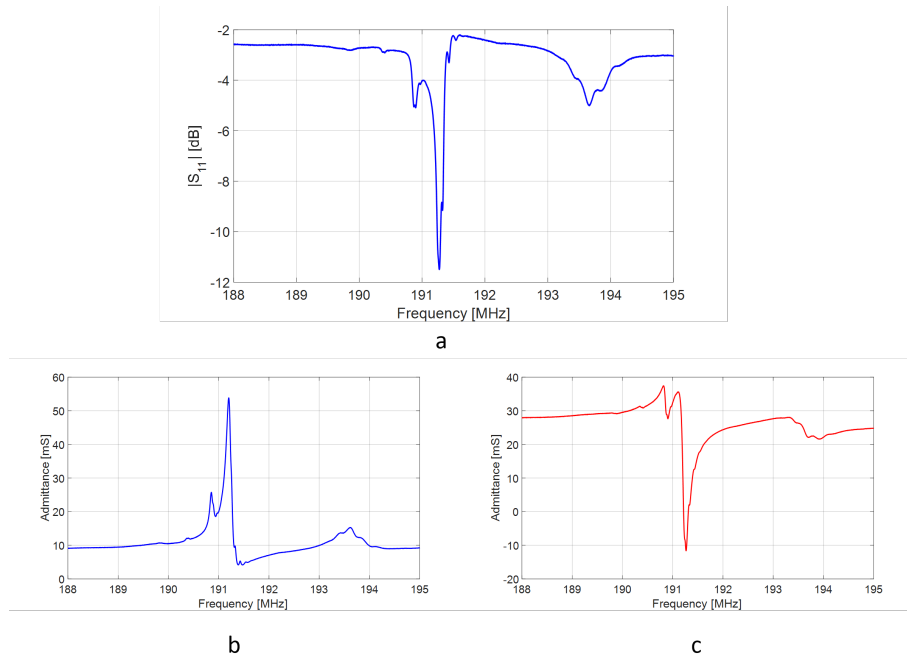


Figure B.3. Typical frequency Response  $\Psi = 14.7^\circ$  IDT placement LC: a)  $|S_{11}|$  in dB; b) real part of admittance in mS; c) imaginary part of admittance in mS.

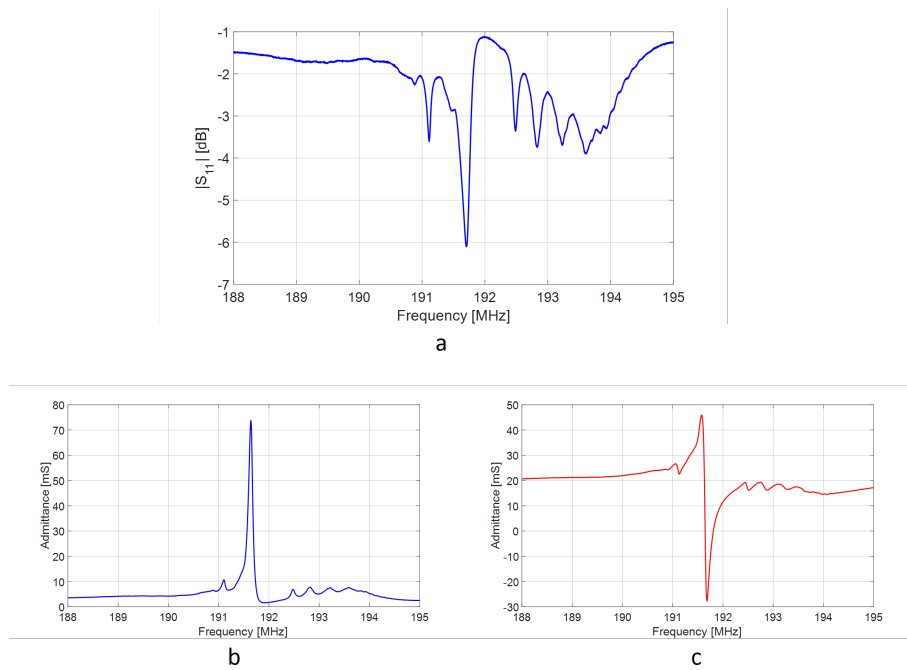


Figure B.4. Typical frequency Response  $\Psi = 20.7^\circ$  IDT placement S: a)  $|S_{11}|$  in dB; b) real part of admittance in mS; c) imaginary part of admittance in mS.

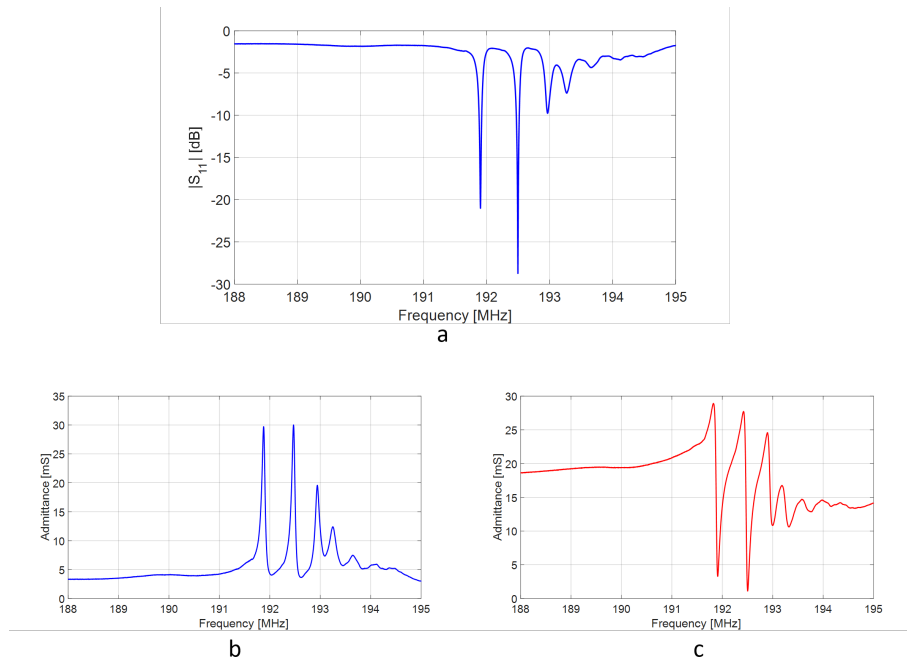


Figure B.5. Typical frequency Response  $\Psi = 20.7^\circ$  IDT placement RC: a)  $|S_{11}|$  in dB; b) real part of admittance in mS; c) imaginary part of admittance in mS.

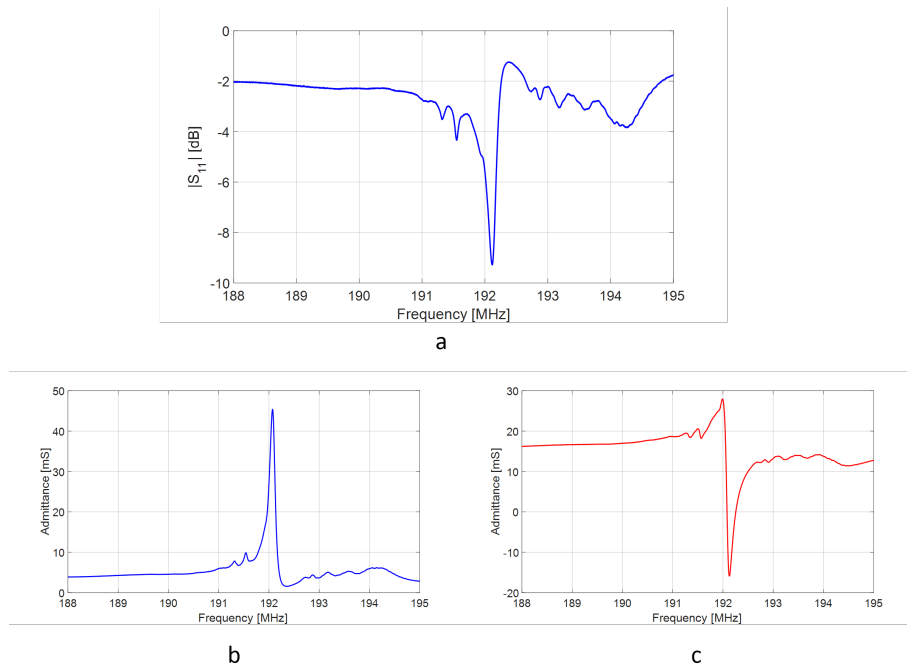


Figure B.6. Typical frequency Response  $\Psi = 20.7^\circ$  IDT placement LC: a)  $|S_{11}|$  in dB; b) real part of admittance in mS; c) imaginary part of admittance in mS.

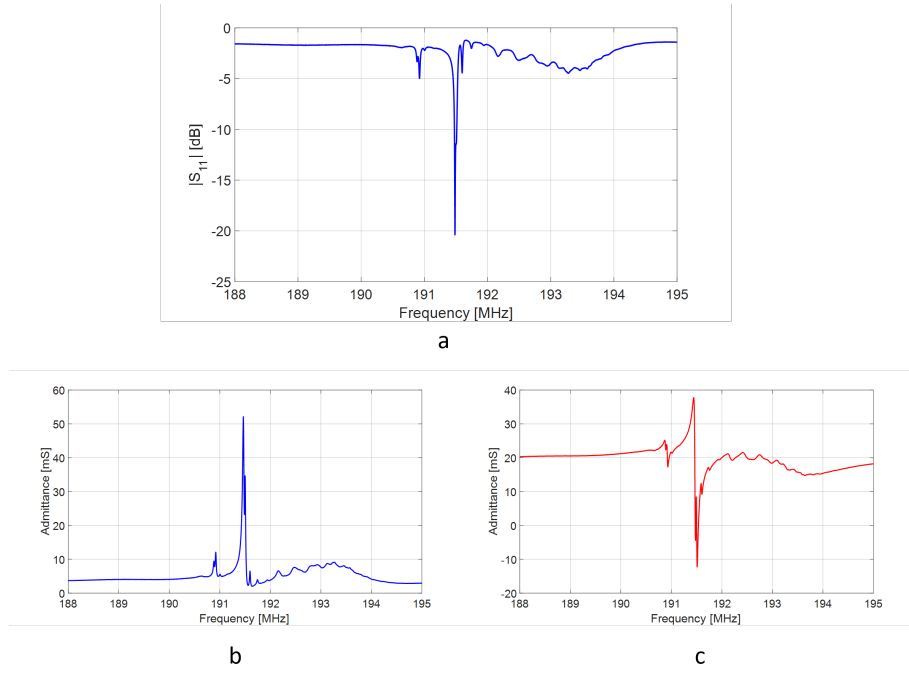


Figure B.7. Typical frequency Response  $\Psi = 32.7^\circ$  IDT placement S: a)  $|S_{11}|$  in dB; b) real part of admittance in mS; c) imaginary part of admittance in mS.

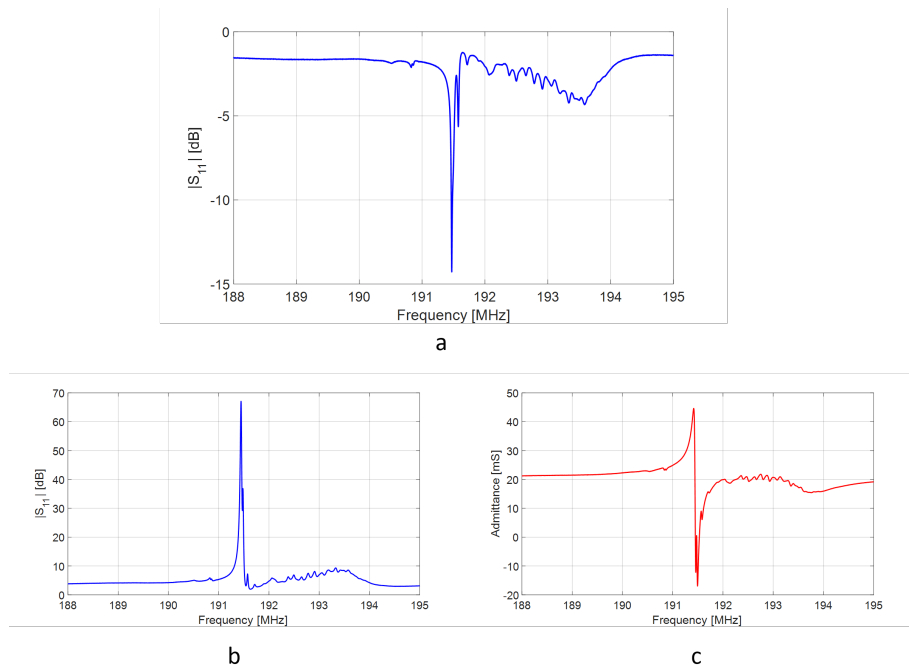


Figure B.8. Typical frequency Response  $\Psi = 32.7^\circ$  IDT placement RC: a)  $|S_{11}|$  in dB; b) real part of admittance in mS; c) imaginary part of admittance in mS.

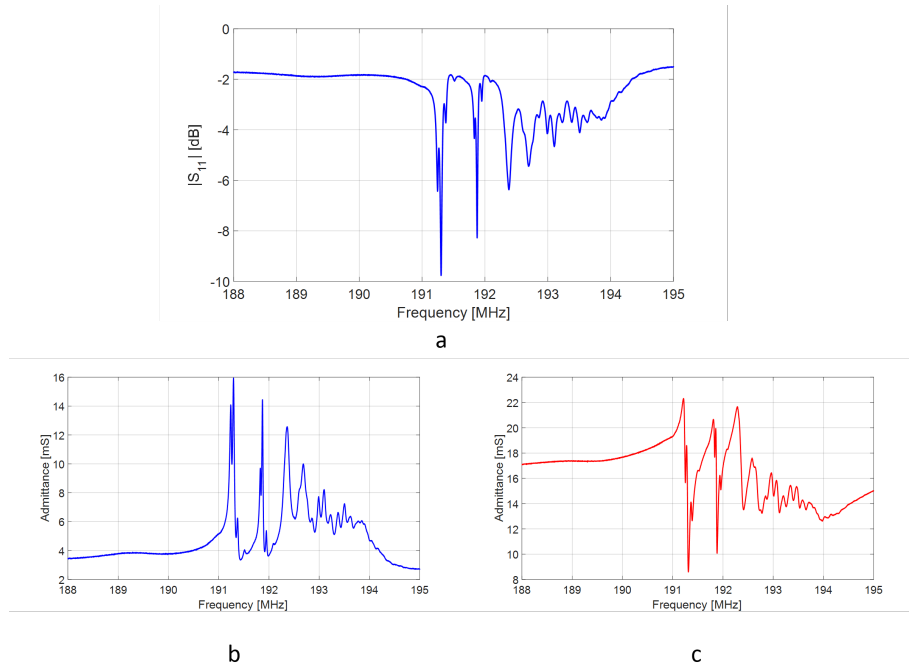


Figure B.9. Typical frequency Response  $\Psi = 32.7^\circ$  IDT placement LC: a)  $|S_{11}|$  in dB; b) real part of admittance in mS; c) imaginary part of admittance in mS.

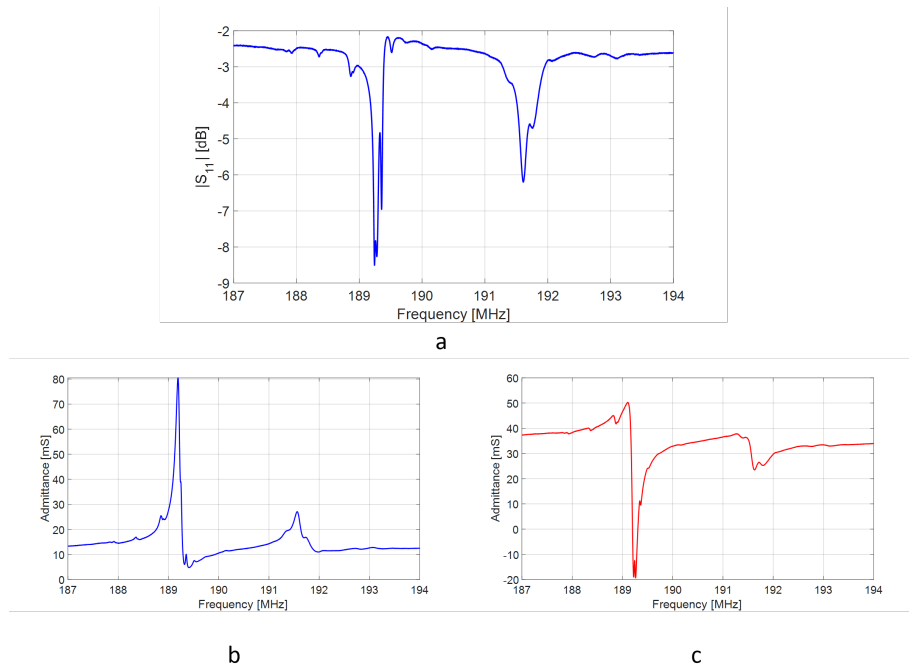


Figure B.10. Typical frequency Response  $\Psi = 77.7^\circ$  IDT placement S: a)  $|S_{11}|$  in dB; b) real part of admittance in mS; c) imaginary part of admittance in mS.

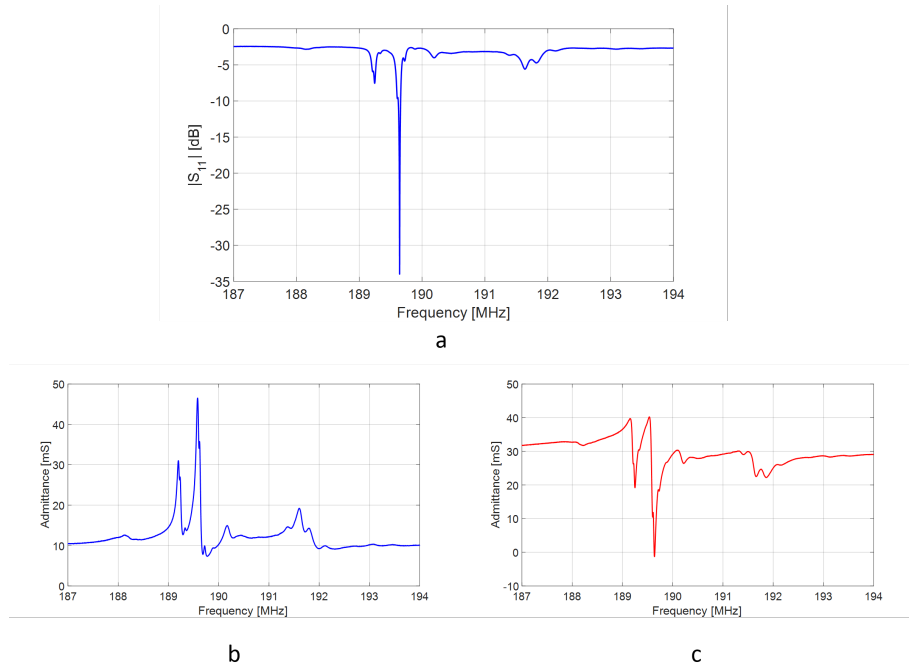


Figure B.11. Typical frequency Response  $\Psi = 77.7^\circ$  IDT placement RC: a)  $|S_{11}|$  in dB; b) real part of admittance in mS; c) imaginary part of admittance in mS.

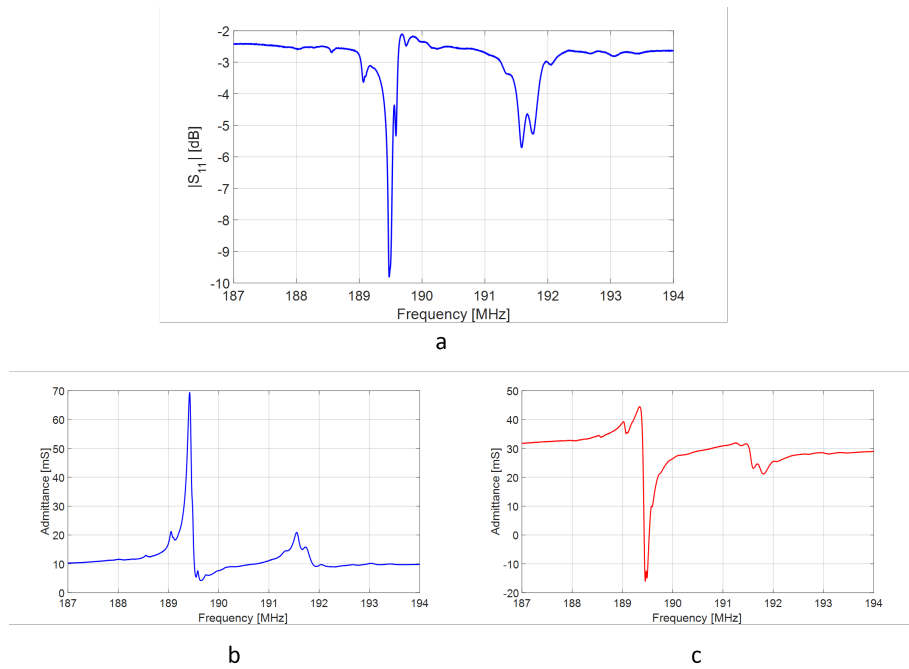


Figure B.12. Typical frequency Response  $\Psi = 77.7^\circ$  IDT placement LC: a)  $|S_{11}|$  in dB; b) real part of admittance in mS; c) imaginary part of admittance in mS.

## APPENDIX C

### COMPILED GAS SENSOR TESTING RESULTS

The compiled gas sensor results are given below for all setups cited in Section 3.2 in Table 3.1. The results are ordered as follows: YSZ-layered vs. Bare results from Setup A4 at nominal furnace temperatures of 200°C, 300°C, and 400°C, referenced in Section 4.4; Results at room temperature from Setups A1, A3 and A4 related to oxygen treatments for devices oriented along  $\Psi = 26.7^\circ$ , referenced in Section 4.5 ; Results from Setup A3 at nominal furnace temperatures of 100°C, 200°C, 300°C, 400°C, and 500°C; Results from Setup A6 for at nominal furnace temperatures of 200°C, 300°C, 400°C and 500°C; Results from Setup A7 for all temperatures tested (100°C to 500°C in 50°C increments); Results from Setup A5 at 200°C, 300°C, 400°C, 500°C, and 600°C.

#### C.1 YSZ vs. Bare SAWR sensor

Table C.1 shows the tabulated results of the YSZ vs. Bare comparison conducted on Setup A4 (Device 1: Film 2 YSZ non-cycled 14.7°, Device 2: Film 2 Bare non-cycled 14.7°, Device 3: Film 2 YSZ non-cycled 26.7°, Device 4: Film 2 Bare non-cycled 26.7°). The average temperature of the corresponding chamber was taken for the test, and the frequency shifts  $\Delta f_A$ ,  $\Delta f_B$ , and  $\Delta f_C$ , as well as the reference frequency  $f_{0i}$  were recorded as described in Section 4.4. The results for all devices at the corresponding nominal furnace temperature are shown in Figures C.1-C.12. All tests shown in this section were conducted with 100 sccm flow rates.

Table C.1. Summary of results using Setup A4 comparing YSZ-layered vs. Bare Devices at 200°C, 300°C and 400 °C.

Temp (°C)	Feature Magnitude (kHz)							
	Device 1				Device 2			
	$f_0$ (MHz)	$\Delta f_A$	$\Delta f_B$	$\Delta f_C$	$f_0$ (MHz)	$\Delta f_A$	$\Delta f_B$	$\Delta f_C$
204	192.401	13.6	10.5	10.0	192.012	19.8	19.7	19.8
297	192.235	17.6	15.7	16.1	190.868	30.9	27.4	26.6
393	191.865	28.8	25.0	25.6	190.545	38.3	33.8	34.2
	Device 3				Device 4			
	$f_0$ (MHz)	$\Delta f_A$	$\Delta f_B$	$\Delta f_C$	$f_0$ (MHz)	$\Delta f_A$	$\Delta f_B$	$\Delta f_C$
208	193.025	43.1	37.3	34.4	191.52	65.1	68.3	69.5
303	192.516	64.3	56.0	52.0	191.043	103.0	97.8	98.4
400	191.804	83.6	73.4	83.8	190.415	132.2	120.7	119.9

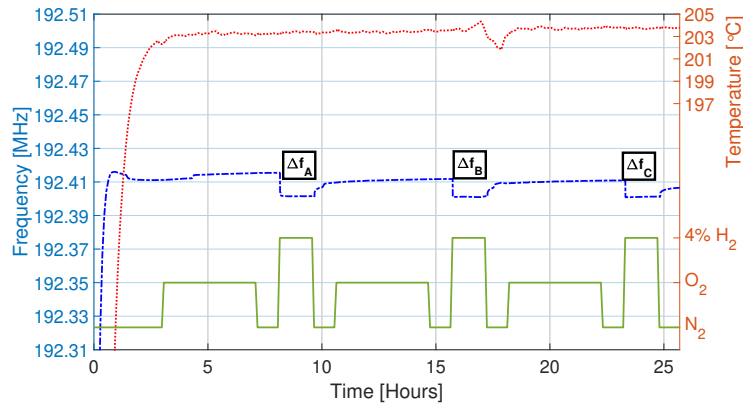


Figure C.1. Setup A4 test results at nominal furnace temperature 200°C for Device 1.

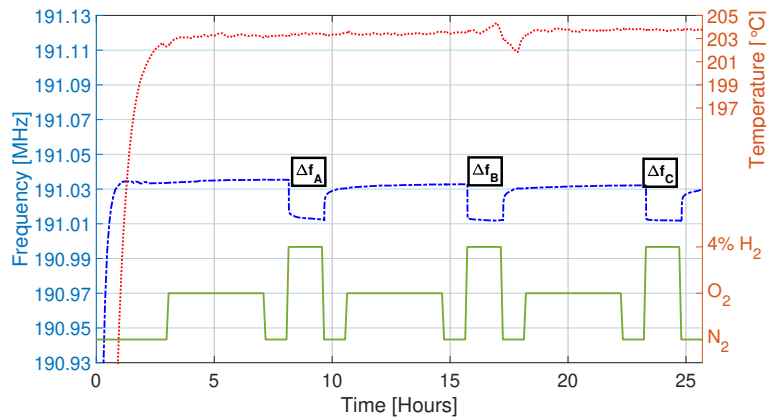


Figure C.2. Setup A4 test results at nominal furnace temperature 200°C for Device 2.

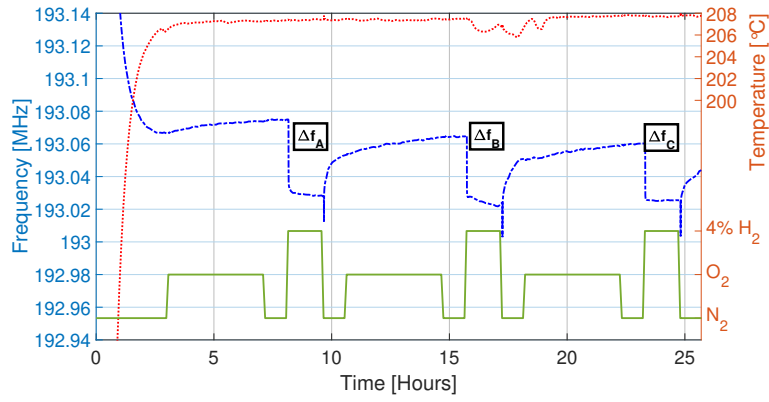


Figure C.3. Setup A4 test results at nominal furnace temperature 200°C for Device 3.

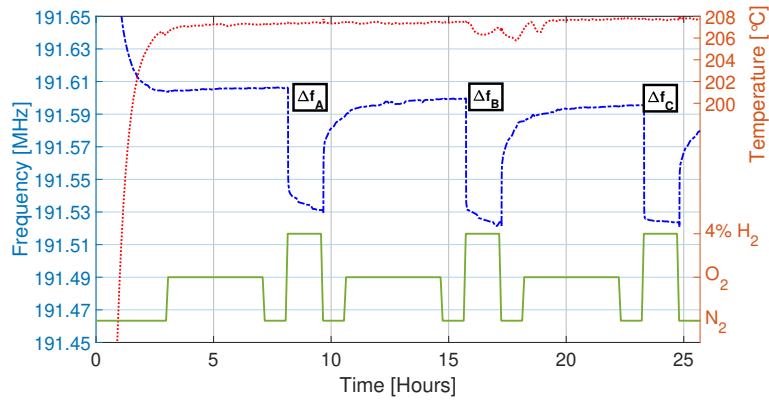


Figure C.4. Setup A4 test results at nominal furnace temperature 200°C for Device 4.

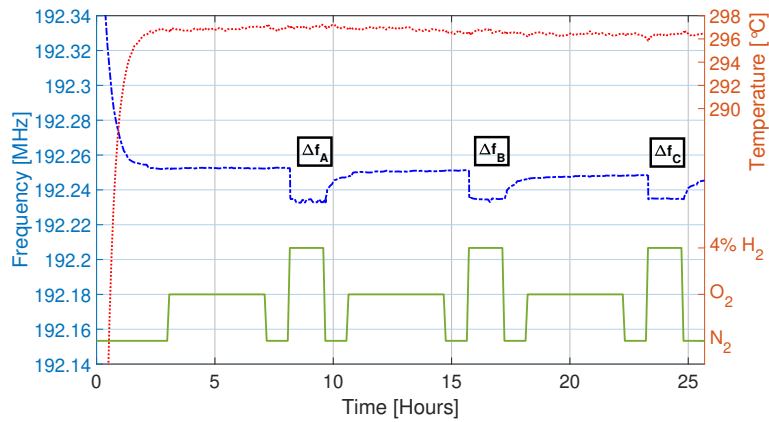


Figure C.5. Setup A4 test results at nominal furnace temperature 300°C for Device 1.

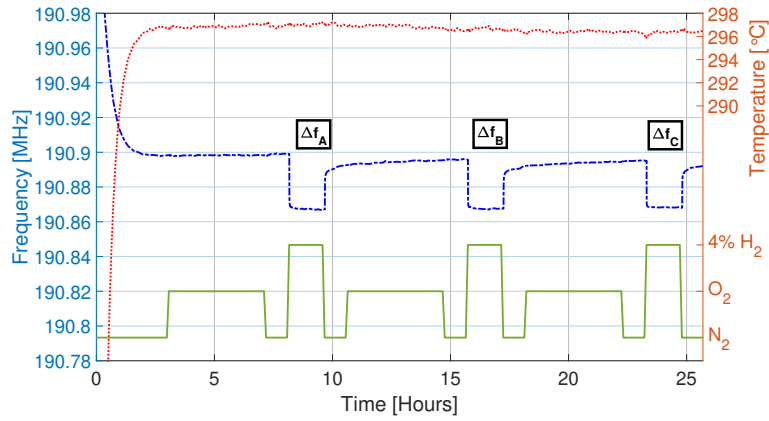


Figure C.6. Setup A4 test results at nominal furnace temperature 300°C for Device 2.

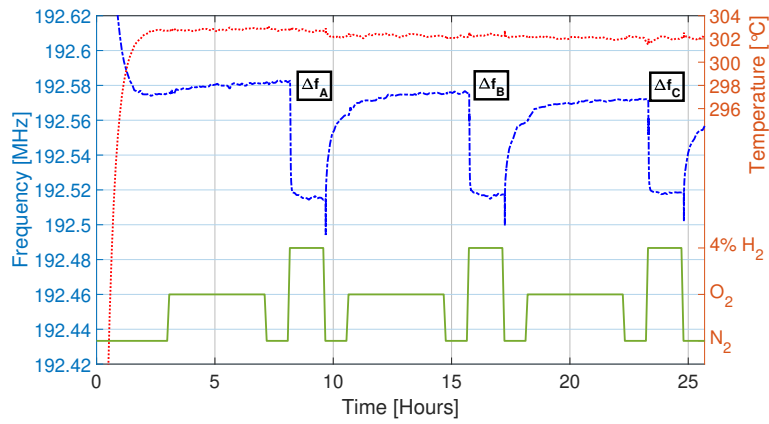


Figure C.7. Setup A4 test results at nominal furnace temperature 300°C for Device 3.

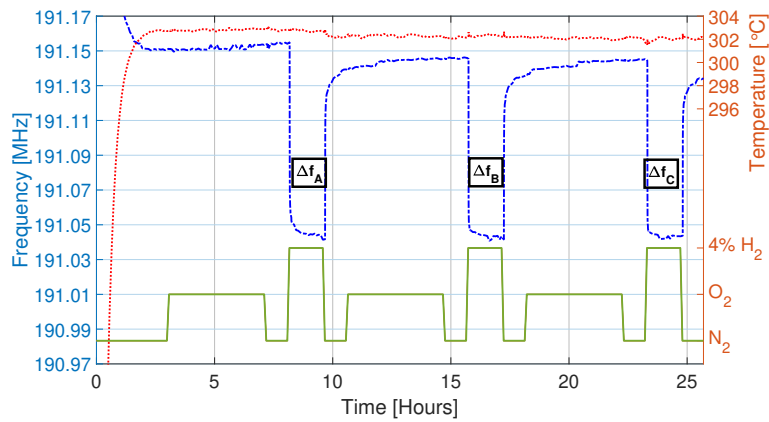


Figure C.8. Setup A4 test results at nominal furnace temperature 300°C for Device 4.

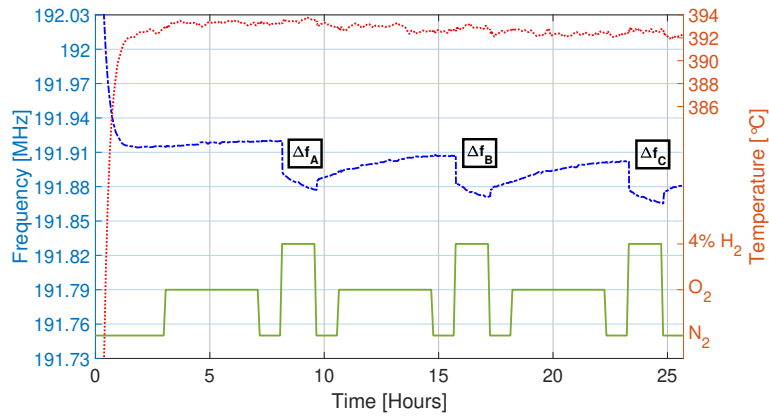


Figure C.9. Setup A4 test results at nominal furnace temperature 400°C for Device 1.

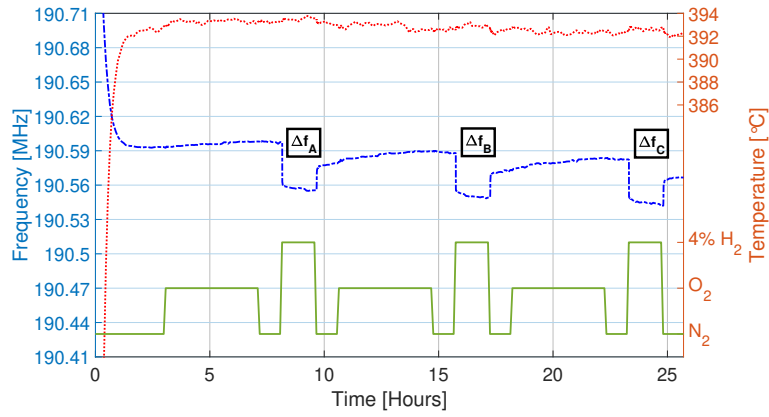


Figure C.10. Setup A4 test results at nominal furnace temperature 400°C for Device 4.

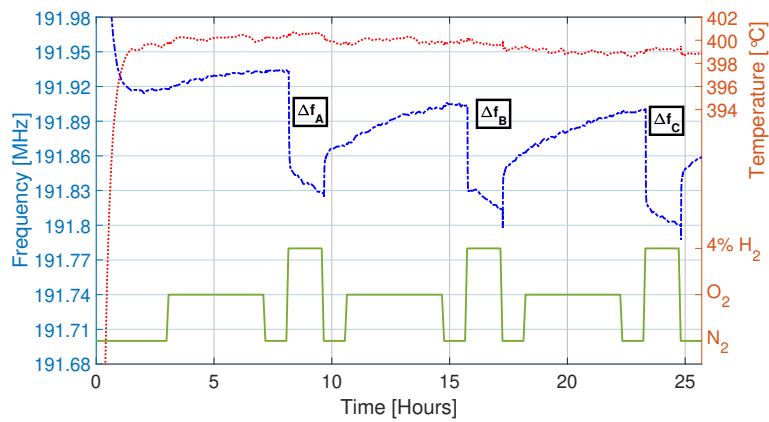


Figure C.11. Setup A4 test results at nominal furnace temperature 400°C for Device 3.

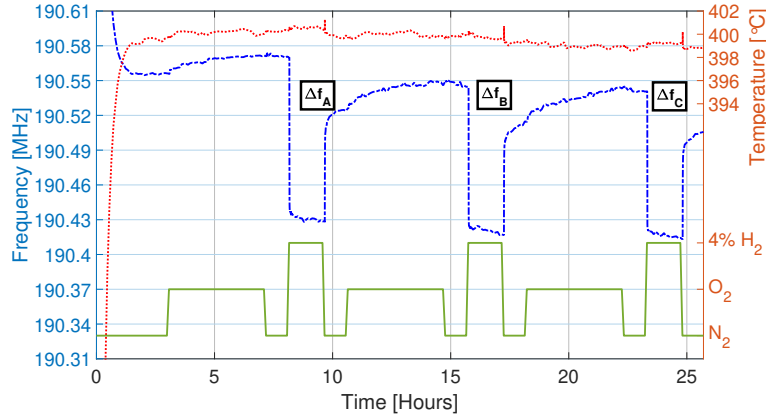


Figure C.12. Setup A4 test results at nominal furnace temperature 400°C for Device 4.

## C.2 O<sub>2</sub> Treatments

Results at room temperature from Setups A1, A3 and A4 related to oxygen treatments for Bare devices oriented along  $\Psi = 26.7^\circ$ , referenced in Section 4.5 are given in this section.

### C.2.1 O<sub>2</sub> Treatments at Room Temperature

Table C.2 shows the calculated frequency shifts as defined in Section 4.5.1 for tests involving room temperature O<sub>2</sub> treatments (13 tests). Tests 1-8 were conducted on Setup A1 (Device 3 and Device 4), Tests 9-11 were conducted on Setup A3 (Device 3), and Tests 12-13 were conducted on Setup A4 (Device 4). All tests documented in this subsection were conducted with 950 sccm flow rates. The corresponding tests are shown in Figures C.13-C.33. The first H<sub>2</sub> exposure frequency shift for Tests 1-8 was not recorded as at this point in time the devices were exposed to air after the end of a test (were not left idling in N<sub>2</sub> flow) and therefore humidity may have formed on the surface due to idling in air.

Table C.2. Compiled room temperature results for  $\Psi = 26.7^\circ$  devices.

Setup	Device	Test	Feature Magnitude (kHz)					
			A	B	C	D	E	
A1	3	1	108;					
A1	3	2		7.6; 4.1; 4.9;				
A1	3	3		5.6; 5.3; 5.5; 4.6;				
A1	3	4		7.3; 6.4; 3.9; 5.3;				
A1	3	5		7.0; 5.8; 7.0; 4.1;				
A1	3	6		7.7; 7.4;	9.8;	35.2;	45.7;	
A1	3	7		9.3; 8.4;	9.8;	34.6;	47.2;	
A1	3	8		8.5; 8.3;	9.0;	35.5;	47.2;	
A1	4	1	115;					
A1	4	2		10.2; 8.1; 7.4				
A1	4	3		6.1; 4.8; 5.3; 5.3;				
A1	4	4		6.2; 5.2; 4.3; 5.2;				
A1	4	5		5.0; 4.3; 3.6; 3.4;				
A1	4	6		6.6; 6.3;	8.2;	37.6;	45.6;	
A1	4	7		6.6; 6.2;	8.1;	38.1;	48.6;	
A1	4	8		6.3; 6.1;	8.0;	39.1;	48.8;	
A3	3	9	90.7;	6.9; 5.2; 6.4; 5.4; 5.9 ;4.5;	6.5; 6.1; 5.9;	28.3; 26.8; 24.5;	34.4; 33.3;	
A3	3	10		5.4; 4.9; 5.1; 4.7; 5.1; 4.6;	5.7; 5.3; 5.7;	24.1; 23.2; 22.3;	35.4; 29.7; 29.1;	
A3	3	11		4.6; 4.4; 4.7; 4.3; 4.9; 4.2;	5.4; 5.4; 5.9;	21.6; 22.3; 22.2;	30.3; 27.9; 28.4;	
A4	4	12	80.1;					
A4	4	13		2.8; 2.4; 2.4; 2.9; 2.5; 2.4; 2.7; 2.5; 2.2;	4.3; 4.3; 4.1;	22.1; 21.2; 20.4;	32.5; 27.0; 25.8;	

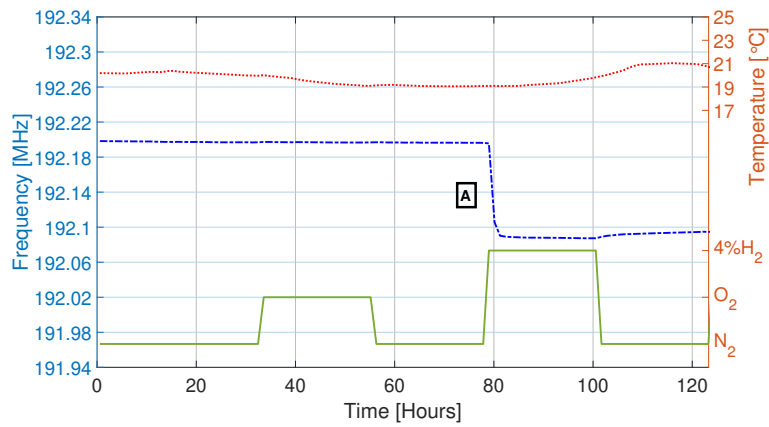


Figure C.13. Setup A1 Device 3 Test 1 results at room temperature.

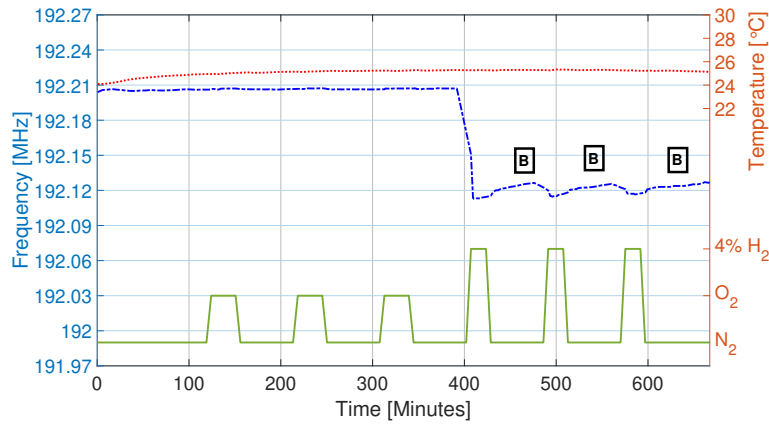


Figure C.14. Setup A1 Device 3 Test 2 results at room temperature.

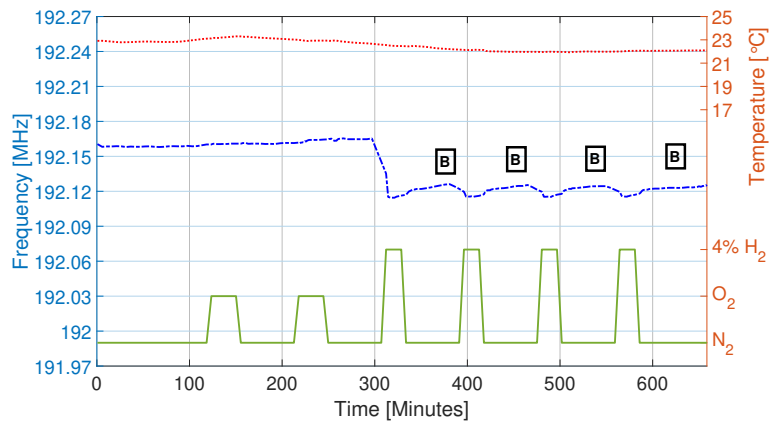


Figure C.15. Setup A1 Device 3 Test 3 results at room temperature.

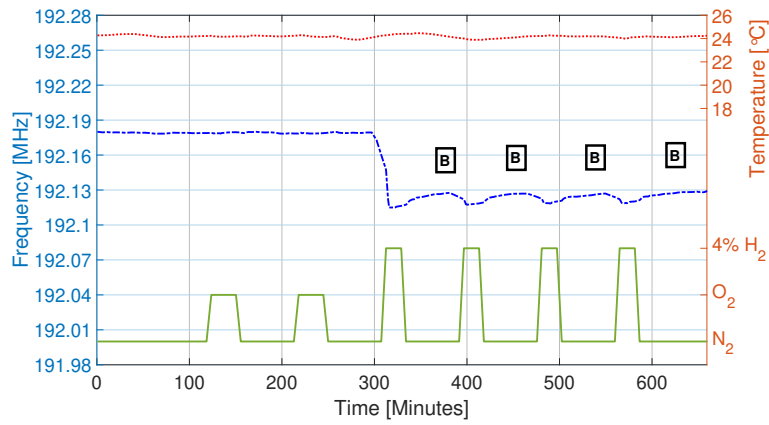


Figure C.16. Setup A1 Device 3 Test 4 results at room temperature.

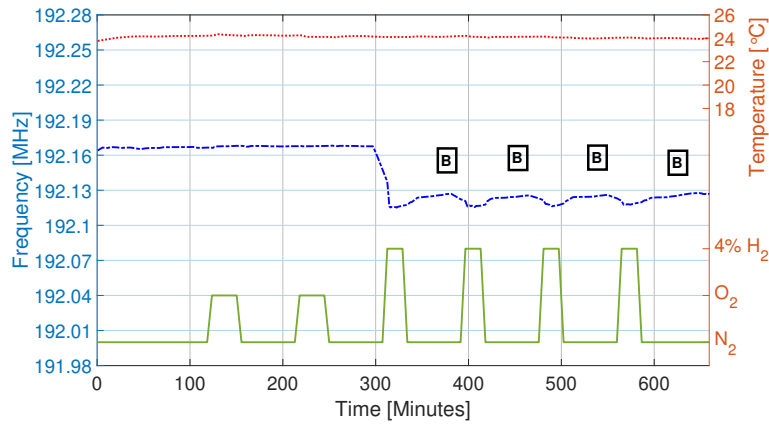


Figure C.17. Setup A1 Device 3 Test 5 results at room temperature.

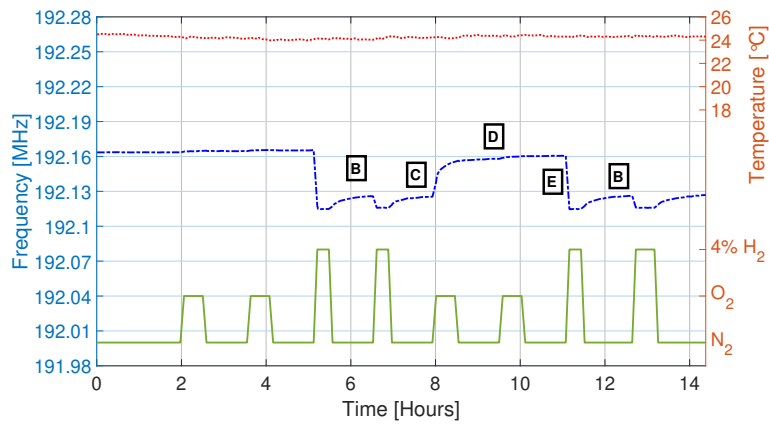


Figure C.18. Setup A1 Device 3 Test 6 results at room temperature.

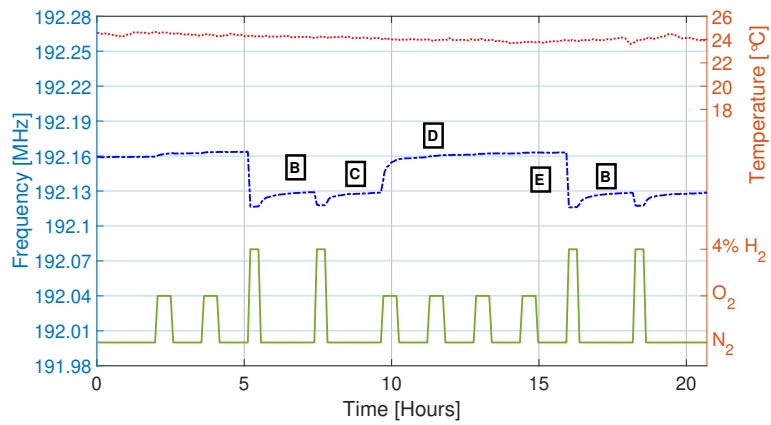


Figure C.19. Setup A1 Device 3 Test 7 results at room temperature.

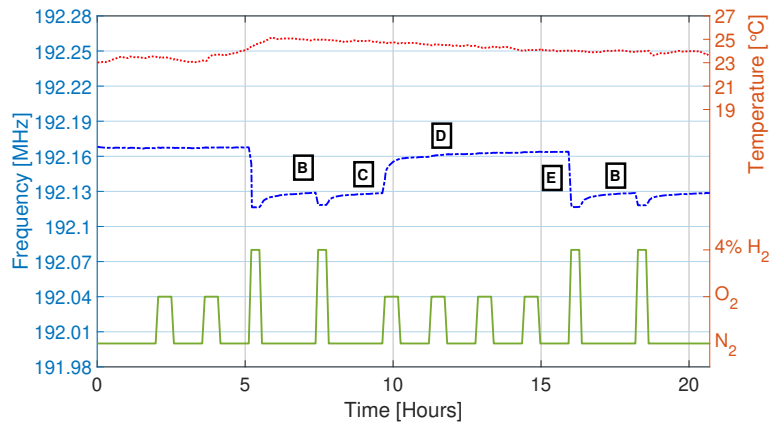


Figure C.20. Setup A1 Device 3 Test 1 results at room temperature.

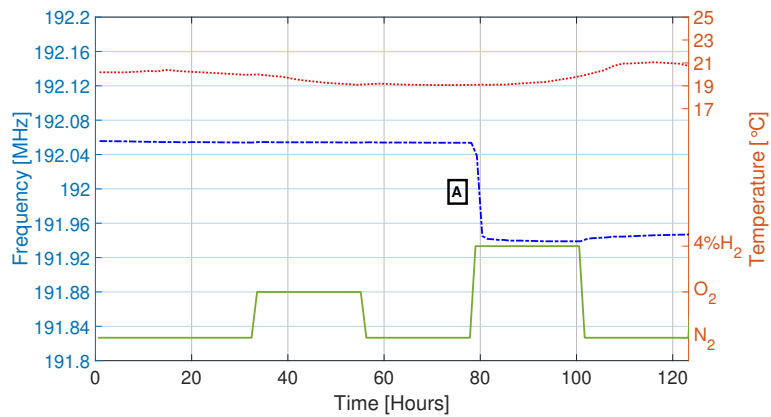


Figure C.21. Setup A1 Device 4 Test 1 results at room temperature.

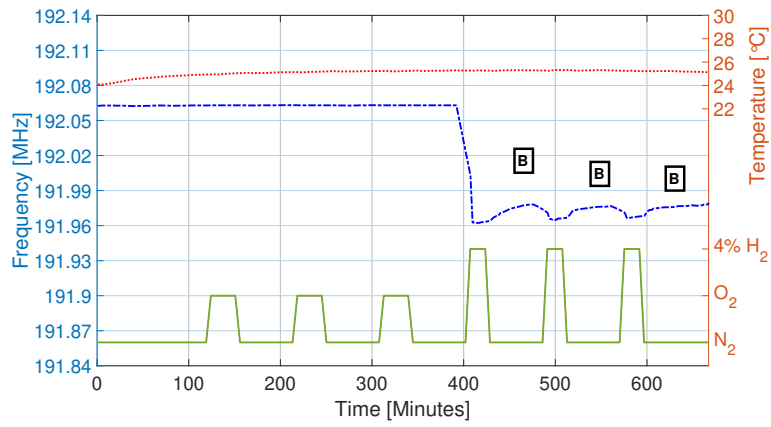


Figure C.22. Setup A1 Device 4 Test 2 results at room temperature.

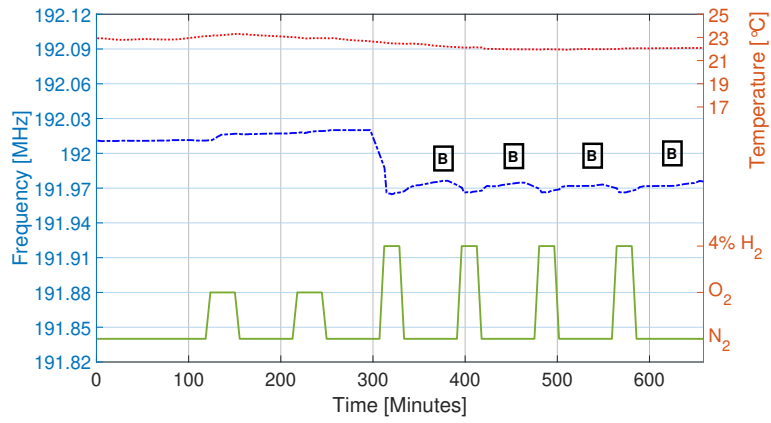


Figure C.23. Setup A1 Device 4 Test 3 results at room temperature.

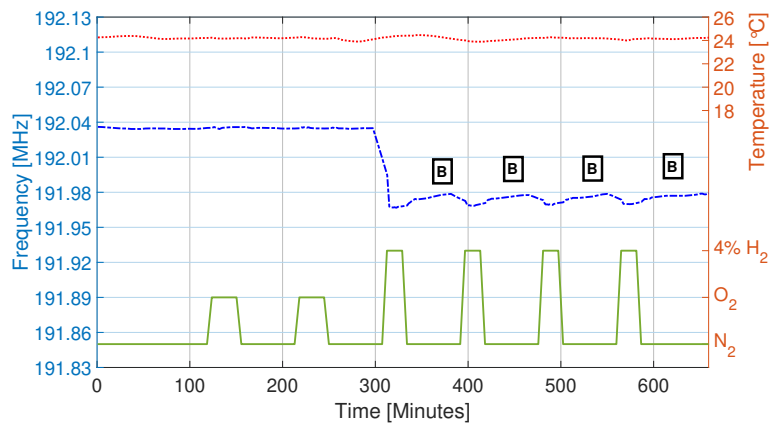


Figure C.24. Setup A1 Device 4 Test 4 results at room temperature.

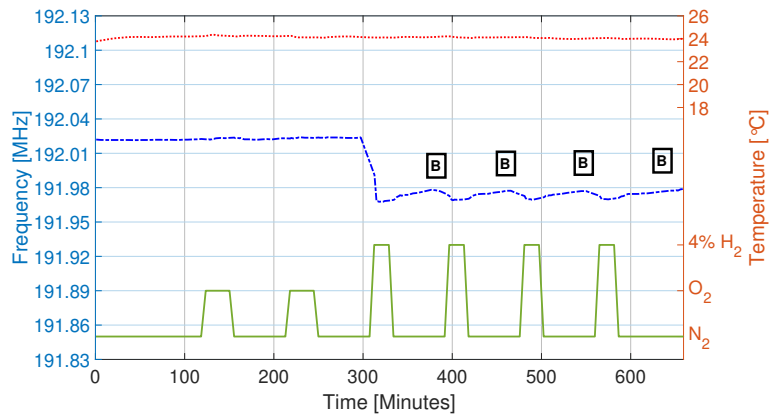


Figure C.25. Setup A1 Device 4 Test 5 results at room temperature.

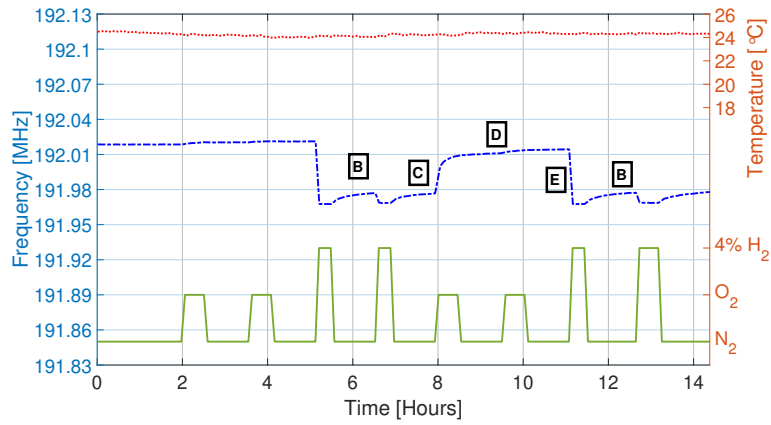


Figure C.26. Setup A1 Device 4 Test 6 results at room temperature.

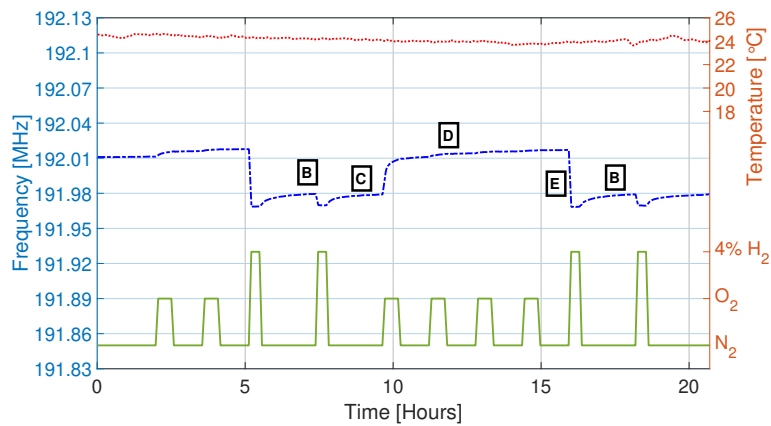


Figure C.27. Setup A1 Device 4 Test 7 results at room temperature.

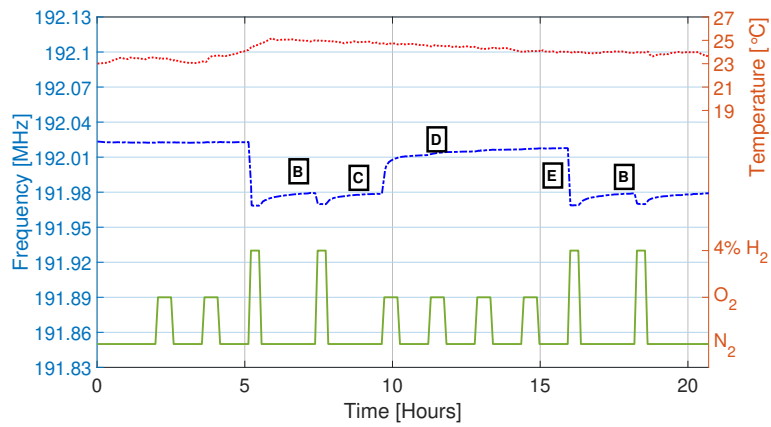


Figure C.28. Setup A1 Device 4 Test 1 results at room temperature.

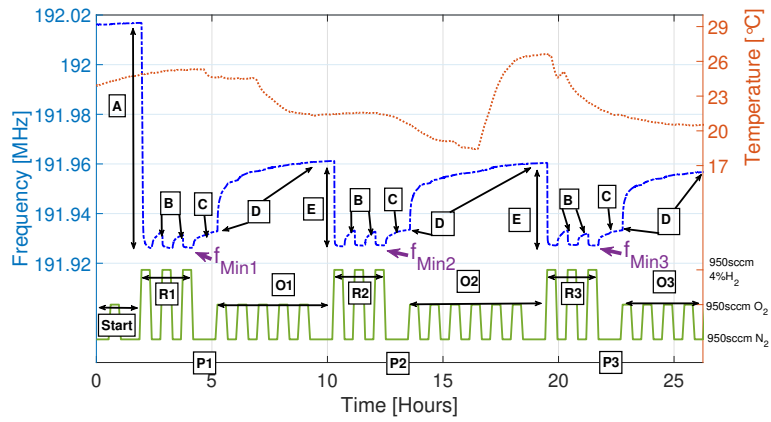


Figure C.29. Setup A3 Device 3 Test 9 results at room temperature.

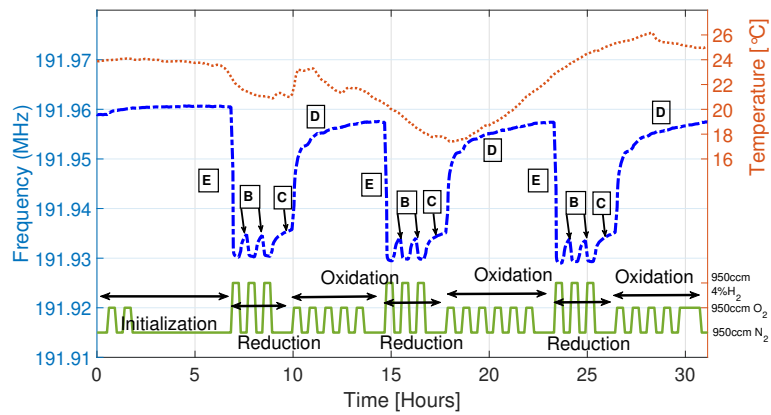


Figure C.30. Setup A3 Device 3 Test 10 results at room temperature.

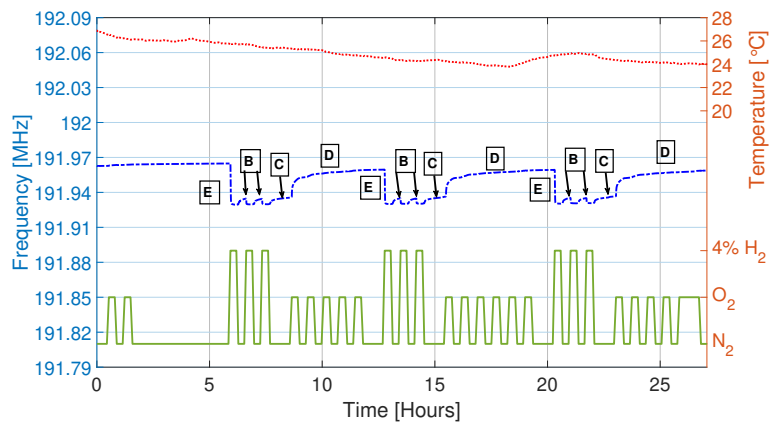


Figure C.31. Setup A3 Device 3 Test 11 results at room temperature.

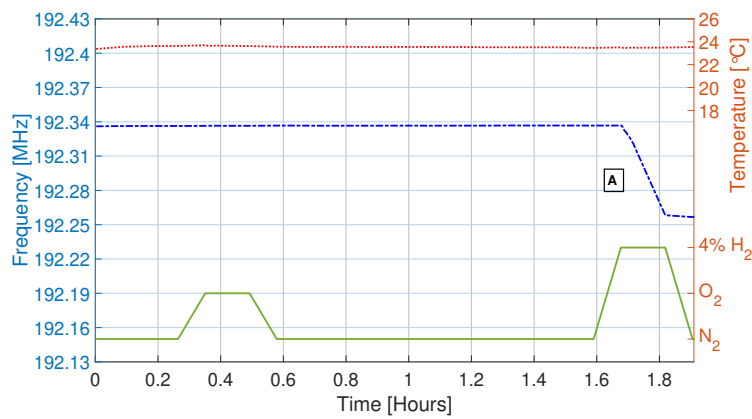


Figure C.32. Setup A4 Device 4 Test 12 results at room temperature.

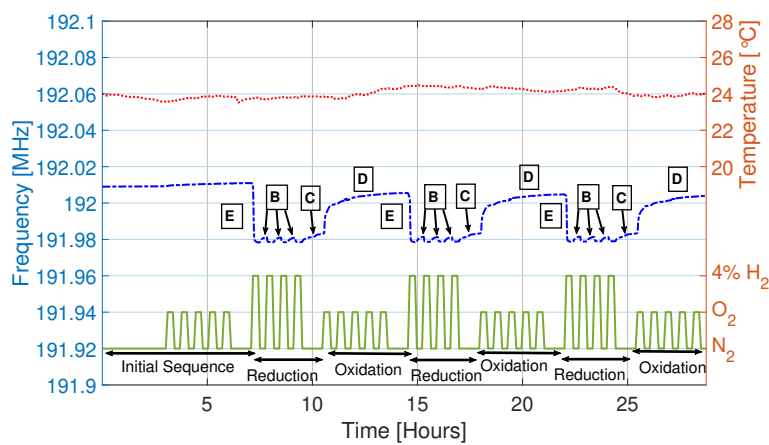


Figure C.33. Setup A4 Device 4 Test 13 results at room temperature.

## C.2.2 O<sub>2</sub> Conditioning at 650°C

For high-temperature conditioning, Setup A3 (Device 3, Film 2 Bare non-cycled 26.7°) and Setup A4 (Device 4, Film 2 Bare non-cycled 26.7°) were heated to 650°C in N<sub>2</sub>, soaked in O<sub>2</sub> for three hours at 650°C and allowed to cool down in O<sub>2</sub>, after which they were tested at room temperature. This was done twice for each device. The results for Setup A3 Device 3 were obtained with 950 sccm flow rates and the results for Setup A4 Device 4 were obtained with 100 sccm flow rates. The results are shown in Figures C.34-C.37 and the frequency shifts are given as referenced in Section 4.5.2.

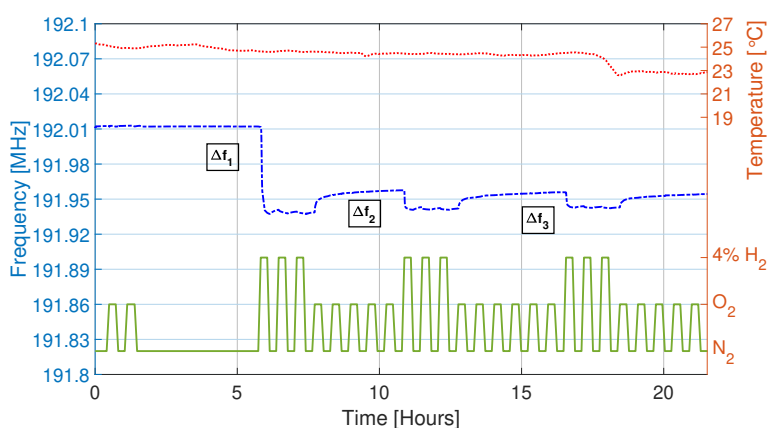


Figure C.34. Setup A3 Device 3 Test 1 results at room temperature after high-temperature conditioning in oxygen at 650°C.

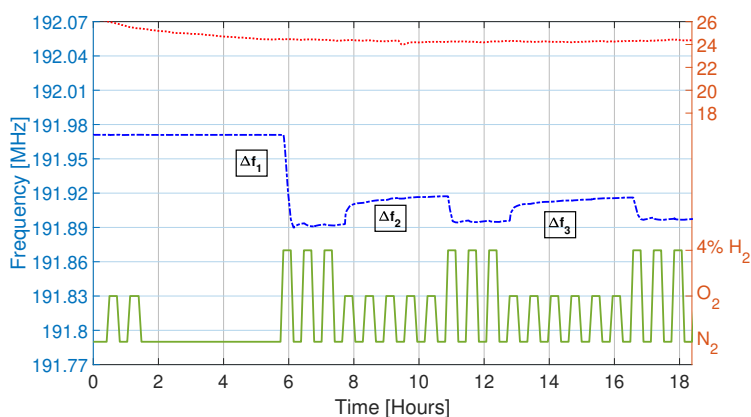


Figure C.35. Setup A3 Device 3 Test 2 results at room temperature after high-temperature conditioning in oxygen at 650°C.

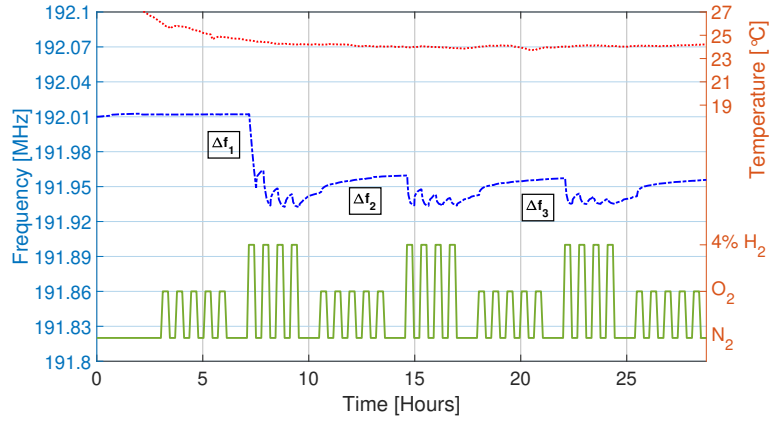


Figure C.36. Setup A Device 4 Test 1 results at room temperature after high-temperature conditioning in oxygen at 650°C.

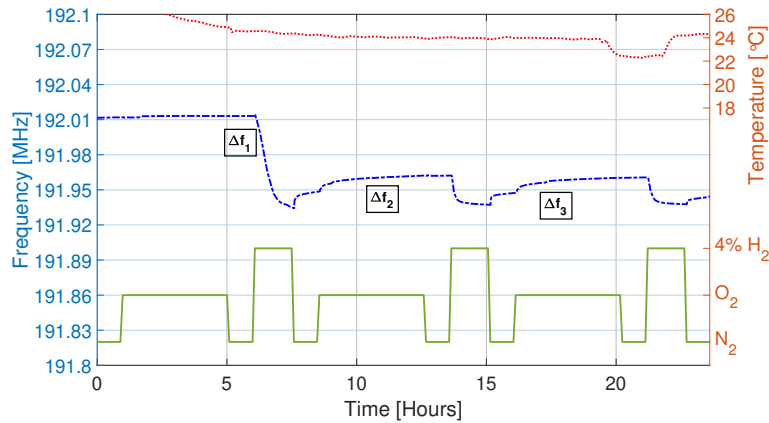


Figure C.37. Setup A4 Device 4 Test 2 results at room temperature after high-temperature conditioning in oxygen at 650°C.

### C.3 Influence of Orientation

This section gives the compiled results for high-temperature gas testing of Setup A3, A6 and A7.

#### C.3.1 Setup A3

The results for Setup A3 (Device 1 Film 2 Bare non-cycled 77.7°; Device 2 Film 2 Bare non-cycled 14.7°; Device 3 Film 2 Bare non-cycled 26.7°; Device 4 Film 2 Bare non-cycled 32.7°) are given as referenced in Section 4.6. Table C.3 shows the summary of compiled results as described for Setup A3 in Section 4.6 at each temperature (average of both chambers), with the corresponding maximum temperature variation  $\Delta T_i$  as described in Section 4.6 and the corresponding maximum normalized frequency variation due to the temperature variation using the temperature sensitivities calculated in Section 4.6. The results are given in Figures C.38-C.57. All results shown for this test were conducted with 950 sccm flow rates.

Table C.3. Tabulated results for Setup A3.

Device	$f_{0i}$ (MHz)	$\Delta f_1$ (kHz)	$\Delta f_2$ (kHz)	$\Delta T_i$ ( $^{\circ}C$ )	Max $\Delta f_T / f_{0i}$
21 $^{\circ}C$					
1	188.962	4	5	-0.61	-0.002
2	190.476	11	11	-0.61	-0.0009
3	191.929	28	28	-0.24	0.00009
4	191.436	22	23	-0.24	0.00001
97 $^{\circ}C$					
1	189.431	5	5	-0.36	-0.0009
2	190.685	12	11	-0.36	-0.0003
3	191.886	35	32	-0.17	0.0002
4	191.441	29	27	-0.17	0.0001
186 $^{\circ}C$					
1	189.776	9	8	-0.4	-0.0006
2	190.743	20	20	-0.4	0.00004
3	191.64	48	47	-0.24	0.0004
4	191.251	42	40	-0.24	0.0004
276 $^{\circ}C$					
1	189.924	16	16	-0.35	-0.0001
2	190.621	37	38	-0.35	0.0003
3	191.215	85	86	-0.34	0.0009
4	190.882	73	72	-0.34	0.0008
373 $^{\circ}C$					
1	189.86	27	26	-0.75	0.0005
2	190.299	58	58	-0.75	0.001
3	190.579	137	137	-0.59	0.002
4	190.314	106	105	0.59	-0.002
471 $^{\circ}C$					
1	189.695	25	28	-0.48	0.0009
2	189.904	58	59	-0.48	0.001
3	190.045	NA	NA	-0.56	0.002
4	189.772	NA	NA	-0.56	0.002

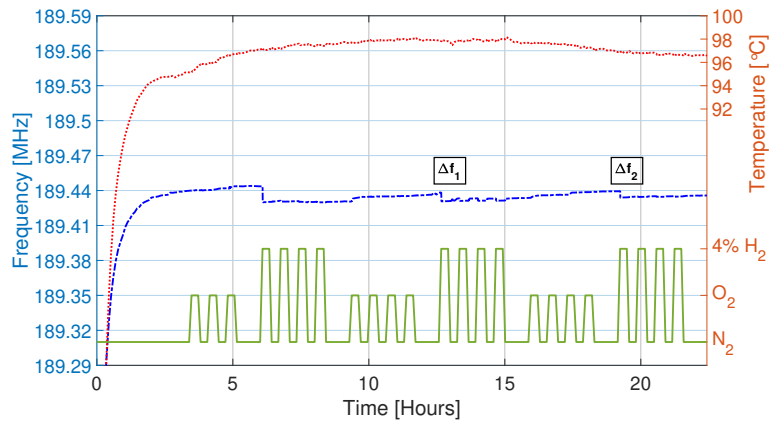


Figure C.38. Setup A3 Device 1 test results at 100°C.

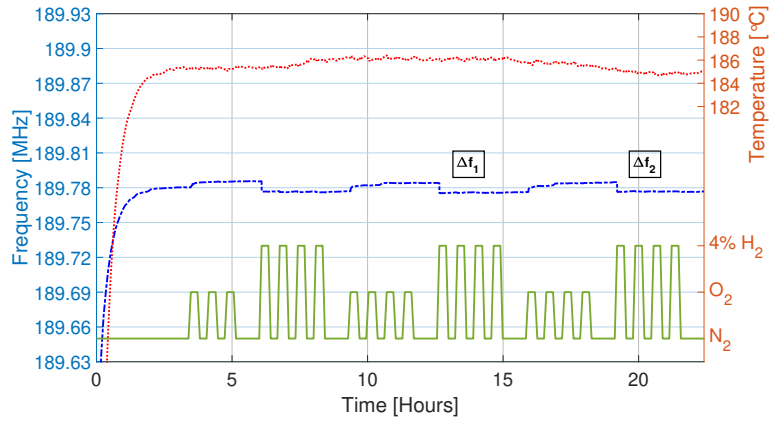


Figure C.39. Setup A3 Device 1 test results at 200°C.

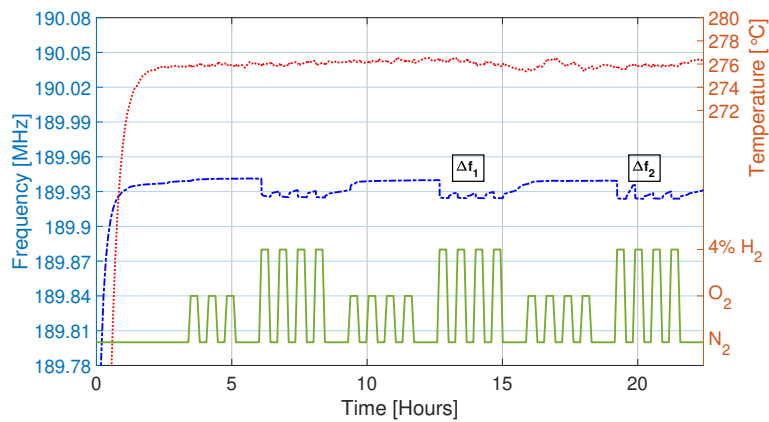


Figure C.40. Setup A3 Device 1 test results at 300°C.

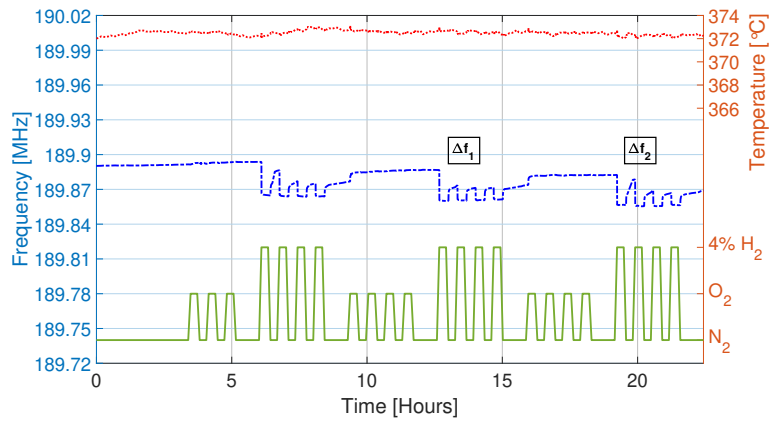


Figure C.41. Setup A3 Device 1 test results at 400°C.

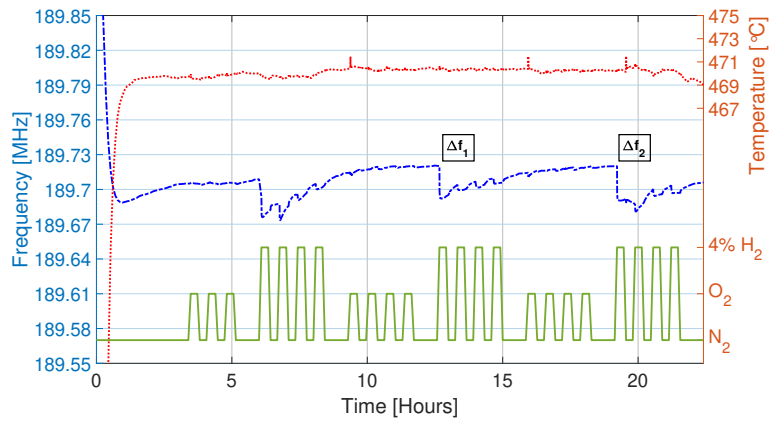


Figure C.42. Setup A3 Device 1 test results at 500°C.

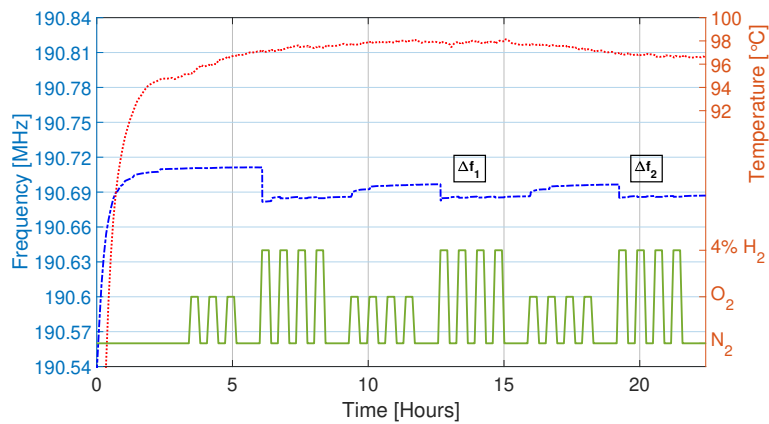


Figure C.43. Setup A3 Device 2 test results at 100°C.

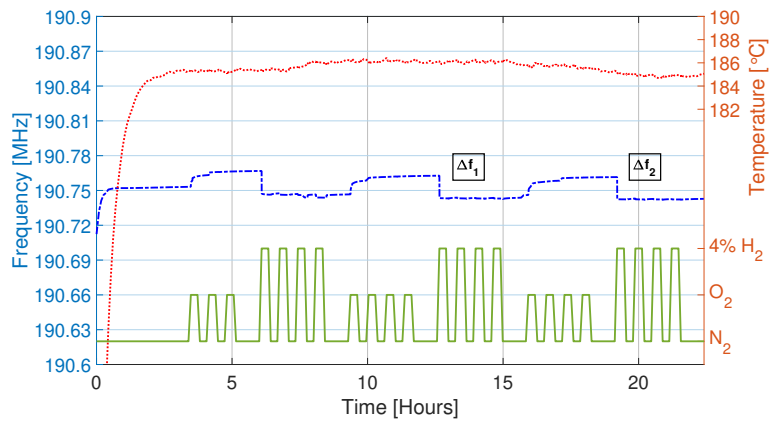


Figure C.44. Setup A3 Device 2 test results at 200°C.

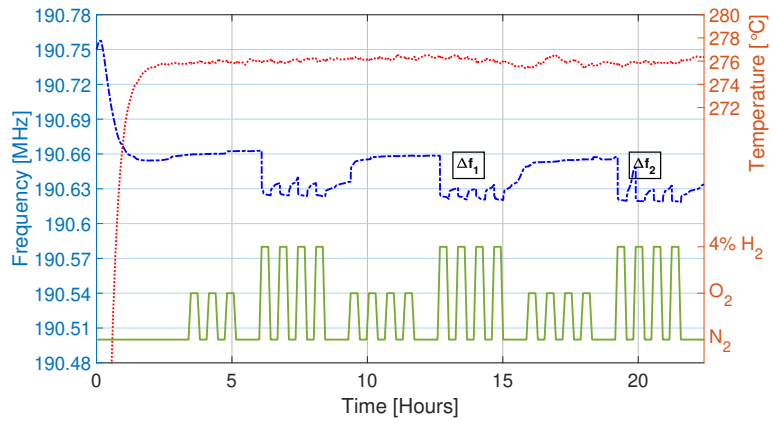


Figure C.45. Setup A3 Device 2 test results at 300°C.

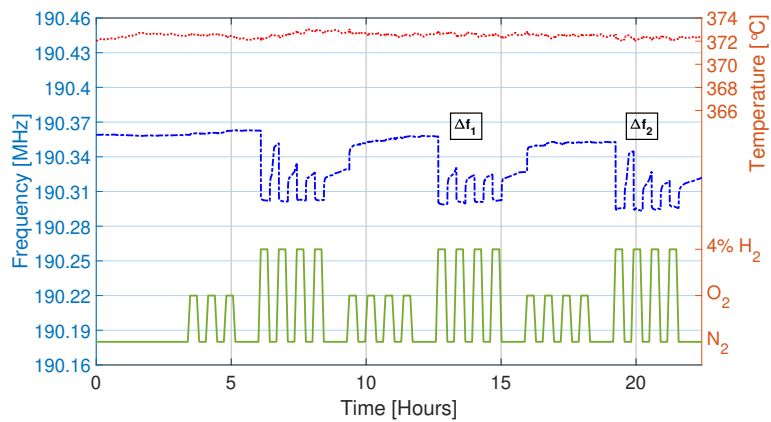


Figure C.46. Setup A3 Device 2 test results at 400°C.

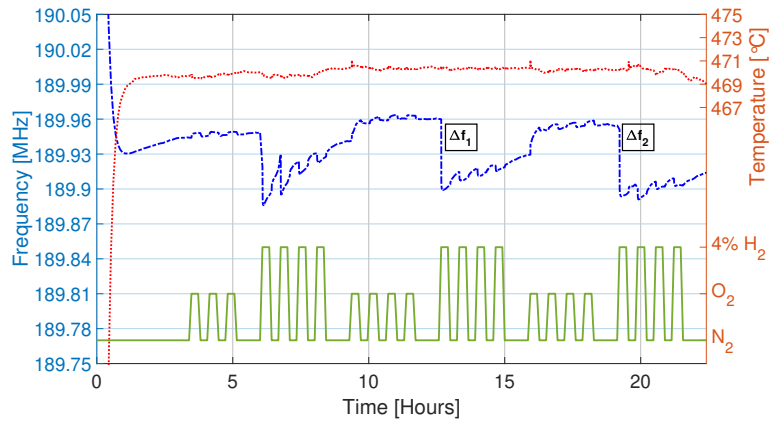


Figure C.47. Setup A3 Device 2 test results at 500°C.

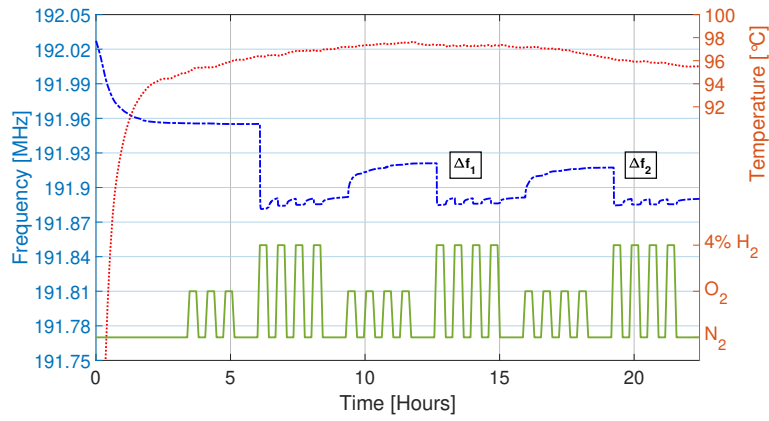


Figure C.48. Setup A3 Device 3 test results at 100°C.

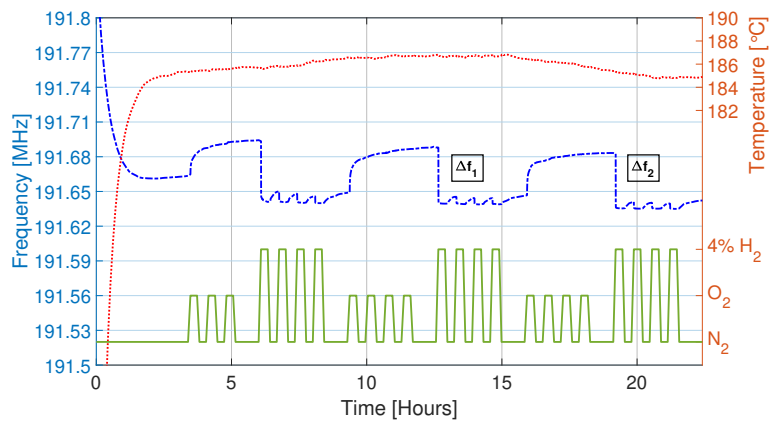


Figure C.49. Setup A3 Device 3 test results at 200°C.

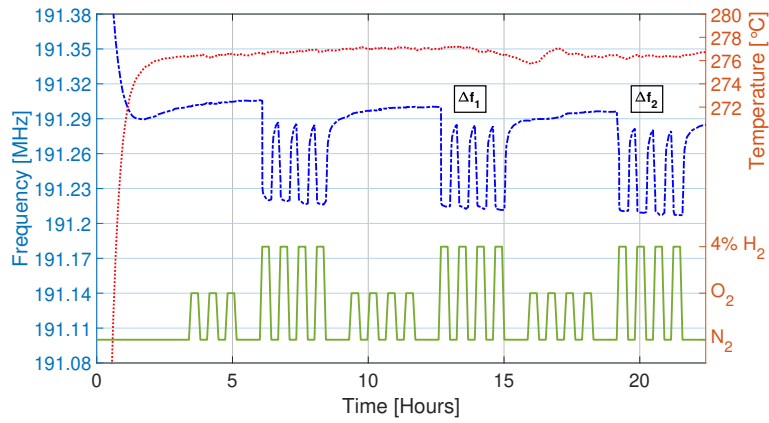


Figure C.50. Setup A3 Device 3 test results at 300°C.

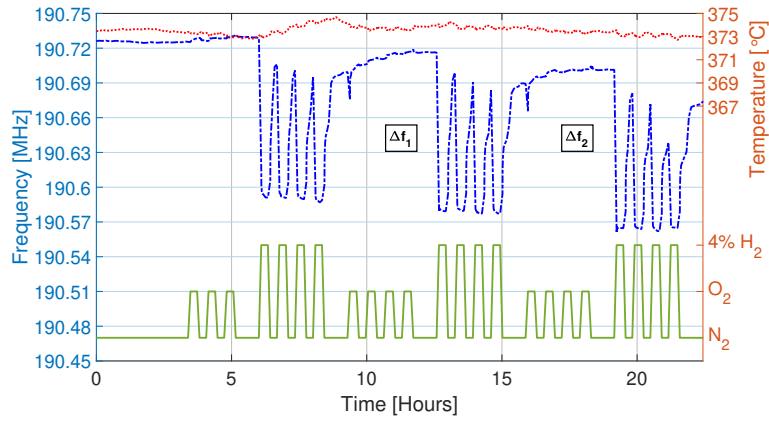


Figure C.51. Setup A3 Device 3 test results at 400°C.

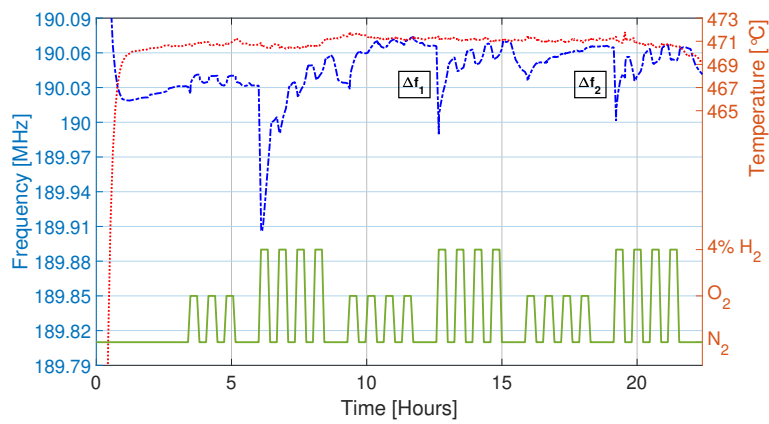


Figure C.52. Setup A3 Device 3 test results at 500°C.

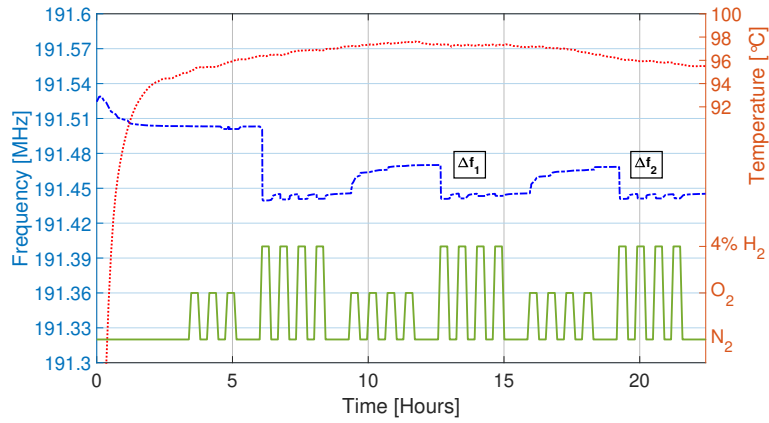


Figure C.53. Setup A3 Device 4 test results at 100°C.

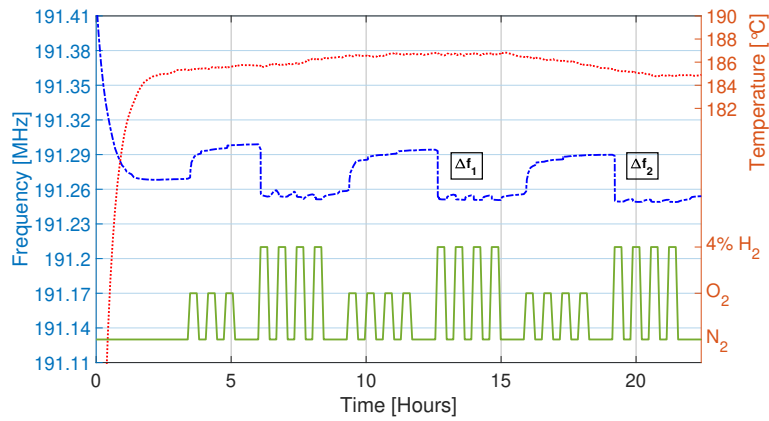


Figure C.54. Setup A3 Device 4 test results at 200°C.

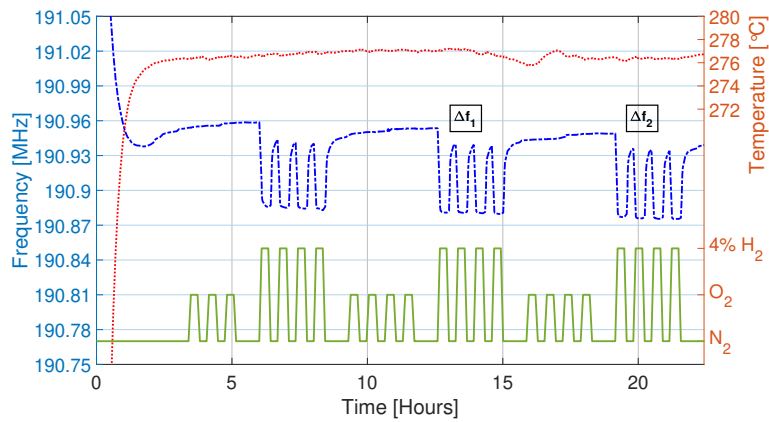


Figure C.55. Setup A3 Device 4 test results at 300°C.

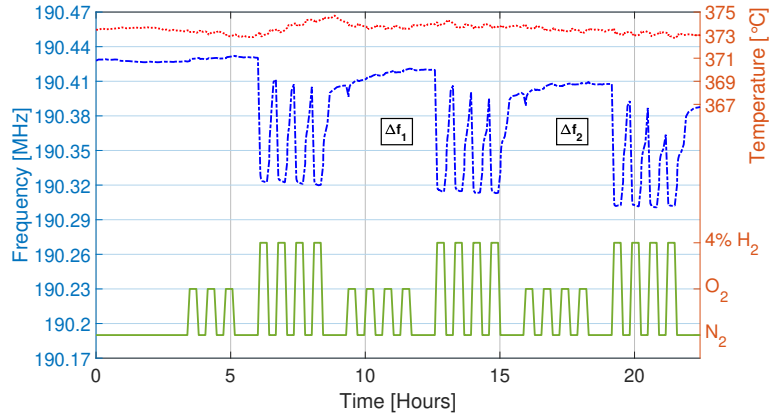


Figure C.56. Setup A3 Device 4 test results at 400°C.

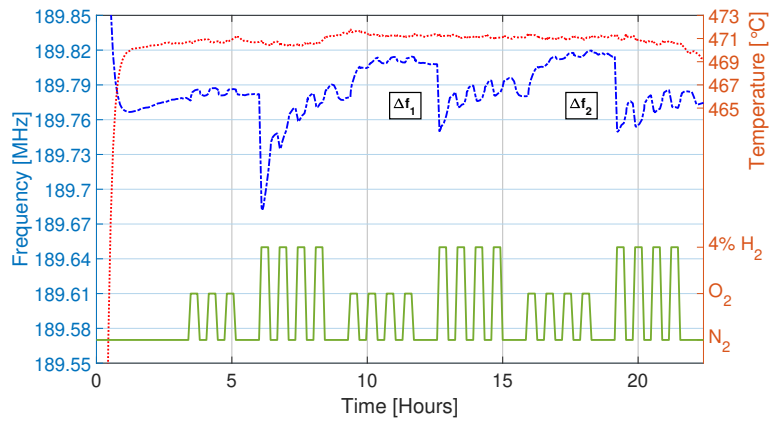


Figure C.57. Setup A3 Device 4 test results at 500°C.

### C.3.2 Setup A6

The results for Setup A6 (Device 1 Film 1 Bare non-cycled 20.7°; Device 2 Film 1 Bare non-cycled 77.7°; Device 3 Film 1 Bare non-cycled 20.7°; Device 4 Film 1 Bare non-cycled 26.7°) are given as referenced in Section 4.6. Table C.3 shows the summary of compiled results as described for Setup A6 in Section 4.6 at each temperature (average of the corresponding chamber). The results are given in Figures C.58-C.73. All results shown for this section were conducted with 100 sccm flow rates.

Table C.4. Tabulated results for Setup A6.

Temp (°C)	$f_{oi}$ (MHz)	A (kHz)	B (kHz)	C (kHz)	D (kHz)
Device 1					
217	191.51	44.5	38.1	41.3	46.6
312	191.088	42.1	35.3	39.6	45.7
409	190.521	52.2	45.3	46.3	52.8
510	189.832	51.1	38.8	40.6	56.3
Device 2					
217	190.421	8.2	8.2	9	9
312	190.951	7.9	7.2	7.4	8.2
409	190.408	12.9	10.2	11.4	13.1
510	190.138	30.3	19.6	23.4	32.1
Device 3					
220	191.532	40.3	37.6	40	42.5
316	191.089	37.6	34.3	38	40.6
412	190.499	46.9	44.6	44.1	49.4
512	189.768	58.2	45.3	47.2	62.3
Device 4					
220	192.102	54.2	47.1	48.6	49.4
316	191.636	43.8	34.2	37.1	40.1
412	191.013	58.1	49.7	51.6	58.8
512	190.256	78	55.6	62	73

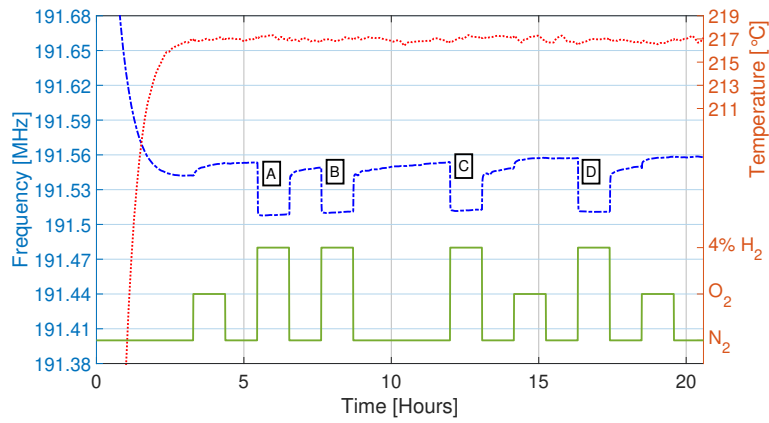


Figure C.58. Setup A6 Device 1 test results at 220°C.

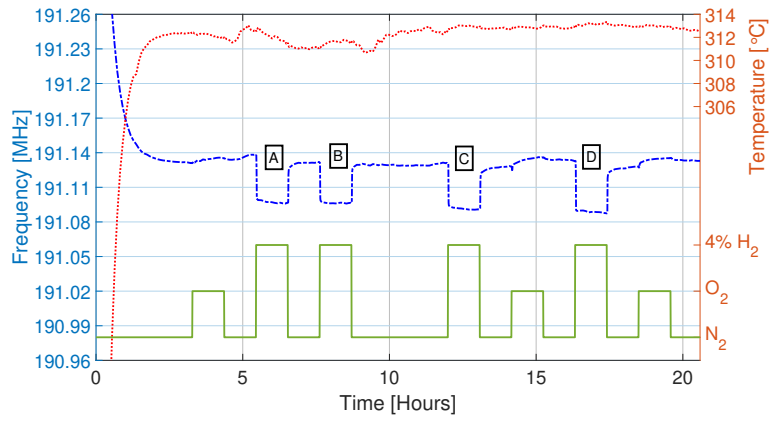


Figure C.59. Setup A6 Device 1 test results at 320°C.

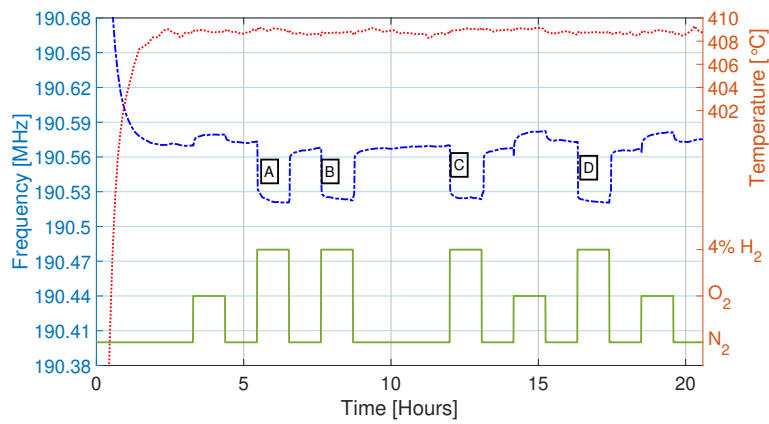


Figure C.60. Setup A6 Device 1 test results at 420°C.

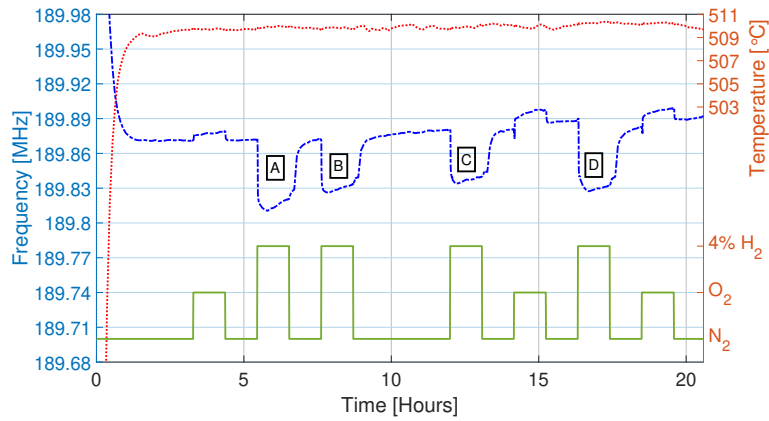


Figure C.61. Setup A6 Device 1 test results at 520°C.

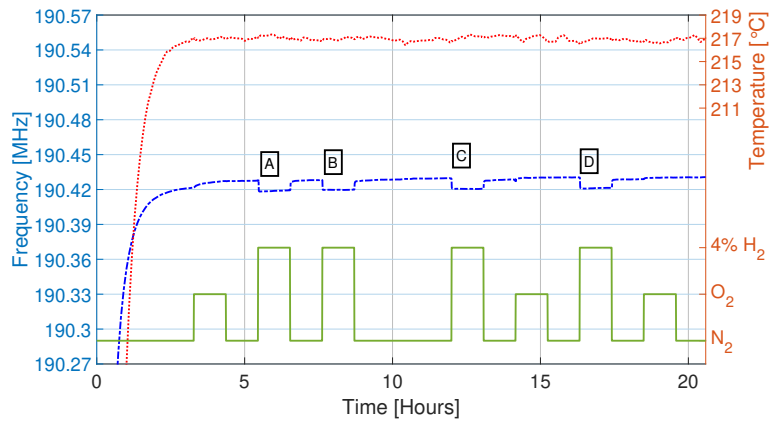


Figure C.62. Setup A6 Device 2 test results at 220°C.

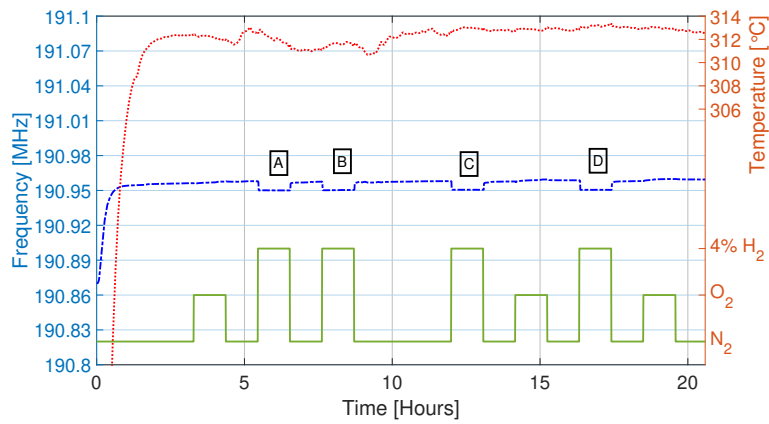


Figure C.63. Setup A6 Device 2 test results at 320°C.

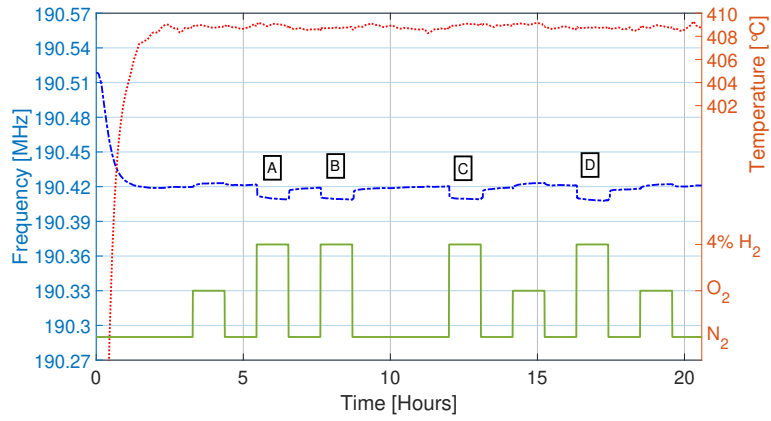


Figure C.64. Setup A6 Device 2 test results at 420°C.

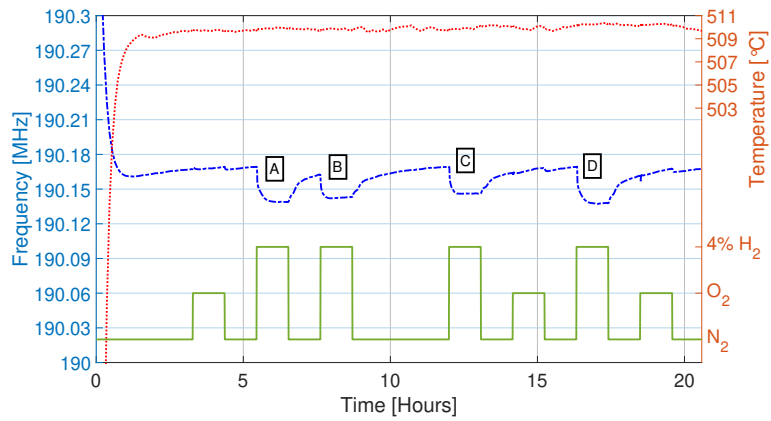


Figure C.65. Setup A6 Device 2 test results at 520°C.

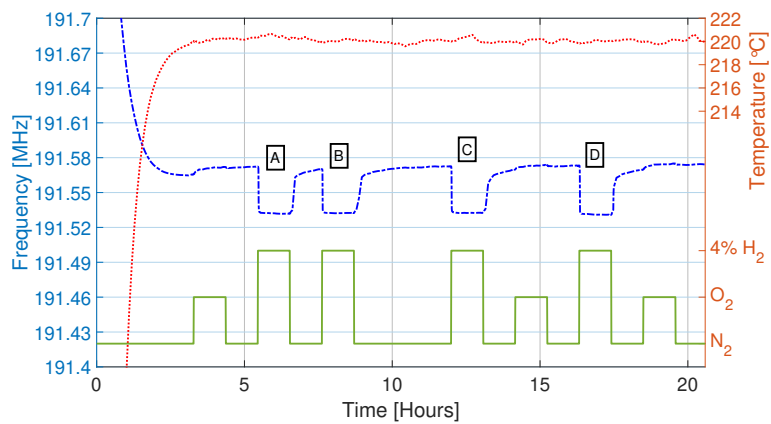


Figure C.66. Setup A6 Device 3 test results at 220°C.

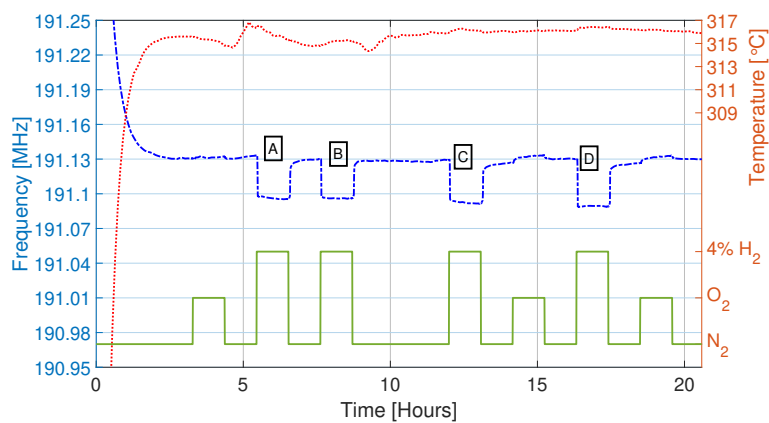


Figure C.67. Setup A6 Device 3 test results at 320°C.

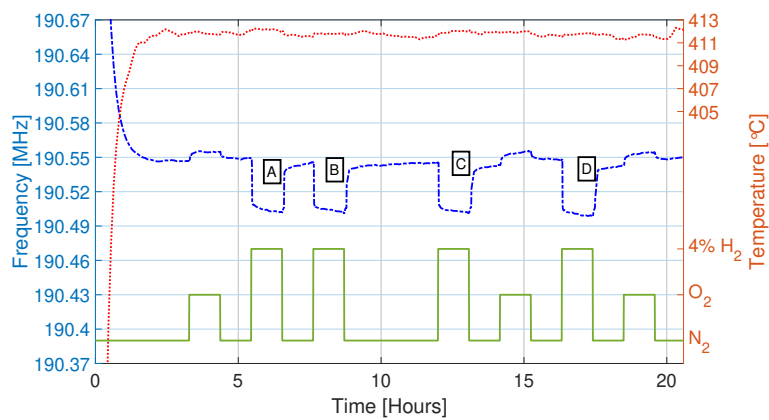


Figure C.68. Setup A6 Device 3 test results at 420°C.

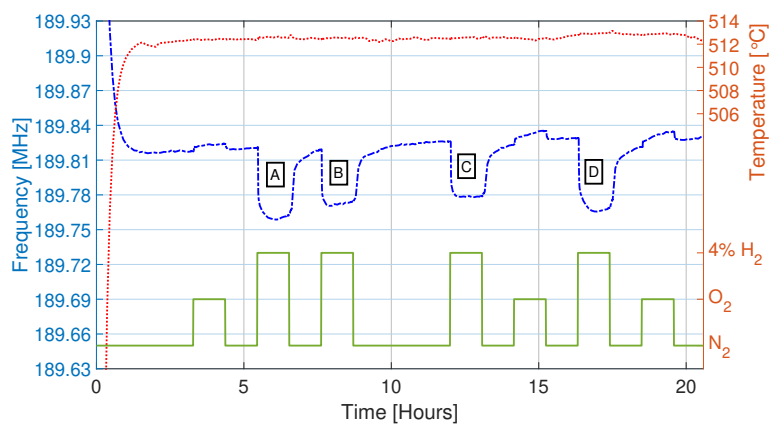


Figure C.69. Setup A6 Device 3 test results at 520°C.

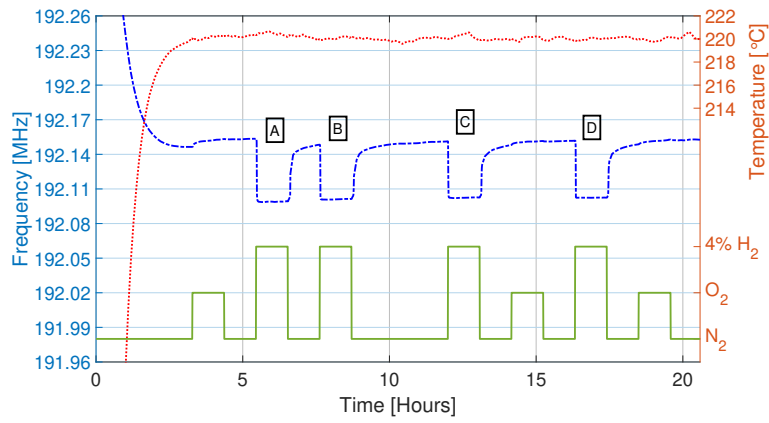


Figure C.70. Setup A6 Device 4 test results at 220°C.

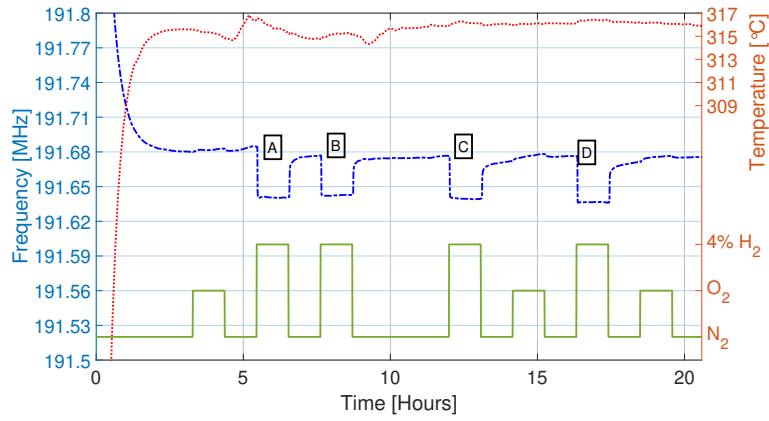


Figure C.71. Setup A6 Device 4 test results at 320°C.

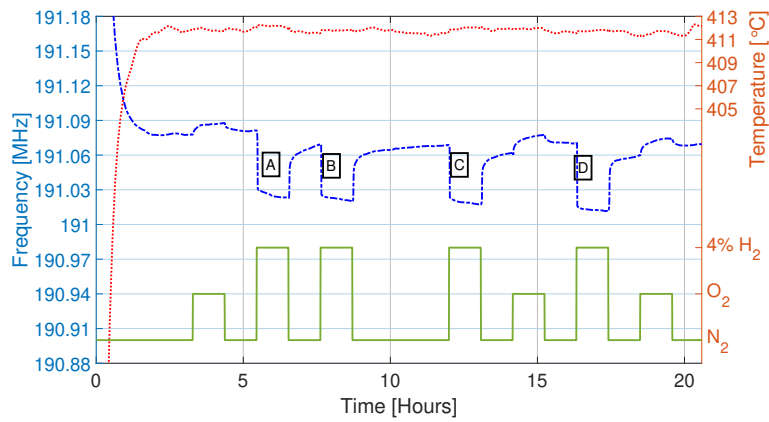


Figure C.72. Setup A6 Device 4 test results at 420°C.

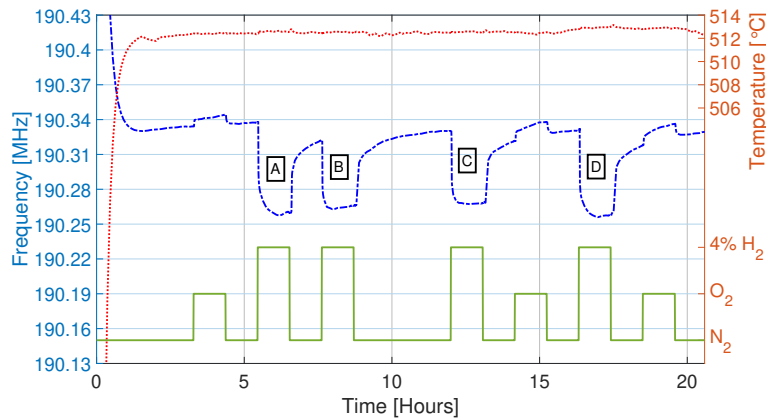


Figure C.73. Setup A6 Device 4 test results at 520°C.

### C.3.3 Setup A7

The results for Setup A7 (Device 1 Film 1 Bare cycled 26.7°; Device 2 Film 1 Bare cycled 77.7°; Device 3 Film 1 Bare cycled 26.7°; Device 4 Film 1 Bare cycled 77.7°) are given as referenced in Section 4.6. Table C.5 shows the summary of compiled results as described for Setup A7 in Section 4.6 at each temperature (average of the corresponding TC measurements alongside standard deviation of temperature for a 4-hour period starting 1.5 hours before the first reduction and ending 1.5 hours after the end of the first reduction) and the recorded frequencies as described in Section 4.6 for Setup A7 results. The results are given in Figures C.74-C.107. All results shown for this section were conducted with 100 sccm flow rates. The results at 400°C and 500°C for Device 3 were not recorded due to a mistake in data acquisition that copied the data for Device 2 instead of the data for Device 3 at those temperatures.

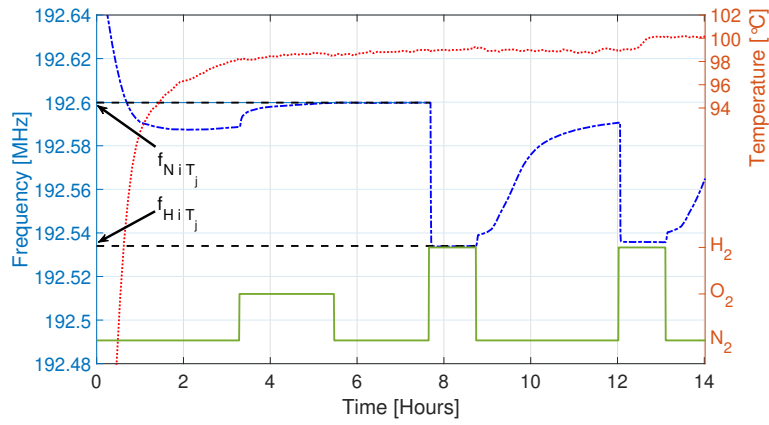


Figure C.74. Setup A7 Device 1 test results at 100°C.

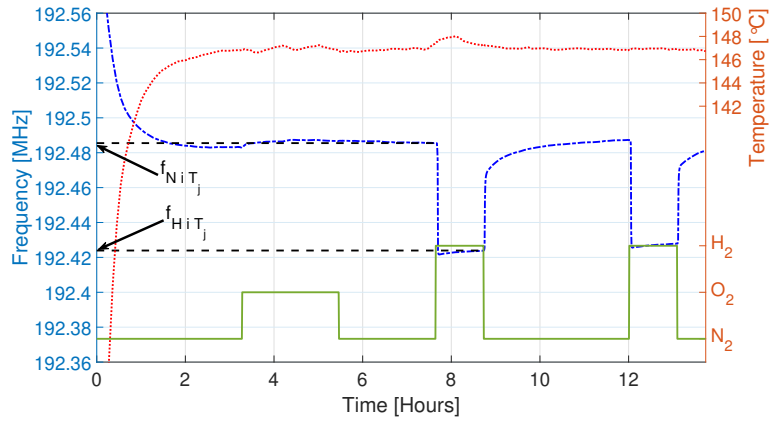


Figure C.75. Setup A7 Device 1 test results at 150°C.

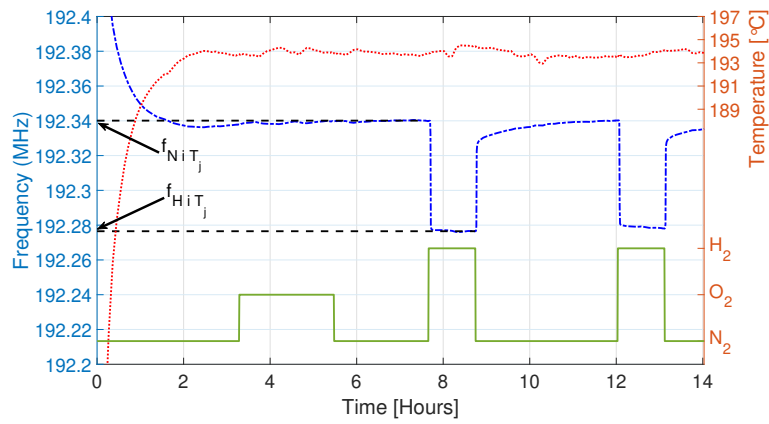


Figure C.76. Setup A7 Device 1 test results at 200°C.

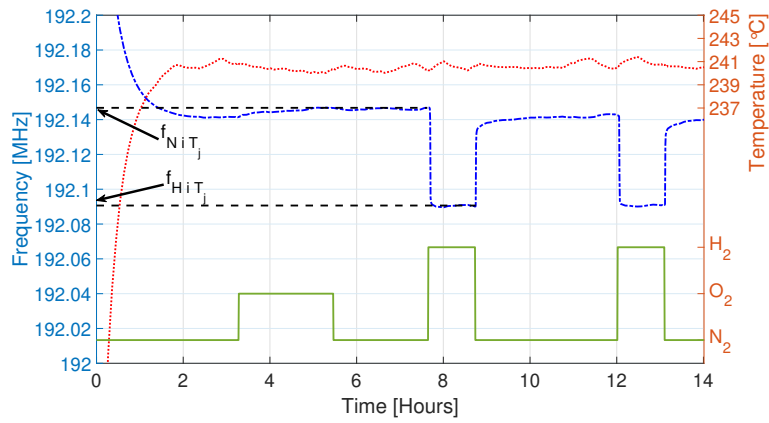


Figure C.77. Setup A7 Device 1 test results at 250°C.

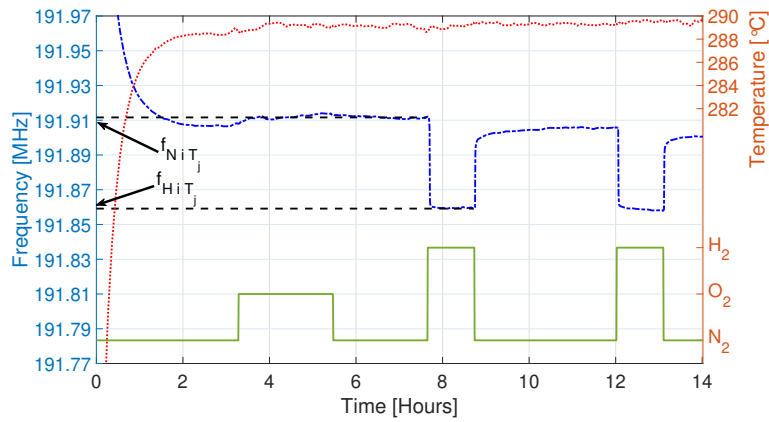


Figure C.78. Setup A7 Device 1 test results at 300°C.

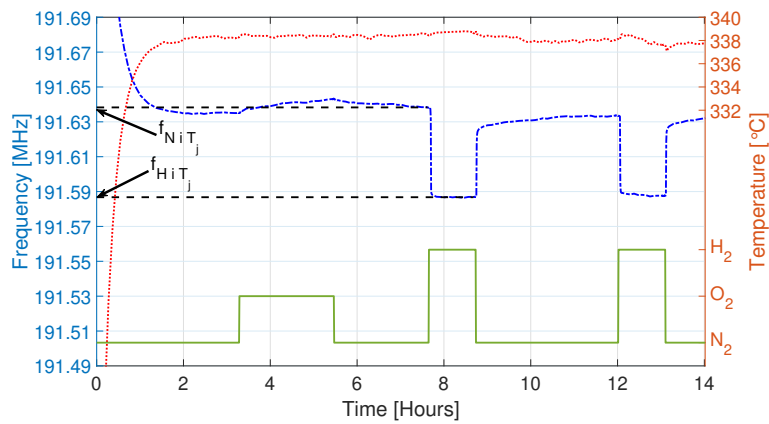


Figure C.79. Setup A7 Device 1 test results at 350°C.

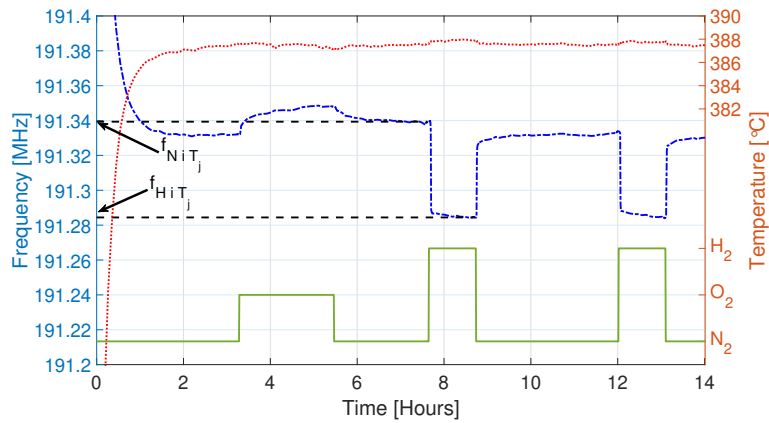


Figure C.80. Setup A7 Device 1 test results at 400°C.

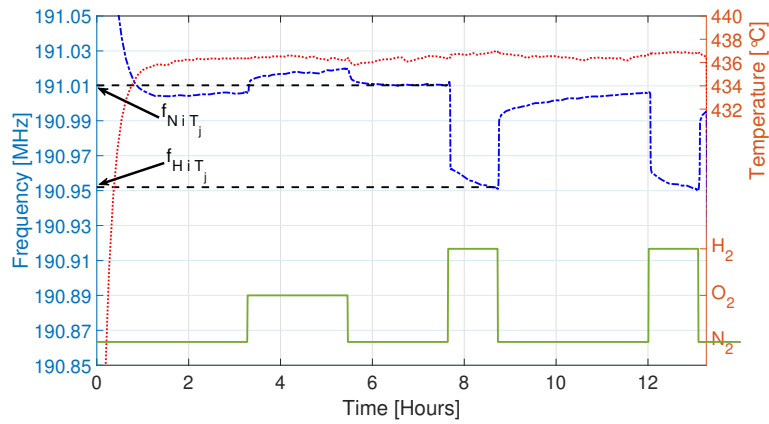


Figure C.81. Setup A7 Device 1 test results at 450°C.

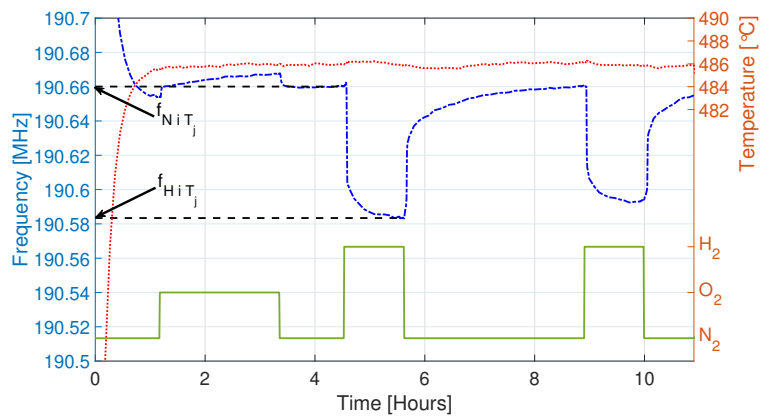


Figure C.82. Setup A7 Device 1 test results at 500°C.

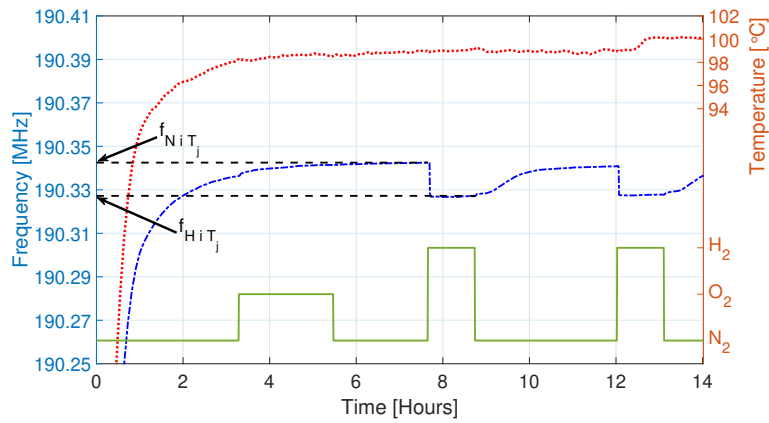


Figure C.83. Setup A7 Device 2 test results at 100°C.

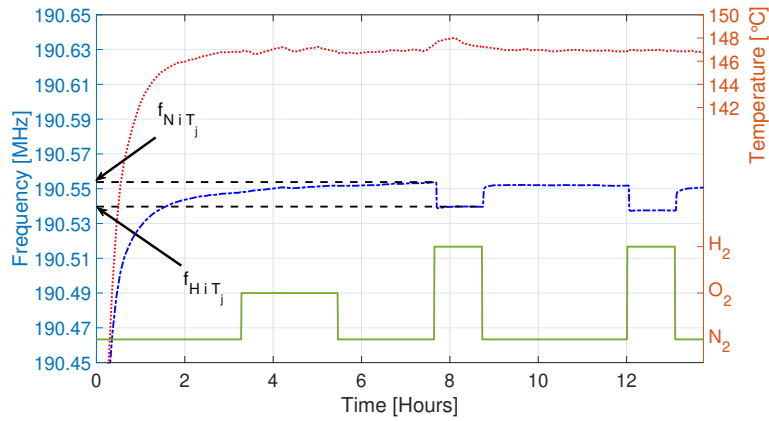


Figure C.84. Setup A7 Device 2 test results at 150°C.

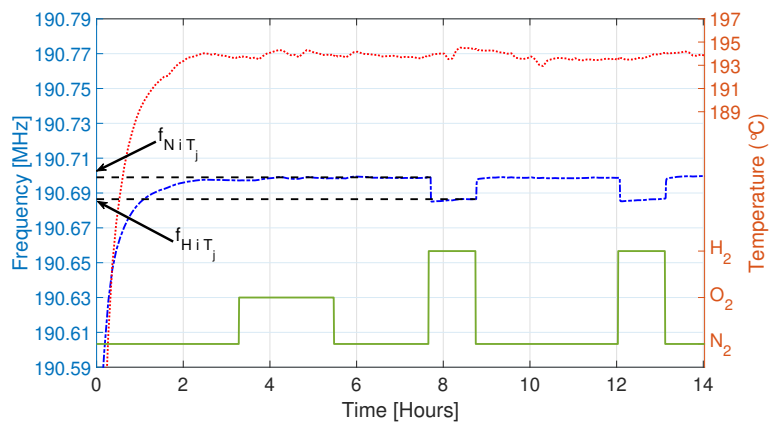


Figure C.85. Setup A7 Device 2 test results at 200°C.

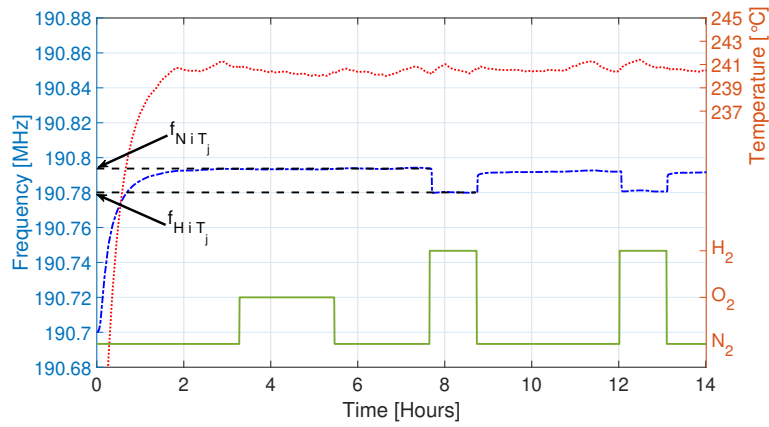


Figure C.86. Setup A7 Device 2 test results at 250°C.

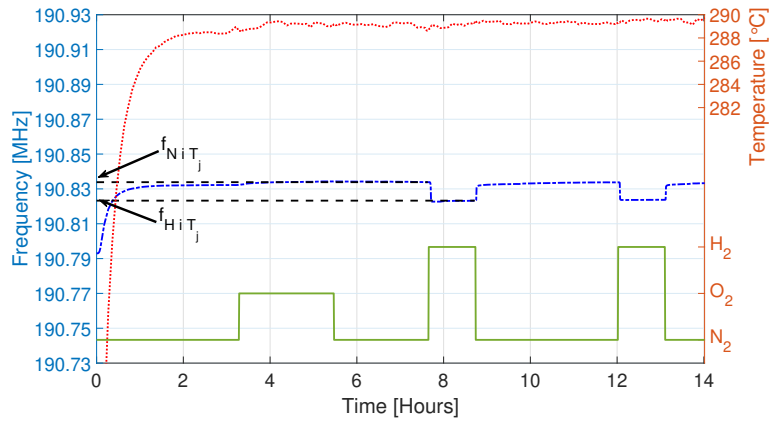


Figure C.87. Setup A7 Device 2 test results at 300°C.

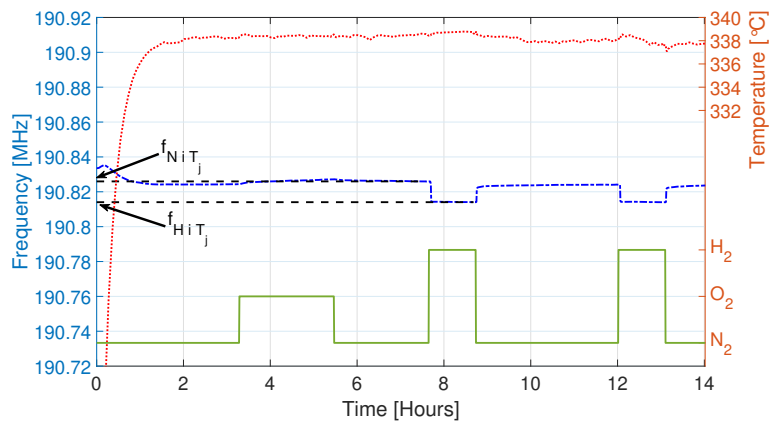


Figure C.88. Setup A7 Device 2 test results at 350°C.

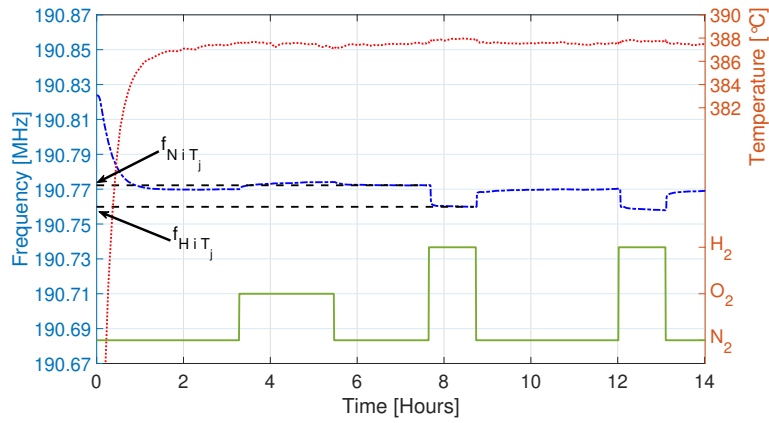


Figure C.89. Setup A7 Device 2 test results at 400°C.

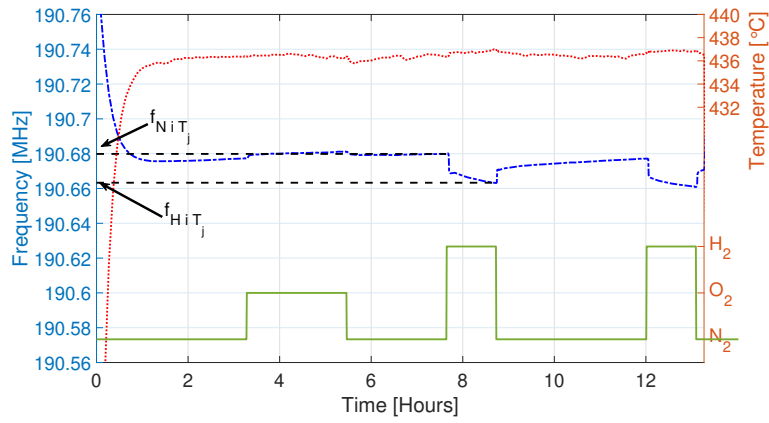


Figure C.90. Setup A7 Device 2 test results at 450°C.

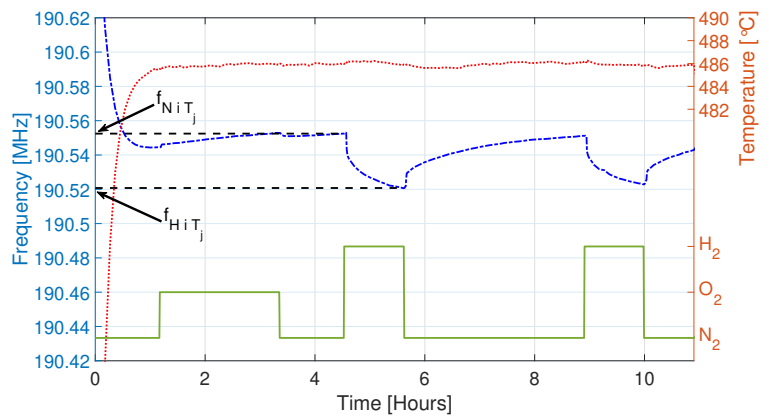


Figure C.91. Setup A7 Device 2 test results at 500°C.

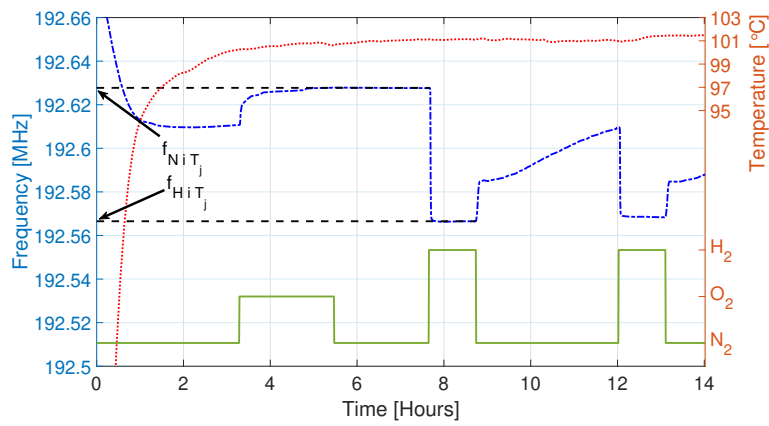


Figure C.92. Setup A7 Device 3 test results at 100°C.

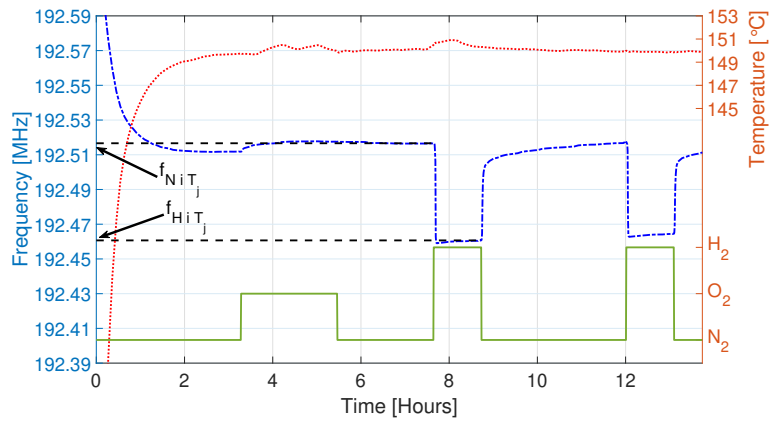


Figure C.93. Setup A7 Device 3 test results at 150°C.

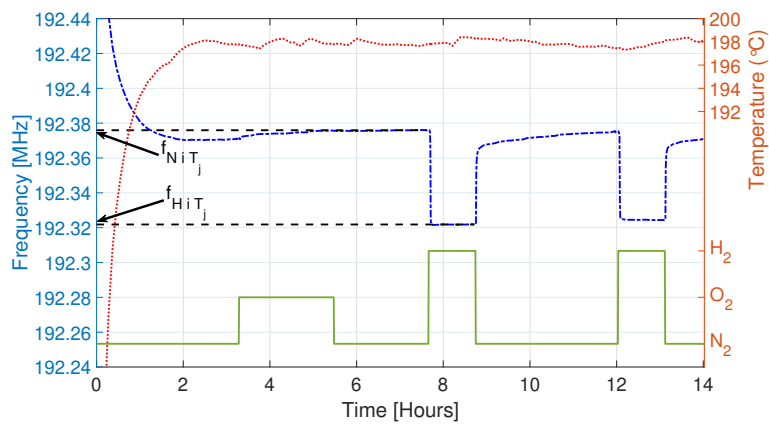


Figure C.94. Setup A7 Device 3 test results at 200°C.

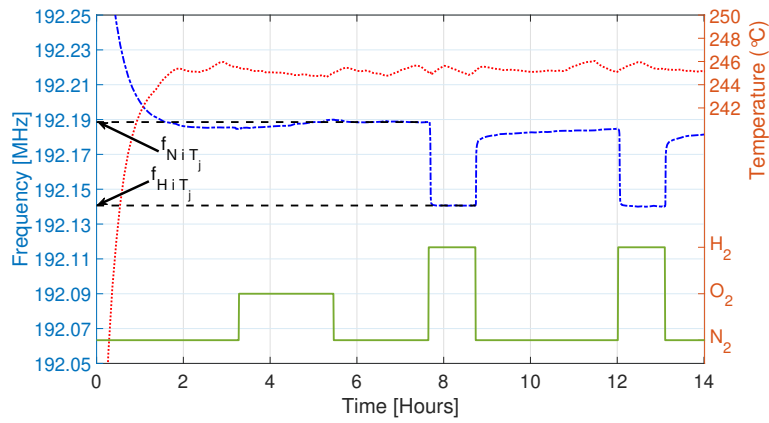


Figure C.95. Setup A7 Device 3 test results at 250°C.

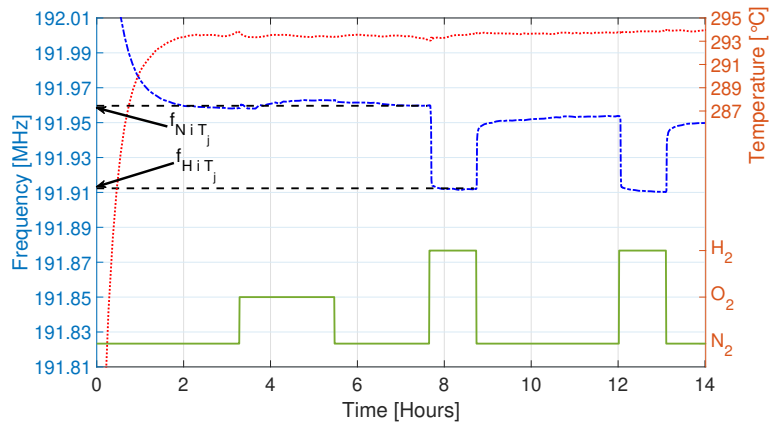


Figure C.96. Setup A7 Device 3 test results at 300°C.

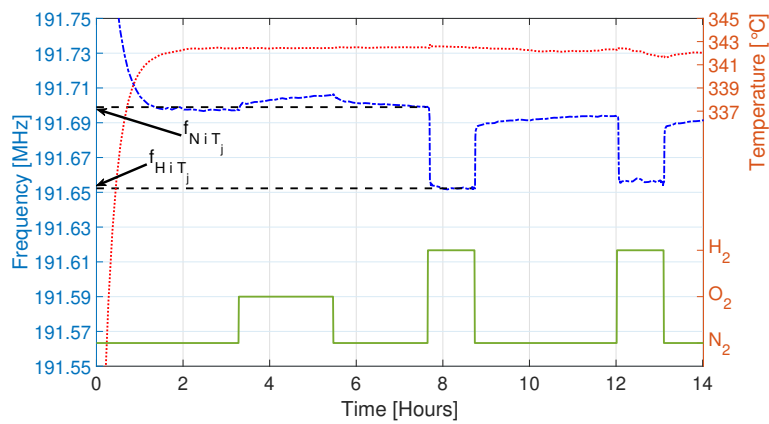


Figure C.97. Setup A7 Device 3 test results at 350°C.

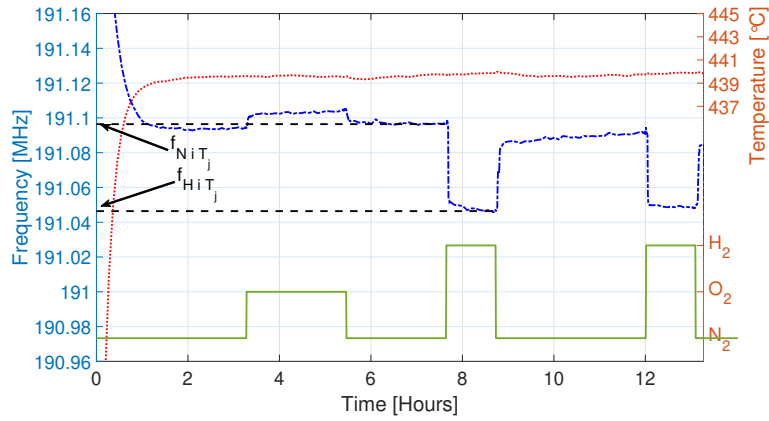


Figure C.98. Setup A7 Device 3 test results at 450°C.

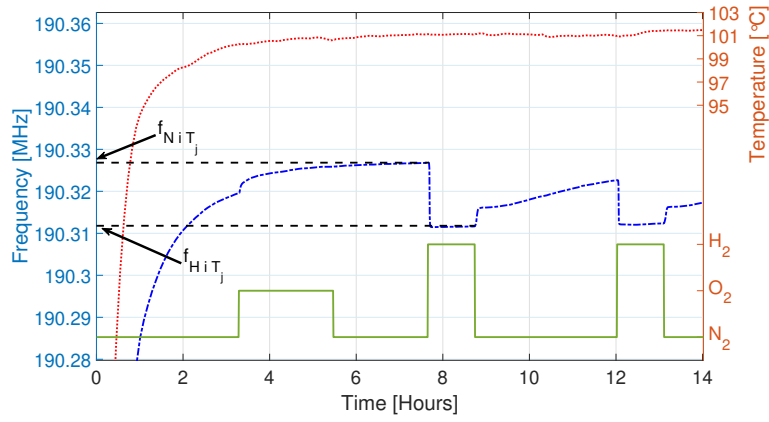


Figure C.99. Setup A7 Device 4 test results at 100°C.

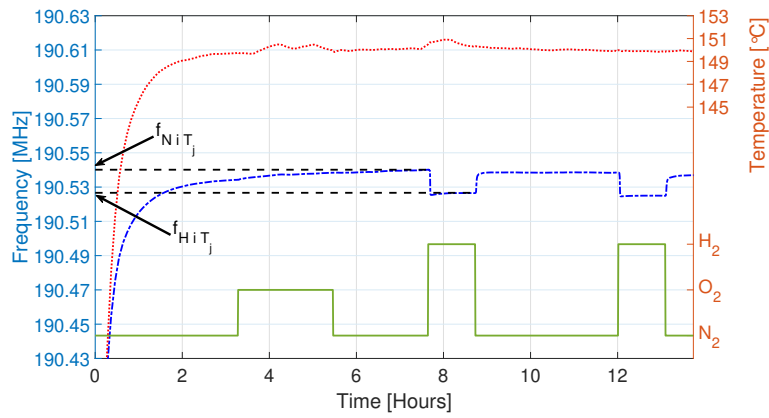


Figure C.100. Setup A7 Device 4 test results at 150°C.

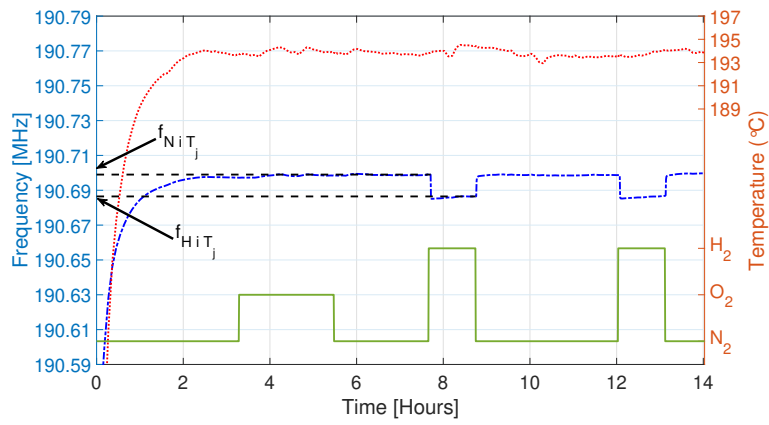


Figure C.101. Setup A7 Device 4 test results at 200°C.

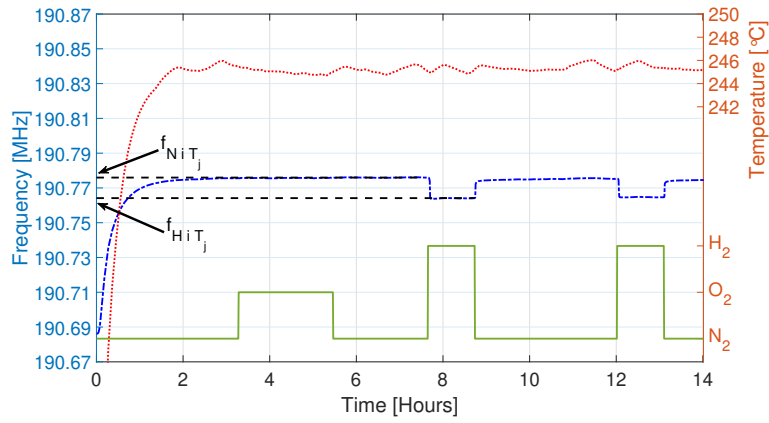


Figure C.102. Setup A7 Device 4 test results at 250°C.

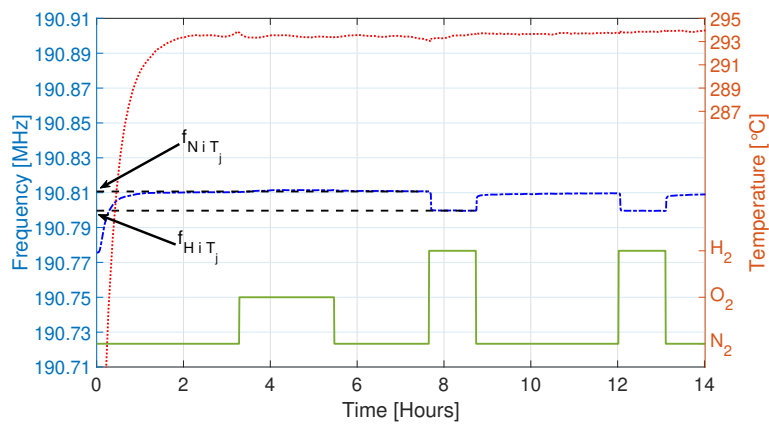


Figure C.103. Setup A7 Device 4 test results at 300°C.

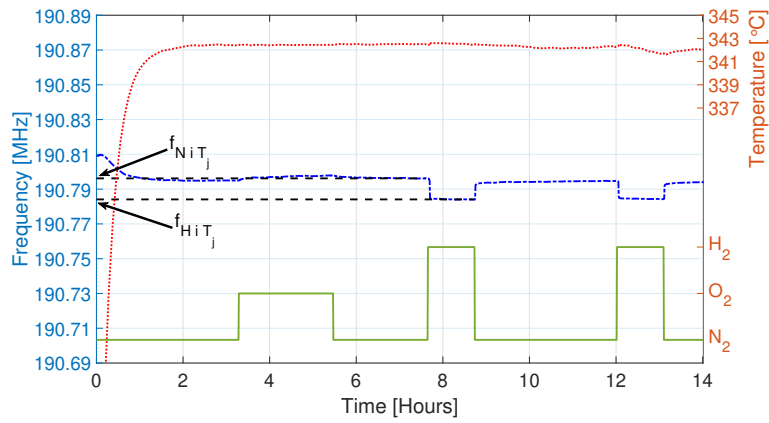


Figure C.104. Setup A7 Device 4 test results at 350°C.

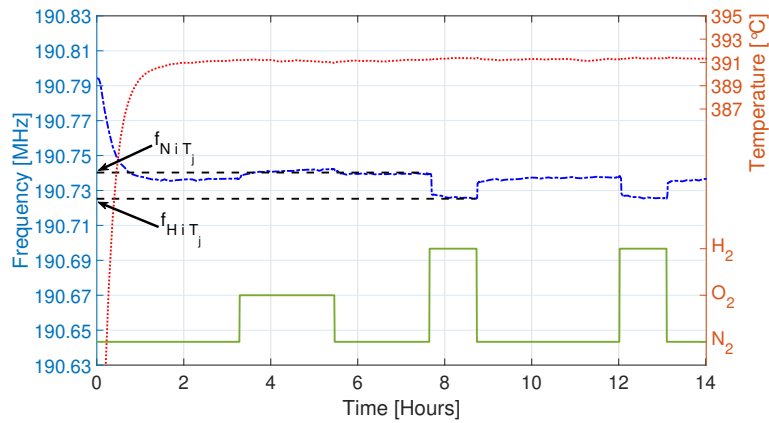


Figure C.105. Setup A7 Device 4 test results at 400°C.

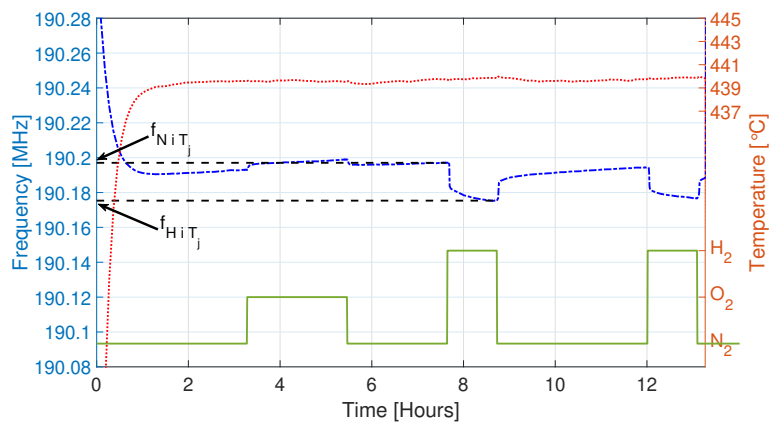


Figure C.106. Setup A7 Device 4 test results at 450°C.

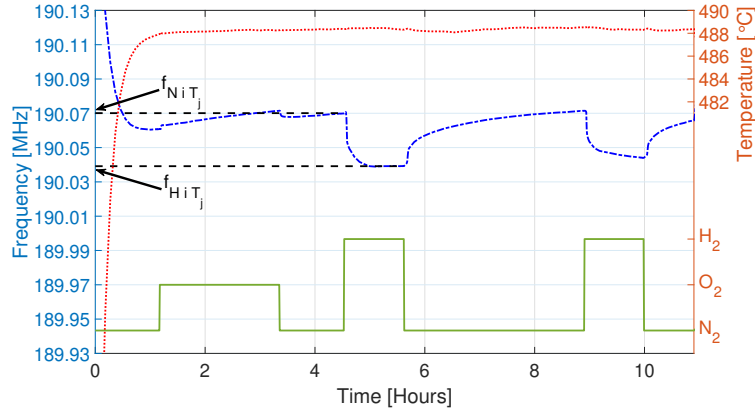


Figure C.107. Setup A7 Device 4 test results at 500°C.

Table C.5. Tabulated results for Setup A7.

$T_j$ (°C)	Std. Dev. $T_j$ (°C)	$f_{NiT_j}$ (MHz)	$f_{HiT_j}$ (MHz)	$\Delta f_i$ (kHz)	$f_{NiT_j}$ (MHz)	$f_{HiT_j}$ (MHz)	$\Delta f_i$ (kHz)
Chamber 1							
		Device 1			Device 2		
99.02	0.13	192.6	192.534	66	190.342	190.327	15
147.24	0.3	192.486	192.424	62	190.554	190.54	14
194.02	0.294	192.34	192.277	64	190.7	190.687	13
240.48	0.21	192.147	192.091	56	190.794	190.78	14
289.12	0.25	191.912	191.859	53	190.834	190.823	11
338.5	0.19	191.638	191.5868	52	190.796	190.784	12
387.67	0.17	191.339	191.285	55	190.772	190.756	16
436.59	0.24	191.01	190.952	58	190.68	190.663	17
485.92	0.15	190.66	190.583	77	190.553	190.521	32
Chamber 2							
		Device 3			Device 4		
101.1	0.04	192.628	192.567	61	190.327	190.312	15
150.33	0.23	192.517	192.461	56	190.54	190.527	13
198.03	0.25	192.376	192.322	54	190.686	190.673	13
245.2	0.2	192.189	192.141	48	190.776	190.764	12
293.46	0.22	191.96	191.912	47	190.811	190.8	11
342.48	0.07	191.699	191.652	47	190.796	190.784	12
391.27	0.07	NA	NA	NA	190.74	190.725	15
439.74	0.13	191.096	191.046	50	190.197	190.175	22
488.34	0.09	NA	NA	NA	190.07	190.039	31

## C.4 Film 1 vs. Film 2 Comparison

The results for Setup A6 (Device 1 Film 2 Bare cycled 14.7°; Device 2 Film 2 Bare cycled 14.7°; Device 3 Film 1 Bare cycled 14.7°; Device 4 Film 1 Bare cycled 14.7°) are given as referenced in Section 4.7. Table C.6 shows the summary of compiled results as described for Setup A6 in Section 4.7 at each temperature (average of the corresponding TC measurements for the test) and the recorded frequency shifts as described in Section 4.7 for Setup A6 results. The results are given in Figures C.74-C.107. All results shown for this section were conducted with 100 sccm flow rates. The results at 600°C for Device 2 were not recorded due to a failure of the 1 mil Pt connection.

Table C.6. Tabulated results for Setup A6.

Temp	$f_{0i}$	$\Delta f$ (kHz)						$f_{0i}$	$\Delta f$ (kHz)					
(°C)	(MHz)	Device 1						(MHz)	Device 2					
	$f_{0i}$	A	B	C	D	E	F	$f_{0i}$	A	B	C	D	E	F
213	191.48	27	21	21	21	20	21	191.494	26	20	19	20	19	20
311	191.308	22	15	17	16	15	17	191.319	24	16	16	17	17	19
412	190.582	24	18	24	26	34	36	190.582	30	18	14	18	32	32
509	190.058	55	46	49	50	62	66	190.096	49	31	25	31	37	42
606	189.428	37	29	28	28	39	48	NA	NA	NA	NA	NA	NA	NA
(°C)	(MHz)	Device 3						(MHz)	Device 4					
	$f_{0i}$	A	B	C	D	E	F	$f_{0i}$	A	B	C	D	E	F
215	191.986	30	22	23	23	23	24	192.168	24	18	19	19	19	19
314	191.394	25	20	21	21	21	22	191.564	20	15	16	16	16	17
415	191.05	29	23	24	24	27	29	191.228	23	19	20	20	23	24
512	190.557	51	45	48	49	51	54	190.735	49	44	47	47	50	52
609	189.908	22	23	25	23	27	28	190.112	19	17	16	15	14	10

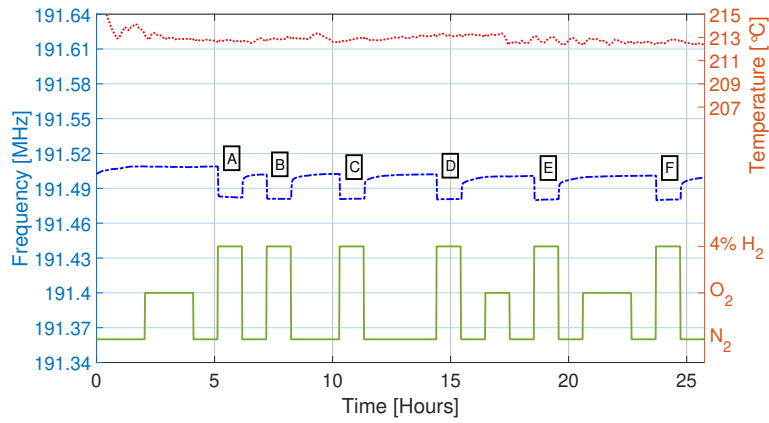


Figure C.108. Setup A5 Device 1 test results at 220°C.

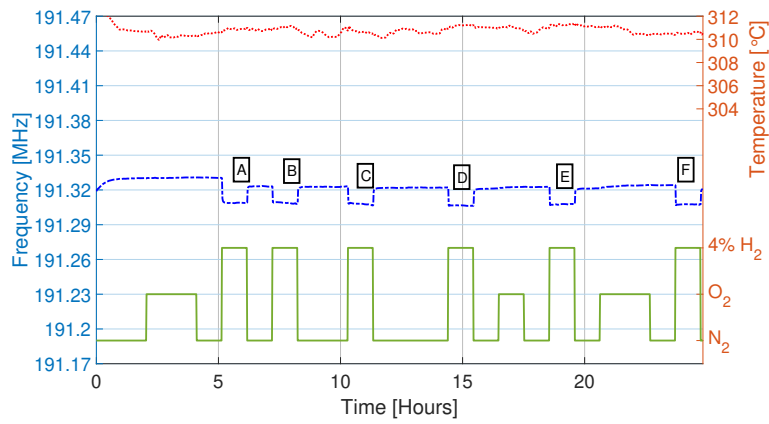


Figure C.109. Setup A5 Device 1 test results at 320°C.

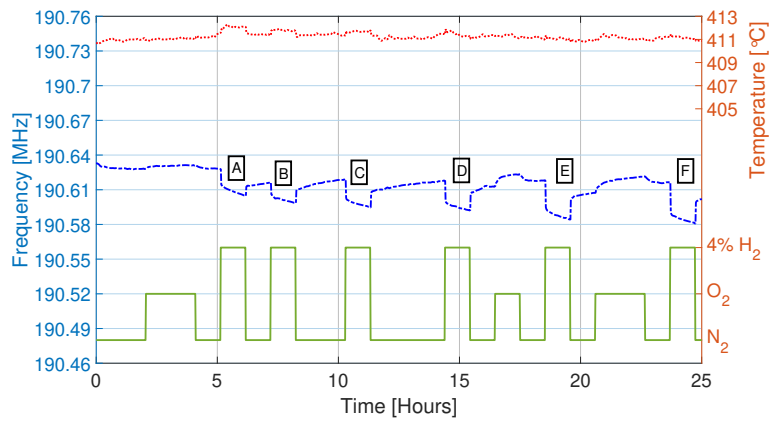


Figure C.110. Setup A5 Device 1 test results at 420°C.

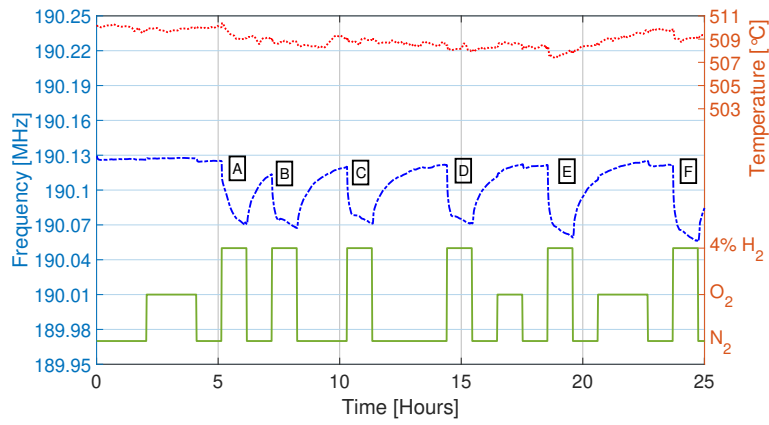


Figure C.111. Setup A5 Device 1 test results at 520°C.

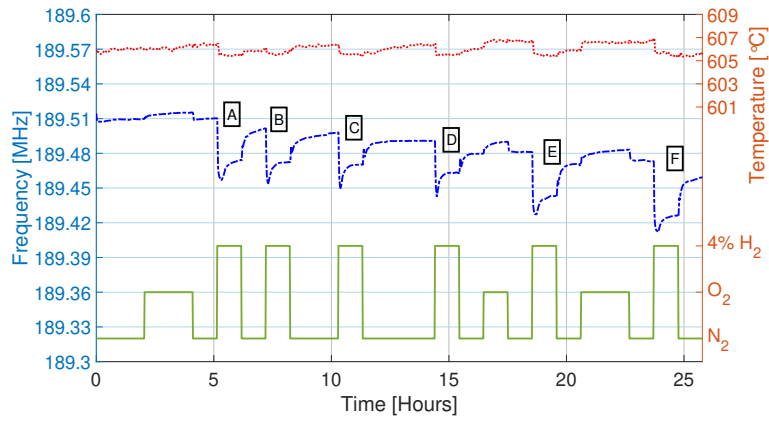


Figure C.112. Setup A5 Device 1 test results at 620°C.

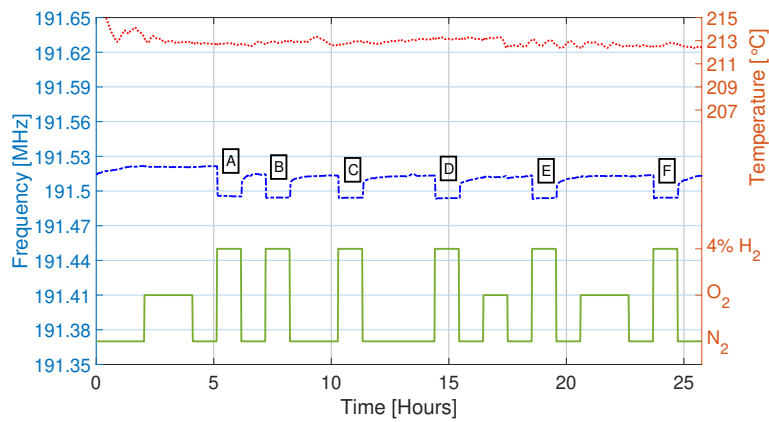


Figure C.113. Setup A5 Device 1 test results at 220°C.

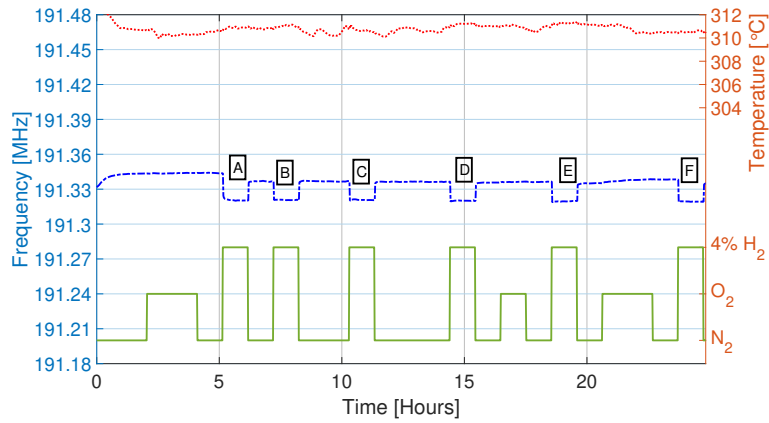


Figure C.114. Setup A5 Device 1 test results at 320°C.

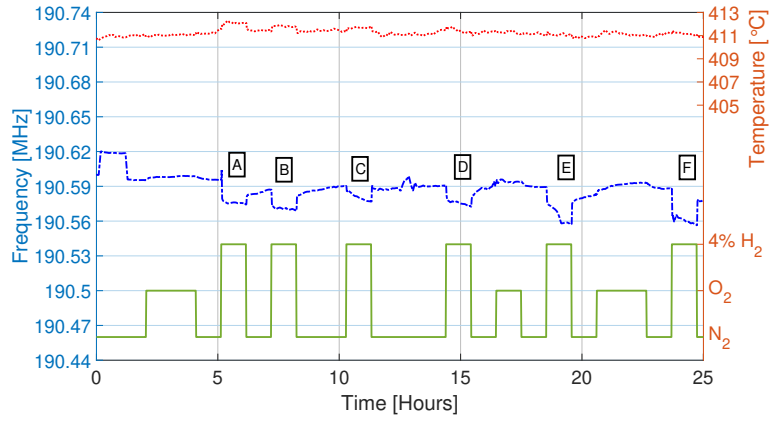


Figure C.115. Setup A5 Device 1 test results at 420°C.

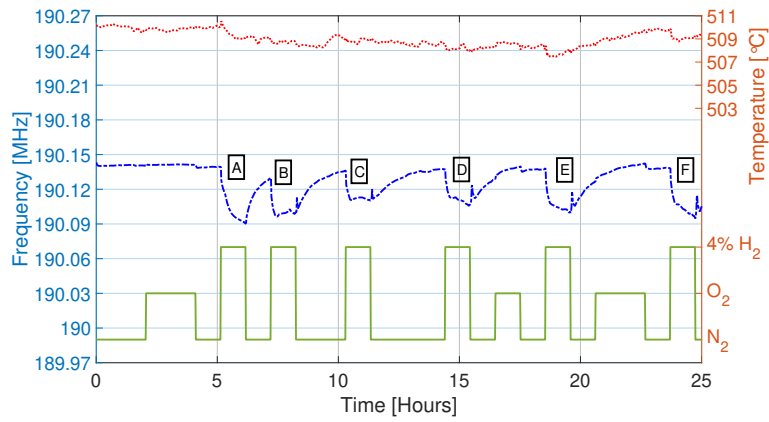


Figure C.116. Setup A5 Device 1 test results at 520°C.

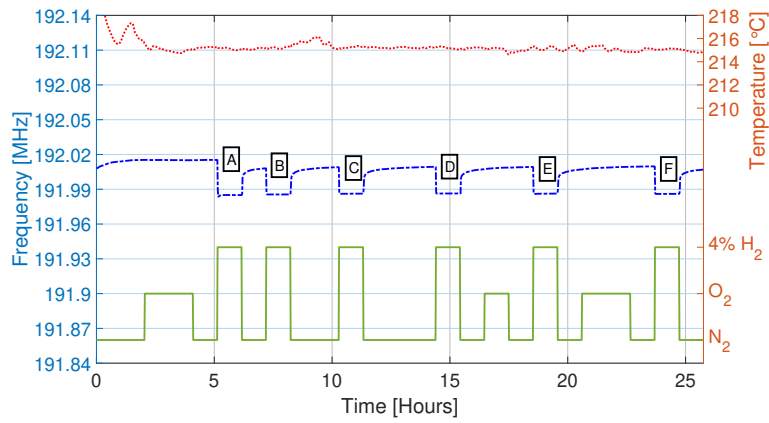


Figure C.117. Setup A5 Device 1 test results at 220°C.

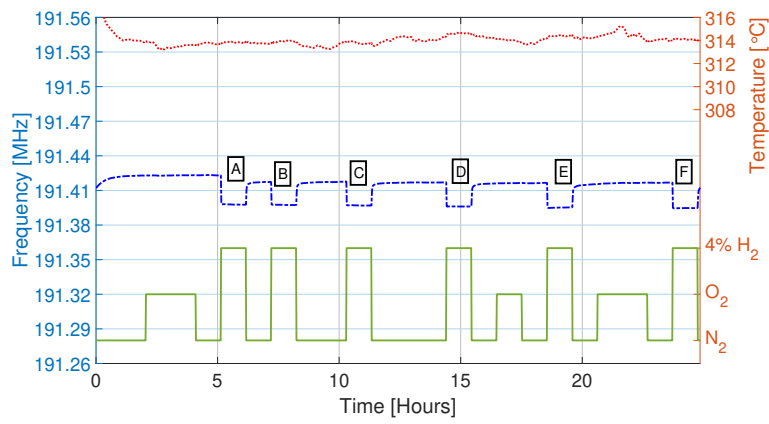


Figure C.118. Setup A5 Device 1 test results at 320°C.

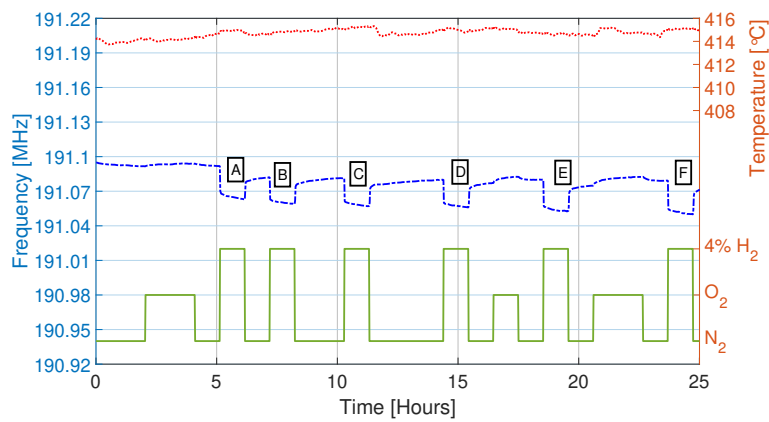


Figure C.119. Setup A5 Device 1 test results at 420°C.

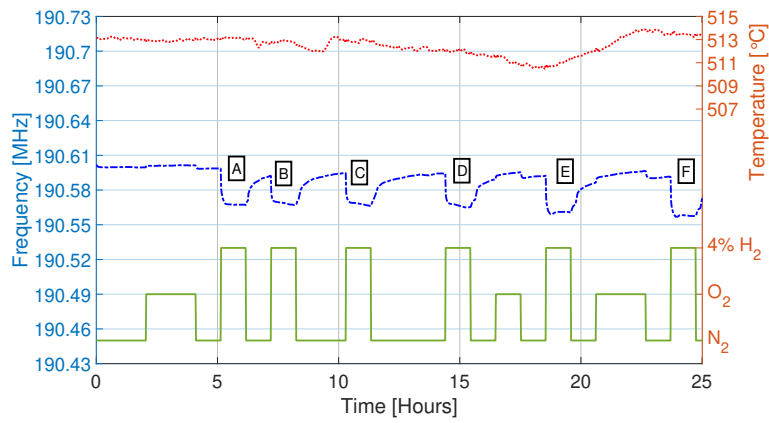


Figure C.120. Setup A5 Device 1 test results at 520°C.

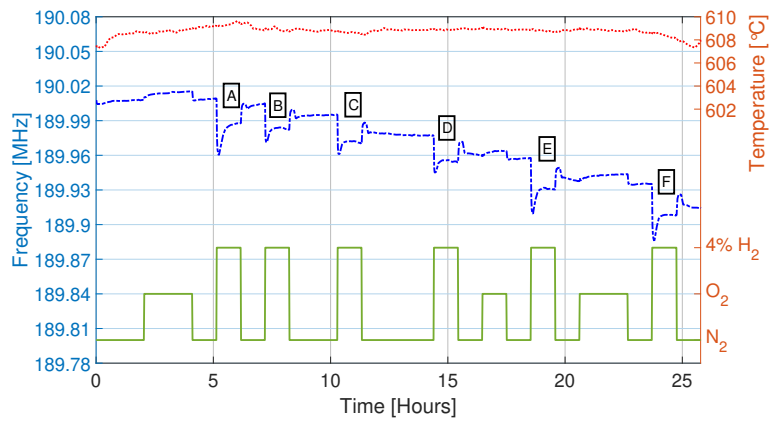


Figure C.121. Setup A5 Device 1 test results at 620°C.

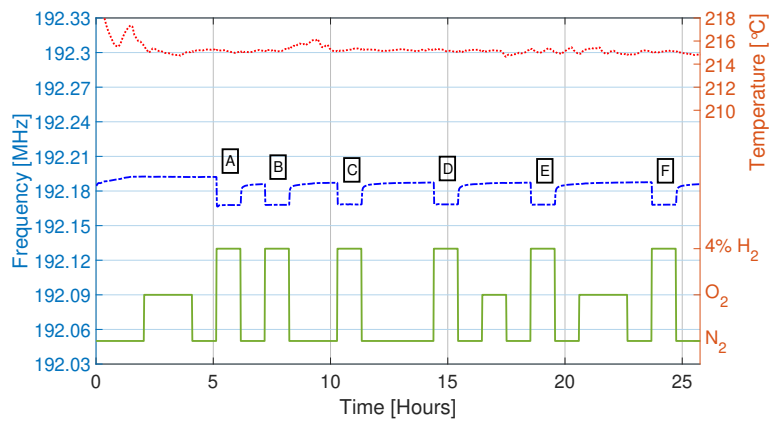


Figure C.122. Setup A5 Device 1 test results at 220°C.

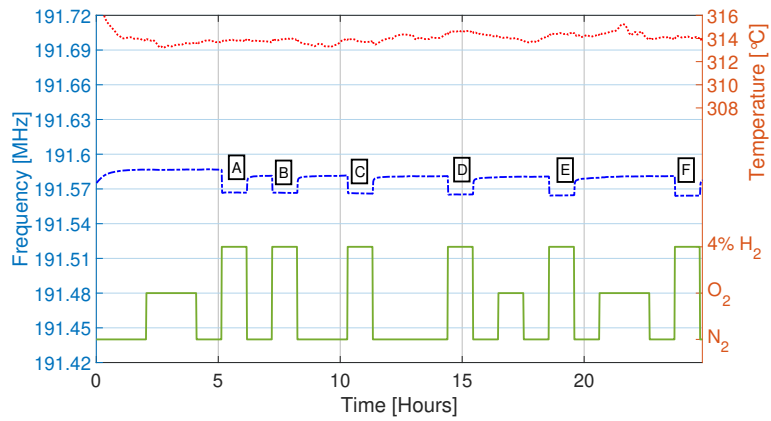


Figure C.123. Setup A5 Device 1 test results at 320°C.

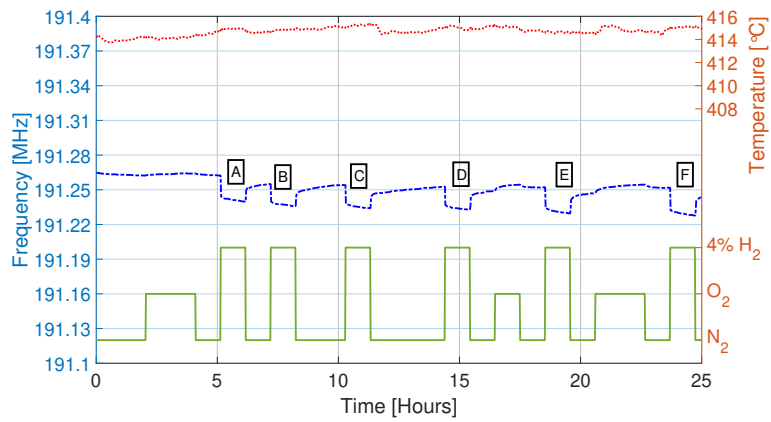


Figure C.124. Setup A5 Device 1 test results at 420°C.

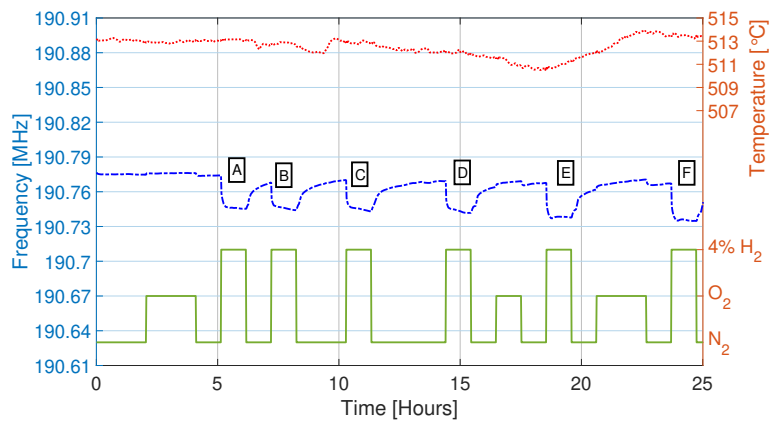


Figure C.125. Setup A5 Device 1 test results at 520°C.

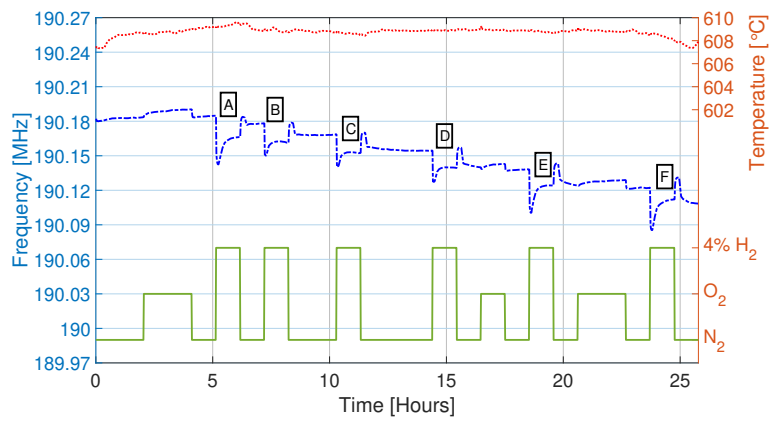


Figure C.126. Setup A5 Device 1 test results at 620°C.

## APPENDIX D

### SIGNAL PROCESSING DETAILS OF TIME-GATING ALGORITHMS

This section details the implementation of two time-gating algorithms in Matlab for frequency tracking of the inductive-loop wireless measurements described in Sections 3.4 and 4.9. A frequency spectrum acquired using the wireless setup described in Section 3.4 with VNA setting of 10 MHz bandwidth centered at 191 MHz, 10,001 points (frequency step of 1 kHz) and 1 kHz IF bandwidth will be used in this appendix as an example. A kaiser window with  $\beta = 15$  was used to avoid the concentration of energy near the edges of the acquired frequency spectrum. A time-gating start of 500 ns and a time-gating stop of  $4\mu s$  was used for time-gating.

#### D.1 Full Frequency Spectrum Representation for Real-valued Time-domain Response

The acquired frequency spectrum may be transformed to a real-valued time-domain response by considering the conjugate spectrum and including it in the Fourier Transform algorithm, as shown in Figure D.1, where the magnitude of the windowed spectrum of measured data is shown [120]. The SAW response is embedded within this spectrum close to the noise level, and the time-gating algorithm will aid in extracting the SAW response. An input to the Matlab `fft()` and `ifft()` functions reflecting this conjugate spectrum was created. For a 1 kHz frequency step, an array extending from  $f = 0Hz$  to the the next power of 2 after the last measurement frequency (196 MHz in this case) was created, and the conjugate values of the measured frequency spectrum mirrored until the end of the mirrored frequency array, as shown in FigureD.2. The Matlab `ifft()` function may then be used to obtain the real-valued time-domain response associated with the windowed spectrum. Time-gating is then applied along the desired time span (500 ns to  $4\mu s$ ) and the `fft()` function is used to

obtain the forward Fourier Transform of the time-gated signal. The implemented code is given below and can be found in in MAL10 under:

```
\\MAL10\Grads\AAyes\MATLAB\TGfullspectrumAA.m
```

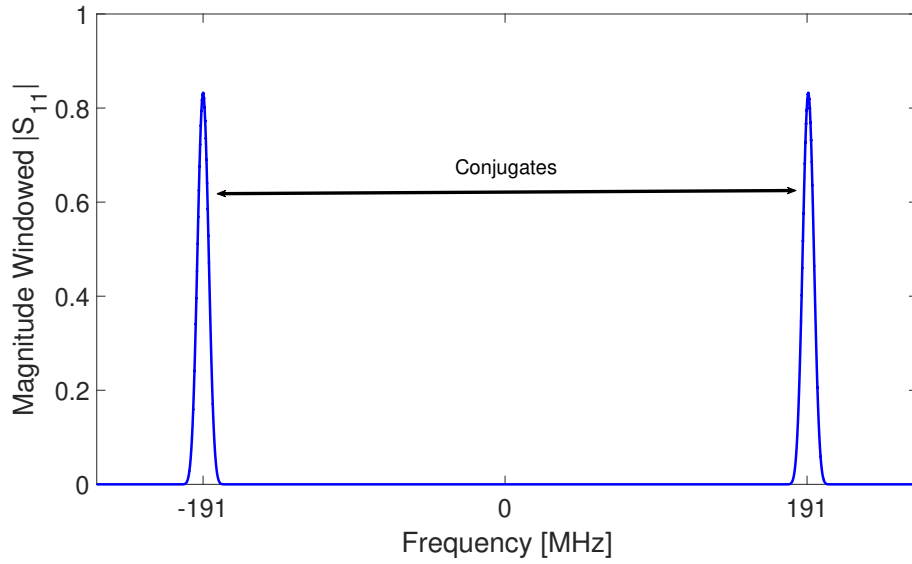


Figure D.1. Conjugate frequency spectrum for real-valued time-domain response.

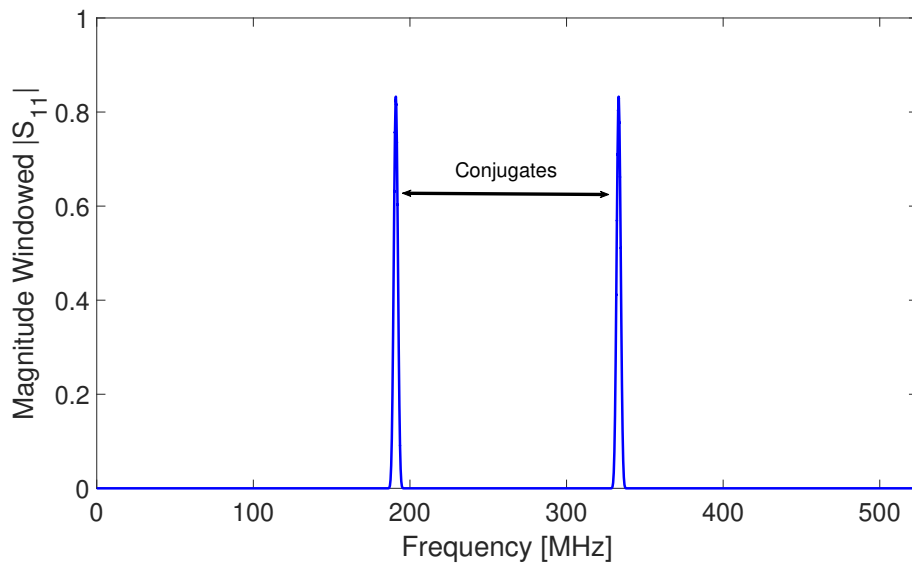


Figure D.2. Array to be passed to Matlab fft functions.

```

function [f3,Hfgated] = TGfullspectrumAA(f,S11,tstart,tstop)
%TGwindowedAA is a time gating funtion to use in conjunction
%with wireless measurements done by inductive loop antenna.
% S11 should be a complex column array with real and
% imaginary components of reflection coefficient and f should
%be a column array in Hz.

```

```

%Variables obtained from frequency information
BW = f(end)-f(1); %Bandwidth of measurement
df = f(2)-f(1); %frequency step

```

```

%Create frequency spectrum for ifft
f1 = (0:df:f(end));
p = nextpow2(length(f1));
f2 = linspace(0,df*(2^(p+1)-1),2^(p+1))';
Hf = zeros(2^(p+1),1);
[ min1, index1 ] = min(abs(f2-f(1)));
[ min2, index2 ] = min(abs(f2-f(end)));
Hf(index1:index2) = S11;

```

```

%Hummels code
N = 2^(p+1);
Hf(N:-1:N/2+2) = conj( Hf(2:N/2));

```

```

%take ifft from frequency to time
Ht = ifft(Hf);

```

```

Ts = 1/df;
t = linspace(0, Ts, 2^(p+1));
%Nowindow
%Htnowindow = ifft(Hfnowindow);

%gate in time using window
[mintime1, indextime1] = min(abs(t-tstart));
[mintime2, indextime2] = min(abs(t-tstop));

%Hummels code
Htgated = zeros(N,1);
Htgated(indextime1:indextime2) = Ht(indextime1:indextime2);

%take fft from time to frequency
Hfgated = fft(Htgated);

f3 = f2(index1:index2);
Hfgated = Hfgated(index1:index2);

end

```

## D.2 Bandpass Spectrum Representation for Complex-valued Time-domain Response

Additionally, the acquired frequency spectrum may be transformed into a complex-valued time-domain response by moving the spectrum to the frequency origin, which is the equivalent of multiplying the time domain signal by an  $e^{j2\pi f_0 t}$  term, where  $f_0$  is the reference frequency (in this case, the center frequency of the measured spectrum, or 191 MHz), as

shown in Figure D.3 [120], where the magnitude of the windowed spectrum has been displaced from the 191 MHz center frequency to have a center frequency of 0 Hz. The SAW response is embedded in the displaced spectrum close to the noise level and the time-gating algorithm will aid in extracting the SAWR sensor peak. The resulting windowed and displaced spectra can be placed in an array with a length of power 2 that is large enough to fit the displaced spectrum. The `ifft()` can then be implemented to obtain the complex-valued time-domain response where the time-gating is implemented. The `fft()` is then taken to obtain the time-gated frequency spectrum.

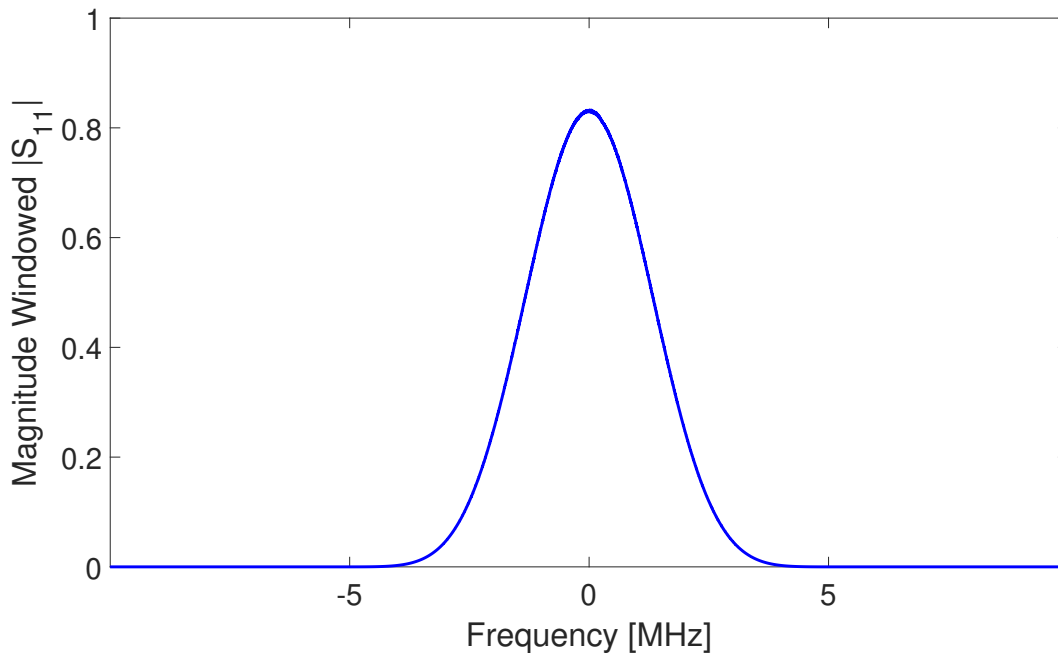


Figure D.3. Displaced spectrum for complex-valued representation of time-domain response.

The advantage of the bandpass spectrum representation is that it allows for the clear identification of the sensor response in the time-domain, which is not possible using the real-valued time-domain response from the full spectrum representation. This is due to the fact that the sensor information is now contained in the phase of the complex-valued time-domain response, as shown in Figure D.4. The slope of the phase in the region marked as sensor response in Figure D.4 denotes the frequency offset of the sensor energy with respect

to the selected value of  $f_0$  (191 MHz), which in this case was the center of the measured spectrum (191 MHz) [120].

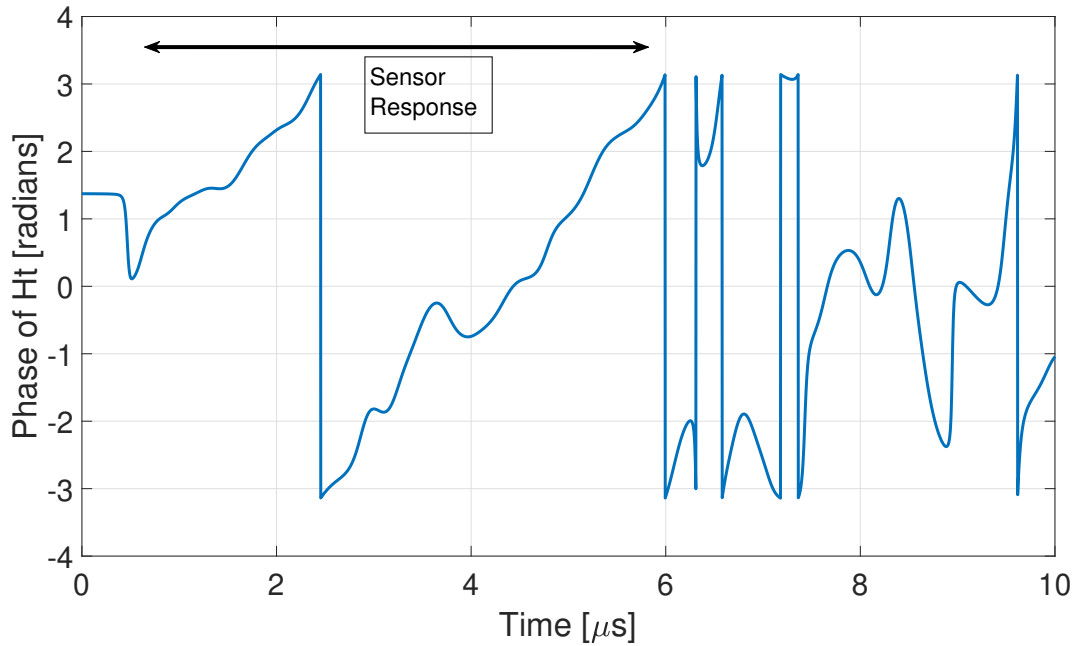


Figure D.4. Phase of the complex-valued time-domain response.

The implemented code is given below and can be found in in MAL10 under:

```
\\MAL10\Grads\AAyes\MATLAB\TGfullcomplexrepAA.m
```

```
function [fout ,Hfout] = TGcomplexrepAA(f ,Hfin ,t_start ,t_end ,N)
%TGcomplexrepAA is a time gating algorithm using a bandpass
%complex representation of the time-domain signal of the
%acquired frequency spectrum. This code was developed with
%help from Dr. Don Hummels
% f is the frequency array of measured data. Hfin is the
% windowed S11 complex data. tstart is the initial time
% of the time gate and tstop is last time of the time gate.
% N is the number of points in the FFTs.
```

```

% Prepare for indexing for the FFT
Nd = length(f);      % Data length
df = f(2)-f(1);     % Frequency resolution of measurement
T = 1/df;           % Total period (seconds) covered by ifft
dt = T/N;           % Time resolution
ff = zeros(N,1);    % frequency offsets from center in fft
ff(1:N/2+1) = (0:N/2)*df;
ff(N:-1:N/2+2) = (-1:-1:-(N/2-1))*df;
tt = (0:N-1)*dt;    % Time values in FFT arrays

% Select the reference frequency for the complex representation
f0 = (f(end)-f(1))/2 + f(1);

[junk,n0] = min(abs(f-f0)); % n0 = index of reference freq
f0 = f(n0);               % Actual reference frequency
n_pos = Nd-n0+1;          % Number of samples at or above f0;
n_neg = Nd-n_pos;         % Number of samples below f0

% Move the measured data into the FFT array
ss11 = zeros(N,1);
ss11(1:n_pos) = Hfin(n0:end);
ss11(N-n_neg+1:N) = Hfin(1:n0-1);

% Inverse transform gives the impulse response
h_ss11 = ifft(ss11);

```

```

% Time window the result
ind = find (tt>t_start & tt<t_end);
twin_N = length(ind);
twin = window(@rectwin,twin_N);
tw = zeros(N,1);
tw(ind) = twin;
h_ss11_w = h_ss11.*tw;

% Back to s11 values using the time-windowed data...
ss11_w = fft(h_ss11_w);

%Outputs
fout = ff+f0;
Hfout = ss11_w;

end

```

### D.3 Comparison of Time-gated Results

Figure D.5 shows the obtained time-gated frequency spectrum results for the Full Spectrum and Bandpass Spectrum algorithms described, as well as the results for the time-gated frequency spectrum results for the Chirp-z transform algorithm implemented by Dr. Thomas Pollard [120], [121]. All of the algorithms coincide for the extraction of the resonant frequency of the SAWR sensor. The resonant frequency of the SAWR can be interpreted to be the maximum value of this time gated response, and corresponds to 191.255 MHz. The slope obtained in Figure D.4 was about 280 kHz, showing that the slope of the phase for the complex valued time-domain response does correspond to the extracted frequency of the SAW sensor.

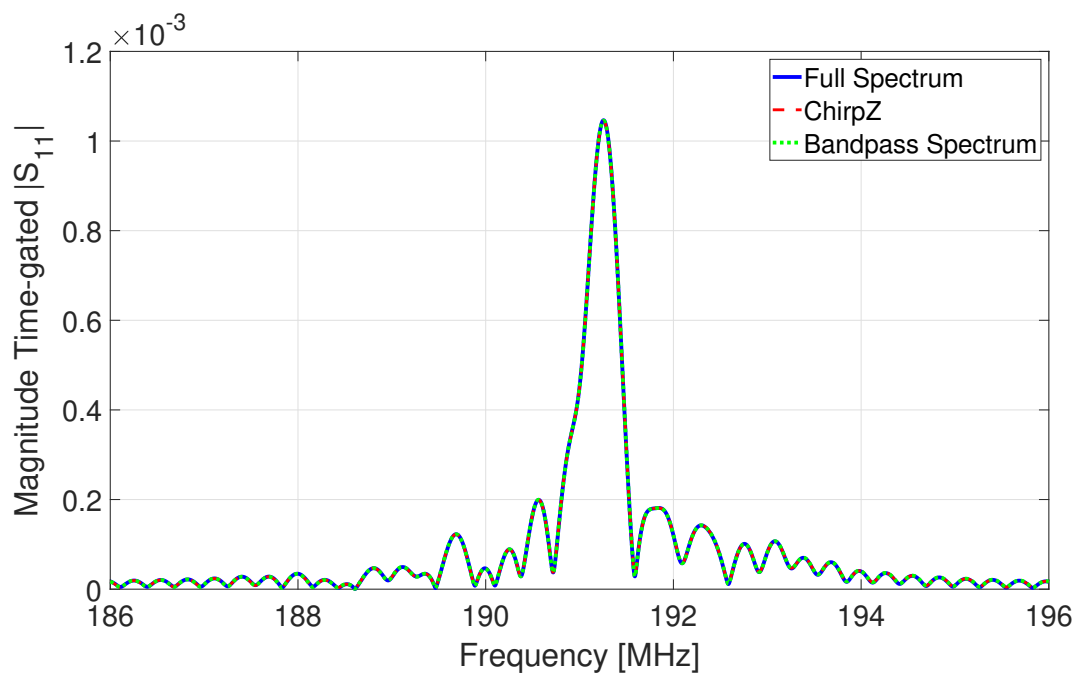


Figure D.5. Time-gated spectra for all algorithms.

## BIOGRAPHY OF THE AUTHOR

Armando Emilio Ayes Moncada was born in Tegucigalpa, Honduras in 1994. He spent a year abroad in Saarbrücken, Germany for his Junior year in High-school. He obtained his B.S. degree in Electrical and Computer Engineering from the University of Maine in 2017. His research interests include microwave acoustics, surface acoustic wave devices, signal processing, and sensors for harsh-environments. Mr. Ayes worked as a graduate research assistant in the Microwave Acoustics Laboratory, and as a graduate teaching assistant for ECE 351 Fields and Waves and ECE 453 Microwave Engineering. Mr. Ayes presented three papers at the 2019 IEEE Ultrasonics Symposium held in Glasgow Scotland. Mr. Ayes will begin his career in industry in 2020 with Qorvo Inc. as a Filter Design Engineer. Armando Emilio Ayes Moncada is a candidate for the Master of Science degree in Electrical Engineering from the University of Maine in May 2020.